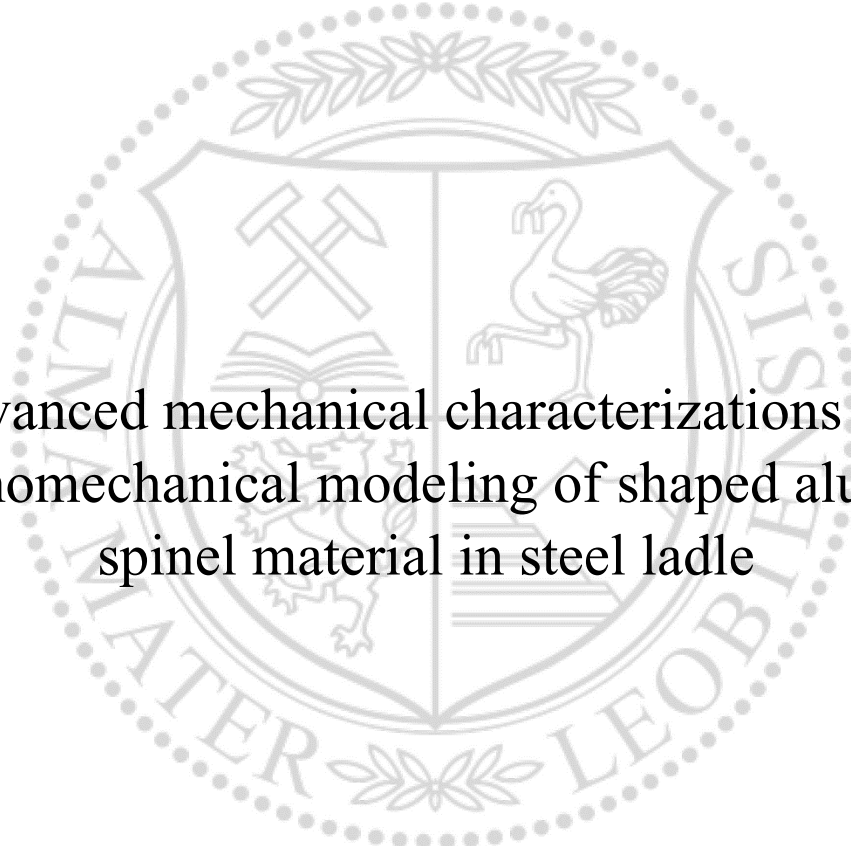




Chair of Ceramics

Doctoral Thesis



Advanced mechanical characterizations and
thermomechanical modeling of shaped alumina
spinel material in steel ladle

Soheil Samadi, M.Sc.

October 2021



AFFIDAVIT

I declare on oath that I wrote this thesis independently, did not use other than the specified sources and aids, and did not otherwise use any unauthorized aids.

I declare that I have read, understood, and complied with the guidelines of the senate of the Montanuniversität Leoben for "Good Scientific Practice".

Furthermore, I declare that the electronic and printed version of the submitted thesis are identical, both, formally and with regard to content.

Date 19.10.2021

A handwritten signature in black ink, appearing to read 'Soheil Samadi', written over a horizontal line.

Signature Author
Soheil Samadi

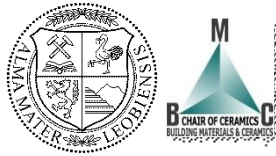
To my beloved Parents and Grandparents,

Aknowledgements

The author gratefully acknowledges that this work was supported by the funding scheme of the European Commission, Marie Skłodowska-Curie Actions Innovative Training Networks in the frame of the H2020 European project ATHOR - Advanced THERmomechanical multiscale modeling of Refractory linings [grant number 764987]. I would like to thank all my **colleagues/friends** in ATHOR for all the help and collaborations we had during the project. I wish that our friendship and connection stay forever.



Secondly, this research work was carried out at the Chair of Ceramics at Montanuniversität Leoben. I would like to thank my supervisors especially **Dr. Shengli Jin** whose constant support was a great help for my PhD work. I learned a lot from his broad knowledge and expertise. I will always remember his patient supervision and friendly working attitude. I am honored to have the opportunity to work under the supervision of **Prof. Harald Harmuth**. I am deeply thankful for his kind guidance. Next, I would express my gratitude to **Dr. Dietmar Gruber** who provided me with his helpful insights. I enjoyed all the discussions with him and his passion in the science inspired me. Finally, I would thank all other **colleagues** of mine at the Chair of Ceramics who helped and supported me during this time.



Additionally, I am grateful to have my **parents** as my support in all stages of my life. They always encouraged me to develop myself and taught me patience, generosity and diligence. Beside my parents, I am thankful to have a supportive family. Here, I would like to mention my grandmother and uncle who passed away when I was doing this research work.

Last but not least, I am indebted to my friends who were there for me in happiness and sadness: **Zahra, Hesam, Majid, Hung, Omid, George**, and many others who I ask for their pardon for not mentioning their names because I really want to finish this in one page!

Abstract

The application of refractory materials at high temperatures necessitates special material properties, which influences the material wear, the energy consumption, and the production cost. Therefore, the failure mechanism investigation of refractory materials is of great importance. The current study aimed to investigate the possible thermomechanical failure of the refractory lining used in a steel ladle with the help of finite element analysis. As different material parameters are required for the FE-simulations, an experimental study was designed to obtain them. Therefore, the outline of this study consists of two main parts, i.e., mechanical characterization and thermomechanical simulation.

In the first part, high-temperature mechanical tests were applied to investigate the necessary material properties of a shaped alumina spinel refractory, which is used in the working lining of the investigated steel ladle. The experimental study included Young's modulus measurements, uniaxial compressive and tensile creep tests, modified shear test and wedge splitting test. In this part of the study, several improvements were implemented in the material characterization methods. Firstly, a statistical study was introduced in the creep behavior investigation since a high scatter was received in the creep results due to the material heterogeneity. The second improvement was applied in tensile failure characterization. A novel material constitutive model was developed to be employed together with wedge splitting test and evaluate the refractory fracture parameters at high temperatures. The model overcomes the limitations of the concrete damaged plasticity model in Abaqus. It could deliver more accurate results by considering simultaneously creep and fracture behavior.

In the second part of the research study, the evaluated material parameters were employed in the thermomechanical simulation of the steel ladle. A unit-cell modeling approach was applied, and three different constitutive material models were considered, each corresponding to an irreversible deformation mechanism. Creep behavior was simulated using the Norton-Bailey creep model, shear failure using the Drucker-Prager yield criterion, and tensile failure using the concrete damaged plasticity. The results of the three models were compared to observe the influence of each failure phenomenon on the stress-strain responses of the lining and the steel shell.

Table of Contents

1. Problem definition and applied methodology	1
2. State of the art.....	2
2.1 Mechanical characterization of ordinary ceramic refractories	3
2.1.1 Elasticity and associated constitutive model	4
2.1.2 Creep behavior and associated constitutive models	5
2.1.3 Shear failure and associated constitutive models	10
2.1.4 Tensile failure and associated constitutive models	13
2.2 Thermomechanical modeling methods for refractory linings	17
2.2.1 Homogenization method	19
2.2.2 Unit-cell method.....	21
2.2.3 Comparison of homogenization technique and unit-cell modeling approach.....	23
3. Results	25
3.1 Mechanical characterization results.....	26
3.1.1 Young's modulus measurements.....	26
3.1.2 Creep behavior characterization	27
3.1.3 Shear failure characterization	33
3.1.4 Tensile failure characterization	34
3.2 Thermomechanical modeling of the steel ladle.....	40
3.2.1 Temperature results	46
3.2.2 Joint size and friction coefficient effect	46
3.2.3 Stress and strain results	47
3.2.4 Influence of steel shell plasticity	50
3.2.5 Joint openings	51
4. Concluding remarks	53
4.1 Mechanical characterization	53
4.2 Thermomechanical simulation	54
5. Outlook.....	55

6. References	56
7. Appendix A	66
8. List of publications	69
9. Appended publications	71

Table of Figures

Figure 1: Refractories application (steel ladle) [4]	2
Figure 2: Refractory lining of a steel ladle	3
Figure 3: Displacement-time curve of three creep stages [21].....	6
Figure 4: (a) Specimen’s geometry for uniaxial compressive creep experiments and (B) the experimental device [23].....	7
Figure 5: Specimen preparation for uniaxial tensile creep testing [23].....	8
Figure 6: Uniaxial tensile creep test device [24]	8
Figure 7: Flow chart of the inverse evaluation method to obtain the creep parameters [31]	10
Figure 8: Three modes of crack opening [32]	11
Figure 9: Linear Drucker-Prager yield surface [28]	11
Figure 10: (a) Modified shear test specimens and (b) determination of Drucker-Prager criterion parameters	13
Figure 11: Fictitious crack model [45]	14
Figure 12: Material behavior under (a) uniaxial tensile load and (b) uniaxial compressive load according to the CDP model [28]	14
Figure 13: WST Specimen’s dimensions (in mm) [55].....	15
Figure 14: Typical load-displacement curve from WST [59]	17
Figure 15: (a) An example of a steel ladle model used in homogenization technique [6] and (b) Biaxial compression test employed for characterization of overall behavior of refractory linings [70].....	19
Figure 16: Possible joint states of dry refractory lining along with the joint closure/opening criteria [6]	20
Figure 17: Unit-cell model of slag zone lining in a steel ladle [76].....	21
Figure 18: Application area of alumina spinel bricks in the steel ladle	25
Figure 19: SEM image of the investigated shaped alumina spinel refractory [83]	25
Figure 20: Specimen dimensions for Young’s modulus measurements	26
Figure 21: Young’s modulus measurements on alumina spinel bricks - room temperature (left) and high temperature (right)	27
Figure 22: (a) Schematic of the specimens drilled out of a brick for study of the influence of their position and drilling direction and (b) their uniaxial compressive creep test results (with the Young's modulus added next to the respective curve). [83]	28
Figure 23: Uniaxial compressive creep test results of alumina spinel bricks [83]	29

Figure 24: Uniaxial tensile creep test results of alumina spinel bricks [85]	30
Figure 25: Comparison of the uniaxial tensile and compressive creep results of the shaped alumina spinel refractory at similar temperatures	31
Figure 26: Comparison of compressive and tensile creep parameters of alumina spinel bricks at similar temperatures	33
Figure 27: Friction angle and cohesion obtained from modified shear test results of alumina spinel bricks	34
Figure 28: Drucker-Prager criterion for different temperatures	34
Figure 29: (a) WST fractured specimen and (b) load-displacement curves from different temperatures	35
Figure 30: Specific fracture energy (Gf'), nominal notch tensile strength (σ_{NT}) and brittleness number (B) at different temperatures for alumina spinel bricks	35
Figure 31: Schematic of the DECR model and its parameters [56]	36
Figure 32: (a) WST 2D and symmetrical model and (b) its boundary conditions [55]	37
Figure 33: WST results of alumina spinel bricks and their simulated curves at room temperature [55].	38
Figure 34: Inverse identified curves of the WST results at 1200 °C using DECR and CDP model [56].	39
Figure 35: 2D Sketch of the industrial steel ladle	40
Figure 36: 3D unit-cell model of the steel ladle refractory lining	41
Figure 37: Insulation board, insulation lining and safety lining in the steel ladle	42
Figure 38: Consideration of joints in the steel ladle unit-cell model	43
Figure 39: Temperature definition at the hot face during preheating and first steel ladle working cycle (together with the measured data during the preheating step)	44
Figure 40: Simulated temperatures of different layers in barrel zone (preheating and five working cycles)	46
Figure 41: Influence of initial vertical joint size and friction coefficient on the maximum von Mises stresses in the working lining and steel shell, and the mean radial displacement of the steel shell	47
Figure 42: Alumina spinel brick model	47
Figure 43: Stress at the hot face and middle of the selected alumina spinel brick	48
Figure 44: Equivalent irreversible strain under different failure mechanisms with time	49

Figure 45: Shear failure simulation p-q diagram at the hot face of the selected AS brick till the end of 1 st pouring.....	49
Figure 46: Volumetric strains on the center path of the selected alumina spinel brick at the end of the 5 th cycle	50
Figure 47: Influence of the shell plasticity on strain energies (E) in different simulations	51
Figure 48: Vertical joint opening on the alumina spinel brick hot face in different simulations	52

Table of Tables

Table 1: XRD measurement semi-quantitative results on a heated and a virgin specimen of alumina spinel bricks.....	27
Table 2: Uniaxial compressive creep testing plan [83]	28
Table 3: Uniaxial tensile creep testing plan [85].....	28
Table 4: Mean correlation coefficients table for Young’s modulus, bulk density, and creep strain rates from the compressive creep tests [83]	31
Table 5: Uniaxial compressive and tensile creep parameters for the primary creep stage at different temperatures [85]	32
Table 6: Uniaxial compressive and tensile creep parameters for the secondary creep stage at different temperatures [85].....	33
Table 7: Material models assigned to the WST model [55,56].....	37
Table 8: Alumina spinel bricks’ fracture properties at room temperature (experimental and inversely evaluated with DE model) [55]......	38
Table 9: Comparison of inversely evaluated fracture parameters at 1200 °C (average of three WST results) using DECR and CDP model [56].	39
Table 10: Inversely evaluated fracture parameters of CDP model for alumina spinel bricks	40
Table 11: Refractory materials used in the steel ladle.....	41
Table 12: Material properties required for the thermomechanical simulations	42
Table 13: Working cycles of the studied steel ladle	44
Table 14: material constitutive models applied for different lining components and simulation cases.....	45

1. Problem definition and applied methodology

Refractory materials are often used in linings of vessels that hold and treat fluids at elevated temperatures (above 1000 °C) to protect their metallic structures from the molten products they contain. Failure of refractory lining might result in the entire process cycle being shut down and a significant financial loss. As a result, the investigation of potential failure causes is critical. On the other hand, application of measurement methods directly on the refractory linings in service, is practically impossible. Therefore, the application of numerical simulations is a necessity to reproduce the refractory material behavior in actual working conditions, analyze their failure mechanisms and predict their lifetime.

Steel ladles are used to transport, refine, and cast molten steel. This vessel can have a direct impact on steel quality and accounts for the highest ratio of total refractory consumption in iron and steel industries. Therefore, the main objective of the current Ph.D. thesis was to investigate the thermomechanical failure mechanisms of a steel ladle refractory lining composed of shaped refractories with the help of finite element method. Three major phenomena, which cause irreversible deformation for refractory linings, were studied, namely creep, shear failure and tensile failure.

The determination of material mechanical properties is a prerequisite for modeling their behavior, and thus experimental studies were planned to identify the necessary parameters for the applied material models. In this part of the study, improvements were made in the characterization methodologies for refractory materials: a statistical study was done on the creep behavior of refractories to assess the effect of microstructure heterogeneity on the creep parameters; In the case of tensile fracture, a damaged elasticity model was developed to mitigate the influence of residual stress defined in the constitutive model, and model combining damaged elasticity and Norton-Bailey creep was developed to simulate the combined effect of tensile fracture and creep during high temperature fracture.

In the simulation part of the research, a unit-cell modeling approach was employed for the thermomechanical simulation of the steel ladle to reduce the computational costs. The Norton-Bailey creep law, Drucker-Prager criterion, and concrete damaged plasticity model were employed to respectively model the creep, shear failure and tensile failure in the working lining of the steel ladle. Five process cycles of the ladle were simulated, and the results of different material models were compared together.

2.State of the art

Refractories are unique ceramic materials, produced from various kind of mineral and chemical raw materials. Their production process contains several steps: it starts with extraction of raw materials; then the raw materials experience various treatment phases such as crushing, sorting by size, calcination and drying; afterwards, different raw materials are mixed based on the desired chemical and thermomechanical properties; dependent on the applications, the mixture might undergo further process steps [1].

Depending on the form of the product, refractories can be categorized into two groups, unshaped refractory products, and shaped refractory products. Unshaped refractory products are mixtures being composed of aggregates and binders, prepared directly in the place where they will be used, such as castable, mortar, ramming mix, etc. On the other hand, shaped refractory products are manufactured by casting, molding, pre-treatment, etc., and later placed in service, such as bricks, shrouds, nozzles, etc. [2].

Refractories can resist complex combinations of thermomechanical loads, chemical and physical wear generated by the high-temperature fluids and chemical agents used during the process. The type of refractories employed in each industrial application has a direct influence on the product quality and energy consumption [3]. High-temperature vessels such as metallurgical vessels for the iron and steel industry (Figure 1), rotary kilns for the cement industry, and channel induction furnaces for the foundry industry require refractory linings. Literally speaking, “lining” term refers to layers of substances that are attached inside of something to protect it. A refractory lining design normally consists of different layers, each responsible for a specific purpose, which is referred as multilayer design.



Figure 1: Refractories application (steel ladle) [4]

For instance, in a steel ladle, the whole lining is normally made of three layers of refractory materials: the working lining, the safety lining, and the insulating lining (Figure 2). In this case, the working lining (also named wear lining) is the most crucial layer since it directly contacts with the molten steel and experiences high thermomechanical loads in a harsh chemical environment. The safety lining serves as a supporting layer after working lining, as well as enhancing the structure's stability and integrity. Finally, the insulation layer role is to decrease the heat loss while protecting the steel shell from high temperatures.

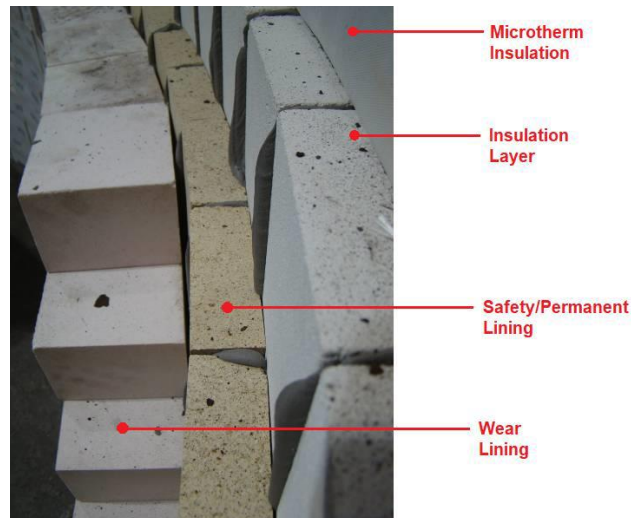


Figure 2: Refractory lining of a steel ladle

If the lining is made of shaped refractories, the design of the brick lining setup is essential given that the joint (gaps) between the blocks alters the behavior of the lining by giving an expansion allowance to the structure. If this expansion allowance is too large, the refractory lining would certainly be loose, and there will be a risk of losing stability and collapse. Contrarily, lining might fail with too tight lining arrangement because of high compressive stresses [5]. Often, these gaps are the outcome of brick surface roughness, brick dimension and shape errors during production. Whereas, occasionally, the initial gaps are considered and created by using cardboards during the masonry installation to compensate for thermal expansion outcome [6].

2.1 Mechanical characterization of ordinary ceramic refractories

Various experimental approaches can be employed for mechanical characterization of ordinary ceramic refractories, which depend mostly on the aim of the study. Some researchers investigate the influences of changes in the material chemical aspects on general mechanical responses such as thermal shock resistance,

cold crushing strength and so on. In numerical studies, on the other hand, the aim is to evaluate the material parameters needed for a specific material model, which represents the refractory behavior at high temperatures.

The mechanical response of the refractory materials can be divided to reversible and irreversible behavior. The most important thermomechanical phenomena, which are responsible for the irreversible deformation of the refractory linings and might lead to the wear of the material, are tensile failure, shear failure and creep of materials [7]. Refractories are exposed to temperature gradients and repeated thermal shocks in service, which can cause substantial tensile stresses and tensile failure of the material. High compressive stresses in refractory linings, on the other hand, are usual owing to the thermal expansion. The shear failure might as well happen for the part of the lining, which is under compression. Finally, creep occurs at high temperatures and is critical in refractory linings because of its impact on the level of stress in the lining and the steel shell. Different experimental approaches are used for characterization of the irreversible deformation, which are explained further in this section.

Additionally, the mechanical and thermomechanical experiments on refractory materials can be divided in three groups based on their specimen size: 1. Micro-scale experiments, which study the physics of interactions between the particles in a refractory product such as the crack propagation within the matrix, grain rotation, and so on. 2. Meso-scale experiments, which are used to assess the mechanical response of refractory products and/or to evaluate the mechanical properties needed in material constitutive model. In this category, the specimens' size is comparable to the size of the refractory products. 3. Macro-scale experiments, which focus on the overall behavior of a refractory lining and are performed on refractory masonries. Often the goal of these experiments is to observe the refractory mechanical behavior at high temperatures close to the service condition, which brings challenges for researchers [8–10].

2.1.1 Elasticity and associated constitutive model

The first behavior to be characterized is the reversible behavior of refractories. It has been shown that linear elasticity can well represent the refractory response before failure. The main parameters for the well-known Hook's law (shown in Eq. 1) are Young's modulus (E) and Poisson's ratio (ν). The other quantities in Eq. 1 are the second order elastic strain tensor ($\bar{\bar{\epsilon}}_e$), stress tensor ($\bar{\bar{\sigma}}$) and identity tensor ($\bar{\bar{I}}$).

$$\bar{\bar{\epsilon}}_e = \frac{1 + \nu}{E} \bar{\bar{\sigma}} - \frac{\nu}{E} \text{tr}(\bar{\bar{\sigma}}) \bar{\bar{I}} \quad \text{Eq. 1[11]}$$

For refractories, Poisson's ratio usually does not vary with temperature as much as Young's modulus does; according to the refractories' handbook [1], the average value is 0.15, and it can be used in the simulations. Therefore, there were no attempt for Poisson's ratio measurements in this study.

For characterization of Young's modulus, two different non-destructive methods are normally utilized, the ultrasonic method and the IET¹, both being standard test methods to determine dynamic Young's modulus of materials. In the case of ultrasonic measurement, Young's modulus is estimated by measuring sound velocity in the specimen; one short pulse of ultrasonic energy is transmitted from a transducer into the specimen and received on the other side. The transmission time is then used for calculation of the Young's modulus [12]. The IET (RFDA² test) measures the resonance frequency and its damping for a rectangular-shaped specimen, which are affected by elastic characteristics (Young's modulus and shear modulus), specimen's geometry and density and the excitation technique [13]. During the test, a mechanical impulse is used to excite the specimen in the flexural vibration mode, resulting in an acoustic signal. A microphone detects the acoustic signal, which is then converted into electric signals, and used with a fast Fourier transformation to compute the Young's modulus [14].

2.1.2 Creep behavior and associated constitutive models

Creep is the time and temperature dependent gradual deformation of materials under constant stress [15,16]. Many materials, including concrete, metals, fine ceramics, and refractory ceramics, exhibit creep [17]. The creep phenomenon starts at different temperatures for different materials, which is dependent on the active creep mechanism. Determination of this temperature is easier for single-phase materials compared to multi-phase materials like refractories[1,18]. As illustrated schematically in Figure 3, a creep displacement-time curve of a specimen mechanically loaded and subjected to a specific temperature consists of three stages [19]. Primary creep is the initial stage, which has a time-dependent strain rate that reduces with time. After that, the strain rate stays constant in the secondary creep stage, and an approximate equilibrium state between softening and hardening

¹ Impulse Excitation Technique

² Resonance Frequency Damping Analysis

processes can be assumed [20]. Finally, in the tertiary creep stage, the strain rate gradually rises until the material fails [7].

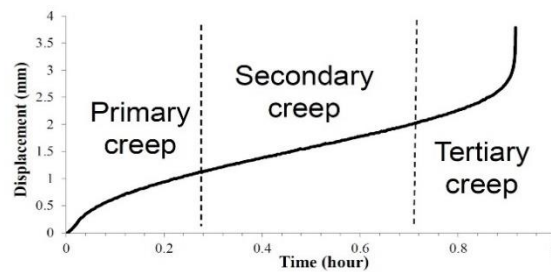


Figure 3: Displacement-time curve of three creep stages [21]

Different standards for investigating creep are available in the field of coarse ceramic refractories, and compressive creep tests are far more prevalent than tensile creep ones. Refractories, unlike metals, alloys, and fine ceramics, have a coarse ceramic structure with varying grain sizes; Therefore, creep testing of refractories demands rather large specimen geometries. In case of compressive creep testing, there are two kinds of conventional testing procedures: creep in compression (CIC) and refractoriness under load (RUL) [22]. The testing equipment and specimen dimensions are the same in both standards. The specimen has a diameter of 50 mm and a height of 50 mm. A constant load of 0.2 MPa is applied during the test, and the specimen's deformation is measured. The RUL technique involves firstly loading the specimen, and then increasing the temperature, and measuring the deformation during the whole heating time. But for CIC the load is applied after the heating phase under constant temperature. The CIC technique was created primarily to compare the creep resistance of different materials qualitatively and to aid in material selection for certain applications. One disadvantage is that the applied load is limited to 0.2 MPa, which is insufficient for determining creep behavior under service-related loading circumstances. For most refractory materials, the small load makes it impossible to determine all three creep stages in an acceptable amount of time. Furthermore, because the CIC technique only investigates one load, it cannot be utilized to derive load-dependent creep laws. In addition, in the RUL method, the creep onset cannot be precisely detected, because creep deformation may begin during the heating process and is superimposed by the thermal expansion.

Jin et al. [7] designed an improved compressive creep testing apparatus for testing of refractories to overcome the drawbacks of the RUL and CIC techniques. This apparatus was used in the current study as well. Loads up to 20 kN may be applied to cylindrical refractory specimens with a diameter of 35 mm and a height of

70 mm (Figure 4). The influence of friction between the specimen and the bearing part on the measured area is reduced by a height to diameter ratio of two. Temperatures of up to 1600 °C can be achieved using an electrical tube furnace. After a heating period with a rate of 10 °C/min and a dwell time for temperature homogeneity of the specimen, the load is applied, and the deformation is measured with two pairs of mechanical extensometers on the front and back sides of the specimen (distance between two corundum arms: 50 mm) (Figure 4). This testing apparatus enables for the observation of all creep stages at varied magnitudes of compressive loads [7].

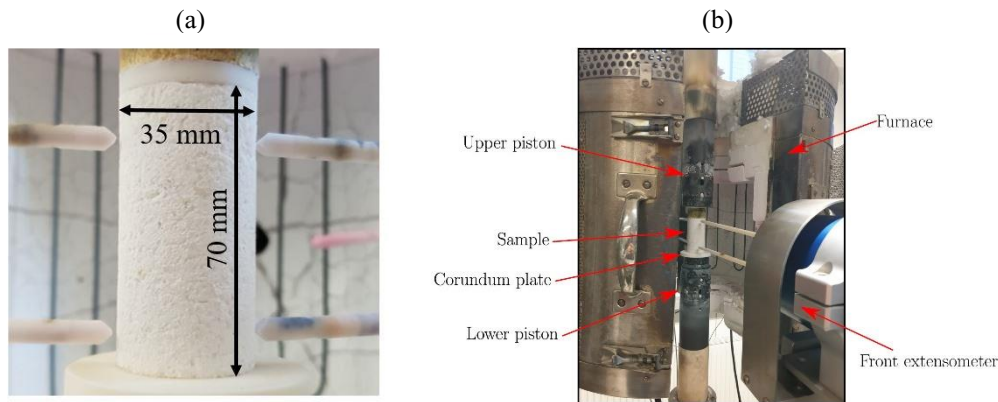


Figure 4: (a) Specimen's geometry for uniaxial compressive creep experiments and (B) the experimental device [23]

For the case of tensile creep measurements, there are several challenges for ordinary ceramic refractories. Firstly, the tensile deformations are relatively small compared to compressive ones. Secondly, due to comparatively large grain sizes and length of pre-existing cracks in the virgin specimen of refractories, the assessment of representative creep characteristics needs a suitably large specimen volume. In addition, it is difficult to build an appropriate testing alignment that prevents specimens from bending and ensures a homogenous uniform stress throughout the cross-section area of the specimens. Furthermore, there are no standardized testing technique for investigating the tensile creep behavior of refractories at high temperatures [24].

As a result, various experimental techniques have been proposed. For instance, three- or four-point bending tests are used to predict creep behavior under tensile stresses [25]. However, using these methods results in a non-uniform stress distribution in the specimen, making direct examination of pure tensile creep behavior difficult. There are just a few uniaxial tensile creep studies of coarse ceramic refractories available. Mong [26], for example, studied the tensile creep behavior of refractory bricks on cylindrical specimens with a diameter of 35 mm and

a length of around 230 mm. During the experiments, an electrical furnace was used to reach a maximum temperature of 950 °C, and the deformation was measured using micrometer slides and gauge markings. Later, Sidi Mammar et al. [24], designed an improved creep testing system based on a universal spindle driven tensile testing apparatus for uniaxial creep testing of refractories, which was used in the current study. To assure the viability of the tensile creep measurements, the specimen dimension was designed with the use of simulation. The specimen is a cylindrical form drilled from bricks with a diameter of 30 mm and a length of 230 mm. The refractory specimens were attached to water-cooled adapters outside the furnace for load application (Figure 5); the fixing device guarantees axial alignment of the sample and adapters during glue hardening.

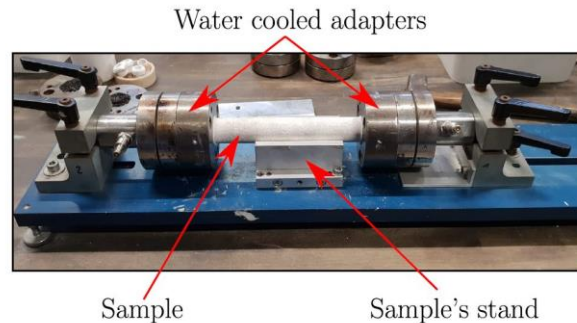


Figure 5: Specimen preparation for uniaxial tensile creep testing [23]

Figure 6 depicts a schematic of the testing apparatus. Loads up to 20 kN and temperatures up to 1600 °C can be applied within this apparatus. Mechanical extensometers were used to quantify creep deformation on the front and rear surfaces of the specimens (initial measurement distance: 50 mm). This apparatus can be used to examine uniaxial three-stage refractory tensile creep under a variety of loads and temperatures.

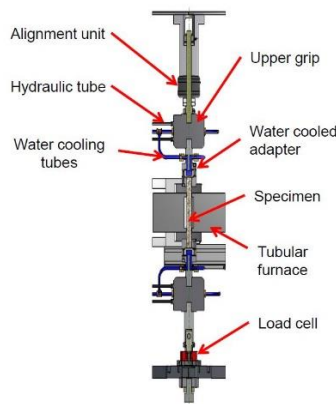


Figure 6: Uniaxial tensile creep test device [24]

Different material models, including asymmetrical creep models, creep damage models, and multiaxial creep models, were created to account for creep behavior in FE simulations. Micromechanical and phenomenological creep models are two types of creep models found in the literature. Micromechanical models are used to determine which creep mechanisms are active in a particular material. Phenomenological models try to assess the consequences of creep in a specific material, independent of the causes that may be responsible. This usually leads to simpler models with fewer parameters, but they are less generic. The Norton-Bailey's creep law is the most often used phenomenological creep strain rate model [11], whose general form is as follows:

$$\dot{\varepsilon}_{cr} = Kq^b \varepsilon_{cr}^a \quad \text{Eq. 2[11]}$$

where ε_{cr} denotes the accumulated creep strain, K , b and a are the material constants and q stands for the equivalent von Mises stress. Particularly in the secondary creep stage, the parameter a is zero, and therefore the creep strain becomes a linear curve. The Norton-Bailey rule has the benefit of being theoretically straightforward and having parameters that are generally easy to determine. This model was demonstrated to properly fit the creep experimental results of refractory materials. As a result, it has been widely utilized to depict refractory creep behavior and to predict refractory lining behavior. For instance, using the mentioned two uniaxial creep testing devices, Schachner et al [27] characterized the asymmetric creep Norton-Bailey parameters of MgO containing refractories under tension and compression.

The Norton-Bailey creep law available in the software Abaqus [28] has a different form (Eq. 3). Nevertheless, the important shortcoming of this model is that it cannot account for the asymmetry of refractory creep behavior, that is, the differences in behavior under tension and compression [29]. Furthermore, because the user must pick only one step to be applied, it is not feasible to model all the three creep phases in one simulation run.

$$\dot{\varepsilon}_{cr} = (Aq^n[(m+1)\varepsilon_{cr}]^m)^{\frac{1}{m+1}} \quad \text{Eq. 3[28]}$$

To identify the material parameters in Eq. 2, it should be integrated using the trapezoidal rule [7], resulting in:

$$\varepsilon_{cr,i+1} \approx \left[\varepsilon_{cr,i}^{1-a} + \frac{(1-a) \cdot K \cdot (q_{i+1}^b + q_i^b) \cdot (t_{i+1} - t_i)}{2} \right]^{\frac{1}{1-a}} \quad \text{Eq. 4}$$

where t and i are the time and time step index, respectively. It is feasible to get an analytic calculation of the resultant time versus creep strain curve, which can then be fitted to the experimental findings to inverse evaluate the creep parameters using an optimization technique.

It should be noted that the experimental creep curves include both elastic and creep strains ε_{tot} , and Eq. 2 does not include the elastic component. As a result, the elastic strains should be incorporated in the equation; in the uniaxial condition, the following formula can be used:

$$\varepsilon_{tot} = \varepsilon_{cr} + \frac{\sigma}{E} \quad \text{Eq. 5}$$

The second part of the right-hand side of Eq. 5 refers to the elastic strain and σ is the applied stress. After obtaining the displacement-time data (like in Figure 3), they are employed with an inverse estimation method (Figure 7.) using Levenberg-Marquardt least-squares algorithm [30], to evaluate Norton-Bailey creep parameters in Eq. 2 [7].

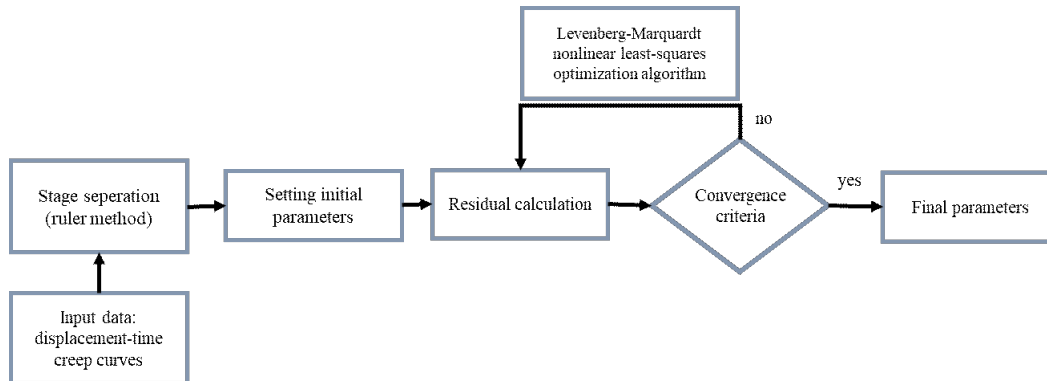


Figure 7: Flow chart of the inverse evaluation method to obtain the creep parameters [31]

2.1.3 Shear failure and associated constitutive models

In fracture mechanics, there are three modes for crack opening (shown in Figure 8). The tensile opening mode (Mode I) occurs when the fracture faces separate in a direction that is normal to the crack plane. In-plane sliding, or shearing (Mode II) is the second mode, in which the crack sides are mutually sheared in the direction normal to the crack front. The tearing (Mode III) or out of plane mode, in which the crack faces are sheared parallel to the crack front, is the third mode [32].

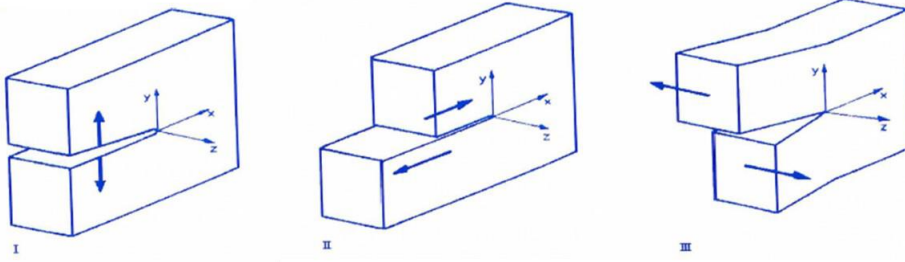


Figure 8: Three modes of crack opening [32]

For the case of fracture in Mode II or III or a mixed mode, suitable material laws like the Drucker-Prager [33] and the Mohr-Coulomb [11] models are commonly applied [34,35]. The Drucker-Prager model is typically used to simulate granular materials such as refractories whose cohesion is affected by hydrostatic pressure [28]. This model exhibits pressure-dependent yield criterion in which the material becomes stronger as the pressure increases. It is based on the form of the yield surface on the $p - q$ plane, where p is the hydrostatic stress and q is the von Mises stress, calculated as:

$$p = -\frac{1}{3} \text{tr}(\bar{\sigma}) \quad \text{Eq. 6}$$

$$q = \sqrt{\frac{3}{2} (\bar{S} : \bar{S})} \quad \text{Eq. 7}$$

where \bar{S} is the deviatoric part of the stress tensor. For instance, a linear yield surface is depicted in Figure 9, and can be formulated as:

$$F = q - p \tan \beta - c = 0 \quad \text{Eq. 8[28]}$$

where β and c stand for the friction angle and the cohesion, respectively.

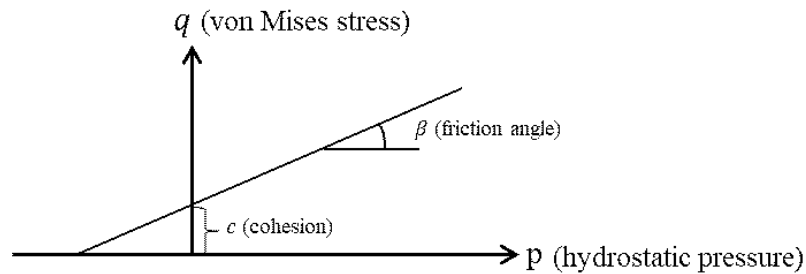


Figure 9: Linear Drucker-Prager yield surface [28]

In contrast to pressure-independent models, which only have a deviatoric component, pressure-dependent models create volume expansion due to the fact that the derivative of the flow potential results in a non-zero volumetric component [55]. The flow potential for the Drucker-Prager model is hyperbolic and is given by:

$$G = \sqrt{(\epsilon\sigma|_0 \tan \psi)^2 + q^2} - p \tan \psi \quad \text{Eq. 9[28]}$$

where ϵ denotes the eccentricity parameter, $\sigma|_0$ is the initial yield stress derived using the hardening properties of the model and ψ is the dilation angle. When $\psi = \beta$, the flow is termed “associated”, although this often produces unrealistic volume expansion, so normally $\psi < \beta$. When $\psi = 0$ is used, the model does not show any dilatancy, and the flow potential is reduced to a von Mises type.

Using the Drucker-Prager creep model and bending and compression tests, Dusserre et al. [36] investigated the asymmetric creep behavior of fiber reinforced refractories at high temperatures. The Drucker-Prager creep model was also utilized by Jin et al. [37] to predict the stresses and strains in a RH-snorkel during operation. The results were compared with calculations utilizing the Norton-Bailey creep model.

Several testing methods to determine shear failure parameters are available. For instance, the Iosipescu shear test [38] was proposed and applied for shear-testing of different materials like metals, composites, and woods [39,40]. Another example is the multistage triaxial tests, which also gives the cohesion and friction angle and have been successfully applied for rock-type materials [41–43]. These testing techniques could be used for refractories, but they are not developed for elevated temperature, which is required for refractory materials. Later, the modified shear test was developed by Dahlem [44] for determining the cohesion and fracture angle in accordance with the Drucker-Prager failure criterion, for refractories and at elevated temperatures.

Modified shear test is performed in a furnace on rectangular specimens ($37.5 \times 37.5 \times 150 \text{ mm}^3$) with notches of two different angles (60° and 80°) as shown in Figure 10-a. Vertical loads are applied at a rate of 0.5 mm/min and are measured using a load cell. The maximum loads of specimens with different angles are then used to determine the cohesion and friction angle of the material using the p-q diagram in conjunction with the Drucker-Prager failure criterion (Figure 10-b).

(a)

(b)

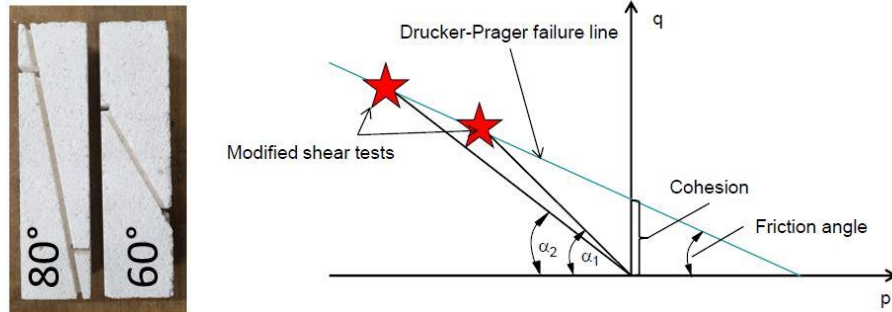


Figure 10: (a) Modified shear test specimens and (b) determination of Drucker-Prager criterion parameters

2.1.4 Tensile failure and associated constitutive models

Linear elastic fracture mechanics (LEFM) is a theory that describes the crack growth and fracture in a material under linear elastic conditions. It is based on the assumptions that the crack displacement is proportional to tension and that energy is solely consumed to create the fracture surface in tensile opening mode (Mode I) [32]. Nevertheless, inelastic events occurring in the crack process zone ahead of the original crack cause deviations from pure linear elastic fracture; for instance, the irreversible deformation near the crack tip, crack branching, and energy consumption by friction of grains [32]. The fictitious crack model by Hillerborg [45] has been proposed to account for these deviations and is used only for Mode I fracture [46]. In this model, the fracture process zone ahead of an existing crack is substituted with a fictitious crack in which the material follows a strain softening behavior. According to the model, the material will act elastically until the maximum stress meets the material's tensile strength, after which the crack is supposed to propagate. When the crack opens, the stress will not drop to zero immediately, but diminish with increasing crack width until a final crack opening is reached. The strain softening behavior describes the relationship between a decrease in stress and an increase in strain. This decrease represents the formation of microcracks and the growth of crack frontal process zone, which is the characteristic of quasi-brittle materials.

As depicted in Figure 11, four material parameters define the fictitious crack model: initial Young's modulus (E_0), tensile strength (f_t), fracture energy (G_f), and post-failure softening law (σ_c). In addition to fracture energy and tensile strength, which can be estimated using experimental data, investigations have revealed that the post-peak softening law has an impact on the simulation of material fracture behavior. Between various softening laws, bilinear, trilinear, and exponential post-peak behavior have been demonstrated to produce better fits to experimental curves [47–49].

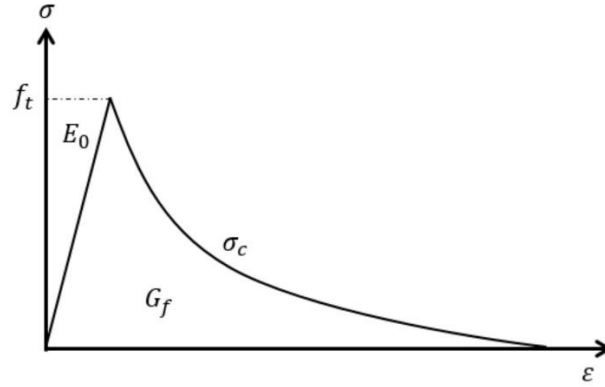


Figure 11: Fictitious crack model [45]

Concrete damaged plasticity (CDP) model in Abaqus includes the fictitious crack model and is used to simulate the fracture behavior of quasi-brittle materials [28]. Firstly, it was proposed for simulating the behavior of concrete materials containing two major failure mechanisms: tensile cracking and compressive crushing [50–52]. The material behavior under uniaxial loadings is described in Figure 12. Another feature of the CDP model is that it can simulate the degradation of material stiffness, in a way that after the maximum stress, the stiffness is lowered based on the user input data, which are the tensile and compressive damage parameters (d_t and d_c), defined as a function of the equivalent tensile and compressive plastic strains ($\tilde{\epsilon}_t^{pl}$ and $\tilde{\epsilon}_c^{pl}$). The damage parameters can be between 0 (with no damage) and 1 (with total damage in the stiffness). Therefore, the stress-strain formulations can be written as Eq. 10 considering the initial stiffness to be E_0 .

$$\begin{aligned} \sigma_t &= (1 - d_t)E_0(\epsilon_t - \tilde{\epsilon}_t^{pl}) \\ \sigma_c &= (1 - d_c)E_0(\epsilon_c - \tilde{\epsilon}_c^{pl}) \end{aligned} \tag{Eq. 10}[28]$$

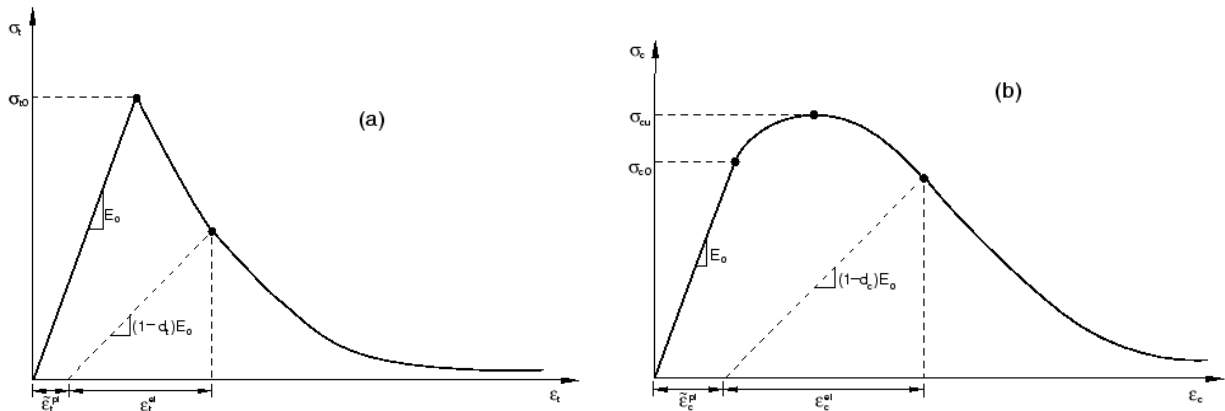


Figure 12: Material behavior under (a) uniaxial tensile load and (b) uniaxial compressive load according to the CDP model [28]

CDP model has been applied to model the fracture phenomenon in refractory materials and linings [35,53,54]. However, there are two disadvantages to utilizing this model. First, a lower limit on post-failure stress is imposed to avoid convergence problems and equals to 1% tensile yield stress. This is a disadvantage, especially when large tensile yield strengths are present, resulting in extra energy consumption in the model and error in the inverse identification of the material parameters, particularly the fracture energy [55]. Second, the CDP model does not include creep behavior. As both creep and tensile failure are important sources of irreversible behavior in refractory linings, they should be modelled simultaneously together [55].

In order to inversely evaluate the tensile failure parameters of the fictitious crack model for a chosen material, an experimental technique is required. In this regard, several testing techniques have been developed, including direct tensile testing, three-point bending testing, wedge splitting testing, and so on. The wedge splitting test (WST) according to Tschegg [57] allows stable crack propagation on relatively large specimens because of the wedge action and the relatively high fracture surface to sample volume. WST has been utilized and proposed in several studies to characterize fracture phenomena in refractory materials [47,48,58].

The new WST testing apparatus at the Chair of Ceramics (MUL) [51] enables precise fracture mechanical characterization of refractories at room and elevated temperatures up to 1500 °C. Carbon-containing refractories can also be tested under reducing conditions [47]. Figure 13 depicts the specimen's dimensions.

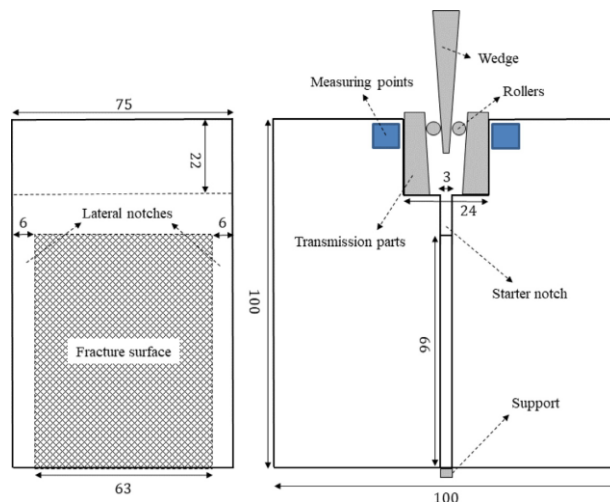


Figure 13: WST Specimen's dimensions (in mm) [55]

Vertical displacement of the wedge is delivered at a rate of 0.5 mm/min, and the vertical load is measured with a load cell. Transformation of the vertical

displacement of the wedge to the crack horizontal opening is not accurate because of the sliding of rollers and contact face compliance. Therefore, the horizontal displacement is measured on the specimen's back and front surfaces using a laser speckle extensometer. The horizontal load (F_H) is then calculated using the measured vertical load (F_V) according to Eq. 11.

$$F_H = \frac{F_V}{2 \tan \frac{\alpha}{2}} \quad \text{Eq. 11}$$

where α denotes the wedge angle.

The results are in the form of load-displacement diagrams (Figure 14), from which the following experimental parameters can be computed directly: specific fracture energy (G'_f), nominal notch tensile strength (σ_{NT}) and brittleness number (B).

$$G'_f = \frac{1}{A} \int F_H dx_H \quad \text{Eq. 12}$$

$$\sigma_{NT} = \frac{F_{H,max}}{bh} \left(1 + \frac{6y}{h}\right) \quad \text{Eq. 13}$$

$$B = \frac{\sigma_{NT} \times h}{G'_f \times E} \quad \text{Eq. 14}$$

where, F_H and x_H stand for the horizontal force and displacement, A is the fracture area (shaded area in Figure 13), b and h denote the width and the height of the ligament area, and y is the vertical distance between the horizontal load point and the center of fracture area. Although y is a variable number during the test, its average value is used in Eq. 13.

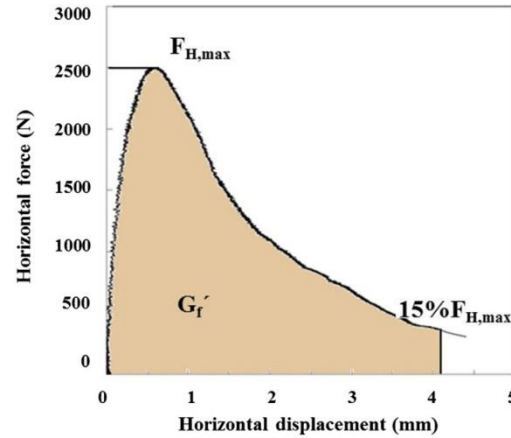


Figure 14: Typical load-displacement curve from WST [59]

The G_f' , σ_{NT} and B are experimental parameters and dependent not only on the material properties but also on the specimen's geometry and testing procedure. For example, the specific fracture energy represents just a portion of the total fracture energy since the experiment must be terminated prematurely (at 15% of the maximum load) to prevent contact between the wedge and the ligament. These parameters are usually used to compare different refractory materials. Therefore, an inverse evaluation technique with the help of numerical modeling is required to obtain the actual material parameters.

In the literature, numerous modeling techniques have been utilized to simulate WST and to obtain the material parameters [47,48,55,56,59]. For instance, Jin et al. [48] defined cohesive elements in the ligament with fictitious crack model and varying softening laws, whereas the specimen's bulk was defined to have elastic behavior. The study showed that the application of bilinear and trilinear softening laws can significantly reduce the residual of the fit compared to a linear one.

2.2 Thermomechanical modeling methods for refractory linings

The qualitative and quantitative predictions of mechanical and thermal variables, as well as the study of refractory material damage and failure mechanics, are favored by mathematical and numerical modeling [35,60–63]. Thermomechanical simulation of a high-temperature vessel is normally divided into two parts: thermal modeling and mechanical modeling. These two modeling methods can be coupled to create a thermomechanical model or can be used separately (named also “weak coupling”). In the latter, a thermal simulation is run first, and then the temperature distribution is utilized as an input in a mechanical simulation, with the premise that the model's mechanical behavior has no effect on its thermal response.

Heat transfer is the active loading field in the thermal simulation part, and it is the phenomenon of energy transfer between two media or within one medium as a result of the temperature difference. Heat transfer has three different types: conduction, convection, and radiation[64]. There are various equations and fundamentals for the computation of the heat flux generated by different mechanisms. Furthermore, heat transfer is modeled in two ways: steady state and transient; the former does not have a time-dependent temperature distribution, but the latter does. The transient version of the energy balance equation is shown in Eq. 15. The temperature distribution in the model over time is determined using this equation and the heat transfer boundary conditions.

$$\rho c_p \frac{\partial T}{\partial t} - \text{div}(k \overrightarrow{\text{grad}}(T)) = 0 \quad \text{Eq. 15}$$

where, ρ , c_p , k , and T denote the density, specific heat, thermal conductivity, and temperature, respectively.

Furthermore, in the mechanical modeling part, due to restriction of the refractory lining by a steel framework, mechanical stresses develop due to thermal expansion of the refractory material. As a result, compressive stresses occur on the heated face of the lining, while tensile stresses are in the steel framework. Additionally, rapid changes in temperature cause thermal shock and tensile stresses for the lining material. In the mechanical modeling of refractory materials, several mechanical constitutive models are used depending on refractory application and position in the lining. The working lining is subjected to the most severe thermomechanical stresses, resulting in the largest amount of wear and material loss in this region. Tensile failure, shear failure, and creep are the most common irreversible behavior phenomena for refractories, all of which are dependent on material characteristics at high temperatures.

The numerical modeling of refractory linings is hindered by two major issues. Firstly, industrial vessels with refractory linings are large constructions with numerous details. This makes a full simulation of the entire structure computationally impossible and simplifications in the modeling part are required. Therefore, researchers in the refractory field proposed two key methodologies for simulation of refractory linings: homogenization technique and unit-cell modeling method. Secondly, measuring and observing the behavior of refractory linings during application is extremely difficult. Despite several advancements in the field of measuring instruments; for instance, in the field of temperature monitoring, reliable

displacement measurement of refractory lining during application is still a challenge. As a result, the validation of the numerical simulations is still a difficult task.

2.2.1 Homogenization method

The homogenization technique considers a homogeneous and anisotropic material that is equivalent to the lining composite under investigation, with different tensile and compressive strengths, as well as different inelastic behavior corresponding to each axis of the lining [65,66]. A 3D model of a steel ladle utilized for thermomechanical modeling using the homogenization approach is shown in Figure 15-a. As can be seen, the entire lining is modeled in one piece, and the number of contacts and pieces in the model are decreased, lowering the calculation costs. On the other hand, tests on large-scale lining constructions are necessary to characterize or assess this modeling method [67–69]. For example, Oliveira et al. [68] investigated the thermomechanical behavior of alumina spinel refractory lining under uniaxial compression and Prietl [70] conducted large-scale biaxial compressive tests to characterize the thermomechanical properties of magnesia-chromite bricks (Figure 15-b).

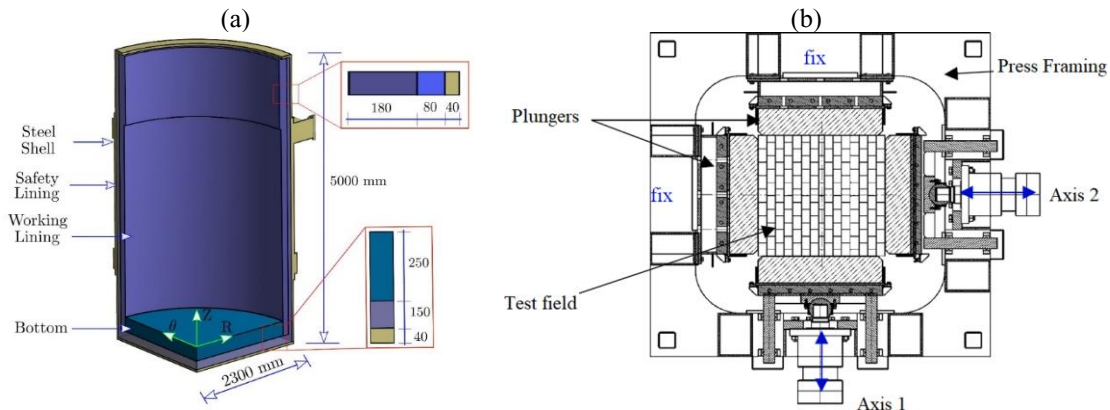


Figure 15: (a) An example of a steel ladle model used in homogenization technique [6] and (b) Biaxial compression test employed for characterization of overall behavior of refractory linings [70]

Almost the first study that used homogenization technique for refractory linings belongs to Boisse et al. [63]. In this study, the aim was to develop a two-layer shell finite element model whose thermomechanical behavior is the same as the lining of a thermal combustor. In another study, Gasser et al. [71], by studying the joint effect on refractory lining behavior, proposed a solution for homogenization of refractory masonry. The material behavior was elastic when all joints were closed, and nonlinear when some joints were open. In this study, two simplifications were assumed. First, the possible sliding between the bricks was not considered, and second, the progressive closure of joints was not defined. This study was extended further by Nguyen et al. [65]. By adding the local joint state, the proposed equivalent

material had four different behaviors (illustrated in Figure 16), each of which was determined by the homogenization technique.

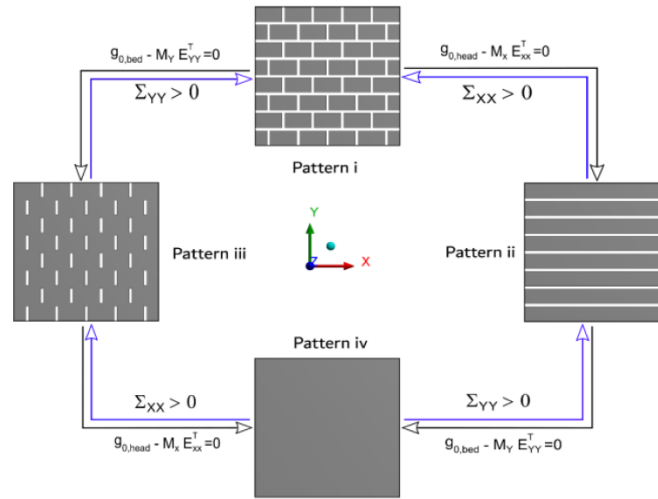


Figure 16: Possible joint states of dry refractory lining along with the joint closure/opening criteria [6]

In another study on refractory applications, a blast furnace was simulated [72] using homogenization technique. The blast furnace working lining were bricks with mortar joints. Firstly, tensile and compression tests were performed on two bricks with mortar between them to investigate the joint behavior at different temperatures. Later, a representative volume element was used to inversely evaluate the homogenized material parameters, including bricks with linear elastic behavior and mortar with linear elastic behavior and a Drucker-Prager with tension cut-off yield criterion. Similar to the work of Nguyen et al. [65], four different joint states were considered for the lining, and for each the material parameters were identified inversely using simulations. The model was tested on a refractory wall simulation and the results were comparable.

In another notable study, Gasser et al. [73] investigated the influence of different masonry designs of the steel ladle bottom lining on the stress and strain levels of the steel shell. Different lining concepts were modeled using their corresponding equivalent homogeneous materials; while joints in the ladle wall have not been taken into account. The results showed that the bottom design and the joint thickness and type affect the stress and displacement of the entire shell structure.

Mahmoud et al. [6] continued the work of Gasser et al. [73], by applying the homogenization technique also to the wall of the steel ladle in addition to the bottom. The goal of the study was to observe the mechanical response of a ladle during its complete working cycle. The homogeneous equivalent material was developed for

dry-joint lining with running bond texture. The same four different joint states were defined in the homogenized model. The model was validated using experimental results of biaxial compression test on refractory wall and later replaced the working lining of the ladle for thermomechanical simulation. For simulation, a weak thermomechanical coupling was used. The results showed that consideration of the orthotropic homogenized material, instead of an isotropic one, decreases the amount of stress in the working lining, and the decrease is proportional to initial gap size [6].

The mentioned studies worked on homogenization of refractory linings while considering the bricks to have elastic or even rigid behavior. This assumption leads to overestimation of stress magnitudes in the refractory lining and in the vessel steel structure since the nonlinear behavior of the refractory material at high temperatures (> 1000 °C) plays an important role in reducing the stress. Therefore, further developments in nonlinear homogenization of refractory linings including refractory material behavior at high temperature are necessary [74].

2.2.2 Unit-cell method

Another approach to alleviate the modeling complexity of the vessel structure and its refractory lining and reduce the computation cost is to apply the unit-cell modeling technique. In this approach, a representative volume element containing all important constitutive information such as units and joints is utilized for the simulations. This is a section of the lining that is repeated throughout the structure. For instance, a unit-cell model of the slag zone lining in a steel ladle is presented in Figure 17. In this approach, the entire structure is not simulated, resulting in smaller model size, but it does need the knowledge of each constituent. Experiments on meso-scale specimens can be used to gain this knowledge. Nevertheless, in the case of complex material constitutive models, modeling will take a long time [75].

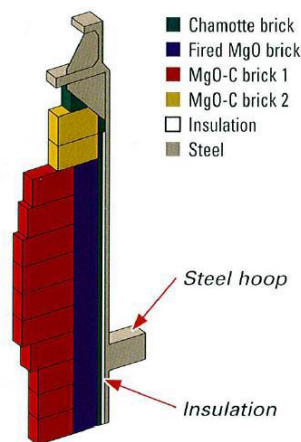


Figure 17: Unit-cell model of slag zone lining in a steel ladle [76]

In the study of Andreev and Harmuth [75], a thermomechanical simulation of refractory linings used in teeming ladles was conducted for four working cycles of the lining. The Drucker-Prager model was coupled with a Rankine tension cut-off criterion for failure under compression. The fracture behavior was studied using the fictitious crack model for failure under tension. The numerical study revealed that the cycling temperature might result in recurrent fracture propagation at the working linings' hot face.

Gruber et al. [77] performed numerical simulations of a blast furnace's refractory lining. The lining of the furnace is composed of multiple layers of varying materials, including refractory bricks and monolithic. The material constitutive model was a combination of the Drucker-Prager model and a Rankine tension cut-off. The simulation was conducted to determine the lining's reaction to thermomechanical loads in service and the interaction between the lining's layers, with the ultimate objective of optimizing the lining's design and material selection.

In the research of Jin et al. [35], a unit-cell model was used to simulate and improve a Ruhrstahl Heraeus snorkel design. The purpose was to determine the thermomechanical causes of the refractory lining failure. The mechanical properties of the refractory utilized in the study were determined experimentally. The Drucker-Prager model, Drucker-Prager with creep model, and the fictitious crack model were employed and compared. The authors determined that thermal shocks caused tensile failure in the wear lining, whereas joint openings were caused by shear failure and creep of the refractories.

Gruber and Harmuth [53] investigated the potential of using a new class of refractories to counteract irreversible strains via controlled expansion and the effect of insulation on the necessary controlled expansion. The Mohr-Coulomb model was employed in the simulation, and the material was considered to be linear elastic till failure. They came to the conclusion that the steel ladle's insulation has a significant effect on the temperature distribution and ultimate stress condition. They discovered that in the case of a ladle with insulation, irreversible strains rise while the necessary controlled expansion of bricks decreases.

Liang et al. [78] used a 3D unit-cell model of a high temperature black liquor gasifier to perform thermomechanical simulation. A continuum damage model was utilized to account for expansion owing to chemical reactions in the refractory material behavior. The damage caused by compressive failure on the hot face of the working lining was the most severe, according to the research, and was mostly

caused by chemical reactions. It also revealed that tensile failure caused by hot shock happened in a distance from the hot face.

2.2.3 Comparison of homogenization technique and unit-cell modeling approach

Based on the modeling decisions made in the previously mentioned research works, special considerations are required when making decision about the refractory lining finite element model and approach. As for the geometry, a 2D or 3D model can be chosen according to the boundary conditions of the structure, and the available calculation power. Units and joints can be modeled separately using unit-cell modeling method or homogenized into a composite material using homogenization technique. Even after choosing one of these approaches, many questions arise regarding the application of material constitutive models. Selection of the most appropriate modeling approach depends on the structure under study, the required accuracy and simplicity level, the available experimental facilities and knowledge of the material properties.

The implementation of homogenization technique in the case of complex material constitutive models is very challenging and still in the beginning stage. For instance, cracking behavior of refractory bricks in case of thermal shocks has not been simulated using homogenization techniques yet. On the other side, some studies with the aid of unit-cell modeling technique could apply various material failure mechanisms, such as tensile failure, shear failure, creep, etc., to the refractory linings in different vessels, e.g., a teeming ladle [75] and a RH-snorkel [35].

The homogenization technique applied in homogenized models demands implicit approximation for some nonlinear behavior mechanisms, such as joint sliding, cracking of units, crushing of unit or mortar, etc. Therefore, evaluation of the models and comparison of the numerical results with experimental ones are more complicated than unit-cell models [79,80].

Although homogenization approach may lead to a decrease in the model accuracy, it saves the computational cost for larger vessel simulation. On the other hand, the unit-cell modeling of refractory linings can produce highly accurate results, particularly at local level; but this approach is not developed for structural design, where the whole structure needs to be simulated, because it requires a separate discretization of bricks and joints. In fact, discretized modeling of masonry structures, which is called micro-modeling in civil engineering, could lead to intractable numerical difficulties with increasing the structure size [67,81,82].

Finally, homogenization techniques require experimental laboratory tests on sufficiently large-sized masonry walls either for a preliminary mechanical characterization of the model, in early studies, or for final evaluation of the model results [67]. Nevertheless, the situation for unit-cell modeling approach is not much better, where the number of necessary laboratory experiments increase largely. In that approach, detailed characterization of the lining constituents is required in addition to the accurate definition of contact behavior. Therefore, in the case of homogenization techniques, preparation and execution of the experiments is costly, but in the case of unit-cell modeling approach, the high cost comes from the variety and number of tests needed.

To sum up, one modeling strategy cannot be said to be better than the other because unit-cell modeling and homogenization techniques service different application purposes. In order to better understand the local behavior of masonry structures, unit-cell modeling approach must be carried out. This type of modeling is particularly suitable for structural details. When the structure is made of solid walls of sufficiently large size and the details' effect on the stress state across the macro axes is negligible, the homogenization technique is suitable. Obviously, due to reduced time and memory requirements and a user-friendly mesh generation, homogenization techniques are more practical with an acceptable accuracy and increased efficiency.

3. Results

In the current research work, the conducted experiments were in the meso-scale category to evaluate the necessary material parameters for the introduced material models in chapter 2. The high temperature mechanical experiments were performed on fired alumina spinel bricks, which are used in the working lining of the steel ladle (shown in Figure 18). The working lining is the largest portion of the steel ladle refractory linings.

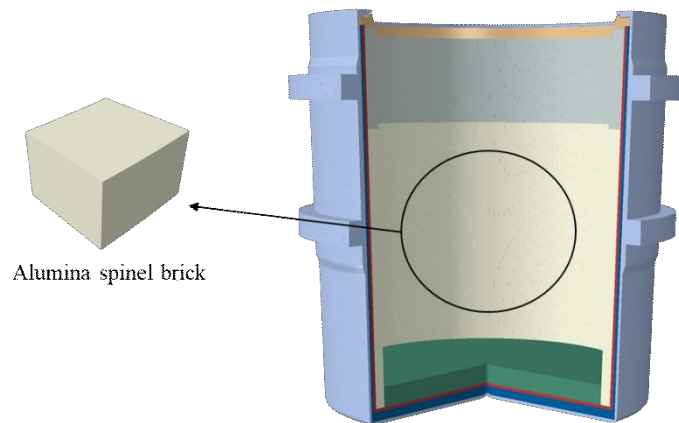


Figure 18: Application area of alumina spinel bricks in the steel ladle

The microstructure of the material observed with the scanning electron microscopic (SEM) is shown in Figure 19. Alumina grains (corundum) of different sizes, spinel in the fines, and pores in the grains and matrix are visible, which shows that the microstructure of this material is heterogeneous.

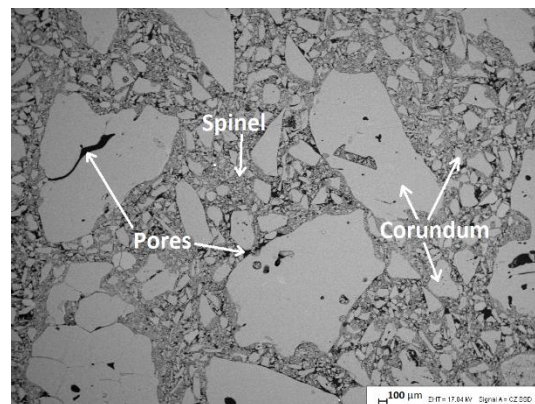


Figure 19: SEM image of the investigated shaped alumina spinel refractory [83]

3.1 Mechanical characterization results

3.1.1 Young's modulus measurements

Both IET and ultrasonic methods, introduced in previous chapter, were used for Young's modulus measurement. Figure 20 shows the specimen; initially, the specimen's Young's modulus was determined at room temperature using both methods. Then the sample was heated to 1500 °C (at a rate of 5 °C/min), with a dwell time of 1 hour at the maximum temperature, then cooled to room temperature in the furnace at the same rate. The real-time measurement at high temperatures was carried out with the IET technique at a frequency of one per minute. Finally, IET and ultrasonic techniques were used on the same specimen at ambient temperature. Three specimens were tested in total.

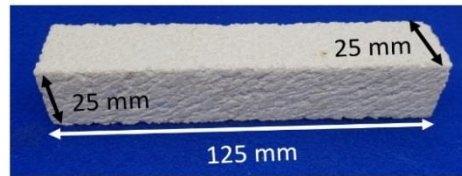


Figure 20: Specimen dimensions for Young's modulus measurements

Figure 21 shows the room temperature and high-temperature measurements of the Young's modulus for the shape alumina spinel refractory. After heating, both methods detected a rise (approximately 3 GPa, 8%) in the Young's modulus, with the ultrasonic method yielding higher (approximately 4 GPa) findings than the IET method. According to the Young's modulus evolution during heating and cooling, at first, the Young's modulus value decreased slightly and then increased till a temperature around 1200 °C. The Young's modulus rose during the cooling phase, reaching its maximum value at a temperature around 700 °C before dropping with further cooling. For the thermomechanical simulation, the mean value of the three curves was utilized. The average standard deviation of the results was around 6 GPa.

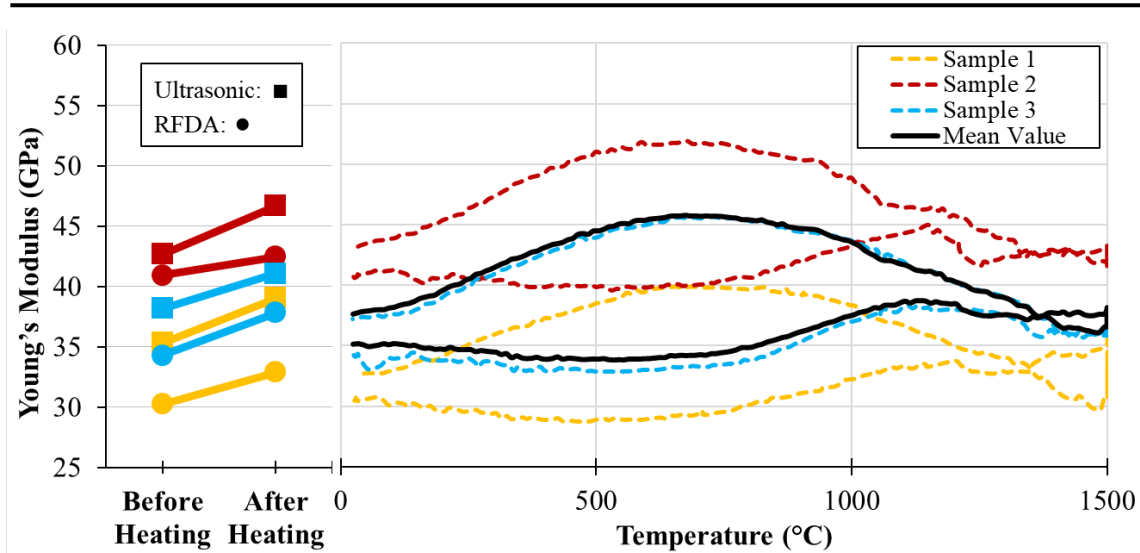


Figure 21: Young's modulus measurements on alumina spinel bricks - room temperature (left) and high temperature (right)

An XRD measurement was used to investigate the cause of Young's modulus increase after heating. Two specimens, one from a virgin specimen and the other from a heated specimen, were examined. Table 1 shows the semi-quantitative calculation results. An increase of 2.6wt% in the spinel amount was observed. Since no magnesia was detected in the burned brick, the increase should come from the inclusion of alumina in the spinel structure. This inclusion benefits the bonding strength and could be the reason for the increase in Young's modulus. More investigation on this topic was done in another study in ATHOR project [84].

Table 1: XRD measurement semi-quantitative results on a heated and a virgin specimen of alumina spinel bricks

Component	Heated specimen	Virgin specimen
Corundum	78.8%	81.4%
Spinel	21.2%	18.6%

3.1.2 Creep behavior characterization

In the current study, the uniaxial compressive and tensile experiments were completed at three different temperatures with three different loads at each temperature. Three specimens were used for each loading condition. The test plan is shown in Table 2 for compressive creep tests and in Table 3 for tensile ones. These test plans required several trial experiments to define proper loads and temperatures with which all three stages of creep could be obtained in a reasonable time. The compressive creep results are reported in PAPER I. The applied tensile stress values are lower compared to the ones in uniaxial compressive creep tests due to the

asymmetry in the creep behavior of refractories. More on this aspect can be read in PAPER II and PAPER III. Here, the most important results are presented.

Table 2: Uniaxial compressive creep testing plan [83]

Uniaxial compressive creep tests	Temperature (°C)	1300	1400	1500
	Applied stresses (MPa)	8.0 9.0 10.0	4.0 4.5 5.0	3.5 4.0 4.5

Table 3: Uniaxial tensile creep testing plan [85]

Uniaxial tensile creep tests	Temperature (°C)	1200	1300	1400
	Applied stresses (MPa)	0.25 0.35 0.45	0.15 0.20 0.25	0.12 0.15 0.18

considering the scatter of compressive creep results, an approach was devised to investigate the impact of the specimens' location and orientation in the brick on the creep behavior. In this regard, from a single brick, six specimens were cut as shown in Figure 22-a. The specimens were then subjected to compressive creep testing under the identical conditions, with the results displayed in Figure 22-b [83].

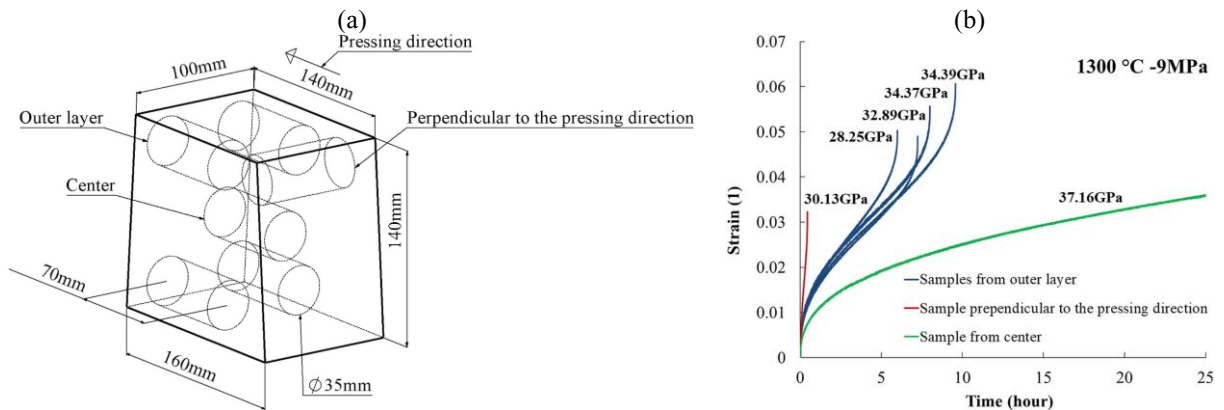


Figure 22: (a) Schematic of the specimens drilled out of a brick for study of the influence of their position and drilling direction and (b) their uniaxial compressive creep test results (with the Young's modulus added next to the respective curve). [83]

Figure 22-b inferred that the inhomogeneity is the source of the scatter. The specimen drilled from the center of the brick showed the highest creep resistance and the specimen drilled perpendicular to the pressing direction showed the lowest creep resistance. Specimens from outer layer produced comparable results, particularly in the primary creep stage. Therefore, to address the issue of heterogeneity of the bricks,

two measures were taken: first, specimens were cut in the pressing direction and from the outer layer, and second, a statistical study was carried out to inverse evaluate the representative creep parameters. The approach was thoroughly explained PAPER I. The results of the uniaxial compressive and tensile creep tests are plotted in Figure 23 and Figure 24, respectively.

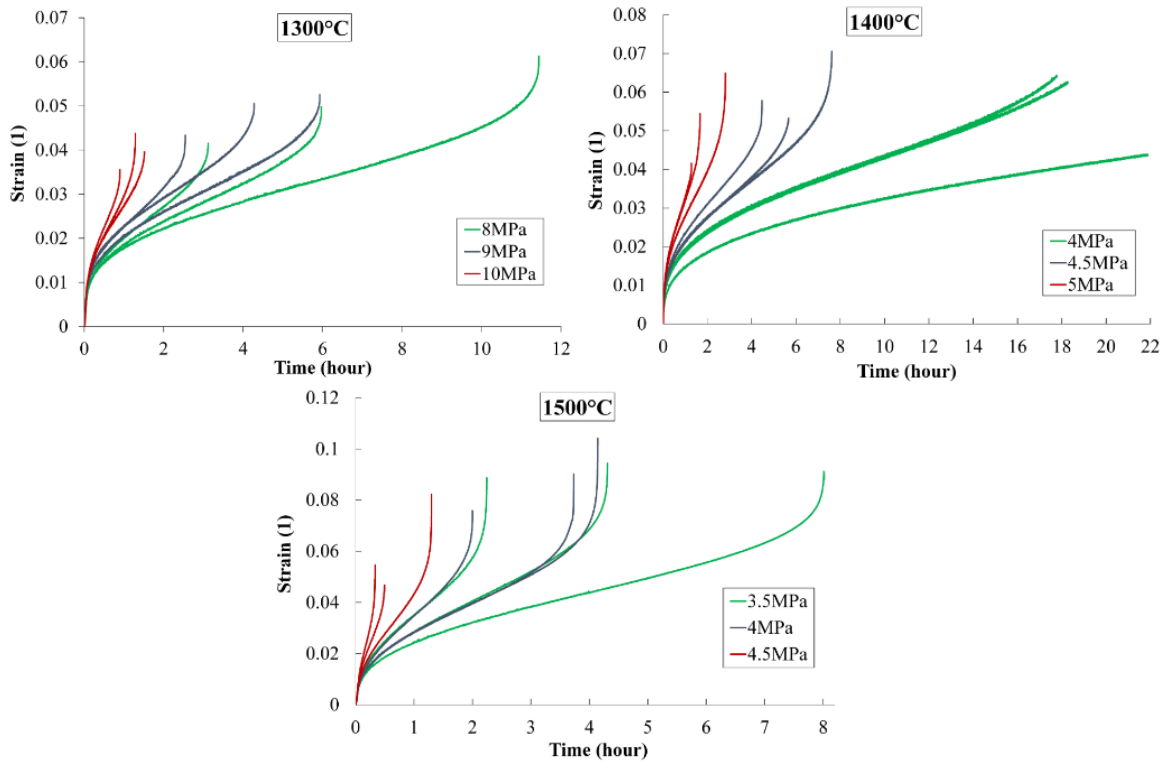


Figure 23: Uniaxial compressive creep test results of alumina spinel bricks [83]

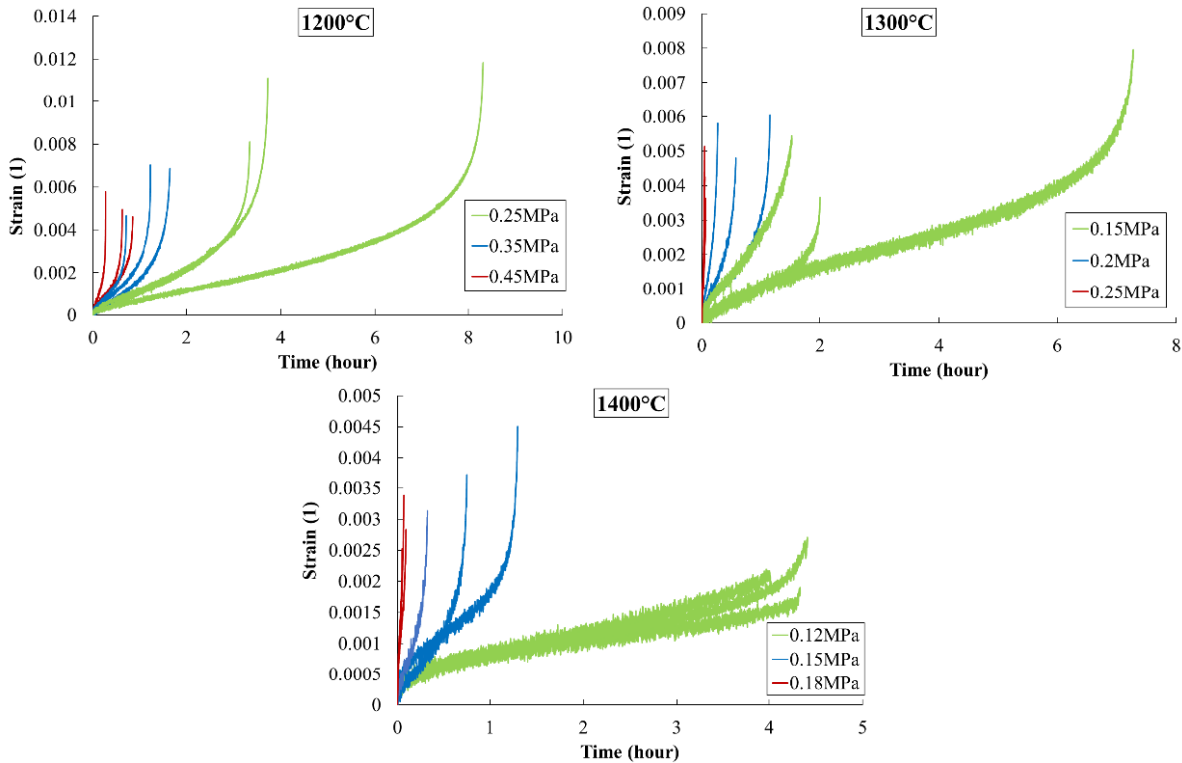


Figure 24: Uniaxial tensile creep test results of alumina spinel bricks [85]

A correlation study was done on the Young's modulus (E) (measured using ultrasonic method), bulk density (ρ) and creep strain rates of the compressive creep specimens. For three specimens with identical mechanical loads and temperature conditions, the correlation coefficient was computed and averaged. The mean primary stage strain rate ($\dot{\epsilon}_1$), the secondary stage strain rate ($\dot{\epsilon}_2$), and the nominal failure strain rate ($\dot{\epsilon}_f$) were calculated. The results are presented in Table 4. Bulk density and Young's modulus were shown to have negative correlation coefficients with creep strain rates. The Young's modulus correlation coefficients were lower than 0.57, whereas the bulk density correlation values were higher than 0.88. Because of the relatively high connection between creep strain rates and bulk density, the porosity of the studied alumina spinel material largely determined its creep resistance.

Table 4: Mean correlation coefficients table for Young's modulus, bulk density, and creep strain rates from the compressive creep tests [83]

	E	ρ	$\dot{\epsilon}_1$	$\dot{\epsilon}_2$	$\dot{\epsilon}_f$
E	1	0.847	-0.570	-0.570	-0.492
ρ		1	-0.927	-0.923	-0.889
$\dot{\epsilon}_1$			1	0.997	0.990
$\dot{\epsilon}_2$				1	0.993
$\dot{\epsilon}_f$					1

Primary and secondary creep stages were substantial in the compressive creep behavior, whilst a short primary creep stage and a significant secondary creep stage were observed in the tensile creep behavior. In addition, tensile failure creep strains were 1-2 order of magnitude lower than compressive failure creep strains, as illustrated in Figure 25. These observations demonstrated a high asymmetry in the creep behavior of the studied alumina spinel refractory [23].

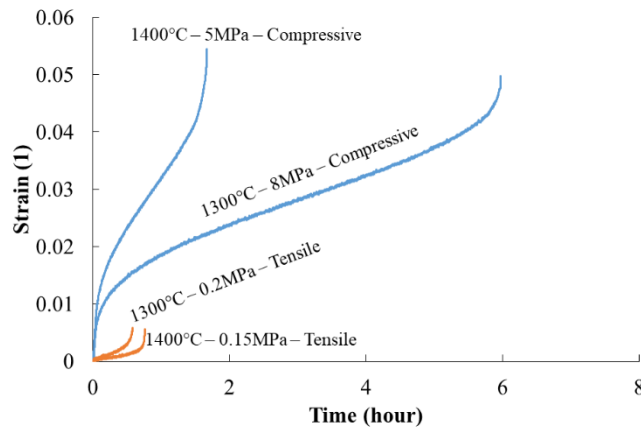


Figure 25: Comparison of the uniaxial tensile and compressive creep results of the shaped alumina spinel refractory at similar temperatures

The input data for the inverse evaluation algorithm (shown in Figure 7) can be chosen in a variety of ways; principally, it requires at least two curves with different constant stresses to obtain the three creep parameters. Input data from different loads would result in the same creep parameters in a perfectly homogenous material, however when there is scatter in the experimental results, different input data can yield different parameters. To examine the effect of input data on the final creep parameters and to find the best representative input sample, a statistical study was conducted for the first time on the creep behavior of shaped refractories. In this study, all combinations from $\binom{9}{2}$ (2 out of 9 curves) to $\binom{9}{9}$ were picked as input datasets (8 in total), with the constraint that at least two distinct stresses exist in the dataset.

To compare the input datasets, the mean value (\bar{y}) and standard deviation (S) were calculated; moreover, confidence intervals for creep parameters in different datasets were produced using Eq. 16 to examine the representativeness of mean values from various combinations.

$$|\mu - \bar{y}| \leq \frac{t_{\frac{\alpha}{2}, n-1} S}{\sqrt{n}} \quad \text{Eq. 16}$$

where μ is the whole population mean value, n denotes the dataset population and α is the significance level. The right side of Eq. 16 is termed “100(1- α) percent confidence interval” for the mean difference. t should be input from the t-distribution table depending on the degree-of-freedom ($n - 1$) of dataset and chosen confidence interval percentage “100(1 - α)” [86]. A confidence interval percentage of 99% was selected in this study.

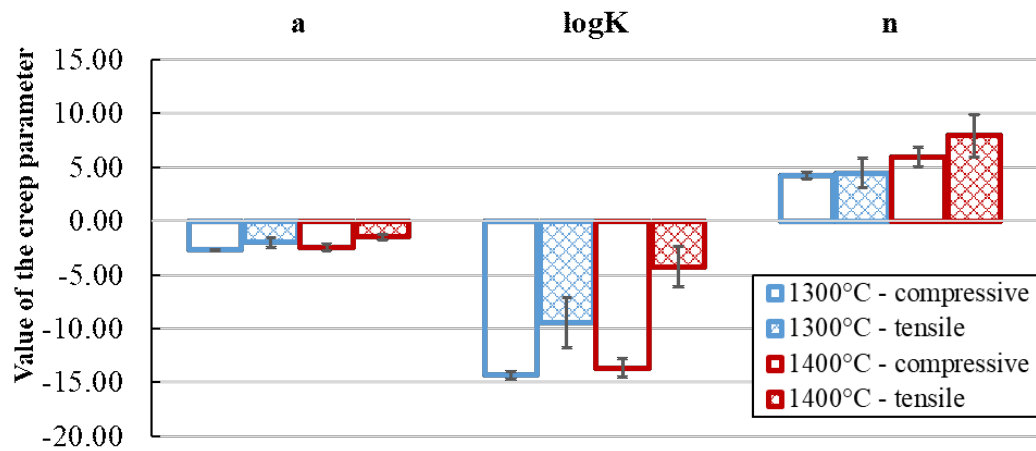
Based on the statistical study, the input datasets of creep curves, which produce better representative mean and standard deviation of the material inhomogeneity could be chosen. For instance, in the case of the compressive creep primary stage parameters, the dataset “Combination of 7 curves” was recommended [83]. More discussions about the statistical study approach can be read in PAPER I and PAPER III. Table 5 and Table 6 provide the uniaxial compressive and tensile creep parameters for primary and secondary creep stages with their standard deviations, respectively. Figure 26 presents a comparison between the compressive and tensile creep parameters of the investigated material. The standard deviation of tensile creep parameters was higher than that of compressive creep parameters. The standard deviation of the secondary creep stage was higher than that of the primary creep stage.

Table 5: Uniaxial compressive and tensile creep parameters for the primary creep stage at different temperatures [85]

	<i>Temperature (°C)</i>	<i>n</i>	<i>a</i>	<i>Log(K[MPa⁻ⁿs⁻¹])</i>
Compressive creep parameters	1300	4.24 ± 0.22	-2.72 ± 0.07	-14.37 ± 0.25
	1400	5.88 ± 0.68	-2.65 ± 0.24	-13.75 ± 0.70
	1500	2.02 ± 0.55	-1.93 ± 0.10	-9.73 ± 0.44
Tensile creep parameters	1200	2.94 ± 0.82	-1.01 ± 0.40	-8.40 ± 1.31
	1300	5.72 ± 1.45	-1.75 ± 0.34	-7.56 ± 2.10
	1400	7.65 ± 1.42	-1.90 ± 0.36	-5.87 ± 1.97

Table 6: Uniaxial compressive and tensile creep parameters for the secondary creep stage at different temperatures [85]

	Temperature (°C)	<i>n</i>	Log(<i>K</i> [MPa ^{-<i>n</i>} s ⁻¹])
Compressive creep parameters	1300	6.22 ± 1.11	-11.68 ± 1.05
	1400	9.32 ± 0.67	-11.87 ± 0.44
	1500	5.54 ± 1.38	-8.70 ± 0.82
Tensile creep parameters	1200	2.61 ± 0.65	-5.14 ± 0.30
	1300	7.44 ± 1.70	-0.53 ± 1.16
	1400	10.83 ± 2.77	2.67 ± 2.26

**Figure 26: Comparison of compressive and tensile creep parameters of alumina spinel bricks at similar temperatures**

3.1.3 Shear failure characterization

The modified shear test, introduced in 2.1.3 Shear failure and associated constitutive models, was used. Three different temperatures were investigated (three specimens for each temperature): room temperature, 1000 °C, and 1200 °C. The limitation of the furnace did not allow applying higher temperatures. According to Dahlem's study [44], the maximum measured load of the modified shear tests was utilized to calculate the cohesion and friction angle in the Drucker-Prager criterion, which are shown in Figure 27. With increasing temperature, the friction angle increased, and the cohesion decreased.

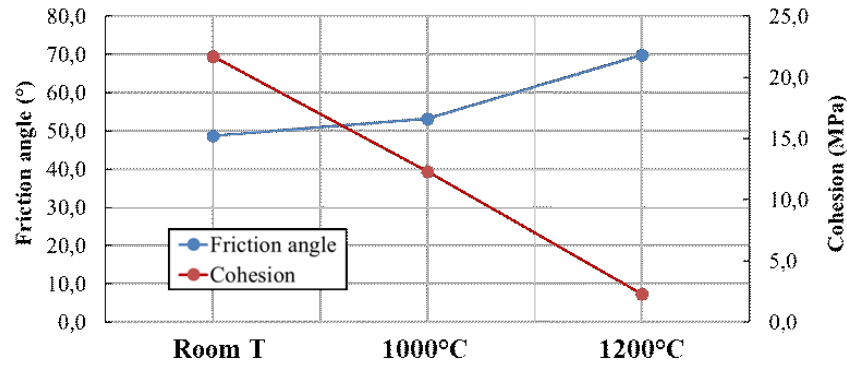


Figure 27: Friction angle and cohesion obtained from modified shear test results of alumina spinel bricks

According to these results, the Drucker-Prager criteria for different temperatures are depicted in Figure 28. It was found that in high hydrostatic pressures (higher than 12 MPa), the shear strength of the material at 1200 °C is higher than the lower temperatures due to the high friction angle.

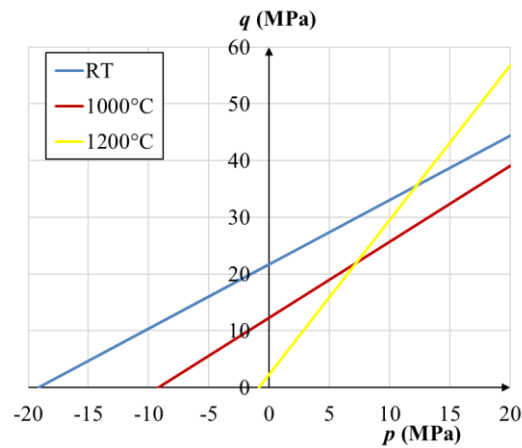


Figure 28: Drucker-Prager criterion for different temperatures

3.1.4 Tensile failure characterization

To characterize the tensile failure parameters of the shaped alumina spinel refractory, the wedge splitting test was conducted at three different temperatures (three specimens per temperature): room temperature, 1200 °C and 1400 °C. A fractured specimen after the test is shown in Figure 29-a. The WST load-displacement curves are depicted in Figure 29-b. It was observed that the maximum applied load was reduced with increasing temperature.

(a)

(b)

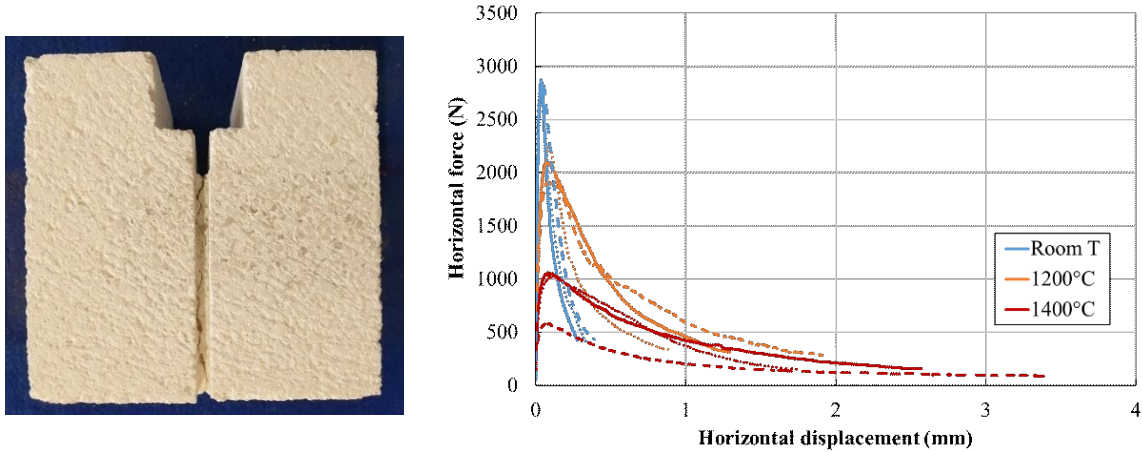


Figure 29: (a) WST fractured specimen and (b) load-displacement curves from different temperatures

The specific fracture energy (G'_f), nominal notch tensile strength (σ_{NT}) and the brittleness number (B) were calculated according to Eq. 12 - Eq. 14 and are depicted in Figure 30. The mean value of the nominal notch tensile strength and the brittleness number reduced with increasing temperature; but the mean value of the specific fracture energy increased from 112 N/m at room temperature to 292 N/m at 1200 °C and then decreased to 221 N/m at 1400 °C.

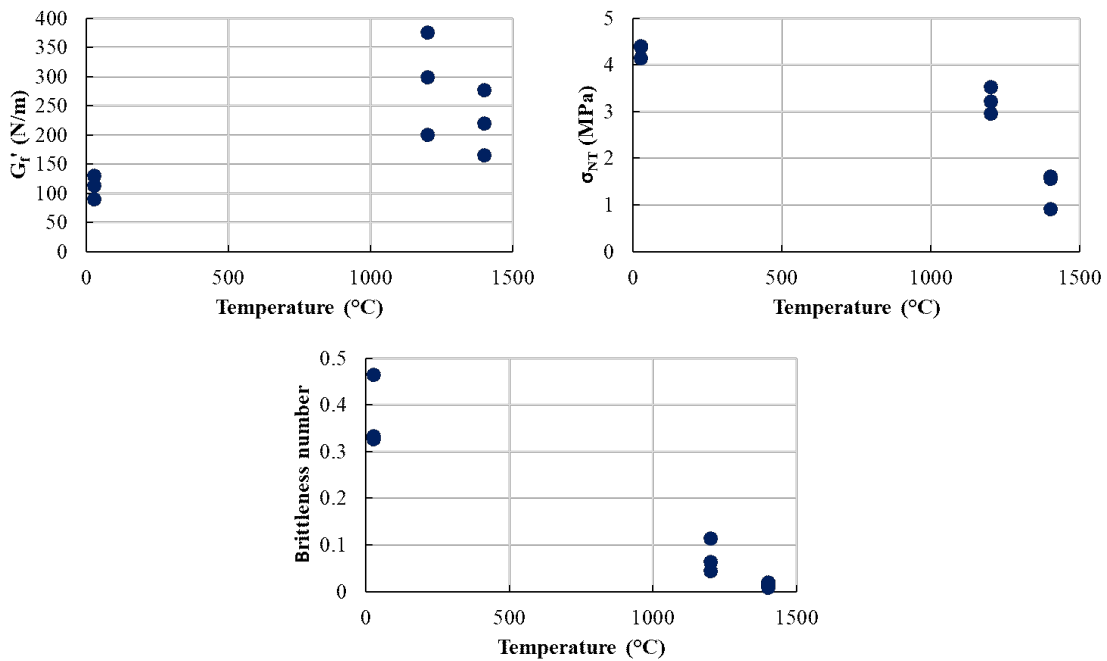


Figure 30: Specific fracture energy (G'_f), nominal notch tensile strength (σ_{NT}) and brittleness number (B) at different temperatures for alumina spinel bricks

The concrete damaged plasticity model has been explained in section 2.1.4 Tensile failure and associated constitutive models. Due to the mentioned

shortcomings of this model in application for refractories, the current study tried to mitigate them with model development. Firstly, an isotropic damaged elasticity model (DE) was developed in which the lower limit for the post-failure stress was decreased to 10^{-6} of tensile yield stress [55]. Secondly, another constitutive material model was developed to combine the mutual influence of tensile failure and creep in one model, termed DECR. In this model, an asymmetric Norton-Bailey type creep model was added in a sequential manner to the DE model as shown in Figure 31 [56]. The goal of the model was to investigate the interaction between fracture and creep in refractory materials with the aid of wedge splitting test. For detailed explanation of the models one can refer to the publications PAPER IV and PAPER V.

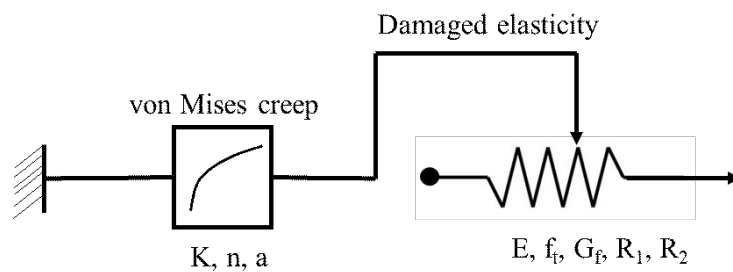


Figure 31: Schematic of the DECR model and its parameters [56]

The fracture parameters of the alumina spinel bricks were inversely evaluated using the WST results and numerical simulations. In the current study, the WST was modeled as shown in Figure 32. A two-dimensional model of half-specimen (according to the symmetry of the specimen and loading conditions) was created utilizing plane strain elements [55]. The transmission component, which is made of corundum with a Young's modulus of 300 GPa, was represented by a trapezoid. The wedge was modeled with an analytical rigid part. The model dimension was $100 \times 50 \text{ mm}^2$ with a ligament of $1.5 \times 66 \text{ mm}^2$. Between the wedge and the transmission part, as well as between the transmission part and the specimen, frictionless contacts were defined.

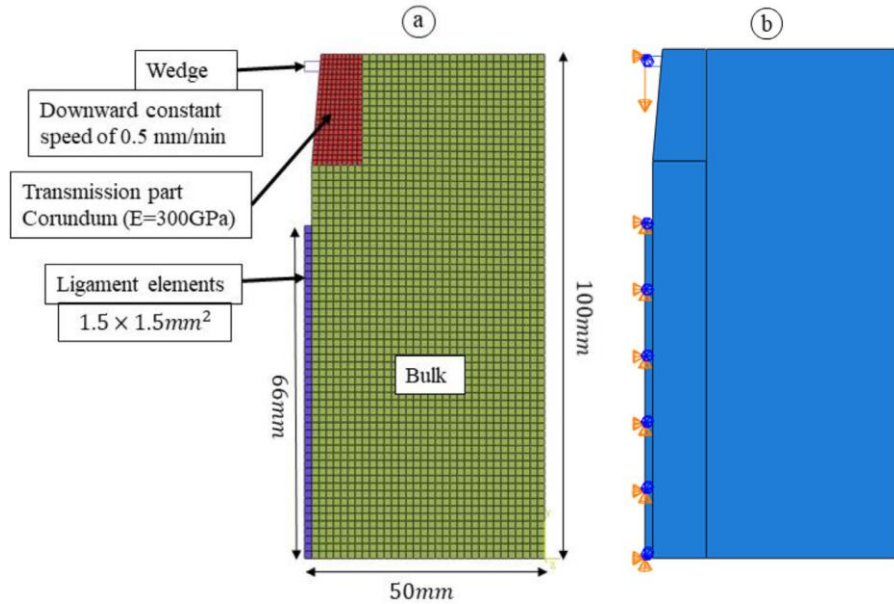


Figure 32: (a) WST 2D and symmetrical model and (b) its boundary conditions [55]

The bulk and ligament material constitutive models were defined as shown in Table 7. Tensile failure was considered just for the ligament and not for the entire specimen in order to direct the macroscopic crack propagation inside the ligament, similar to the experiment in which this is ensured by adding pre-cut lateral notches to the specimen (shown in Figure 13).

Table 7: Material models assigned to the WST model [55,56]

	Room temperature		High temperatures	
	Case 1	Case 2	Case 1	Case 2
Ligament	DE subroutine	CDP model	DECR subroutine	CDP model
Bulk	Elasticity	Elasticity	Asymmetric creep subroutine	Asymmetric creep subroutine

The primary creep stage parameters obtained for the shaped alumina spinel refractory at 1200 °C were used in the asymmetric creep model. An adaptive nonlinear least-square minimization algorithm, termed NL2SOL, implemented in the open-source code DAKOTA [87], was utilized for inverse evaluation of the model parameters.

The WST results at room temperature were fitted and plotted in Figure 33. There was almost no difference between the fittings of DE and CDP models. As expected, the bilinear post-peak behavior showed better fittings compared to the linear one. The fracture parameters were obtained and given in Table 8.

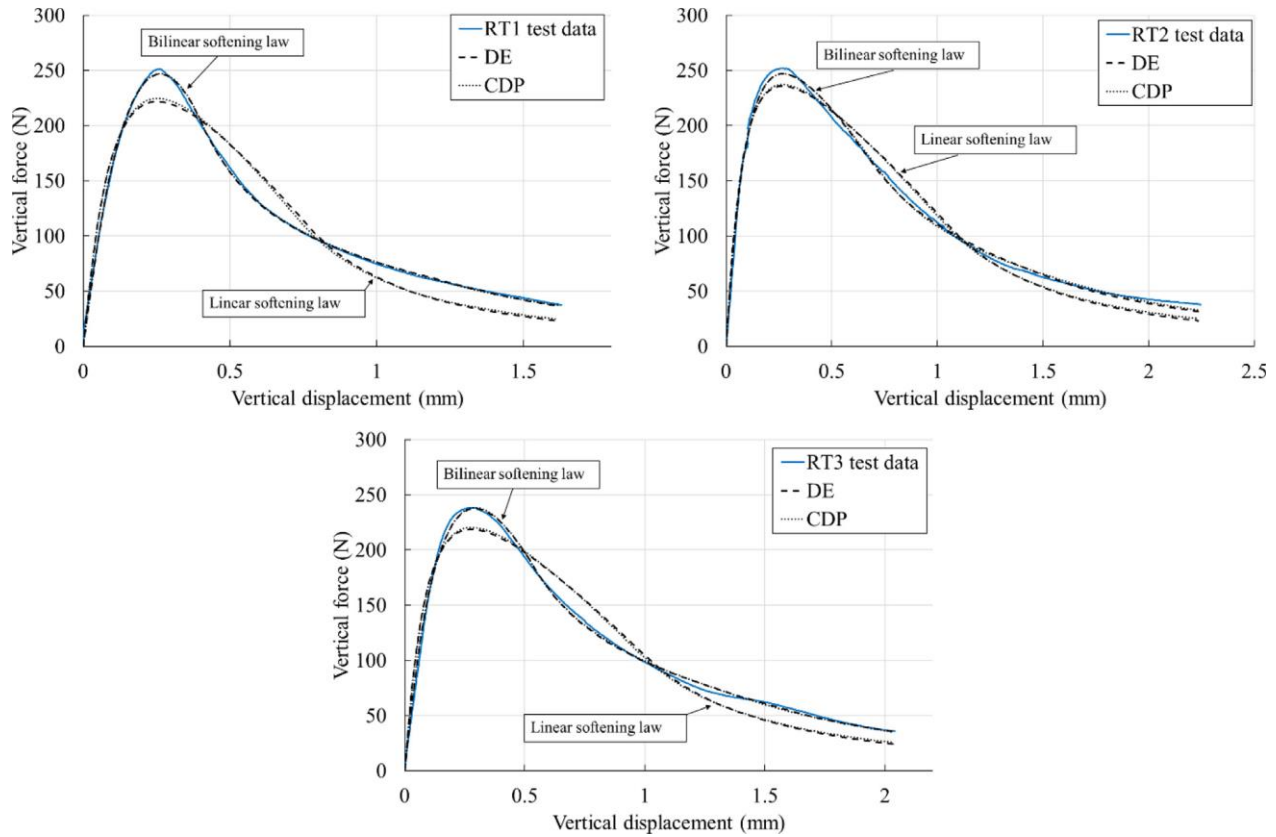


Figure 33: WST results of alumina spinel bricks and their simulated curves at room temperature [55].

Table 8: Alumina spinel bricks’ fracture properties at room temperature (experimental and inversely evaluated with DE model) [55].

	G'_f (N/m)	G_f (N/m)	$\frac{G'_f}{G_f}$ (%)	σ_{NT} (MPa)	f_t (MPa)	$\frac{\sigma_{NT}}{f_t}$	E_0 (GPa)	E' (GPa)	B'	B	$\frac{B'}{B}$
RT-1	91.2	114.1	79.9	4.39	3.24	1.35	41.63	Ultrasonic Mean \pm STD 38.72 \pm 3.70	0.359	0.146	2.46
RT-2	130.3	159.6	81.6	4.41	2.64	1.67	58.20		0.254	0.049	5.18
RT-3	113.6	147.3	77.1	4.15	2.79	1.49	42.41		0.259	0.082	3.16
RT-Mean	111.7	140.3	79.6	4.32	2.89	1.49	47.41		0.291	0.092	3.16
RT-STD	19.7	23.5	2.3	0.14	0.31	0.16	9.34		0.059	0.049	1.39

The WST results at 1200 °C were fitted and are shown in Figure 34. In the case 1 with the DECR model the fit was better than the case 2 with CDP model, particularly to the tail of the curve. Table 9 shows the average of inversely evaluated parameters. Fracture energy was found to be 17% higher with DECR than it was with CDP. The reason for this is because in CDP, the post-peak failure limit prevents the load from dropping to zero, increasing the amount of energy consumed. In addition,

it was found that in average, 12.9% of the energy was consumed by creep at 1200 °C.

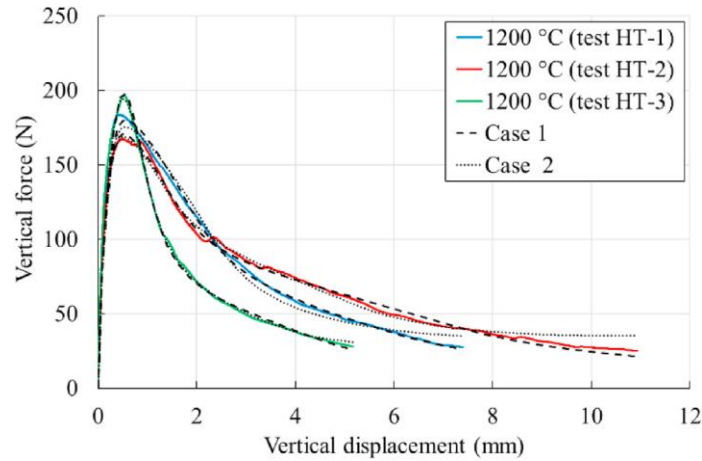


Figure 34: Inverse identified curves of the WST results at 1200 °C using DECR and CDP model [56].

Table 9: Comparison of inversely evaluated fracture parameters at 1200 °C (average of three WST results) using DECR and CDP model [56].

	Case 1 (DECR + Creep)					Case 2 (CDP + Creep)				
	G_f (N/m)	f_t (MPa)	R_1	R_2	R^2 $RMSE (MPa^2)$	G_f (N/m)	f_t (MPa)	R_1	R_2	R^2 $RMSE (MPa^2)$
HT-1	309.0	1.62	0.239	0.264	0.979 4.137	273.0	1.57	0.104	0.315	0.961 5.609
HT-2	384.0	1.53	0.380	0.167	0.995 2.729	314.3	1.53	0.438	0.214	0.988 4.049
HT-3	195.2	1.90	0.239	0.134	0.992 4.606	172.4	1.87	0.238	0.192	0.993 4.137
HT-Mean	296.0	1.68	0.286	0.188	0.993 3.824	253.2	1.65	0.260	0.240	0.989 4.598

The DECR model still needs some improvements to become capable of simulating the refractory linings. For instance, a better asymmetric creep assumption needs to be considered for the creep calculations in the model. Therefore, in this study the CDP model was used for the thermomechanical simulation of the ladle. In Table 10, the corresponding parameters of the CDP model are listed. These

parameters were inversely evaluated for the CDP model using the WST tests without considering creep at high temperatures.

Table 10: Inversely evaluated fracture parameters of CDP model for alumina spinel bricks

Parameter	Room temperature	1200 °C	1400 °C
G_f (Nm/m ²) (mean \pm STD)	136.0 \pm 21.9	337.5 \pm 90.8	258.7 \pm 67.1
f_t (MPa) (mean \pm STD)	2.91 \pm 0.33	1.66 \pm 0.16	0.68 \pm 0.21
R_1	0.213	0.239	0.272
R_2	0.295	0.263	0.305

3.2 Thermomechanical modeling of the steel ladle

The objective of the current study was thermomechanical simulation of a steel ladle refractory lining. Therefore, a 3D unit-cell model of the steel ladle was built according to its industrial design shown in Figure 35. As shown in Figure 36, the model is a wedge-shaped cut from the ladle structure, and its thickness was considered half of a brick in the working lining barrel zone considering symmetry conditions. The model was built in the software Abaqus [28].

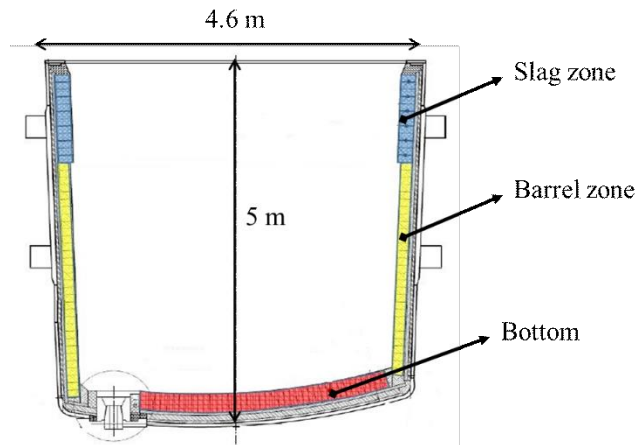


Figure 35: 2D Sketch of the industrial steel ladle

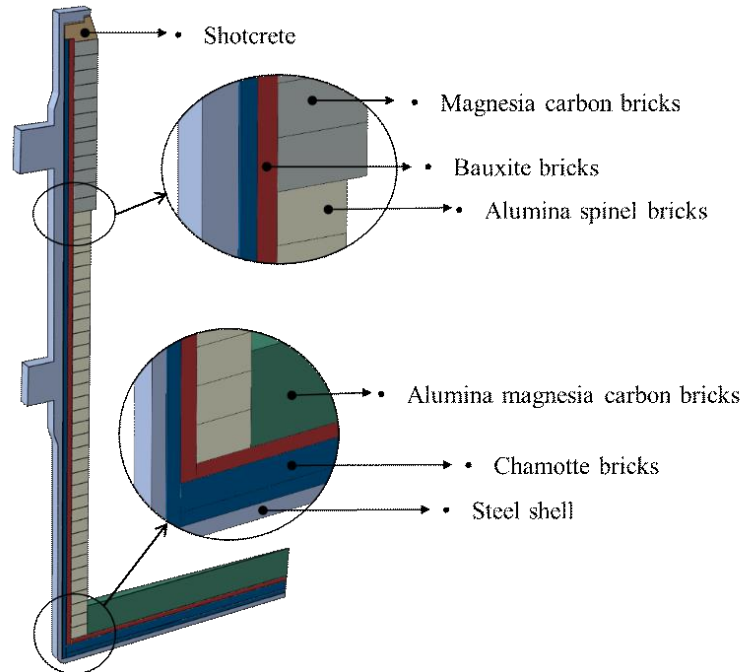


Figure 36: 3D unit-cell model of the steel ladle refractory lining

The refractory materials for each section are also listed in Table 11. In addition to the mentioned refractories, two other materials were used in the structure of the ladle, shotcrete and insulation board. Shotcrete was used in the top part of the lining due to its low stiffness and formability. The insulation board was used between the steel shell and the chamotte bricks. It was a microporous material composed of 25 – 55wt% vermiculite and 5 – 25wt% forsterite [88]. The application objectives of the insulation board together with the insulation lining (shown in Figure 37) are the following. Firstly, it reduces the heat losses and keeps the molten steel at the desired temperature to guarantee the product quality. Secondly, it saves energy and reduces the environmental harm. Lastly, it maintains the lining in a stable compressed condition to prevent joints opening.

Table 11: Refractory materials used in the steel ladle

Section	Material
Working lining Barrel zone	Alumina spinel bricks
Working lining Slag zone	Magnesia carbon bricks
Working lining bottom	Alumina magnesia carbon bricks
Safety lining	Bauxite bricks
Insulation lining	Chamotte bricks

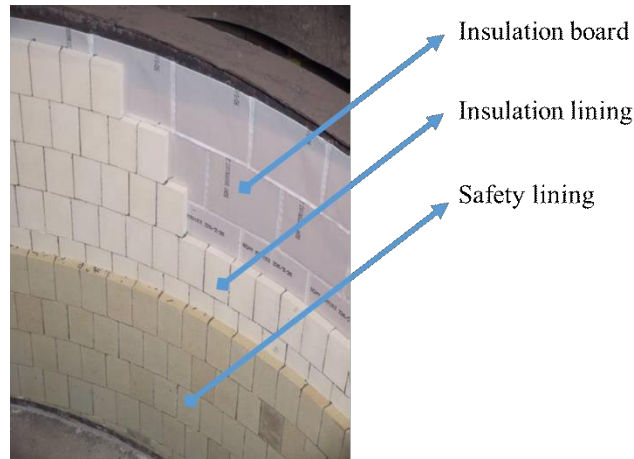


Figure 37: Insulation board, insulation lining and safety lining in the steel ladle

The material properties necessary for the thermomechanical simulation can be categorized according to Table 12. Young's modulus, Poisson's ratio, density and all the thermal properties were required for all the materials. In addition, the irreversible material constitutive models were assigned to the working lining, and their corresponding material parameters were required.

Table 12: Material properties required for the thermomechanical simulations

General properties for all Materials		Mechanical properties for irreversible behavior of the working lining		
Physical properties	Thermal properties	Tensile failure	Creep	Shear failure
Young's modulus	Coefficient of thermal expansion	Fracture energy	Norton-Bailey parameters	Cohesion
Poisson's ratio	Conductivity	Tensile strength		Friction angle
Density	Specific heat			

The material properties for different parts of the model were obtained from different sources and reported in Appendix A. Young's modulus and mechanical properties of the alumina spinel bricks were investigated and evaluated in the current study. Regarding the creep parameters, only primary stage creep parameters of the compressive creep tests were used because the creep model in Abaqus receives parameters of only one stage. The choice of compressive creep parameters is because most of the brick volume in the working lining is under large compressive stresses in circumferential direction especially where the temperature is high enough for creep to occur. The thermal properties of the alumina spinel brick, and the insulation

board were obtained from the research work of Diana Vitiello, another Ph.D. student in ATHOR project [87,88]. The other material properties were received from the industrial partners.

Material properties were assigned to their corresponding parts in the model. The insulation board between the chamotte bricks and the steel shell has a thickness of 5 mm and very low stiffness; therefore, it has low influence on the stress distribution. Instead of explicitly including this part in the model, the contact definition between the chamotte bricks and steel shell was defined based on the conductivity of the insulation board, which was 0.06 J/smK. In this way the effect of the insulation board on the thermal distribution of the model is considered without increasing the complexity of the model. To consider the joints between the bricks in the working lining, the following measures were taken (as shown in Figure 38). A rigid plate was applied to consider the vertical joints (head joints). Initial 1 cm gap between the shotcrete and shell is defined to consider the horizontal joints between the bricks (bed joints).

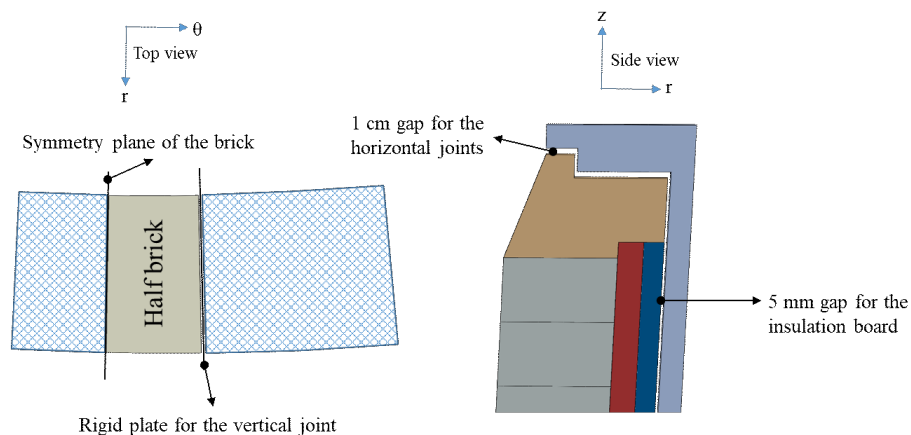
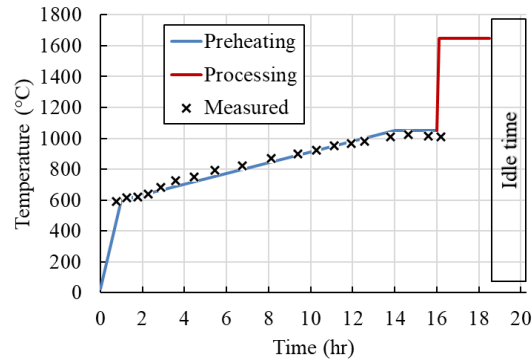


Figure 38: Consideration of joints in the steel ladle unit-cell model

The working cycle of a steel ladle is defined dependent on its purpose. The steel ladle studied in this research work was employed in a working cycle plan according to Table 13 and Figure 39.

Table 13: Working cycles of the studied steel ladle

Title	Duration	Temperature
Preheating	1 hour	25 °C – 600 °C
	13 hours	600 °C – 1050 °C
	2 hours	1050 °C
Pouring	7 minutes	1050 °C – 1650 °C
Processing	125 minutes	1650 °C
Casting	45 minutes	1650 °C
Idle time	2 hours	Adiabatic condition

**Figure 39: Temperature definition at the hot face during preheating and first steel ladle working cycle (together with the measured data during the preheating step)**

In the next step, thermomechanical simulations were planned in different categories according to

Table 14. Two studies on the effect of joint size and friction between the bricks were done before the simulations for comparison of different material constitutive models. The so-called Penalty friction formulation [28], which is based on the Coulomb friction model, was used between the bricks. For the alumina magnesia carbon bricks in the bottom working lining, only creep parameters were available. Therefore, it was only assigned with creep behavior in order to have the similar conditions in simulations with irreversible behavior. All the simulations were defined in a coupled manner (called coupled temp-displacement in Abaqus [28]) with a transient heat transfer condition.

Table 14: material constitutive models applied for different lining components and simulation cases

Simulation cases	Joint size study	Friction coefficient study	Elasticity simulation	Consideration the creep at the working lining	Consideration of tensile failure at the working lining	Consideration of shear failure at the working lining		
Part	Material constitutive model							
Alumina spinel bricks	Linear elasticity	Linear elasticity	Linear elasticity	Abaqus creep	Concrete damaged plasticity	Drucker Prager		
Magnesia Carbon bricks					Concrete damaged plasticity	Drucker Prager		
Alumina magnesia carbon bricks					Abaqus creep	Abaqus creep		
Chamotte bricks				Linear elasticity	Linear elasticity	Linear elasticity	Linear elasticity	Linear elasticity
Bauxite bricks								
Shotcrete								
Steel shell			Linear elasticity / von Mises plasticity	Linear elasticity / von Mises plasticity	Linear elasticity / von Mises plasticity	Linear elasticity / von Mises plasticity		
Number of working cycles	1	1	5	5	5	5		
vertical joint size (mm)	0.2, 0.3, 0.4, 0.5	0.4	0.4	0.4	0.4	0.4		
Friction coefficient (1)	0	0.1, 0.2, 0.4	0	0	0	0		

The working lining is the most significant component of the ladle lining since it has the majority of refractory consumption and receives the harshest working environment conditions. The present study mainly focuses on the thermomechanical behavior of steel ladle barrel zone.

3.2.1 Temperature results

In total, five steel ladle process cycles were simulated. The temperature results are shown in Figure 40. The temperature on the steel shell increased to around 290 °C at the end of fifth idle time; nevertheless, the temperature increase rate slowed down with time. The insulation layer cold face temperature was around 900 °C at the end of fifth idle time, which proved the importance of the insulation board located between the insulation bricks and the steel shell. Moreover, the temperature of the lining was increasing constantly due to the fact that adiabatic condition was considered for the hot face of the bricks, which represented the case where the lid of the ladle was not removed during the idle time.

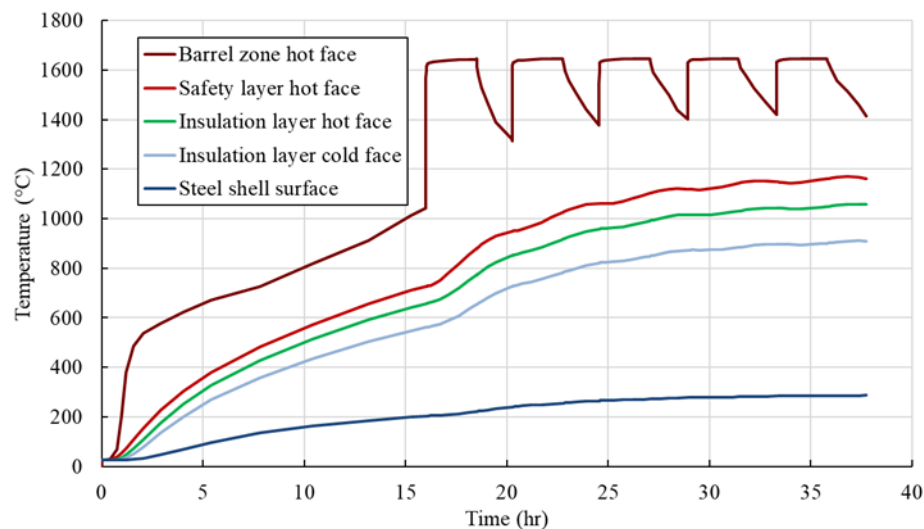


Figure 40: Simulated temperatures of different layers in barrel zone (preheating and five working cycles)

3.2.2 Joint size and friction coefficient effect

The vertical joints of MC bricks at the end of preheating were completely closed for all initial joint opening sizes, but for AS bricks some joints were still open at the cold side of the bricks. This was due to the larger expansion coefficient of the MC bricks compared to AS bricks. Increasing the initial joint size decreased the radial displacement of the steel shell, and also maximum von Mises stress in the shell and barrel area. In addition, increase of the friction coefficient elevated the maximum von Mises stress at the working lining, but reduced it at the steel shell (Figure 41).

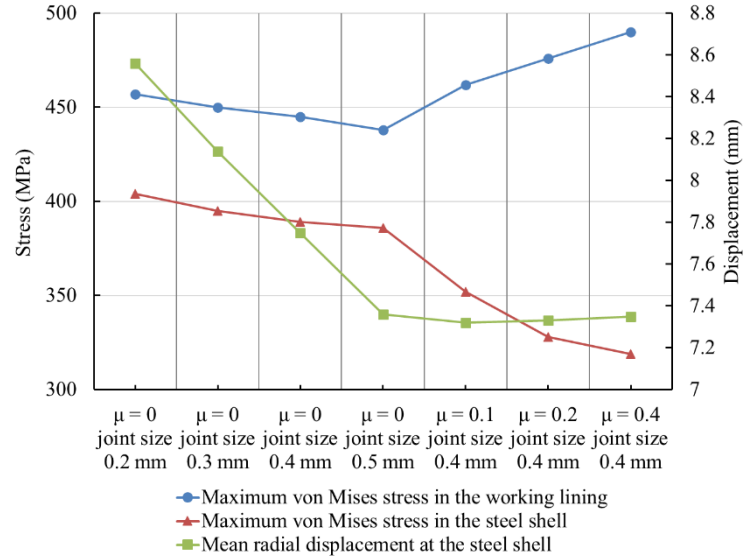


Figure 41: Influence of initial vertical joint size and friction coefficient on the maximum von Mises stresses in the working lining and steel shell, and the mean radial displacement of the steel shell

3.2.3 Stress and strain results

In the working lining, it was observed that the highest maximum von Mises stress occurred for the elastic simulation and the least maximum von Mises stress occurred for the creep model due to the relaxation. For better comparison of the simulations, one brick from the middle of barrel zone was chosen (Figure 42).

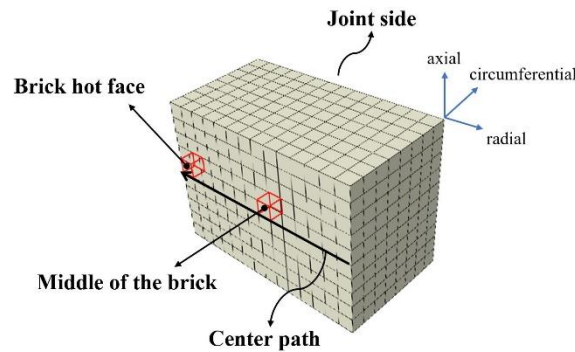


Figure 42: Alumina spinel brick model

In Figure 43, radial, circumferential, and axial stresses at the hot face and the middle of the selected alumina spinel brick were shown with respect to the process time. The stresses are the mean values of 8 integration points in the element. The first observation was that a biaxial compressive stress state existed in the center of brick, i.e., radial stress was negligible compared to axial and circumferential stress. The stress magnitudes during the preheating were around the same magnitude for elastic, creep and tensile failure simulations but lower for shear failure model, which shows

that shear failure already occurred at the hot face during the preheating period. In addition, the creep decreased the stress at the hot face in the beginning of 1st cycle, and in the middle of the brick, during the 2nd cycle. In other three models, the stresses had similar raise and drop profile caused by pouring and idle status. It was also observed that shear failure had more influence on decreasing the axial stress than the circumferential stress; it reduced axial and circumferential stresses at the hot face about 58% and 16% at the end of 5th cycle, respectively. The tensile failure only reduced the stresses in the middle of the bricks about 29% compared to the elastic simulation, at the end of 5th cycle.

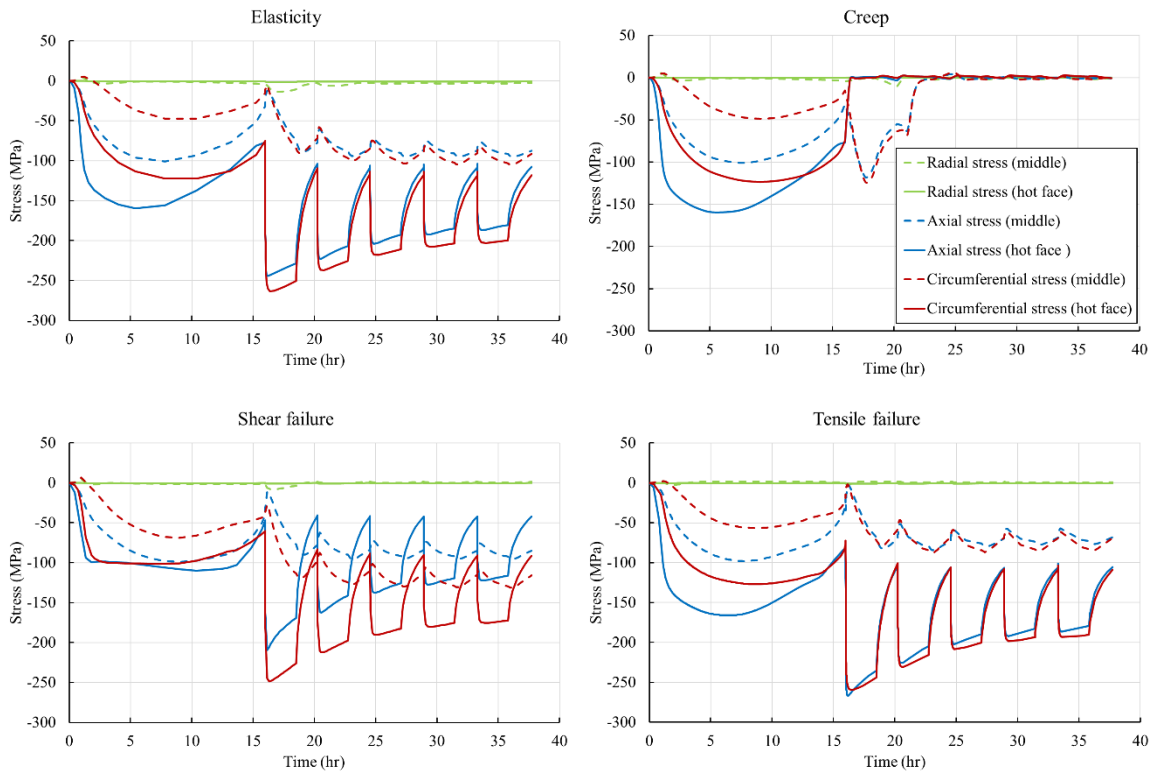


Figure 43: Stress at the hot face and middle of the selected alumina spinel brick

The equivalent irreversible strains at the hot face and middle of the brick over time are illustrated in Figure 44. The values of the equivalent strains were normalized to their maximum for each failure mechanism for better observation. This was done because the formulation of equivalent irreversible strains is different in Abaqus for different material models; therefore, their actual values cannot be compared. It was observed that the shear failure occurred during the preheating at hot face and middle of the brick, being higher at the hot face. But it did not occur afterwards because the material yield criteria changes with increasing temperature and as shown in Figure 45, the stress state at higher temperatures lies under the Drucker-Prager yield line.

The tensile failure did not occur at the hot face since the material is always under compression stresses. But it occurred at the middle of the brick already during the preheating and increased after each hot shock. Finally, the creep occurred after the temperature increased sufficiently and it started at the hot face and then at middle of the brick. As expected, the value of the equivalent creep strain was higher at the hot face.

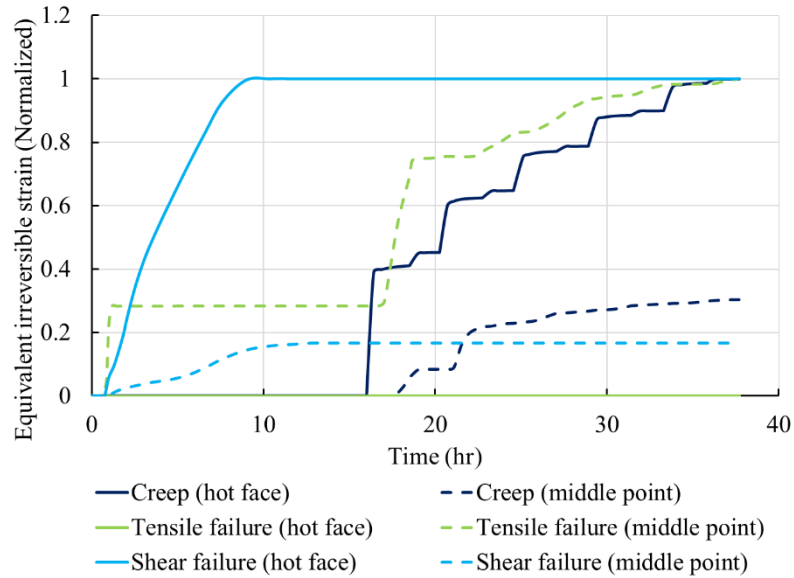


Figure 44: Equivalent irreversible strain under different failure mechanisms with time

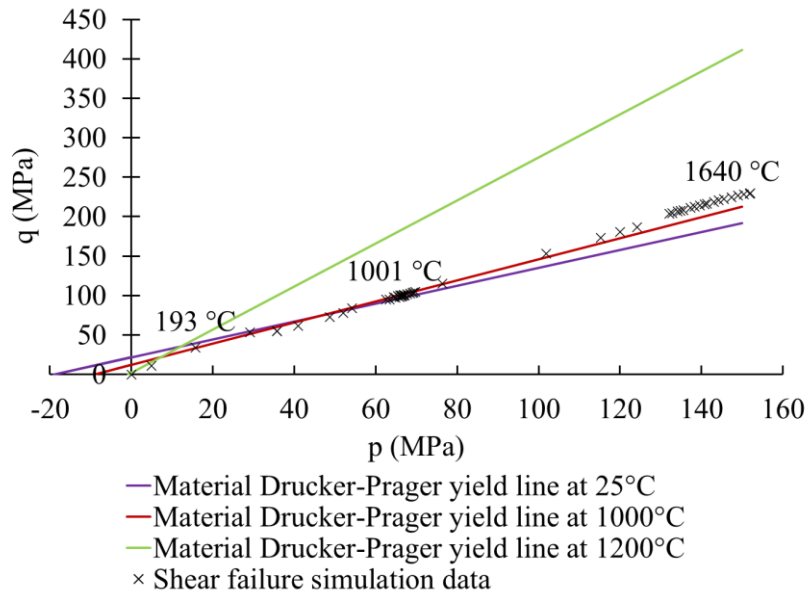


Figure 45: Shear failure simulation p-q diagram at the hot face of the selected AS brick till the end of 1st pouring

Another important observation was the effect of dilation angle on the irreversible strains. For that, the volumetric strains were plotted in Figure 46. The dilation angle in the flow rule influences the expansion ratio caused by mechanical loads directly. In the Abaqus creep model, zero expansion is defined with a 0° dilation angle, which is a factor for incompressible flow. In Figure 46, it was shown also that the irreversible volumetric strain in creep simulation was zero. On the other hand, in the Drucker-Prager model the dilation angle was defined to be the same as the friction angle, which is the characteristic of a so-called associated flow. This assumption caused a high expansion and high volumetric irreversible strain in the shear failure simulation. In the concrete damaged plasticity model, a non-associated flow rule with a dilation angle of 38° was considered. This assumption caused expansion in tensile failure simulations but not as high as the shear failure simulations. Finally, it should be noted that the actual dilation angle for refractories has not been measured so far, and other studies considered either associated [75,90] or incompressible [34] flow in the simulations. The effect of the dilation angle was checked by changing its value in shear failure simulations. It was observed that the influence on the stress magnitudes and joint openings were negligible. Nevertheless, high-temperature measurement of the dilation angle for refractory materials is necessary for more accurate results.

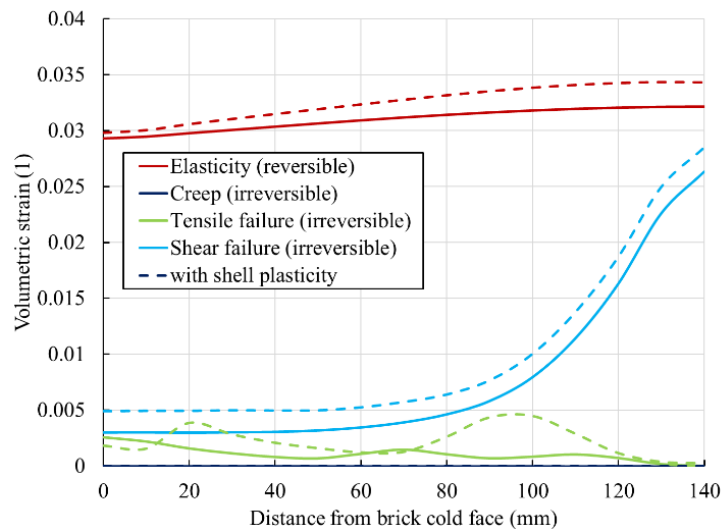


Figure 46: Volumetric strains on the center path of the selected alumina spinel brick at the end of the 5th cycle

3.2.4 Influence of steel shell plasticity

The maximum von Mises stress in the steel shell occurred at the top part of the shell structure. Its value in creep and shear failure simulations occurred at the end of first pouring stage with the values of 1.02 GPa and 2.13 GPa, respectively. Conversely, the maximum value in tensile failure and elastic simulations occurred at

the end of last pouring stage with the values of 3.44 GPa and 3.78 GPa. This shows that creep and shear failure at the working lining alleviate the stress at the steel shell to larger extent than the tensile failure at the working lining. In addition, the stress magnitude at the steel shell was higher than the steel strength; therefore, the plasticity of steel was added to the simulations for comparison. Isotropic von Mises plasticity model in Abaqus [28] was assigned to the steel shell according to the standard DIN EN 10028-2 [91].

After consideration of the steel shell plasticity, the maximum plastic strain (≈ 0.21 for Elasticity simulation) occurred at the top part of the steel shell and at its other areas, the plastic strain was below 0.005. Strain energies from different simulations are compared in Figure 47. The recoverable strain energy at the end of 5th idle time decreased after including shell plasticity for all simulations. Dissipated energy due to plasticity increased because of additional plasticity of the steel shell. However, dissipated energy due to creep decreased in corresponding models.

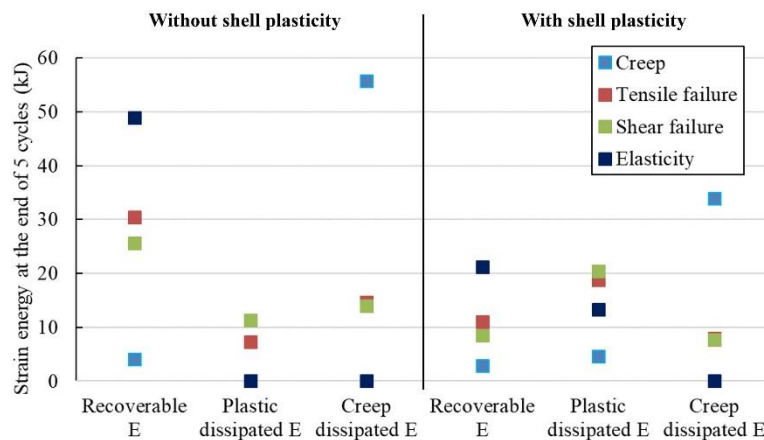


Figure 47: Influence of the shell plasticity on strain energies (E) in different simulations

3.2.5 Joint openings

The horizontal joint openings were negligible compared to the vertical ones, and they occurred mostly at the cold side of bricks. It was observed that at the end of 5th cycle, for the creep simulation there was joint opening for all working lining bricks at the hot face, while other simulations did not show opening at this time point. Figure 48 shows the vertical joint opening at the hot face of the selected alumina spinel brick against the process time. It was observed that including shell plasticity increased the vertical joint opening slightly in the case of creep simulation. It did not affect the joint opening on the hot face in other simulations. Other important results can be seen in PAPER VI.

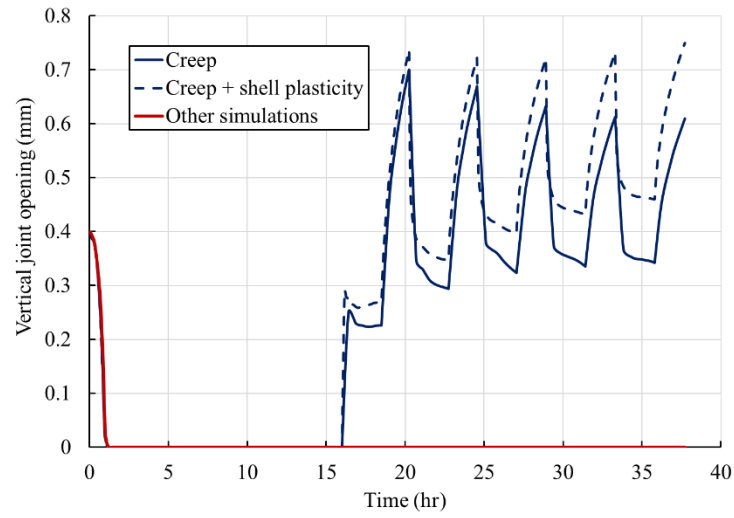


Figure 48: Vertical joint opening on the alumina spinel brick hot face in different simulations

4. Concluding remarks

The main objective of the research work was to investigate the high-temperature failure behavior of refractory linings used in a steel ladle. This goal was reached by performing high-temperature mechanical experiments, analysis of their results, evaluations of material parameters, and applying them in thermomechanical simulations. The concluding remarks of the research work are categorized in two groups as follows:

4.1 Mechanical characterization

- Shaped alumina spinel refractory, which is used in the working lining of steel ladles, was selected for the experimental study. This study included Young's modulus measurement, uniaxial compressive and tensile creep tests, modified shear test, and wedge splitting test.
- In the current study, a scatter in the experimental results was received in all experiments, which was more evidence in the case of high-temperature experiments. The scattered results were not only received from the specimens of different bricks but also from the specimens within one brick. This showed the effect of production process on the material microstructure, which is a common case for refractories.
- A statistical study was conducted on the creep behavior of the studied refractory. A novel approach was proposed for the first time to investigate the effect of material heterogeneity on the evaluated creep parameters.
- High creep asymmetry was observed in the creep behavior of the shaped alumina spinel refractory. The material showed higher resistance to creep under compression than tension.
- According to the study on fracture characterization using wedge splitting test, it was concluded that the developed model (DECR) is a more accurate means for inverse evaluation of fracture parameters compared to the CDP model.
- The developed model showed that the impact extent of the reduced post-failure stress limit on the fracture parameters identification depends on the brittleness of the defined material. Additionally, considering creep and tensile failure together in the ligament contributes to accurate determination of the fracture energy.

4.2 Thermomechanical simulation

- Reduction of the joint size from 0.5 mm to 0.2 mm, in elastic simulations, increased the maximum circumferential stress in the working lining by 26%, but its effect on the other two directions was smaller and it did not change the joint state at the hot face.
- Consideration of friction between the bricks increased the maximum von Mises stress at the bricks but decreased it at the steel shell.
- Creep contributed to joint opening and stress reduction in the working lining more than shear failure and tensile failure.
- Shear failure and tensile failure already occurred during the preheating, but creep started during the first process cycle. Mainly the hot face of the working lining experienced creep and shear failure and the area around 30 mm from the hot face of the working lining confronted tensile failure.
- Consideration of plasticity in the steel shell had considerable influences on the stresses in the axial direction and the recoverable energy. It decreased the irreversible strains in the working linings due to creep, shear failure and tensile failure.
- Evident multiaxial stresses occurred in the working lining. The application of uniaxial creep parameter may overestimate the creep strains and joint openings in creep simulation because the refractories might show different creep behavior under multiaxial stresses.

5. Outlook

The current study proposed an approach for thermomechanical simulation of a refractory lining with all the steps necessary. In the core of this study, several important improvements were implemented, which can be applied in further studies in this field. On the other hand, some open questions arise after the current study. In the following items, the important outlook of this research work is described.

- Due to the heterogeneous nature of refractories and its influence on the material properties, statistical studies might be necessary to other mechanical characterizations of refractory materials.
- A material model (DECR) was developed to combine the effect of tensile failure and creep and improve the characterization of refractories fracture behavior using the wedge splitting test results. Nevertheless, for applying the model to thermomechanical simulation of refractory linings, further improvements are required. Firstly, DECR model was tested and verified only on 2D simulations and it should get updated for 3D thermomechanical simulations. In addition, including a complete asymmetric creep model that represent the refractory creep behavior under multiaxial stress condition could be the next important improvement..
- In the thermomechanical simulations of the current study, the refractory parts were considered as homogenous materials with specified material properties, which only changed with temperature. On the other hand, the mechanical characterization of the alumina spinel refractory showed larger standard deviations for several material parameters. Therefore, the effect of refractories' heterogeneity on the thermomechanical simulation of the refractory linings should be studied in future.

6. References

- [1] C. Schacht, *Refractories handbook*, CRC Press, 2004.
- [2] DIN EN 1402-1, *Unshaped refractory products - Part 1: Introduction and classification*, 2004.
- [3] M. Schnabel, A. Buhr, R. Exenberger, C. Rampitsch, Spinel: in-situ versus preformed - clearing the myth, *Refractory Worldforum*. 2 (2010) 87–93.
- [4] <https://www.alteo-alumina.com/en/refractory/>, (2021).
- [5] K. Andreev, S. Sinnema, A. Rekik, S. Allaoui, E. Blond, A. Gasser, Compressive behaviour of dry joints in refractory ceramic masonry, *Construction and Building Materials*. 34 (2012) 402–408. <https://doi.org/10.1016/j.conbuildmat.2012.02.024>.
- [6] M. Ali, T. Sayet, A. Gasser, E. Blond, Transient Thermo-Mechanical Analysis of Steel Ladle Refractory Linings Using Mechanical Homogenization Approach, *Ceramics*. 3 (2020) 171–189. <https://doi.org/10.3390/ceramics3020016>.
- [7] S. Jin, H. Harmuth, D. Gruber, Compressive creep testing of refractories at elevated loads - Device, material law and evaluation techniques, *Journal of the European Ceramic Society*. 34 (2014) 4037–4042. <https://doi.org/10.1016/j.jeurceramsoc.2014.05.034>.
- [8] R. Kaczmarek, J.-C. Dupré, P. Doumalin, O. Pop, L. Teixeira, M. Huger, High-temperature digital image correlation techniques for full-field strain and crack length measurement on ceramics at 1200°C: Optimization of speckle pattern and uncertainty assessment, *Optics and Lasers in Engineering*. 146 (2021) 106716. <https://doi.org/10.1016/j.optlaseng.2021.106716>.
- [9] I. Kieliba, I. Dominik, K. Lalik, T. Tonnesen, J. Szczerba, R. Telle, Self-excited acoustical system frequency monitoring for refractory concrete under uniaxial compression, *Energies*. 14 (2021). <https://doi.org/10.3390/en14082222>.
- [10] K. Andreev, V. Tadaion, Q. Zhu, W. Wang, Y. Yin, T. Tonnesen, Thermal and mechanical cyclic tests and fracture mechanics parameters as indicators of thermal shock resistance – case study on silica refractories, *Journal of the European Ceramic Society*. 39 (2019) 1650–1659. <https://doi.org/10.1016/j.jeurceramsoc.2018.12.062>.

-
- [11] J. Lemaitre, J.L. Chaboche, *Mechanics of solid materials*, Cambridge university press, 1994.
- [12] J.P.L. dos Santos, P.M. Amaral, A.C. Diogo, L.G. Rosa, Comparison of Young's Moduli of Engineered Stones Using Different Test Methods, *Key Engineering Materials*. 548 (2013) 220–230. <https://doi.org/10.4028/www.scientific.net/KEM.548.220>.
- [13] W. Węglewski, K. Bochenek, M. Basista, T. Schubert, U. Jehring, J. Litniewski, S. Mackiewicz, Comparative assessment of Young's modulus measurements of metal-ceramic composites using mechanical and non-destructive tests and micro-CT based computational modeling, *Computational Materials Science*. 77 (2013) 19–30. <https://doi.org/10.1016/j.commatsci.2013.04.007>.
- [14] G. Roebben, B. Bollen, A. Brebels, J. van Humbeeck, O. van der Biest, Impulse excitation apparatus to measure resonant frequencies, elastic moduli, and internal friction at room and high temperature, *Review of Scientific Instruments*. 68 (1997) 4511–4515. <https://doi.org/10.1063/1.1148422>.
- [15] G.R. Terwilliger, K.C. Radford, HIGH-TEMPERATURE DEFORMATION OF CERAMICS. 1. BACKGROUND, *AMERICAN CERAMIC SOCIETY BULLETIN*. 53 (1974) 172–179.
- [16] M. Stueckelschweiger, D. Gruber, S. Jin, H. Harmuth, Creep testing of carbon containing refractories under reducing conditions, *Ceramics International*. 45 (2019) 9776–9781. <https://doi.org/https://doi.org/10.1016/j.ceramint.2019.02.013>.
- [17] J.T. Boyle, J. Spence, *Stress analysis for creep*, Butterworths, England, 1983.
- [18] J. Rösler, H. Harders, M. Bäker, *Mechanical behaviour of engineering materials: metals, ceramics, polymers, and composites*, Springer Science & Business Media, 2007.
- [19] J. Kang, F. Zhou, C. Liu, Y. Liu, A fractional non-linear creep model for coal considering damage effect and experimental validation, *International Journal of Non-Linear Mechanics*. 76 (2015) 20–28. <https://doi.org/10.1016/j.ijnonlinmec.2015.05.004>.

-
- [20] K. Naumenko, H. Altenbach, *Modeling of Creep for Structural Analysis*, Springer Berlin Heidelberg, Berlin, Heidelberg, 2007. <https://doi.org/10.1007/978-3-540-70839-1>.
- [21] W.D. Callister, *Fundamentals of materials science and engineering*, Wiley London, 2000.
- [22] I. Matsumura, Y. Hayashi, Y. Hiyama, A. Ijiri, *Refractories under load and hot creep measurements*, *Taikabutsu Overseas*. 2 (1982) 36–42.
- [23] L. Teixeira, S. Samadi, J. Gillibert, S. Jin, T. Sayet, D. Gruber, E. Blond, *Experimental Investigation of the Tension and Compression Creep Behavior of Alumina-Spinel Refractories at High Temperatures*, *Ceramics*. 3 (2020) 372–383. <https://doi.org/10.3390/ceramics3030033>.
- [24] A. Sidi Mammam, D. Gruber, H. Harmuth, S. Jin, *Tensile creep measurements of ordinary ceramic refractories at service related loads including setup, creep law, testing and evaluation procedures*, *Ceramics International*. 42 (2016) 6791–6799. <https://doi.org/10.1016/j.ceramint.2016.01.056>.
- [25] E. Blond, N. Schmitt, F. Hild, P. Blumenfeld, J. Poirier, *Modelling of high temperature asymmetric creep behavior of ceramics*, *Journal of the European Ceramic Society*. 25 (2005) 1819–1827. <https://doi.org/10.1016/j.jeurceramsoc.2004.06.004>.
- [26] L.E. Mong, *Elastic behaviour and creep of refractory bricks under tensile and compressive loads*, *Journal of the American Ceramic Society*. 30 (1947) 69–78.
- [27] S. Schachner, S. Jin, D. Gruber, H. Harmuth, *Three stage creep behavior of MgO containing ordinary refractories in tension and compression*, *Ceramics International*. 45 (2019) 9483–9490. <https://doi.org/10.1016/j.ceramint.2018.09.124>.
- [28] Dassault systems, ABAQUS (2018) ‘ABAQUS Documentation,’ (2018).
- [29] S. Schachner, S. Jin, D. Gruber, H. Harmuth, *A method to characterize asymmetrical three-stage creep of ordinary refractory ceramics and its application for numerical modelling*, *Journal of the European Ceramic Society*. 39 (2019) 4384–4393. <https://doi.org/https://doi.org/10.1016/j.jeurceramsoc.2019.06.010>.

-
- [30] D.W. Marquardt, An algorithm for least-squares estimation of nonlinear parameters, *Journal of the Society for Industrial and Applied Mathematics*. 11 (1963) 431–441.
- [31] D. Gruber, M. Huger, E. Blond, T.H. Nguyen, S. Samadi, L. Teixeira, F. Asadi, R. Kaczmarek, I. Kieliba, V. Tadaion, T. Tonnesen, Deliverable D1. 4 Devices for mechanical characterisation at laboratory scale that are operational, 2019. <https://www.etn-athor.eu/wp-content/uploads/sites/18/2019/05/D-1.4-Devices-for-mechanical-characterisation-v2.5.pdf> (accessed October 14, 2021).
- [32] H. Harmuth, E.K. Tschegg, Fracture mechanical characterisation of ordinary ceramic refractory materials, *Veitsch-Radex Rundsch.* (1994) 465–480.
- [33] D.C. Drucker, W. Prager, Soil mechanics and plastic analysis or limit design, *Quarterly of Applied Mathematics*. 10 (1952) 157–165.
- [34] D. Gruber, H. Harmuth, Durability of Brick Lined Steel Ladles from a Mechanical Point of View, *Steel Research International*. 79 (2008) 913–917. <https://doi.org/10.1002/srin.200806220>.
- [35] S. Jin, D. Gruber, H. Harmuth, R. Rössler, Thermomechanical failure modeling and investigation into lining optimization for a Ruhrstahl Heraeus snorkel, *Engineering Failure Analysis*. 62 (2016) 254–262. <https://doi.org/10.1016/j.engfailanal.2016.01.014>.
- [36] G. Dusserre, O. Valentin, F. Nazaret, T. Cutard, Experimental and numerical investigation of the asymmetric primary creep of a fibre reinforced refractory concrete at 1200 °C, *Journal of the European Ceramic Society*. 36 (2016) 2627–2639. <https://doi.org/10.1016/j.jeurceramsoc.2016.03.007>.
- [37] S. Jin, H. Harmuth, D. Gruber, R. Rössler, Influence of creep on the thermomechanical behavior of a rh-snorkel, in: 14th Biennial Worldwide Congress on Unified International Technical Conference on Refractories, UNITECR 2015, in Conjunction with the 58th International Colloquium on Refractories, 2015.
- [38] N. Iosipescu, New accurate procedure for single shear testing of metals, *J Mater.* 2 (1967) 537–566.
- [39] J.S. Hawong, D.C. Shin, U.C. Baek, Validation of pure shear test device using finite element method and experimental methods, *Engineering Fracture*

- Mechanics. 71 (2004) 233–243. [https://doi.org/10.1016/S0013-7944\(03\)00084-5](https://doi.org/10.1016/S0013-7944(03)00084-5).
- [40] E.C. Botelho, L.C. Pardini, M.C. Rezende, Evaluation of hygrothermal effects on the shear properties of Carall composites, *Materials Science and Engineering A*. 452–453 (2007) 292–301. <https://doi.org/10.1016/j.msea.2006.10.127>.
- [41] E. Selig, M. Kim, H.-Y. Ko, Multistage Triaxial Testing of Rocks, *Geotechnical Testing Journal*. 2 (1979) 98. <https://doi.org/10.1520/GTJ10435J>.
- [42] K. Kovari, A. Tisa, Multiple Failure State and Strain Controlled Triaxial tests, *Rock Mechanics Felsmechanik Mecanique Des Roches*. 7 (1975) 17–33. <https://doi.org/10.1007/BF01239232>.
- [43] H. Youn, F. Tonon, Multi-stage triaxial test on brittle rock, *International Journal of Rock Mechanics and Mining Sciences*. 47 (2010) 678–684. <https://doi.org/10.1016/j.ijrmms.2009.12.017>.
- [44] E. Dahlem, Characterisation of refractory failure under combined hydrostatic and shear loading at elevated temperatures, Ph.D. thesis at university of Leoben, 2011. <https://pure.unileoben.ac.at/portal/files/3368862/AC15256338n01.pdf> (accessed October 14, 2021).
- [45] A. Hillerborg, M. Modéer, P.-E. Petersson, Analysis of crack formation and crack growth in concrete by means of fracture mechanics and finite elements, *Cement and Concrete Research*. 6 (1976) 773–781. [https://doi.org/10.1016/0008-8846\(76\)90007-7](https://doi.org/10.1016/0008-8846(76)90007-7).
- [46] A. Hillerborg, Application of the fictitious crack model to different types of materials, in: *Current Trends in Concrete Fracture Research*, Springer Netherlands, Dordrecht, 1991: pp. 95–102. https://doi.org/10.1007/978-94-011-3638-9_7.
- [47] Stückelschweiger, Gruber, Jin, Harmuth, Wedge-Splitting Test on Carbon-Containing Refractories at High Temperatures, *Applied Sciences*. 9 (2019) 3249. <https://doi.org/10.3390/app9163249>.
- [48] S. Jin, D. Gruber, H. Harmuth, Determination of Young’s modulus, fracture energy and tensile strength of refractories by inverse estimation of a wedge

- splitting procedure, *Engineering Fracture Mechanics*. 116 (2014) 228–236. <https://doi.org/10.1016/j.engfracmech.2013.11.010>.
- [49] M. Sitek, G. Adamczewski, M. Szyszko, B. Migacz, P. Tutka, M. Natorff, Numerical simulations of a wedge splitting test for high-strength concrete, *Procedia Engineering*. 91 (2014) 99–104. <https://doi.org/10.1016/j.proeng.2014.12.021>.
- [50] R.G. Oliveira, J.P.C. Rodrigues, J. Miguel Pereira, P.B. Lourenço, R.F.R. Lopes, Experimental and numerical analysis on the structural fire behaviour of three-cell hollowed concrete masonry walls, *Engineering Structures*. 228 (2021). <https://doi.org/10.1016/j.engstruct.2020.111439>.
- [51] J. Lubliner, J. Oliver, S. Oller, E. Onate, A plastic-damage model for concrete, *International Journal of Solids and Structures*. 25 (1989) 299–326. [https://doi.org/10.1016/0020-7683\(89\)90050-4](https://doi.org/10.1016/0020-7683(89)90050-4).
- [52] J. Lee, G.L. Fenves, Plastic-Damage Model for Cyclic Loading of Concrete Structures, *Journal of Engineering Mechanics*. 124 (1998) 892–900. [https://doi.org/10.1061/\(ASCE\)0733-9399\(1998\)124:8\(892\)](https://doi.org/10.1061/(ASCE)0733-9399(1998)124:8(892)).
- [53] D. Gruber, H. Harmuth, Thermomechanical Behavior of Steel Ladle Linings and the Influence of Insulations, *Steel Research International*. 85 (2014) 512–518. <https://doi.org/10.1002/srin.201300129>.
- [54] D. Gruber, M. Sistaninia, C. Fasching, O. Kolednik, Thermal shock resistance of magnesia spinel refractories—Investigation with the concept of configurational forces, *Journal of the European Ceramic Society*. 36 (2016) 4301–4308. <https://doi.org/10.1016/j.jeurceramsoc.2016.07.001>.
- [55] S. Samadi, S. Jin, D. Gruber, H. Harmuth, A comparison of two damage models for inverse identification of mode I fracture parameters: case study of a refractory ceramic, *International Journal of Mechanical Sciences*. (2021) 106345. <https://doi.org/10.1016/j.ijmecsci.2021.106345>.
- [56] S. Samadi, S. Jin, H. Harmuth, Combined damaged elasticity and creep modeling of ceramics with wedge splitting tests, *Ceramics International*. 47 (2021) 25846–25853. <https://doi.org/10.1016/j.ceramint.2021.05.315>.
- [57] E.K. Tschegg, Equipment and appropriate specimen shapes for tests to measure fracture values, Patent AT-390328. (1986).

-
- [58] H. Harmuth, K. Rieder, M. Krobath, E. Tschegg, Investigation of the nonlinear fracture behaviour of ordinary ceramic refractory materials, *Materials Science and Engineering A*. 214 (1996) 53–61. [https://doi.org/10.1016/0921-5093\(96\)10221-5](https://doi.org/10.1016/0921-5093(96)10221-5).
- [59] Y. Dai, D. Gruber, S. Jin, H. Harmuth, Modelling and inverse investigation of the fracture process for a magnesia spinel refractory using a heterogeneous continuum model, *Engineering Fracture Mechanics*. 182 (2017) 438–448. <https://doi.org/10.1016/j.engfracmech.2017.05.005>.
- [60] D. Ramanenka, J. Stjernberg, P. Jonsén, FEM investigation of global mechanisms affecting brick lining stability in a rotary kiln in cold state, *Engineering Failure Analysis*. 59 (2016) 554–569. <https://doi.org/10.1016/j.engfailanal.2015.10.023>.
- [61] D. Ramanenka, M.L. Antti, G. Gustafsson, P. Jonsén, Characterization of high-alumina refractory bricks and modelling of hot rotary kiln behaviour, *Engineering Failure Analysis*. 79 (2017) 852–864. <https://doi.org/10.1016/j.engfailanal.2017.04.038>.
- [62] P. Boisse, A. Gasser, J. Rousseau, Computations of refractory lining structures under thermal loadings, *Advances in Engineering Software*. 33 (2002) 487–496. [https://doi.org/10.1016/S0965-9978\(02\)00064-9](https://doi.org/10.1016/S0965-9978(02)00064-9).
- [63] P. Boisse, A. Gasser, J. Poirier, J. Rousseau, Simulations of thermomechanical behavior of composite refractory linings, *Composites Part B:Engineering*. 32 (2001) 461–474. [https://doi.org/10.1016/S1359-8368\(01\)00005-1](https://doi.org/10.1016/S1359-8368(01)00005-1).
- [64] R.W. Lewis, P. Nithiarasu, K.N. Seetharamu, *Fundamentals of the Finite Element Method for Heat and Fluid Flow*, John Wiley & Sons, Ltd, Chichester, UK, 2004. <https://doi.org/10.1002/0470014164>.
- [65] T.M.H. Nguyen, E. Blond, A. Gasser, T. Prietl, Mechanical homogenisation of masonry wall without mortar, *European Journal of Mechanics, A/Solids*. 28 (2009) 535–544. <https://doi.org/10.1016/j.euromechsol.2008.12.003>.
- [66] M. Ali, T. Sayet, A. Gasser, E. Blond, Computational homogenization of elastic-viscoplastic refractory masonry with dry joints, *International Journal of Mechanical Sciences*. 196 (2021) 106275. <https://doi.org/10.1016/j.ijmecsci.2021.106275>.

-
- [67] A. Rekik, S. Allaoui, A. Gasser, E. Blond, K. Andreev, S. Sinnema, Experiments and nonlinear homogenization sustaining mean-field theories for refractory mortarless masonry: The classical secant procedure and its improved variants, *European Journal of Mechanics - A/Solids*. 49 (2015) 67–81. <https://doi.org/10.1016/j.euromechsol.2014.05.006>.
- [68] R.L.G. Oliveira, J.P.C. Rodrigues, J.M. Pereira, P.B. Lourenço, H.U. Marschall, Thermomechanical behaviour of refractory dry-stacked masonry walls under uniaxial compression, *Engineering Structures*. 240 (2021). <https://doi.org/10.1016/j.engstruct.2021.112361>.
- [69] R.L.G. Oliveira, J.P.C. Rodrigues, J.M. Pereira, P.B. Lourenço, H. Ulrich Marschall, Normal and tangential behaviour of dry joints in refractory masonry, *Engineering Structures*. 243 (2021) 112600. <https://doi.org/10.1016/j.engstruct.2021.112600>.
- [70] T. Prietl, Ermittlung materialspezifischer Kennwerte von feuerfesten Werkstoffen und Zustellungen unter uni-und biaxialen Lastbedingungen für die Nichteisenmetallindustrie, Ph.D. thesis at University of Leoben, na, 2006.
- [71] A. Gasser, K. TERNY-REBEYROTTE, P. Boisse, Modelling of joint effects on refractory lining behaviour, *Proceedings of the Institution of Mechanical Engineers, Part L: Journal of Materials: Design and Applications*. 218 (2004) 19–28. <https://doi.org/10.1243/146442004322849881>.
- [72] J. Brulin, F. Roulet, A. Rekik, M. Micollier, E. Blond, A. Gasser, R. Mc Nally, Latest Evolution in Blast Furnace Hearth thermo-Mechanical Stress Modelling The BF hearth, in: *4th International Conference on Modelling and Simulation of Metallurgical Processes in Steelmaking*, 2011: pp. 1–7.
- [73] A. Gasser, E. Blond, J.-L. Daniel, K. Andreev, Influence of different masonry designs of refractory bottom linings, in: *9th International Masonry Conference*, 2014: p. Electronic--file.
- [74] M. Ali, T. Sayet, A. Gasser, E. Blond, Computational Homogenization of Elastic-Viscoplastic Refractory Masonry with Dry Joints, *International Journal of Mechanical Sciences*. (2021) 106275. <https://doi.org/10.1016/j.ijmecsci.2021.106275>.
- [75] K. Andreev, H. Harmuth, FEM simulation of the thermo-mechanical behaviour and failure of refractories—a case study, *Journal of Materials Processing*

- Technology. 143–144 (2003) 72–77. [https://doi.org/10.1016/S0924-0136\(03\)00322-4](https://doi.org/10.1016/S0924-0136(03)00322-4).
- [76] S. Jin, D. Gruber, H. Harmuth, M.H. Frechette, Thermomechanical steel ladle simulation including a Mohr–Coulomb plasticity failure model, *RHI Bull.* 1 (2012) 39–43.
- [77] D. Gruber, K. Andreev, H. Harmuth, Optimisation of the Lining Design of a BOF Converter by Finite Element Simulations, *Steel Research International.* 75 (2004) 455–461. <https://doi.org/10.1002/srin.200405796>.
- [78] X. Liang, W.L. Headrick, L.R. Dharani, S. Zhao, Modeling of failure in a high temperature black liquor gasifier refractory lining, *Engineering Failure Analysis.* 14 (2007) 1233–1244. <https://doi.org/10.1016/j.engfailanal.2006.11.043>.
- [79] P.B. Lourenço, J.G. Rots, J. Blaauwendraad, Continuum Model for Masonry: Parameter Estimation and Validation, *Journal of Structural Engineering.* 124 (1998) 642–652. [https://doi.org/10.1061/\(asce\)0733-9445\(1998\)124:6\(642\)](https://doi.org/10.1061/(asce)0733-9445(1998)124:6(642)).
- [80] R. Senthivel, P.B. Lourenço, Finite element modelling of deformation characteristics of historical stone masonry shear walls, *Engineering Structures.* 31 (2009) 1930–1943. <https://doi.org/10.1016/j.engstruct.2009.02.046>.
- [81] P. de Buhan, G. de Felice, A homogenization approach to the ultimate strength of brick masonry, *Journal of the Mechanics and Physics of Solids.* 45 (1997) 1085–1104. [https://doi.org/10.1016/S0022-5096\(97\)00002-1](https://doi.org/10.1016/S0022-5096(97)00002-1).
- [82] H.R. Lotfi, P.B. Shing, Interface Model Applied to Fracture of Masonry Structures, *Journal of Structural Engineering.* 120 (1994) 63–80. [https://doi.org/10.1061/\(ASCE\)0733-9445\(1994\)120:1\(63\)](https://doi.org/10.1061/(ASCE)0733-9445(1994)120:1(63)).
- [83] S. Samadi, S. Jin, D. Gruber, H. Harmuth, S. Schachner, Statistical study of compressive creep parameters of an alumina spinel refractory, *Ceramics International.* 46 (2020) 14662–14668. <https://doi.org/10.1016/j.ceramint.2020.02.267>.
- [84] R. Kaczmarek, J.C. Dupre, P. Doumalin, O. Pop, L. Breder-Teixeira, J. Gillibert, E. Blond, M. Huger, Thermomechanical behaviour of an alumina spinel refractory for steel ladle applications, in: *Unified International Technical Conference on Refractories, UNITECR, 2019.*

-
- [85] S. Samadi, S. Jin, D. Gruber, H. Harmuth, Creep parameter determination of a shaped alumina spinel refractory using statistical analysis, in: Proceedings of 63rd International Colloquium on Refractories, Raw Materials and Reuse, 2020: pp. 1–5.
- [86] D.C. Montgomery, Design and analysis of experiments, John Wiley & Sons, 2017.
- [87] DAKOTA, User's Manual, (2011).
- [88] D. Vitiello, Thermo-physical properties of insulating refractory materials, Ph.D. thesis at University of Limoges, 2021.
- [89] D. Vitiello, B. Nait-Ali, N. Tessier-Doyen, T. Tonnesen, L. Laím, L. Rebouillat, D.S. Smith, Thermal conductivity of insulating refractory materials: Comparison of steady-state and transient measurement methods, *Open Ceramics*. 6 (2021). <https://doi.org/10.1016/j.oceram.2021.100118>.
- [90] J. Poirier, E. Blond, E. de Bilbao, R. Michel, A. Coulon, J. Gillibert, M. Boussuge, Y. Zhang, D. Ryckelynck, G. Dusserre, T. Cutard, P. Leplay, New advances in the laboratory characterization of refractories: Testing and modelling, *Metallurgical Research and Technology*. 114 (2017). <https://doi.org/10.1051/metal/2017068>.
- [91] DIN EN 10028-2, Flat products made of steels for pressure purposes - Part 2: Non-alloy and alloy steels with specified elevated temperature properties., 2017.

7. Appendix A

The material properties utilized in the thermomechanical simulations are reported in this appendix.

Table A - 1: Alumina spinel bricks material properties used in thermomechanical simulation

	Material properties	Value							
<i>Physical</i>	<i>Temperature (°C)</i>	25	250	500	750	1000	1250	1500	
	Young's modulus (GPa)	35.1	34.7	33.9	34.5	37.5	37.5	38.0	
	Poisson's ratio (-)	0.2							
	Density (kg/m³)	3130							
Thermal [88]	<i>Temperature (°C)</i>	25	200	400	800	1000	1200	1500	
	Conductivity (J/smK)	6.42	4.85	3.79	2.94	2.66	2.41		
	Specific heat (J/kgK)	805	1073	1161	1263	1293	1318		
	CET (10⁻⁶/K)	5.40	7.08	7.56	8.23	8.47	8.66	8.65	
Tensile failure	<i>Temperature (°C)</i>	25	1200	1400					
	Fracture energy (N.m/m²)	136.0	337.5	258.7					
	Tensile strength (MPa)	2.91	1.66	0.68					
	<i>R₁</i>	0.213	0.239	0.272					
	<i>R₂</i>	0.295	0.263	0.305					
Creep [85]	<i>Temperature (°C)</i>	900	1300	1400	1500				
	A (Pa⁻ⁿ/s)	1e ⁻²⁶	7.75e ⁻¹²	1.72e ⁻¹⁴	2.18e ⁻⁰⁸				
	n	0.0001	1.1387	1.5905	0.6749				
	m	-0.5	-0.7322	-0.7257	-0.6631				
Shear failure	<i>Temperature (°C)</i>	25	1000	1200					
	Cohesion (MPa)	21.7	13.5	2.3					
	Friction angle (°)	48.6	49.0	69.9					

Table A - 2: Magnesia carbon bricks material properties used in thermomechanical simulation

	Material properties	Value						
<i>Physical*</i>	<i>Temperature (°C)</i>	25	600	1070	1170	1270	1370	1470
	Young's modulus (GPa)	21.0	21.0	24.3	25.2	26.2	27.2	27.5
	Poisson's ratio (-)	0.2						
	Density (kg/m³)	3070						
Thermal*	<i>Temperature (°C)</i>	25	800	1000	1200	1600		
	Conductivity (J/smK)			7.5				
	Specific heat (J/kgK)	1000						
	CET (10⁻⁶/K)		7.5		10.0	10.6		
Tensile failure [47]	<i>Temperature (°C)</i>	25	1100	1370	1470			
	Fracture energy (N.m/m²)	270	162	453	563			
	Tensile strength (MPa)	1.51	1.42	2.26	2.4			
Creep [16]	<i>Temperature (°C)</i>	900	1270	1370	1470			
	A (Pa⁻ⁿ/s)	1e ⁻²⁶	4.01e ⁻¹⁰	4.19e ⁻¹⁰	4.58e ⁻¹⁰			
	n	0.0001	0.8013	0.8013	0.8013			
	m	-0.5	-0.8025	-0.8025	-0.8025			
Shear failure*	<i>Temperature (°C)</i>	25	1000	1200				
	Cohesion (MPa)	40	40	10				
	Friction angle (°)	49.2	49.2	60				

*These material parameters were received from industrial partners or other research studies at Chair of Ceramics, Montanuniversität Leoben.

Table A - 3: Alumina magnesia carbon bricks material properties used in thermomechanical simulation

Material properties		Value								
<i>Physical*</i>	<i>Temperature (°C)</i>	25								
	Young's modulus (GPa)	60								
	Poisson's ratio (-)	0.2								
	Density (kg/m ³)	3000								
<i>Thermal*</i>	<i>Temperature (°C)</i>	25	125	250	375	500	625	750	875	1100
	Conductivity (J/smK)	9.9		10.2		9		8.3		
	Specific heat (J/kgK)	1242		1586		1616		1368		
	CET (10 ⁻⁶ /K)		7.20		8.53		9.20		1.05	1.10
<i>Creep*</i>	<i>Temperature (°C)</i>	900	1300	1350	1400	1450	1500			
	A (Pa ⁻ⁿ /s)	1e ⁻²⁶	2.73e ⁻²⁵	6.63e ⁻²³	2.00e ⁻¹⁵	1.71e ⁻¹⁵	1.13e ⁻¹⁵			
	n	0.0001	2.391	2.162	1.150	1.210	1.292			
	m	0	0	0	0	0	0			

*These material parameters were received from industrial partners or other research studies at Chair of Ceramics, Montanuniversität Leoben.

Table A - 4: Bauxite bricks material properties used in thermomechanical simulation

Material properties		Value				
<i>Physical*</i>	<i>Temperature (°C)</i>	25				
	Young's modulus (GPa)	45				
	Poisson's ratio (-)	0.2				
	Density (kg/m ³)	2750				
<i>Thermal*</i>	<i>Temperature (°C)</i>	25	400	800	1000	1200
	Conductivity (J/smK)		2.7	2.45		2.35
	Specific heat (J/kgK)	1000				
	CET (10 ⁻⁶ /K)			7.00		6.43

*These material parameters were received from industrial partners or other research studies at Chair of Ceramics, Montanuniversität Leoben.

Table A - 5: Chamotte bricks material properties used in thermomechanical simulation

Material properties		Value			
<i>Physical*</i>	<i>Temperature (°C)</i>	25			
	Young's modulus (GPa)	45			
	Poisson's ratio (-)	0.2			
	Density (kg/m ³)	2175			
<i>Thermal*</i>	<i>Temperature (°C)</i>	25	400	700	1100
	Conductivity (J/smK)		1.2	1.3	1.4
	Specific heat (J/kgK)	1000			
	CET (10 ⁻⁶ /K)	5			

*These material parameters were received from industrial partners or other research studies at Chair of Ceramics, Montanuniversität Leoben.

Table A - 6: Shotcrete material properties used in thermomechanical simulation

Material properties		Value			
<i>Physical*</i>	<i>Temperature (°C)</i>	25	1000	1200	1400
	Young's modulus (GPa)	4.456	4.456	1.854	1.412
	Poisson's ratio (-)	0.2			

Thermal*	Density (kg/m³)	2175
	<i>Temperature (°C)</i>	25
	Conductivity (J/smK)	1.2
	Specific heat (J/kgK)	1000
	CET (10⁻⁶/K)	12

*These material parameters were received from industrial partners or other research studies at Chair of Ceramics, Montanuniversität Leoben.

Table A - 7: Steel material properties used in thermomechanical simulation

		Material properties						
<i>Physical*</i>	<i>Temperature (°C)</i>	25	100	150	200	250	300	350
	Young's modulus (GPa)	192	191	189	186	183	179	173
	Poisson's ratio (-)	0.2						
	Density (kg/m³)	7850						
	<i>Temperature (°C)</i>	25	100	150	200	250	300	350
Thermal*	Conductivity (J/smK)	50						
	Specific heat (J/kgK)	447						
	CET (10⁻⁶/K)	10.9	11.5	11.9	12.3	12.6	12.9	13.3
	Von Mises plasticity [91]							
	Yield stress (MPa)	280	325	345	360	380		
	Plastic strain (1)	0	0.025	0.06	0.1	0.2		

*These material parameters were received from industrial partners or other research studies at Chair of Ceramics, Montanuniversität Leoben.

8. List of publications

PAPER I

S. Samadi, S. Jin, D. Gruber, H. Harmuth, S. Schachner
Statistical study of compressive creep parameters of an alumina spinel refractory
Ceramics International 46 (10), 14662-14668, July 2020

PAPER II

L. Teixeira, S. Samadi, J. Gillibert, S. Jin, T. Sayet, D. Gruber, E. Blond
Experimental Investigation of the Tension and Compression Creep Behavior of Alumina-Spinel Refractories at High Temperatures
Ceramics 3 (3), 372-383, September 2020

PAPER III

S. Samadi, L. Teixeira, S. Jin, D. Gruber, H. Harmuth
Creep Parameter Determination of a Shaped Alumina Spinel Refractory Using Statistical Analysis
Proceedings of 63rd International Colloquium on Refractories (ICR 2020), September 2020, raw materials and reuse, 1-5

PAPER IV

S. Samadi, S. Jin, D. Gruber, H. Harmuth
A comparison of two damage models for inverse identification of mode I fracture parameters: Case study of a refractory ceramic
International Journal of Mechanical Sciences 197, 106345, May 2021

PAPER V

S. Samadi, S. Jin, H. Harmuth
Combined damaged elasticity and creep modeling of ceramics with wedge splitting tests
Ceramics International 47 (18), 25846-25853, September 2021

PAPER VI

S. Samadi, S. Jin, D. Gruber, H. Harmuth

Thermomechanical finite element modelling of steel ladle containing alumina spinel refractory lining

Prepared to be submitted

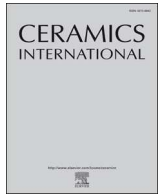
Contribution of the author to the appended publications:

Paper/Article	Conception and planning	Experiments/ Simulations	Analysis and interpretation	Manuscript preparation
I	90%	100%	90%	80%
II	30%	75%	10%	30%
III	90%	100%	90%	90%
IV	90%	100%	90%	90%
V	90%	100%	90%	90%
VI	90%	100%	90%	90%

Signature: Soheil Samadi 21/10/2021



9. Appended publications



Statistical study of compressive creep parameters of an alumina spinel refractory



Soheil Samadi, Shengli Jin*, Dietmar Gruber, Harald Harmuth, Stefan Schachner

Chair of Ceramics, Montanuniversitaet, Leoben, 8700, Austria

ARTICLE INFO

Keywords:
Creep
Heterogeneity
Statistical study
Refractories

ABSTRACT

Refractory microstructure and phase composition play important roles in the creep resistance of refractories at high temperatures. The production processing causes heterogeneity of refractory microstructure, which affects the determination of representative creep parameters. The present study focused on the statistical study of compressive creep parameters with a limited number of tests. Different sampling approaches were applied to examine the influence of the heterogeneity. A correlation analysis exhibited an evident negative correlation coefficient between the bulk density of specimens and their creep strain rates. The Norton-Bailey creep parameters of the primary creep stage were received with an inverse evaluation method from datasets with different number of uniaxial compressive creep curves under at least two different constant loads. Their mean values and standard deviations were evaluated for different temperatures. The statistical results of the dataset with combined 7 creep curves (out of 9) allow for elaborated considering the microstructural heterogeneity of refractories in the thermomechanical modelling of industry vessels.

1. Introduction

Common refractory ceramics are applied in high temperature industries and typically show an inhomogeneous microstructure, which contains various phases, grains up to several millimeters, matrix composed of bonded fines and defects (pores and cracks) of various sizes unevenly distributed in different areas [1,2]. The complex production processes, e.g., shaping process, thermal processes, and finishing treatments, contribute to their inhomogeneous microstructure, which influences their material properties. For instance, it was shown that during molding of a granular material, several factors such as friction between the die wall and the compact, the ejection force, and type of pressing affect the stress, density and bulk modulus distribution in the compact [3,4]. In another study, Hubalkova and Stoyan reported that the cold crushing strength of high alumina refractory castables is influenced by the spatial arrangement and shape of aggregates [5]. Heindl and Mong [6] examined 22 brands of common refractory ceramics from 10 manufacturers, which were prepared by dry-press, stiff-mud or handmade processes. It was concluded that the setting method and positions of the bricks in the kiln during firing affect the tensile strength and Young's modulus of bricks and the different areas of the same brick. Dahlem et al. [7–9] investigated the influences of different specimen preparation parameters on the refractoriness under load, bulk

density, open porosity, and cold crushing strength measurements. The studies revealed that the cold crushing strength and refractoriness under load of specimens drilled along the pressing direction are different to those of specimens drilled perpendicular to the pressing direction, whilst the differences in bulk density and open porosity for different cutting positions are negligible.

Common refractory ceramics usually experience creep at high temperatures under thermomechanical loads in service [10]. Their creep is mainly controlled by diffusion and boundary mechanisms, which are more sensitive to the microstructure of matrix compared to dislocation mechanisms. Therefore, scatters in the creep results are likely, even in refractories with similar chemical compositions [11]. The current study investigated the influence of the inhomogeneous material microstructure on the determination of creep parameters at different temperatures. Uniaxial compressive creep tests were performed with specimens drilled from different positions and drilling directions in one brick and with specimens randomly selected from different bricks. A correlation analysis between creep behavior and bulk density and Young's modulus of samples was carried out, and a statistical analysis was performed on the creep parameters obtained with different combinations of creep curves from the randomly selected specimens. This analysis proposed an approach to consider the influence of the inhomogeneity of the microstructure in testing and modelling.

* Corresponding author.

E-mail address: shengli.jin@unileoben.ac.at (S. Jin).

<https://doi.org/10.1016/j.ceramint.2020.02.267>

Received 30 January 2020; Received in revised form 19 February 2020; Accepted 27 February 2020

Available online 01 March 2020

0272-8842/ © 2020 Elsevier Ltd and Techna Group S.r.l. All rights reserved.

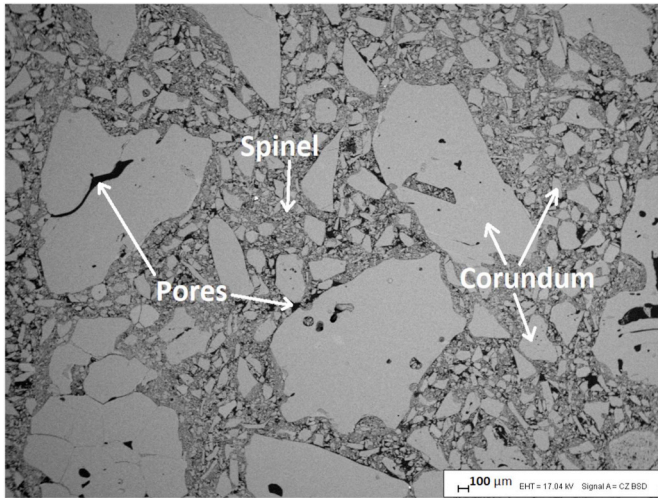


Fig. 1. SEM image of fired alumina spinel refractory.

2. Experimental and creep parameters identification

Alumina spinel refractory bricks, which consisted of 94 wt% alumina, 5 wt% magnesia, and 1 wt% other oxides such as, silica, iron oxide, were the study case. The raw material base for these bricks is white fused alumina, calcined alumina and some spinel. The bulk density was 3.13 g/cm³, and open porosity was 19 vol%. The scanning electron microscopic (SEM) image of the investigated material is shown in Fig. 1. It is observed that the microstructure of the material includes alumina grains with various sizes, spinel in the fines, pores in the matrix, and pores and cracks in the grains.

The uniaxial compressive creep test developed in Ref. [12] was employed for creep testing. The specimen was a cylinder with a diameter of 35 mm and a height of 70 mm (the height/diameter ratio of 2 is adequate to avoid friction effect on the measured area).

Two groups of experiments were planned. The first group was used to investigate the influence of specimen's position and drilling direction in one brick; therefore, six specimens were drilled from one brick (Fig. 2). Five specimens were drilled along the pressing direction, four of which were close to the molding surface (termed outer layer) and one was from the center of the brick. The sixth specimen was cut

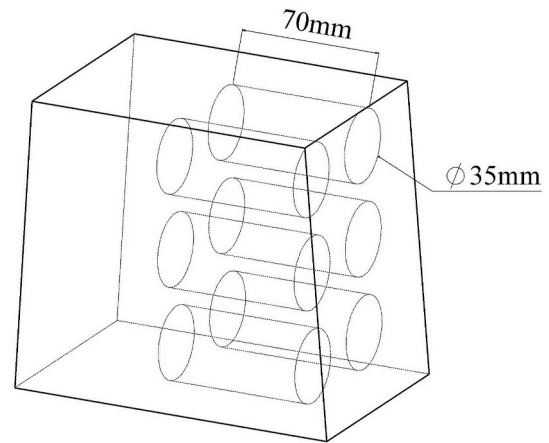


Fig. 3. Schematic of the specimens' positions in a brick for characterization of the creep behavior.

Table 1

Loading conditions for characterization of the creep behavior.

Temperature (°C)	1300	1400	1500
Applied stress (MPa)	8–9–10	4–4.5–5	3.5–4–4.5

Table 2

Dataset size from different number of curves in combination.

Number of curves in combination	2	3	4	5	6	7	8	9
Dataset size	27	81	126	126	84	36	9	1

perpendicular to the pressing direction. The compressive creep tests for this group were performed at 1300 °C and 9 MPa.

The second group of experiments was designed to characterize the creep behavior of alumina spinel bricks considering the variations in a brick and among the bricks. Twenty seven samples (from 5 bricks) were drilled in the pressing direction according to Fig. 3. The pressing direction was chosen for the study because the significant thermo-mechanical stresses occur in this direction when the refractories serve in a ladle [13]. Three randomly selected specimens were used at each

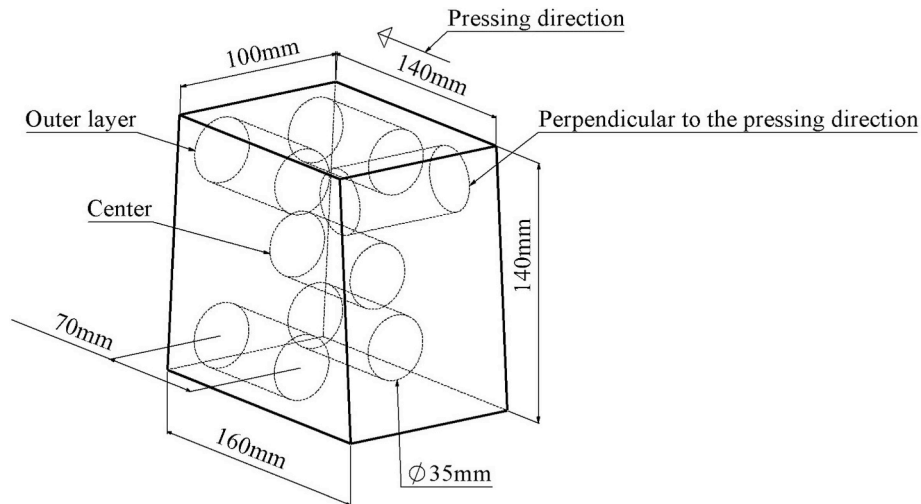


Fig. 2. Schematic of the specimens drilled out of a brick for investigation of the influence of specimen position and drilling direction.

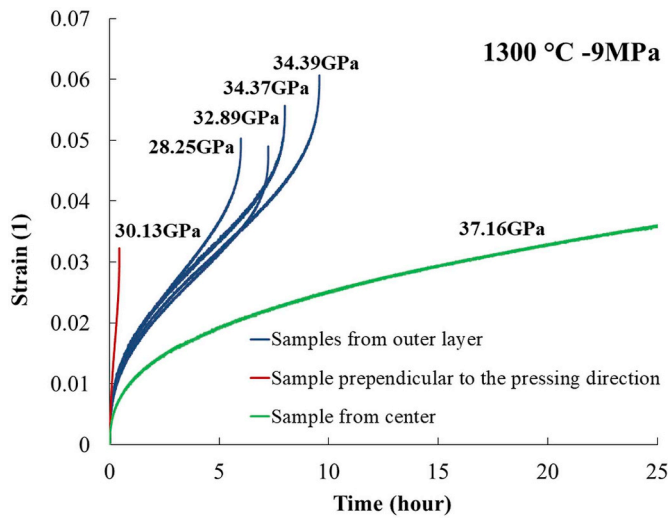


Fig. 4. Test results of samples from one brick (with the Young's modulus added next to the respective curve).

loading condition. The loading conditions were defined in Table 1.

After specimen alignment in the testing apparatus, a small preload of around 0.05 MPa was applied for stabilization during the heating process. The specimen was heated in a cylindrical electrical furnace up to the desired temperature with a rate of 10 °C/min followed by a dwell time of 1 h for thermal homogenization; afterwards, the defined testing force was applied on the specimen. The deformation measurement started simultaneously with the mechanical loading procedure. Two pairs of mechanical extensometers were placed in front and rear sides of the furnace for displacement measurement directly on the surface of the specimen; the initial distance between two extensometer arms was 50 mm.

Before creep measurements, the bulk density of each specimen was calculated by measurement of its diameter, height, and mass; and its Young's modulus was measured at room temperature using the ultrasonic method according to ASTM standard C597–09 [14]. Additionally, high-temperature impulse excitation technique [15] was employed to assess the Young's modulus of the material at high temperatures, as it is required for calculation of elastic deformation in the inverse evaluation of creep parameters.

Three-stage creep curves of alumina spinel refractories were obtained. Nevertheless, the present statistical study mainly focused on the primary creep stage. Therefore, the ruler method was applied to identify the transitions of the three stages, i.e., the linear part of the curves, which corresponds to the secondary stage, is determined by a ruler. The strain hardening form of the Norton-Bailey creep rate equation [1,12,16–18] was applied to describe the creep behavior, as displayed in Eq. (1).

$$\dot{\epsilon}_{cr} = K(T)\sigma^n \epsilon_{cr}^a \tag{1}$$

where σ denotes the applied load, $\dot{\epsilon}_{cr}$ is the creep strain rate, ϵ_{cr} is the creep strain, $K(T)$ is a temperature dependent function, n is the stress exponent and a is the strain exponent, which is negative for the primary stage. The inverse identification of creep parameters was done according to the method developed in Refs. [12], where the Levenberg-Marquardt optimization algorithm was used [19].

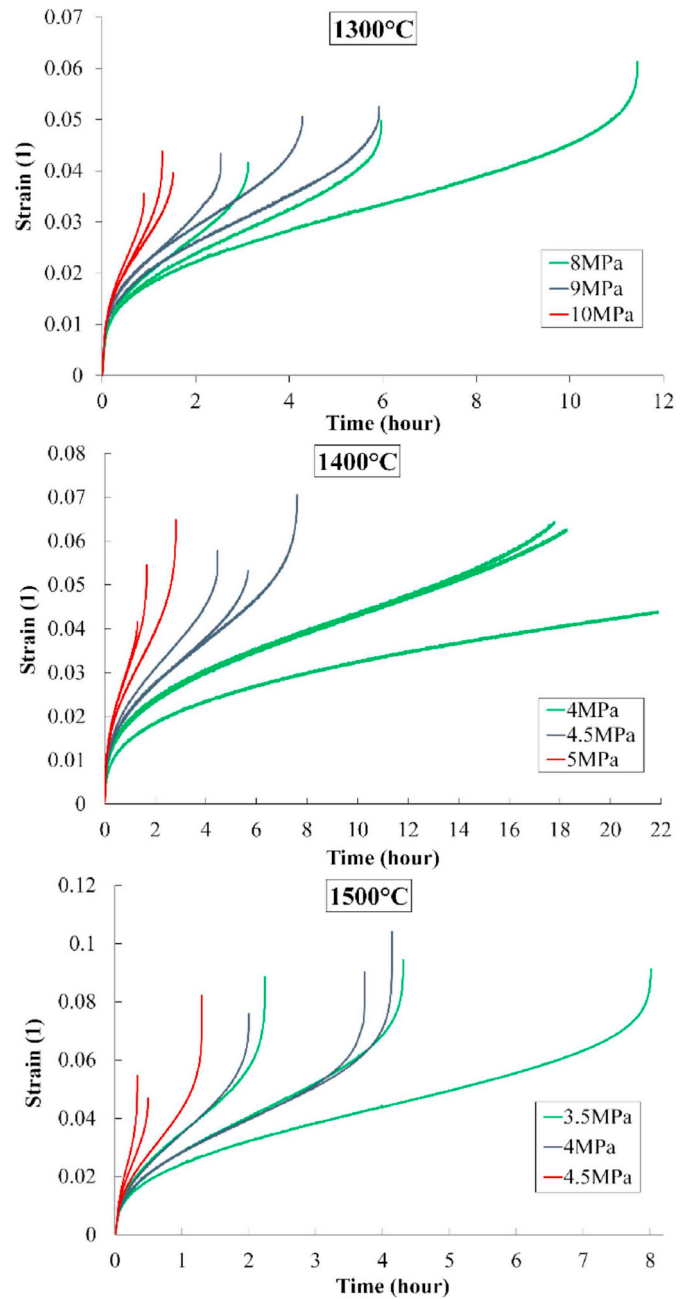


Fig. 5. Test results for 1300 °C–1400 °C – 1500 °C.

Table 3

Mean correlation coefficients table for Young's modulus, bulk density and creep strain rates.

	E	ρ	$\dot{\epsilon}_1$	$\dot{\epsilon}_2$	$\dot{\epsilon}_f$
E	1	0.847	-0.570	-0.570	-0.492
ρ		1	-0.927	-0.923	-0.889
$\dot{\epsilon}_1$			1	0.997	0.990
$\dot{\epsilon}_2$				1	0.993
$\dot{\epsilon}_f$					1

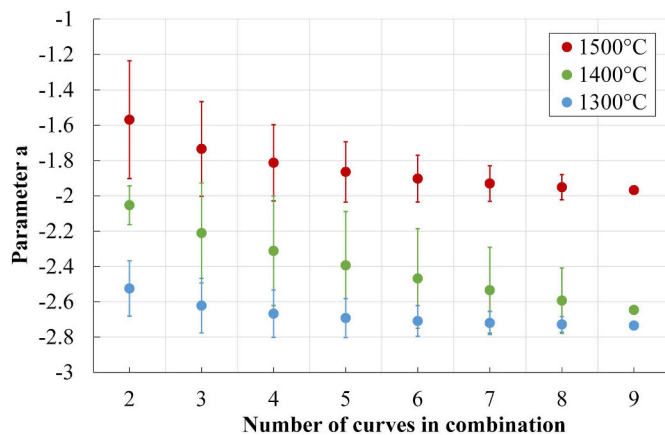


Fig. 6. Parameter *a* of different datasets for different temperature (with standard deviations).

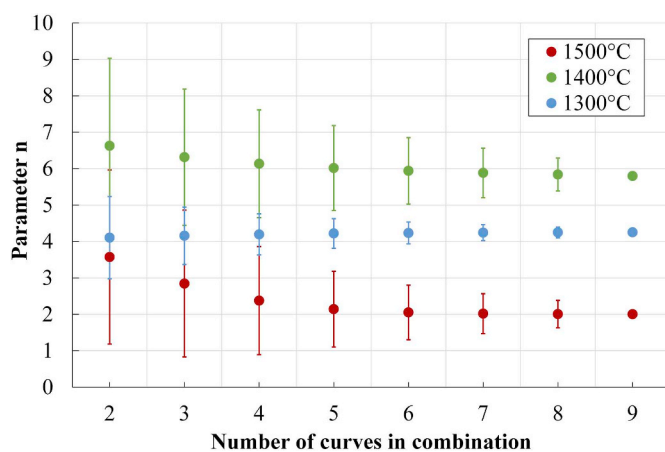


Fig. 7. Parameter *n* of different datasets for different temperature (with standard deviations).

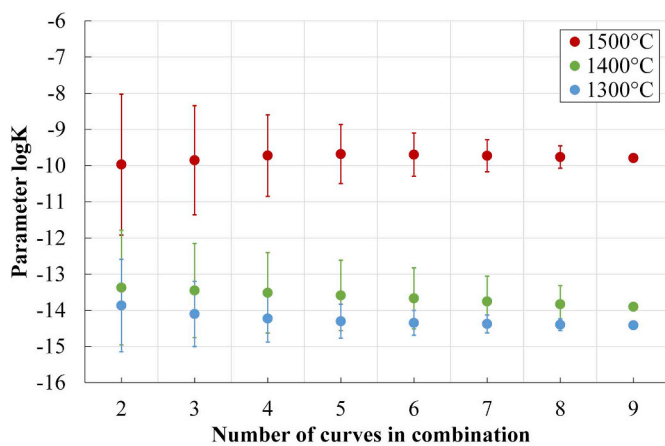


Fig. 8. Parameter $\log K$ of different datasets for different temperature (with standard deviations).

3. Statistical study

A correlation calculation analysis was performed to investigate the relation among creep rates and physical properties, i.e., Young's modulus and bulk density. In order to investigate the effect of the inhomogeneity, different combinations of experimental curves at the same temperature were used as input datasets for inverse evaluation of the creep parameters. Theoretically, to achieve a unique solution for *a*, *n* and *K*, minimum two curves with different constant stresses at one temperature are necessary as input data. Therefore, all the possible combinations of 2–9 curves (out of 9 curves) were used, which yield 8 datasets with different sizes. Each dataset contained at least two curves received from two different mechanical loads. The size of each dataset is listed in Table 2.

The mean value and the standard deviation were calculated for the datasets. Additionally, to assess the representative of mean values from various combinations, confidence intervals for creep parameters in different datasets can be obtained using the following equation.

$$|\mu - \bar{y}| \leq \frac{t_{\frac{\alpha}{2}, n-1} S}{\sqrt{n}} \tag{2}$$

where $|\mu - \bar{y}|$ is the difference between the mean value of the dataset (\bar{y}) and the mean value of the whole population (μ), $\frac{t_{\frac{\alpha}{2}, n-1} S}{\sqrt{n}}$ is termed 100*(1- α) percent confidence interval for the mean difference, *n* is the dataset size, *n* - 1 is the number of degrees of freedom, α denotes the significance level of the test, and *S* is the dataset standard deviation. The *t* value is obtained from the t-distribution table based on the degrees-of-freedom of the dataset and the chosen α value (Table II in Ref. [20]). A common confidence interval percentage of 99% was selected in the current study.

4. Results and discussion

4.1. Impact of spatial variations on creep behavior

The uniaxial compressive creep test results from the first group of experiments were plotted in Fig. 4. The same loading condition, 1300 °C and 9 MPa, was applied for the first group of samples. The Young's modulus of each sample was measured using the ultrasonic method and is added close to its creep curve in Fig. 4. The specimens from the outer layer showed slight different Young's moduli compared to the specimen from the center; the creep rupture time slightly increased with Young's modulus.

The drilling direction has significant influence on the creep behavior of specimens. Evidently, the specimen drilled perpendicular to the pressing direction showed the weakest creep resistance even though its Young's modulus was in the range of those from the outer layer; it failed in 0.5 h. The specimen from the center of brick in the pressing direction displayed the highest Young's modulus and the strongest creep resistance; it was still in the primary stage after 25 h. Given that the specimen cut perpendicular to the pressing direction was from the outer layer, it is concluded that the pore shape may mainly contribute to the difference in creep resistance in different directions, as the pore shapes and packing of particles are significantly affected by the molding method and the pressing direction.

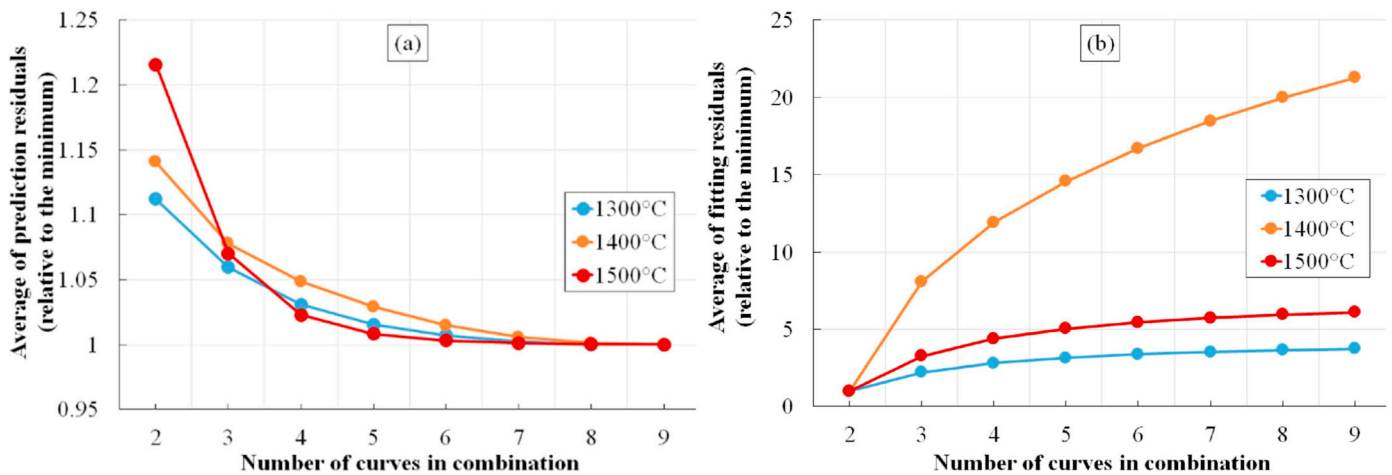


Fig. 9. Average of (a) prediction and (b) fitting residuals calculated at different temperatures relative to the respective minimum.

4.2. Correlation analysis of randomly selected specimens

As mentioned before, the specimens were cut in the pressing direction and randomly selected from different bricks. Their creep curves under various mechanical loads and temperatures are shown in Fig. 5. Noticeable scatters of the creep curves can be observed. Overlapping also occurred for the curves with different mechanical loads. This highlighted the existing variations among the bricks, which most likely arises from the process conditions.

The correlation coefficients of Young's modulus (E), bulk density (ρ) and creep strain rates were investigated. The correlation coefficient was calculated for three samples from the same mechanical load and temperature conditions. An average value was calculated for the coefficients obtained at various temperatures and mechanical load conditions (9 in total), and are shown in Table 3. The mean primary stage strain rate ($\dot{\epsilon}_1$) was calculated by making an average of the strain rate over time in the primary creep stage (with 200 intervals). The secondary stage strain rate ($\dot{\epsilon}_2$) is the slope of the straight line of secondary stage. The nominal failure strain rate ($\dot{\epsilon}_f$) is the ratio of the total strain to the total time.

It was observed that bulk density and Young's modulus had negative correlation coefficients with creep strain rates. The correlation coefficients for the Young's modulus were lower than 0.57 and those for the bulk density were higher than 0.88. This relatively strong correlation between the creep strain rates and the bulk density implies that the porosity mainly ruled the creep resistance of the investigated alumina spinel material. In addition, a correlation coefficient of 0.847 was received between the Young's modulus and the bulk density; and correlation coefficients higher than 0.99 were obtained between different creep strain rates.

4.3. Statistical analysis of creep parameters

The primary creep stage curves were identified at each temperature by applying the ruler method. Afterwards, the creep parameters (k , n and a) of this stage were inversely evaluated with respect to various combinations of curves. The mean values and standard deviations of a , n , and the common logarithm of K ($\log K$) were plotted in Figs. 6–8, with respect to the number of curves in combination. The use of total 9 curves does not yield a standard deviation, because just one set of creep parameter is obtained.

Generally speaking, the standard deviations of datasets decreased significantly with increasing the number of combined curves; and the mean values changed monotonically. Besides, the mean values of a and $\log K$ increased evidently with the temperature, whilst the mean value of n was ranked in the order of 1400 °C, 1300 °C and 1500 °C. This order was observed for all the datasets, which indicates that the various number of creep curves in combination did not change the evolution trend of creep parameters with respect to the temperature. In other words, for the current material, the influence of temperature is more significant than the inhomogeneity of microstructure.

To assess the prediction of experimental curves using different datasets, all 9 curves were predicted using the mean values of each dataset, and then the average of prediction residuals was calculated according to Eq. (3) considering 1800 data points for each curve, in which ϵ_p and ϵ_e are the predicted and experimental creep strains, respectively. The values were plotted in Fig. 9-a, normalized by the lowest one for each temperature that was evidently obtained from the dataset with combined 9 curves. The prediction residuals increased when using the datasets with lower number of combined creep curves. The difference of the average of prediction residuals obtained by applying creep parameters from the datasets with more than combined 6 curves with that from the dataset with combined 9 curves was less than 1.5% for three temperatures.

$$\text{Average of prediction residuals} = \sqrt{\frac{1}{9} \sum_{i=1}^9 \frac{\sum_{j=1}^{1800} (\epsilon_p - \epsilon_e)^2}{1800}} \quad (3)$$

Nevertheless, one should notice that the prediction residuals are different from the fitting residuals. The fitting residuals were calculated and minimized within the inverse evaluation method for obtaining the creep parameters. The average of fitting residuals can be calculated using Eq. (4), where n is the number of curves in combination and m is the dataset size. In the case of the dataset with 9 combined curves, Eq. (4) will yield the same result as Eq. (3). As shown in Fig. 9-b, it is obvious that the fitting residuals decrease with lower number of curves in combination.

$$\text{Average of fitting residuals} = \frac{1}{m} \sum_{i=1}^m \sqrt{\frac{1}{n} \sum_{j=1}^n \frac{\sum_{k=1}^{1800} (\epsilon_p - \epsilon_e)^2}{1800}} \quad (4)$$

Ninety nine percent confidence intervals were calculated according

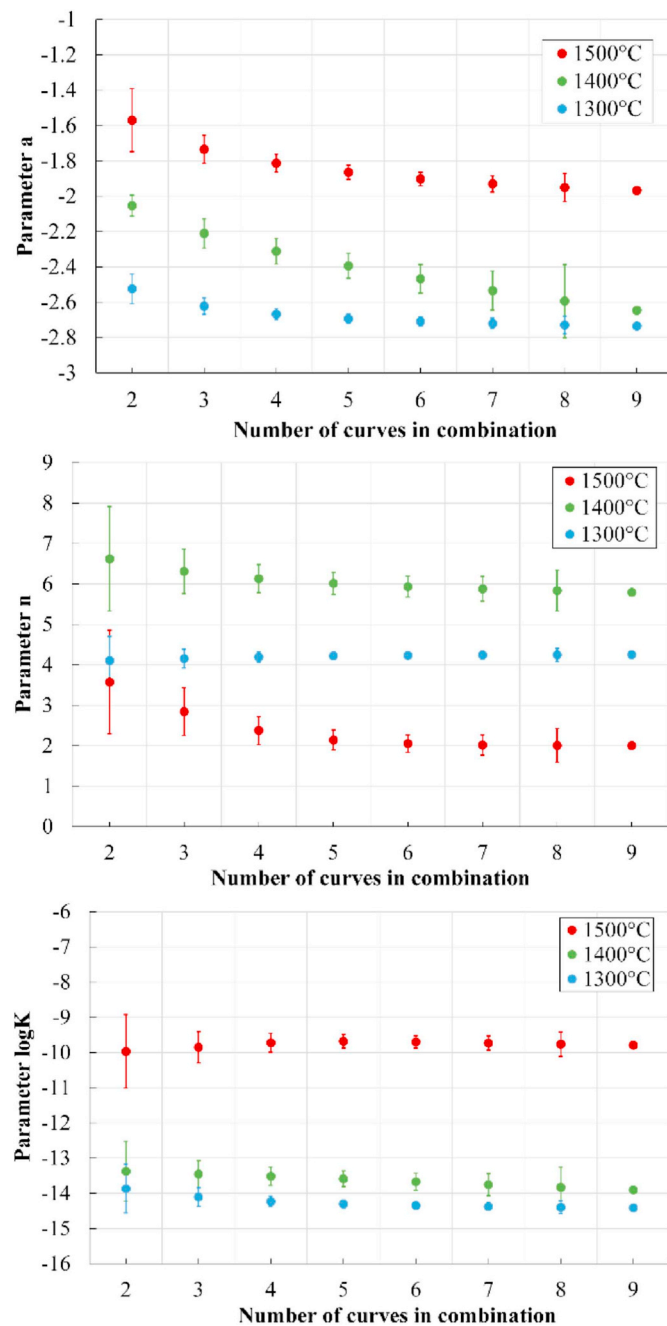


Fig. 10. Evaluated parameters at different temperatures considering 99% confidence interval.

to Eq. (2) with respect to the temperature and creep parameters. Fig. 10 presents the confidence intervals for 3 parameters determined at all temperatures. It shows that the confidence intervals decreased significantly with increasing combined curve number to 6 except the parameter a at 1400 °C; and a further slight increase of relative intervals at curve numbers of 7 and 8 can be observed. The shorter confidence interval indicates a closer proximity to the mean value of whole population and a better sampling for the input data. According to Eq.

(2), three factors affect the confidence interval: t , standard deviation and dataset size. These factors contribute to low confidence intervals for datasets with combined 5, 6 and 7 curves.

Fig. 10 also shows that parameter n and $\log K$ of the dataset with combined 9 curves lied in the confidence intervals of most of the other datasets with significance level of 0.01; whilst parameter a of dataset with combined 9 curves lied in the confidence intervals of the datasets with combined 7 and 8 curves at all three temperatures. This indicates that parameter a is intensely influenced by the heterogeneity of the material and parameters from datasets with combined 7 and 8 curves are more representative.

The creep parameters obtained from the dataset with combined 7 curves were recommended for applications to account for the scatter, as it showed a short confidence interval, a low average of prediction residuals, and all the three parameters of the dataset with combined 9 curves lied in its confidence interval. The experimental creep curves and the simulated ones at 1500 °C with the creep parameters from the datasets with combined 2 curves, 7 curves and 9 curves were plotted in Fig. 11. The predicted curve using the dataset with combined 2 curves deviated from the ones predicted by the latter two sets of creep parameters, and the latter two didn't show a significant difference. The advantage to use the creep parameters obtained from combined 7 curves is that the evident inhomogeneity of the investigated refractory can be representatively considered in the thermomechanical modelling in future taking into account the standard deviations.

5. Conclusion

The current study investigated the scatter in compressive creep behavior of a shaped alumina spinel containing refractory material. A sampling scheme was considered to examine the effect of specimen's spatial position in a brick on the creep behavior. It showed that the drilling position and direction of specimens in a brick had an evident influence on their creep resistance. The specimens drilled in the pressing direction had stronger creep resistance, and specimens closer to the molding surface had weaker creep resistance.

The correlation study on randomly chosen specimens drilled in the pressing direction reveals an intense negative correlation between bulk density and the creep strain rates. The statistical study was performed to account for the heterogeneity of the material. Norton-Bailey creep parameters of the primary creep stage were inversely evaluated from various combinations of creep curves at three temperatures. Although the standard deviations of the datasets were different, consistent tendency in the mean creep parameters with respect to the temperature was still observed. The statistical analysis considering a 99% confidence interval showed that the dataset with combined 7 curves out of 9 curves can well represent the material heterogeneity. This will offer a quantitative consideration of material heterogeneity in the thermo-mechanical modelling of refractory linings in industrial vessels.

Nevertheless, the received high scatter might be particular for the investigated material and other refractories may need to be studied further.

Declaration of competing interest

The authors declare that they have no known competing financial interests or personal relationships that could have appeared to influence the work reported in this paper.

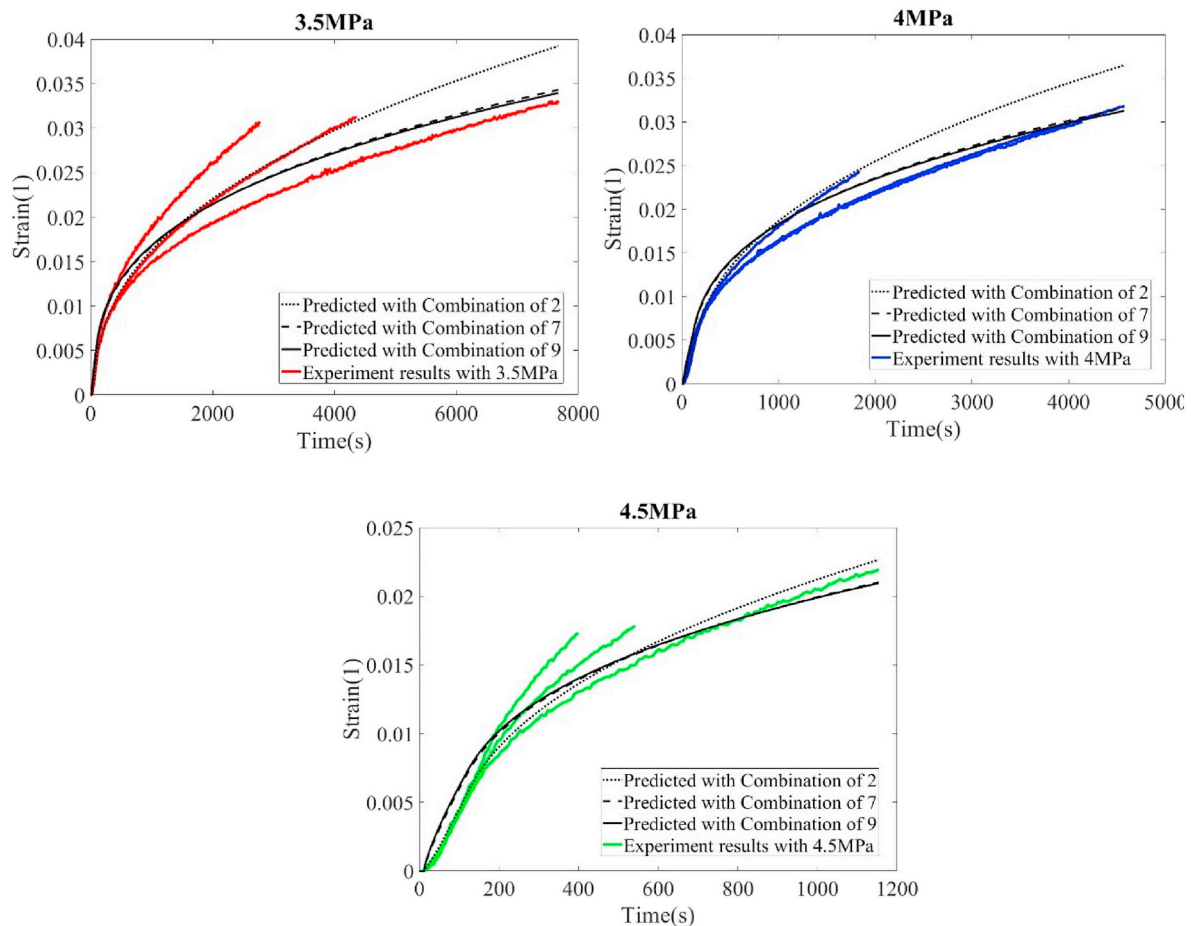


Fig. 11. Primary creep stage prediction for 1500 °C with different loads using the mean value of the datasets with combined 2 curves, 6 curves and 9 curves.

Acknowledgements

This work was supported by the funding scheme of the European Commission, Marie Skłodowska-Curie Actions Innovative Training Networks in the frame of the project ATHOR - Advanced Thermomechanical multiscale mOdeling of Refractory linings 764987 Grant.

References

- [1] S. Schachner, S. Jin, D. Gruber, H. Harmuth, Three stage creep behavior of MgO containing ordinary refractories in tension and compression, *Ceram. Int.* 45 (2019) 9483–9490, <https://doi.org/10.1016/j.ceramint.2018.09.124>.
- [2] D.N. Boccaccini, C. Leonelli, M.R. Rivasi, M. Romagnoli, A.R. Boccaccini, Microstructural investigations in cordierite–mullite refractories, *Ceram. Int.* 31 (2005) 417–432, <https://doi.org/10.1016/j.ceramint.2004.06.005>.
- [3] D. Gruber, H. Harmuth, Simulation of molding of refractory bricks, *Adv. Sci. Technol.* 70 (2010) 167–172 <https://doi.org/10.4028/www.scientific.net/AST.70.167>.
- [4] C.C. Melo, A.L.I. Moraes, F.O. Rocco, F.S. Montilha, R.B. Canto, A validation procedure for numerical models of ceramic powder pressing, *J. Eur. Ceram. Soc.* 38 (2018) 2928–2936, <https://doi.org/10.1016/j.jeurceramsoc.2018.01.009>.
- [5] J. Hubalkova, D. Stoyan, On a qualitative relationship between degree of inhomogeneity and cold crushing strength of refractory castables, *Cement Concr. Res.* 33 (2003) 747–753, [https://doi.org/10.1016/S0008-8846\(02\)01056-6](https://doi.org/10.1016/S0008-8846(02)01056-6).
- [6] R.A. Heindl, L.E. Mong, Young's modulus of elasticity, strength, and extensibility of refractories in tension, *J. Res. Natl. Bur. Stand.* 17 (1936) 463–482.
- [7] A. Stuppler, E. Dahlem, Investigation of the parameters influencing the refractoriness under load (RuL) testing results for refractory materials, *Refract. Worldforum* 7 (2015) 87–93.
- [8] E. Dahlem, S. Clasen, C. Dannert, Investigation of the factors influencing the bulk density and open porosity testing results for refractory materials, *Refract. Worldforum* 7 (2015) 95–104.
- [9] J. Czechowski, A. Gerle, J. Podworny, E. Dahlem, Investigation of the testing parameters influencing the cold crushing strength testing results of refractory materials, *Refract. Worldforum* 7 (2015) 105–112.
- [10] S. Jin, D. Gruber, H. Harmuth, R. Rössler, Thermomechanical failure modeling and investigation into lining optimization for a Ruhrstahl Heraeus snorkel, *Eng. Fail. Anal.* 62 (2016) 254–262, <https://doi.org/10.1016/j.engfailanal.2016.01.014>.
- [11] V.S. Bakunov, A.V. Belyakov, Role of structural characteristics in high-temperature creep of ceramics, *Refract. Ind. Ceram.* 41 (2000) 349–355, <https://doi.org/10.1023/A:1011376921847>.
- [12] S. Jin, H. Harmuth, D. Gruber, Compressive creep testing of refractories at elevated loads—device, material law and evaluation techniques, *J. Eur. Ceram. Soc.* 34 (2014) 4037–4042, <https://doi.org/10.1016/j.jeurceramsoc.2014.05.034>.
- [13] A. Hou, S. Jin, H. Harmuth, D. Gruber, A method for steel ladle lining optimization applying thermomechanical modeling and taguchi approaches, *J. Miner. Met. Mater. Soc.* 70 (11) (2018) 2449–2456, <https://doi.org/10.1007/s11837-018-3063-1>.
- [14] ASTM C 597-09, Standard Test Method for Pulse Velocity through Concrete, ASTM International, West Conshohocken, PA, USA, 2009.
- [15] G. Roebben, B. Bollen, A. Brebels, J. Van Humbeeck, O. Van der Biest, Impulse excitation apparatus to measure resonant frequencies: elastic moduli, and internal friction at room and high temperature, *Rev. Sci. Instrum.* 68 (12) (1997) 4511–4515, <https://doi.org/10.1063/1.1148422>.
- [16] J.T. Boyle, J. Spence, *Stress Analysis for Creep*, Butterworths, England, 1983.
- [17] A. Sidi Mammari, D. Gruber, H. Harmuth, S. Jin, Tensile creep measurements of ordinary ceramic refractories at service related loads including setup, creep law, testing and evaluation procedures, *Ceram. Int.* 42 (2016) 6791–6799, <https://doi.org/10.1016/j.ceramint.2016.01.056>.
- [18] S. Schachner, S. Jin, D. Gruber, H. Harmuth, A method to characterize asymmetrical three-stage creep of ordinary refractory ceramics and its application for numerical modelling, *J. Eur. Ceram. Soc.* 39 (2019) 4384–4393, <https://doi.org/10.1016/j.jeurceramsoc.2019.06.010>.
- [19] D.W. Marquardt, An algorithm for least-squares estimation of nonlinear parameters, *J. Soc. Ind. Appl. Math.* 11 (1963) 431–441, <https://doi.org/10.1137/0111030>.
- [20] C.D. Montgomery, *Design and Analysis of Experiments*, Wiley, 2017.



Article

Experimental Investigation of the Tension and Compression Creep Behavior of Alumina-Spinel Refractories at High Temperatures

Lucas Teixeira ^{1,*}, Soheil Samadi ², Jean Gillibert ¹, Shengli Jin ², Thomas Sayet ¹, Dietmar Gruber ² and Eric Blond ¹

¹ Université d'Orléans, Université de Tours, INSA-CVL, LaMé, 45072 Orléans, France;

jean.gillibert@univ-orleans.fr (J.G.); thomas.sayet@univ-orleans.fr (T.S.); eric.blond@univ-orleans.fr (E.B.)

² Chair of Ceramics, Montanuniversität Leoben, 8700 Leoben, Austria; soheil.samadi@unileoben.ac.at (S.S.); Shengli.Jin@unileoben.ac.at (S.J.); dietmar.gruber@unileoben.ac.at (D.G.)

* Correspondence: lucas.breder-teixeira@univ-orleans.fr

Received: 3 September 2020; Accepted: 18 September 2020; Published: 22 September 2020



Abstract: Refractory materials are subjected to thermomechanical loads during their working life, and consequent creep strain and stress relaxation are often observed. In this work, the asymmetric high temperature primary and secondary creep behavior of a material used in the working lining of steel ladles is characterized, using uniaxial tension and compression creep tests and an inverse identification procedure to calculate the parameters of a Norton-Bailey based law. The experimental creep curves are presented, as well as the curves resulting from the identified parameters, and a statistical analysis is made to evaluate the confidence of the results.

Keywords: refractories; creep; parameters identification

1. Introduction

Refractory materials, known for their physical and chemical stability, are used in high temperature processes in different industries, such as iron and steel making, cement and aerospace. These materials are exposed to thermomechanical loads, corrosion/erosion from solids, liquids and gases, gas diffusion, and mechanical abrasion [1]. In the steel industry, for equipment such as the steel ladle and BOF furnaces, the effect of creep strains and stress relaxation is of ultimate importance in the prediction of the lining performance.

Generally, the creep behavior of materials can be split in three stages. The first stage, called primary creep, presents a time-dependent strain rate which decreases with time. In the secondary creep stage, the strain rate is considered to be constant, and an approximate equilibrium between hardening and softening processes can be assumed [2]. Finally, in the third creep stage, the strain rate increases with time until the failure of the material [3].

The creep strain of a given material is highly dependent on the temperature and the applied stress or deformation [2]. For ceramic materials, including refractories, it has been demonstrated that the creep strain rate at one-dimensional tension load is considerably higher than the strain rate caused by a load with the same absolute value in compression [4]. It should be also noticed that some materials don't present all creep stages, sometimes going from primary to tertiary stage, or presenting only secondary and tertiary stages [5].

The creep models available in the literature are categorized into micromechanical and phenomenological models. Micromechanical models are used to evaluate what are the creep mechanisms taking place at a given material. The most common mechanisms that contribute for the

creep of ceramics are grain boundary sliding, diffusion and dislocation motion [5]. This methodology was applied to refractory materials by Martinez et al. [6]. The one-dimensional form of the most frequently used model for secondary creep strain rate equation in the context of micromechanical models is [7]:

$$\dot{\varepsilon} = \frac{KDGb}{kT} \left(\frac{b}{d}\right)^p \left(\frac{\sigma}{G}\right)^n \quad (1)$$

where σ is the applied stress, K , p and n are material's constants, G is the shear modulus, b is the Burger's vector, k is the Boltzmann's constant, T is the temperature, D is the diffusion coefficient and d is the grain size.

Conversely, phenomenological models attempt to evaluate the effects of creep in a given material regardless of the possible mechanisms that could cause them. This normally results in simpler models with less parameters, at the cost of being less general. The most used phenomenological creep strain rate model is the Norton-Bailey's creep law. Its one-dimensional form is shown in Equation (2):

$$\dot{\varepsilon}_{cr} = A\sigma_{eq}^n \varepsilon_{cr}^a \quad (2)$$

where ε_{cr} is the accumulated creep strain, A , n and a are temperature dependent material parameters and σ_{eq} is the von Mises equivalent stress.

In the framework of nonlinear structural mechanics, phenomena involving permanent strains can be classified as time-independent and time-dependent plasticity (referred here as creep). The fundamental difference between them is that, in the later, the strain rate $\dot{\varepsilon}_{cr}$ can be explicitly defined as a function of the stress, while in the former this isn't possible due to mathematical constraints [8].

The function describing the creep strain rate can take many forms, depending on the material's behavior to be described. The Norton-Bailey law has been used to model the creep of refractories [3,4,9], and it seems to be appropriated also in the current work, as is shown in Section 5. For three-dimensional calculations, the Norton-Bailey equation is [10]:

$$\underline{\dot{\varepsilon}}_{cr} = \frac{3}{2} \frac{\underline{s}}{\sigma_{eq}} A \sigma_{eq}^n \varepsilon_{eq}^a \quad (3)$$

where \underline{s} is the deviatoric stress tensor, and ε_{eq} is the equivalent creep strain tensor.

In the particular case of secondary creep, the parameter $a = 0$, and therefore the creep strain presents a linear curve.

In this work, the creep behavior of a shaped Alumina-Spinel refractory used as working lining material in steel ladles was characterized at 1300 °C using tension and compression tests. The main goal is to show how the scatter in the strain vs time curves can influence in the range of variation of the identified material parameters. This is done by plotting the confidence intervals for the curves based on a statistical procedure. Section 2 describes the material used for the mechanical tests. Section 3 shows the main characteristics of the mechanical tests used to obtain the creep curves. Section 4 presents the methodology used for the inverse identifications. Section 5 presents the experimental results and the identified parameters, as well as a discussion regarding the confidence interval of the data. Finally, in Section 6 the main conclusions of the work are presented.

2. Material

The Alumina-Spinel brick studied in this work has a maximum grain size of 3 mm, and it's used in the working lining of steel ladles in steel plants. According to the material's technical data sheet, it is mainly composed of 94% Al₂O₃, 5% MgO, 0.3% SiO₂ and 0.1% Fe₂O₃, with a bulk density of 3.13 g/cm³ and apparent porosity of 19 vol%.

3. Experiments

The experimental creep curves were obtained using dedicated compression and tension testing machines. These machines were successfully used in previous works [3,9,11,12], and their main characteristics are presented in the next sections. The Alumina-Spinel material creep behavior was characterized at 1300 °C both in tension and in compression. For each load case, three different stress values were used, and for each stress value three different specimens were tested.

3.1. Uniaxial Compression Tests

To measure the displacements during the compression creep, two extensometers were positioned with a difference of 180° in relation to each other, and the distance between their corundum rods was 50 mm. The entire sample, the upper and the lower SiC pistons were located inside of a tubular furnace. A schematic representation of the compression creep experimental setup can be seen on Figure 1.

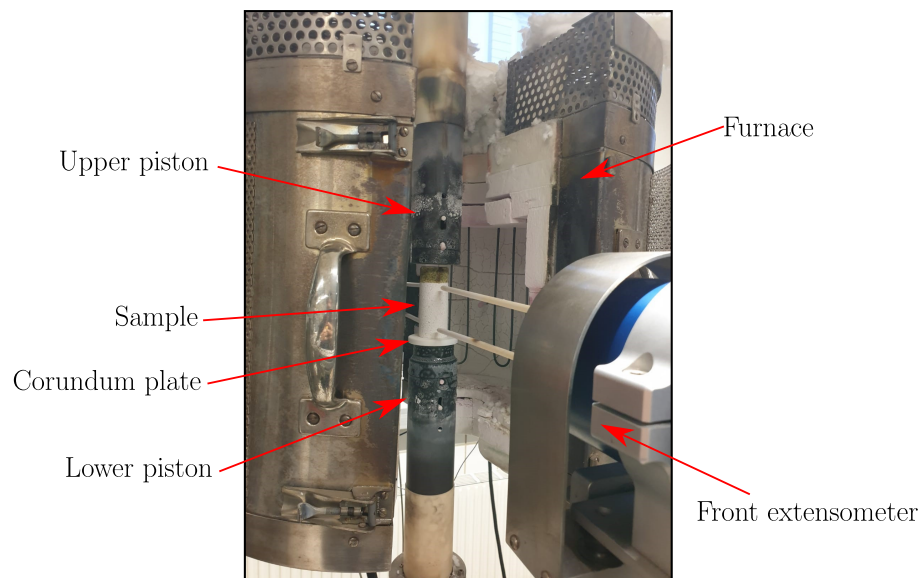


Figure 1. Compression creep experimental setup.

The samples used in the compression tests were drilled with 35 mm diameter and cut to a length of 70 mm, and a corundum plate was used at the contact between the sample and the lower piston to avoid chemical interactions.

At the beginning of the test a compressive pre-load of 50 N was applied to the sample to hold it in the correct position during the heating. The heating rate for the compression tests was 10 °C/min, and a 1h dwell was used to homogenize the sample's temperature.

The stress values used for the tests were 8 MPa, 9 MPa and 10 MPa.

3.2. Uniaxial Tensile Tests

For the tensile creep, two extensometers were used, with a distance between their corundum rods of 50 mm. To avoid damaging the sample during the gripping and consequent application of the load, the sample was glued to two water cooled adapters using a dedicated gluing device (Figure 2a). This device was designed to improve the alignment of the sample, avoiding the occurrence of bending loads [9]. The sample and the adapters were positioned at the testing machine and connected to water cooled grips, standing outside the furnace to avoid burning the glue. In this way, only a part of the sample stays inside the furnace. The tensile creep experimental setup is shown in Figure 2b.

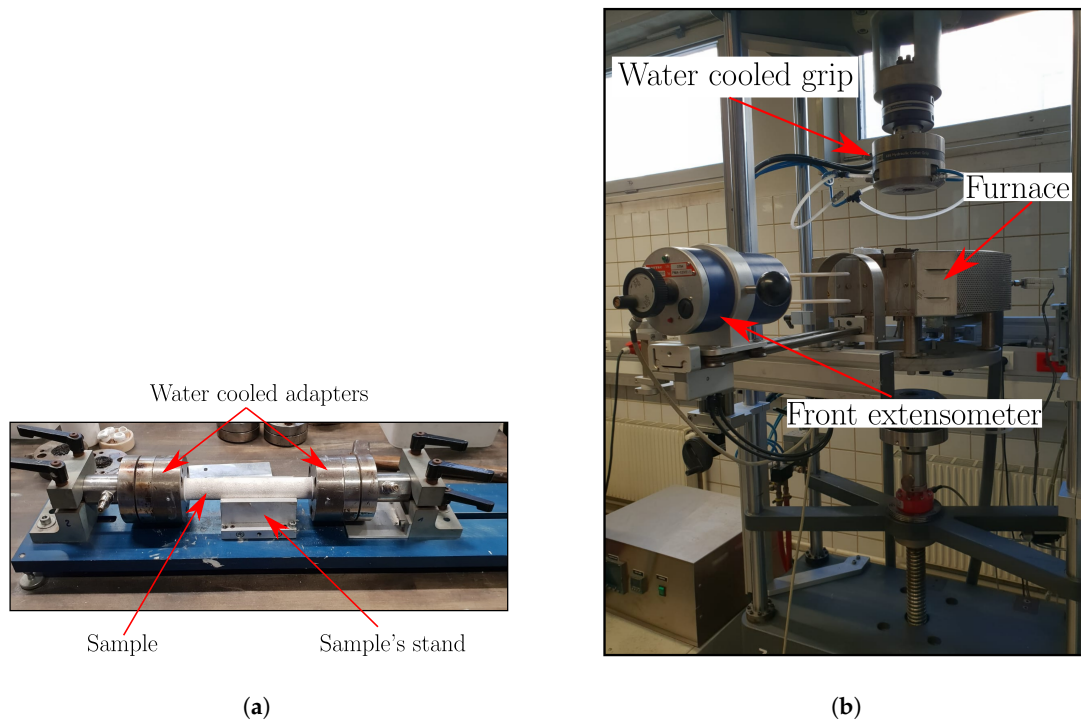


Figure 2. Tensile creep experimental setup. (a) Gluing device. (b) Testing machine.

The samples used in the tensile tests were drilled with 30 mm diameter and cut to a length of 230 mm. A pre-load of 50 N was also applied in the tensile test, and the heating rate as 5 °C/min, with 1h dwell to reach the steady state temperature.

The stress values used for the tests were 0.15 MPa, 0.20 MPa and 0.25 MPa. Nevertheless, for the tensile load of 0.15 MPa the results of the three different tests presented a significant scatter, and they weren't considered during the calculations.

4. Methodology

4.1. Inverse Identification

To identify the material parameters from tension or compression creep tests, Equation (2) can be integrated using the trapezoidal rule [3], resulting in:

$$\varepsilon_{cr,i+1} \approx \left[\varepsilon_{cr,i}^{1-a} + \frac{(1-a) \cdot A \cdot (\sigma_{i+1}^n + \sigma_i^n) \cdot (t_{i+1} - t_i)}{2} \right] \frac{1}{1-a} \tag{4}$$

where t is the time and i is the time step index. In this way, depending on the stress variation over time and on a given set of material's parameters, it's possible to obtain an analytic calculation of the resulting time vs creep strain curve, which can later be compared to the experimental results using a least squares approach.

It should be taken into account that the experimental creep curves comprise both the elastic and creep strains (ε_{tot}), but Equation (2) doesn't account for the elastic part. Therefore, either the experimental data should be treated or the elastic strains should be included in the equation, following the expression for the one-dimensional case:

$$\varepsilon_{tot} = \varepsilon_{cr} + \frac{\sigma}{E} \tag{5}$$

where the second part of the right hand side of the equation corresponds to the elastic strain, being E the Young's modulus of the material.

The inverse identifications carried out in this work were done according to the following steps:

- **Step 1:** Definition of the input variables.
 1. Sample's diameter
 2. Young's modulus
 3. Type of creep (primary or secondary)
 4. Allowed range of variation for the material's properties
 5. Raw data from the tests (time-force-displacement tables)
- **Step 2:** Random definition of the initial guesses, depending on the variable's range of variation and the number of initial guesses.
- **Step 3:** For each of the initial guesses and each of the stress levels, calculate the analytic time-strain curves using Equation (4), at the same time points as the ones available from the experimental data.
- **Step 4:** For each time point, calculate the difference between the experimental and analytic values (identification error).
- **Step 5:** Using a Levenberg-Marquardt optimization algorithm [13], change the material's parameters in order to minimize the identification error.

As explained in Section 3, three creep tests were done for each stress value, therefore nine curves were available for compression and six for tension. The procedure described above was repeated for all possible combinations of curves available at the different stresses. For the identification of compression creep parameters, the curve were combined on sets of three (one at each stress), and for the tensile creep parameters the curves were combined in sets of two.

4.2. Statistical Analysis

The main idea in this paper is to show how the scatter in the tests can influence the identified material parameters, in terms of their range of variation.

First, two concepts should be defined:

- Statistical population: group of all possible items in the study domain. In the present case, the population is the infinite number of creep tests that could be done.
- Statistical sample: the actual subset of the population being studied. In this study, the statistical sample is used to draw conclusions about the statistical population, since the mean and the standard deviations of the population are unknown.

Confidence intervals can be used to predict what is the confidence level that one parameter of the statistical population (for example, the average) lies in a given range, calculated using the statistical sample.

For example, if one defines a 70% confidence interval for the average of the material parameter A in Equation (2), this means that the interval resulted from the estimation procedure is 70% reliable, not that there is 70% probability that the parameter A for the statistical population lies within this interval.

Once the inverse identifications were made using the different possible combinations of curves, the average and standard deviation were calculated.

Assuming a normal distribution for the results, confidence intervals can be calculated according to the following expression:

$$\left(\bar{x} - t^* \frac{\eta}{\sqrt{n}}, \bar{x} + t^* \frac{\eta}{\sqrt{n}} \right) \quad (6)$$

where \bar{x} is the average, η is the standard deviation of the statistical sample, n is the number of observations and t^* is the critical value according to Student's t-distribution, that can be found in specialized tables [14].

Once the confidence intervals were obtained, the strain vs time curves were plotted using their extreme values, to check the variation of the creep curves within the chosen confidence level.

Due to the high heterogeneity of refractories and limited amount of experimental data available, it was decided to plot 70% confidence intervals for all the analyses in Section 5.

5. Results and Discussions

All the curves presented in this work represent the average of the two extensometers used to measure the displacements over time, as explained in Section 3. The compression creep curves were already reported by Samadi et al. [12], where a different statistical approach was applied for the parameter determination.

Figure 3, shows the effect of the stress increase on the creep strain for the studied material. It can be observed that for a compression stress $\sigma = 8$ MPa, the time to the complete failure of the sample is approximately 11.5 h, while at $\sigma = 10$ MPa it is reduced to less than 1.5 h. The same effect can be observed in tension, where a variation from $\sigma = 0.20$ MPa to $\sigma = 0.25$ MPa resulted in a decrease in the test time from approximately 33 min to 2.5 min.

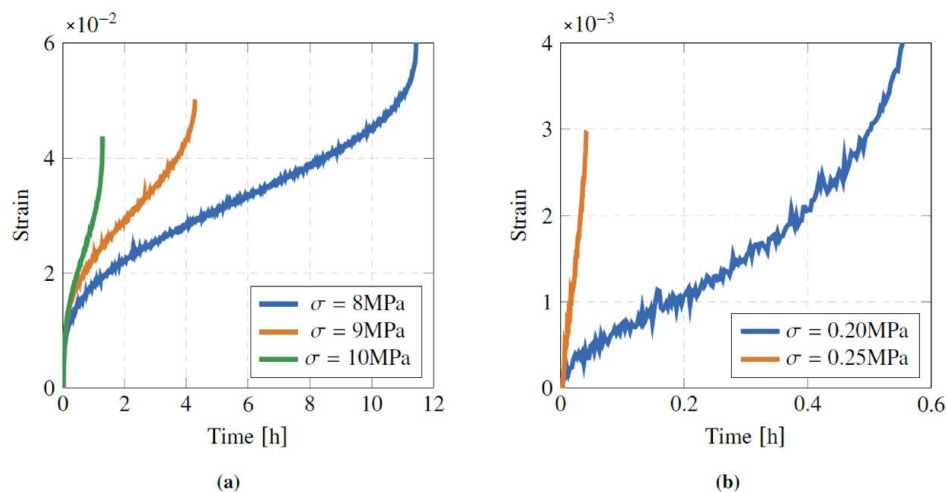


Figure 3. Creep tests at 1300 °C. (a) Compression. (b) Tension.

It's well known that refractories are heterogeneous materials, since normally they have large grain sizes compared to the size of the samples used for mechanical test, with some exceptions. As such, it is common to observe a considerable scatter in the data regarding their mechanical properties. Figure 4a shows that, for the material studied in this work, under a compression stress $\sigma = 8$ MPa, Sample 1 failed after 11.5 h, while Sample 3 failed after 3 h. Under a tension load of $\sigma = 0.2$ MPa, Sample 1 failed after 1.1 h, while Sample 3 failed after 30 min of test. For Sample 2 the test was interrupted after 20 min due to sudden failure of the glue, although the resulting creep curve is similar to the one of Sample 3.

Figure 5a shows all the compression creep curves obtained experimentally at the three different stress levels, but only for the primary and secondary creep stages. Although it is still possible to observe a scatter in the data, this effect is much less pronounced than when the third creep stage is also considered, like in Figure 4. More particularly, the results of Samples 3 and 6 are very similar, although the stress levels were $\sigma = 8$ MPa and $\sigma = 9$ MPa, respectively. The results of the tensile creep tests are plotted in Figure 5b.

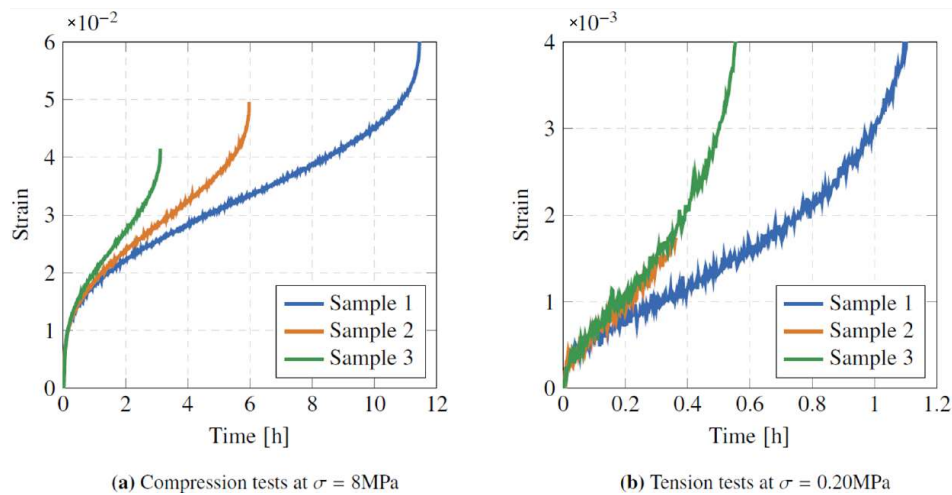


Figure 4. Three stages of creep at $T = 1300 \text{ }^\circ\text{C}$ under tensile and compressive loads.

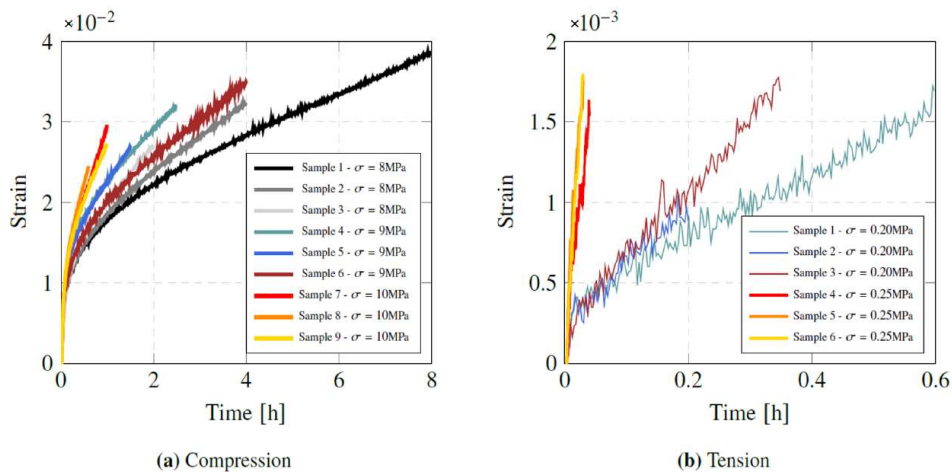


Figure 5. Creep tests at $1300 \text{ }^\circ\text{C}$.

The scatter in the data, that is considered to be rather normal for refractory materials, can be explained by many factors. From the material's point of view, the heterogeneity in the bricks used to produce the samples can come from the production processes, such as the pressing and the heat treatment. From the testing procedures, micro-cracking of the sample during its production and misalignment of the load can contribute to the variations in the results. It's out of the scope of this work to precisely define the causes of this scatter, although the authors believe it can come from a combination of all factors mentioned.

Identification of the Creep Parameters

The curves presented in Figure 5 were used to identify the creep parameters related to Equation (2). It should be noticed that frequently the main goal of creep parameters identification for a given material is to later model more complex structures under multidimensional loads. In this case, the stage of the creep needed for simulation must be defined (primary or secondary), since Equation (2) does not provide a criteria to transit from the first to the second creep stages during the calculations.

From Figure 5a, it is observed that primary creep stage has an important influence in the time-strain response under compression, and therefore it will be considered during the identification. However, the tensile creep data presented in Figure 5b shows that, although the occurrence of primary creep stage can be observed, it finishes after a few minutes and secondary creep holds for most of the test time. For this reason, the secondary creep assumption (Equation (2) with $a = 0$) seems

to be a feasible approximation of the material behavior in tensile creep regime, and was used for the identifications.

Table 1 shows the inversely identified compressive creep parameters. The nine experimental curves were combined in sets of 3, resulting in 27 combinations. The 70% confidence interval was calculated using a Student’s t-distribution critical value of $t^* = 1.057$.

In Figure 6 the creep curves resulting from the average of the identification parameters were plotted together with the experimental curves. It is possible to observe a good agreement between the experimental and identified results. The figure also shows the upper and lower bound creep curves resulted from the extreme values of the confidence intervals. It can be concluded that, to be 70% confident about the identification procedure, the possibility of a large variation of the average values must be assumed. This fact is due to the limited number of tests that could be done, considering the high cost and the time demand to perform them.

Table 1. Results of the inverse identification—Compression creep.

Parameter	Average	Std. Deviation	70% Confidence Interval
$\log_{10}(A[\text{MPa}^{-n}\text{s}^{-1}])$	-13.52	0.925	(-14.08, -12.95)
n [-]	3.56	0.554	(3.22, 3.90)
a [-]	-2.59	0.218	(-2.73, -2.46)

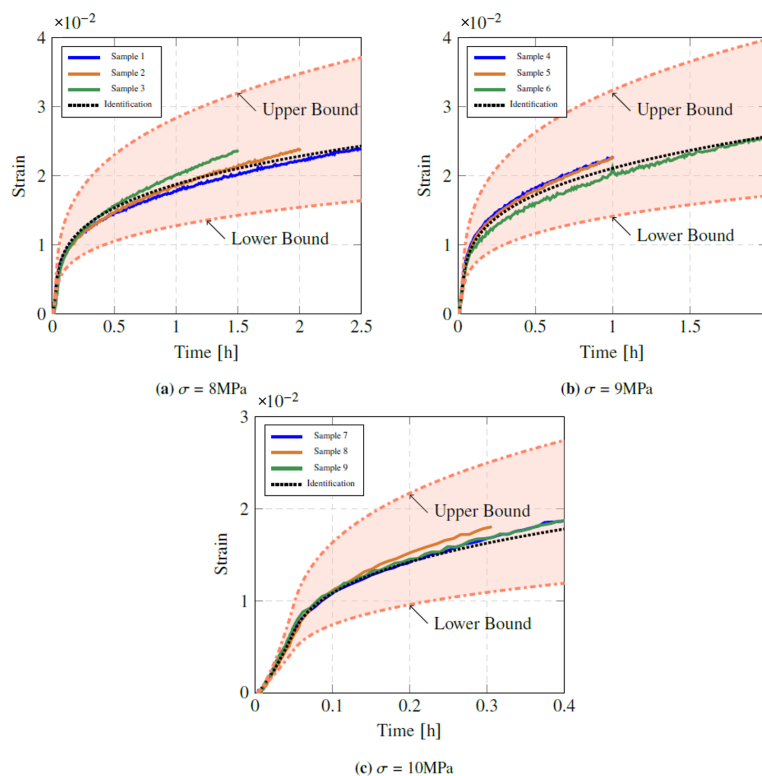


Figure 6. Compressive creep identification results at $T = 1300\text{ }^{\circ}\text{C}$.

Table 2 shows the identified parameters for the tensile creep and a 70% confidence interval, calculated with $t^* = 1.108$, and Figure 7 shows the experimental and identified creep curves. Such as in the compression case, the creep curve resulting from the average identification is in a good agreement with the experimental curves, but the standard deviation has a very high value compared to the average. This fact, combined with the resulted number of experimental data available, results in a broad confidence interval, and the upper and lower bounds were not plotted in Figure 7.

Table 2. Results of the inverse identification—Tensile creep.

Parameter	Average	Std. Deviation	70% Confidence Interval
$\log_{10}(A[\text{MPa}^{-n}\text{s}^{-1}])$	2.52	1.14	(1.62, 3.42)
n [-]	12.05	1.78	(10.65, 13.45)

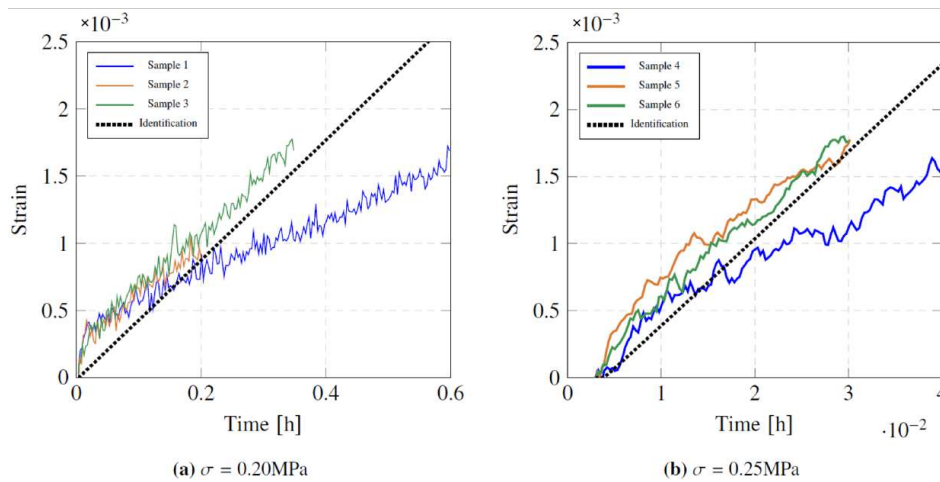


Figure 7. Tensile creep identification results at $T = 1300 \text{ }^\circ\text{C}$.

Considering the possible effects the test procedures as well as the material heterogeneity, another approach for the inverse identification is to only consider the two closer curves at each load, and to eliminate the curve that deviate considerably from them. For example, considering the compressive creep curves presented in Figure 5a at $\sigma = 9 \text{ MPa}$, Samples 4 and 5 are in good agreement between each other, while Sample 6 seems to deviate. In the same way, for the tensile tests at $\sigma = 0.20 \text{ MPa}$, Sample 1 presents a considerable difference when compared with Samples 2 and 3.

This methodology needs to be used carefully, because is not always obvious when a deviating result comes from a problem due to the testing procedure or due to an abnormal variation of the material, and when it is due to its actual normal heterogeneity. A reliable way to make this verification is to perform a higher number of tests, what presents the difficulties already mentioned.

To apply this methodology, Samples 3, 6 and 8 were removed from the identification of compressive parameters, and Samples 1 and 4 were removed from the identification of tensile parameters.

Table 3 shows the identification results for the compressive creep tests with the reduced number of samples, and Table 4 the results of the tensile creep parameters. It can be seen that, when comparing to Tables 1 and 2, the average of the parameters changed less than 10%, but the standard deviation was reduced up to 50%. It should be noticed that, since the number of experimental curves being considered decreased, the critical value of the Student’s t-distribution increased, being now $t^* = 1.134$ for compression and $t^* = 1.25$ for tension. Nevertheless, the decrease of the standard deviation was more influential than the increase of t^* , resulting in a more restricted range of variation for the confidence interval. Figures 8 and 9 show the plots of the results.

Table 3. Results of the inverse identification—Compression creep—Reduced number of samples.

Parameter	Average	Std. Deviation	70% Confidence Interval
$\log_{10}(A[\text{MPa}^{-n}\text{s}^{-1}])$	-14.16	0.506	(-14.49, -13.83)
n [-]	3.96	0.257	(3.79, 4.13)
a [-]	-2.74	0.142	(-2.83, -2.64)

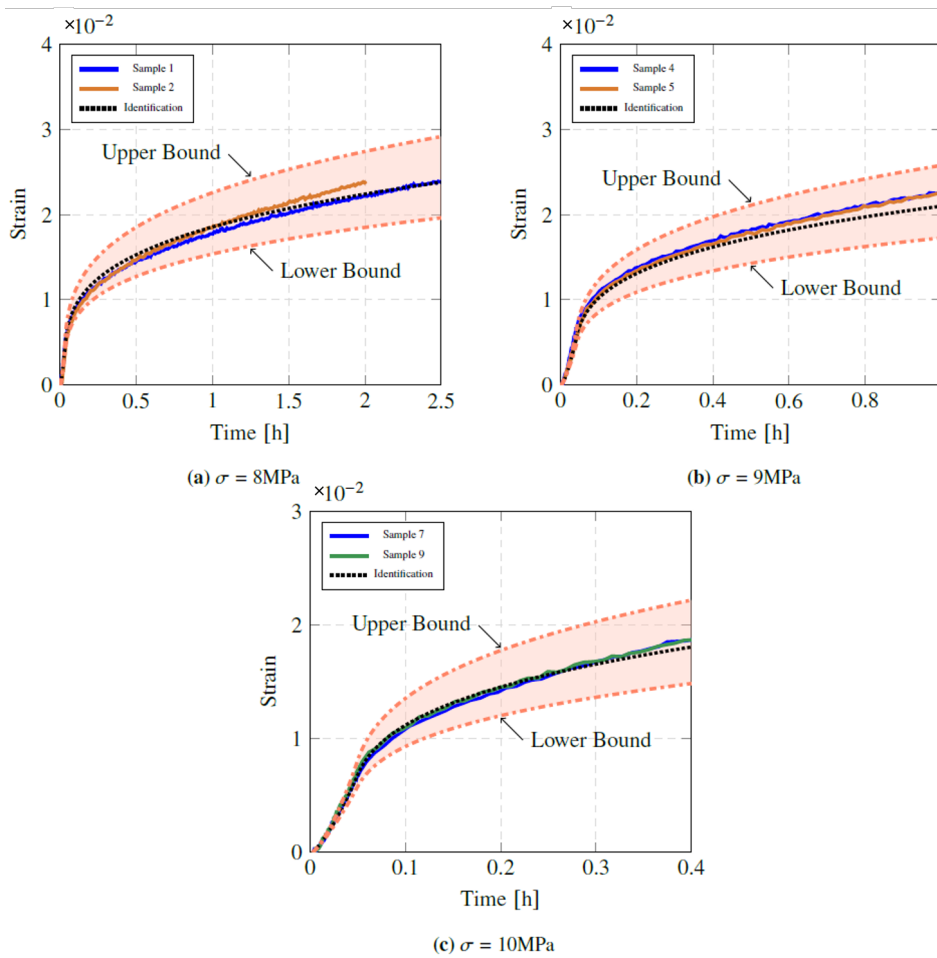


Figure 8. Compressive creep identification results at $T = 1300\text{ }^{\circ}\text{C}$ —Reduced number of samples.

Table 4. Results of the inverse identification—Tensile creep—Reduced number of samples.

Parameter	Average	Std. Deviation	70% Confidence Interval
$\log_{10}(A[\text{MPa}^{-n}\text{s}^{-1}])$	2.48	0.107	(2.39, 2.56)
n [-]	11.86	0.168	(11.73, 11.99)

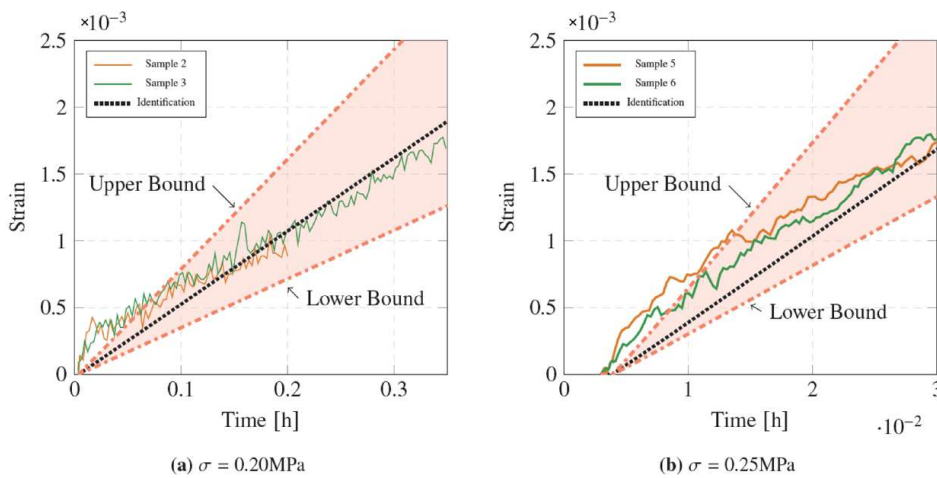


Figure 9. Tensile creep identification results at $T = 1300\text{ }^{\circ}\text{C}$ —Reduced number of samples.

6. Conclusions

This work presented the characterization of the tensile and compressive creep behavior of a shaped Alumina-Spinel material used in the working lining of steel ladles. Experimental curves were presented, as well as the results of an inverse identification of the parameters of a Norton-Bailey creep law.

The analytic creep curves resulting from the average of the identified parameters showed a good agreement with the experimental curves, although the variation range of the confidence intervals can be decreased if more experimental curves are available, what is not always possible due to limitations of cost and time.

The parameters identified in this work can be used in finite elements software to predict the creep strains and stress relaxations of complex refractory structures.

Author Contributions: Conceptualization, L.T., D.G. and E.B.; Formal analysis, L.T.; Funding acquisition, D.G. and E.B.; Investigation, L.T. and S.S.; Methodology, L.T. and S.J.; Project administration, D.G. and E.B.; Resources, J.G., D.G. and E.B.; Software, L.T.; Supervision, J.G., S.J., T.S., D.G. and E.B.; Visualization, L.T.; Writing—original draft, L.T.; Writing—review & editing, S.S., J.G., S.J., T.S., D.G. and E.B. All authors have read and agreed to the published version of the manuscript.

Funding: This work was supported by the funding scheme of the European Commission, Marie Skłodowska-Curie Actions Innovative Training Networks in the frame of the project ATHOR—Advanced THERmomechanical multiscale mOdelling of Refractory linings 764987 Grant.

Acknowledgments: This work was supported by the funding scheme of the European Commission, Marie Skłodowska-Curie Actions Innovative Training Networks in the frame of the project ATHOR—Advanced THERmomechanical multiscale mOdelling of Refractory linings 764987 Grant. The authors acknowledge the company RHI Magnesita for providing the materials.

Conflicts of Interest: The authors declare no conflict of interest. The funders had no role in the design of the study; in the collection, analyses, or interpretation of data; in the writing of the manuscript, or in the decision to publish the results.

References

1. Banerjee, S. Properties of Refractories. In *Refractories Handbook*; Schacht, C.A., Ed.; Marcel Dekker, Inc.: New York, NY, USA, 2004; Chapter 1, pp. 1–10.
2. Naumenko, K.; Altenbach, H. *Modeling of Creep for Structural Analysis*; Springer: Berlin/Heidelberg, Germany, 2007.
3. Jin, S.; Harmuth, H.; Gruber, D. Compressive creep testing of refractories at elevated loads—Device, material law and evaluation techniques. *J. Eur. Ceram. Soc.* **2014**, *34*, 4037–4042. [[CrossRef](#)]
4. Blond, E.; Schmitt, N.; Hild, F.; Blumenfeld, P.; Poirier, J. Modelling of high temperature asymmetric creep behavior of ceramics. *J. Eur. Ceram. Soc.* **2005**, *25*, 1819–1827. [[CrossRef](#)]
5. Hynes, A.; Doremus, R. Theories of Creep in Ceramics. *Crit. Rev. Solid State Mater. Sci.* **1996**, *21*, 129–187. [[CrossRef](#)]
6. Martinez, A.T.; Luz, A.; Braulio, M.; Pandolfelli, V. Creep behavior modeling of silica fume containing Al₂O₃–MgO refractory castables. *Ceram. Int.* **2012**, *38*, 327–332. [[CrossRef](#)]
7. Cannon, W.R.; Langdon, T.G. Creep of ceramics. *J. Mater. Sci.* **1983**, *18*, 1–50. [[CrossRef](#)]
8. de Souza Neto, E.A.; Peric, D.; Owen, D.R.J. *Computational Methods for Plasticity*; Wiley: West Sussex, UK, 2008.
9. Mammari, A.S.; Gruber, D.; Harmuth, H.; Jin, S. Tensile creep measurements of ordinary ceramic refractories at service related loads including setup, creep law, testing and evaluation procedures. *Ceram. Int.* **2016**, *42*, 6791–6799. [[CrossRef](#)]
10. Lemaitre, J.; Chaboche, J.L. *Mechanics of Solid Materials*; Cambridge University Press: Cambridge, UK, 1990.
11. Schachner, S.; Jin, S.; Gruber, D.; Harmuth, H. Three stage creep behavior of MgO containing ordinary refractories in tension and compression. *Ceram. Int.* **2019**, *45*, 9483–9490. [[CrossRef](#)]
12. Samadi, S.; Jin, S.; Gruber, D.; Harmuth, H.; Schachner, S. Statistical study of compressive creep parameters of an alumina spinel refractory. *Ceram. Int.* **2020**. [[CrossRef](#)]

13. Marquardt, D.W. An Algorithm for Least-Squares Estimation of Nonlinear Parameters. *J. Soc. Ind. Appl. Math.* **1963**, *11*, 431–441. [[CrossRef](#)]
14. Box, G.E.P.; Hunter, J.S.; Hunter, W.G. *Statistics for Experimenters: Design, Innovation, and Discovery*; Wiley: Hoboken, NJ, USA, 2005.



© 2020 by the authors. Licensee MDPI, Basel, Switzerland. This article is an open access article distributed under the terms and conditions of the Creative Commons Attribution (CC BY) license (<http://creativecommons.org/licenses/by/4.0/>).

CREEP PARAMETER DETERMINATION OF A SHAPED ALUMINA SPINEL REFRACTORY USING STATISTICAL ANALYSIS

Soheil Samadi, Shengli Jin, Dietmar Gruber, Harald Harmuth
Chair of Ceramics, Montanuniversitaet Leoben, Leoben, Austria

Lucas Teixeira
Univ. Orléans, Univ., Tours, INSA-CVL, LaMé, Orléans, Franc

ABSTRACT

Refractories often show heterogeneous microstructure, which contributes to the scatter of their mechanical properties in laboratory tests. To account for this characteristic, statistical analysis is necessary. The present paper investigates the effect of the heterogeneity of a shaped alumina spinel refractory on its creep behavior. The creep tests were performed at various temperatures and stresses under uniaxial compressive and tensile loads. For each temperature, the combination of different numbers of curves was considered for the inverse estimation of Norton-Bailey creep parameters. The mean value of each parameter and its standard deviation was compared for different combinations of curves, temperatures, and the different loading regimes (uniaxial tension and uniaxial compression). The confidence intervals and residuals were used to determine the representative set of curves for the material creep behavior.

INTRODUCTION

At high temperatures, creep is one of the major causes of irreversible deformations in refractory linings. Creep resistance of the refractories is affected by their microstructure, and studies showed that refractories present higher creep resistance under compressive stresses compared to tensile ones [1-3]. Furthermore, the heterogeneity of refractories microstructure often influences their mechanical properties evaluation and contributes to the scatter in the experimental results, which demands a statistical analysis approach for investigation of the mechanical properties. Several studies investigated the effect of refractory heterogeneity on their mechanical properties [4-6]. In the study of Samadi, et al. [4], it was shown that a high scatter existed in the compressive creep behavior of a shaped alumina spinel refractory. Additionally, with the aid of a statistical study, the representative creep parameters of the primary compressive creep stage were determined.

In the current paper, the statistical analysis approach explained in Ref. [4] was considered to compare the scatter of creep parameters in different loading regimes and different creep stages at various temperatures. Uniaxial compressive and tensile creep tests were performed at three different temperatures, under three load magnitudes, for three samples for each condition. The asymmetric creep behavior of the shaped alumina spinel refractory is discussed. Combinations of different number of curves at each temperature were used to inversely evaluate the Norton-Bailey creep law parameters for primary and secondary stages. Finally, the representative creep parameters are reported and compared for various loading regimes and creep stages.

METHODOLOGY

A burned alumina spinel refractory was selected for the case study. The oxide analysis consisted of 94 wt% alumina, 5 wt% magnesia, and 1 wt% other oxides such as, silica, iron oxide.

The uniaxial compressive creep test according to Ref. [7] and the uniaxial tensile creep test developed by Ref. [8] were chosen for creep testing. The cylindrical specimens had a diameter of 35 mm

and a height of 70 mm for uniaxial compressive creep tests and a diameter of 30 mm and a height of 230 mm for uniaxial tensile creep tests. Testing apparatuses and specimens are presented schematically in Ref. [7] and [8]. Twenty-seven specimens drilled from bricks within the same batch were used for each loading regime. For characterization of asymmetric creep behavior of the material at various temperatures, the loading conditions were defined as shown in table 1. For each loading condition, three randomly selected specimens were used. The loads were defined in a way that all the three creep stages were obtained in a reasonable testing time; nevertheless, not all the tests could reach the third stage in 24 hours (had to be interrupted due to the safety measures).

Tab. 1: Applied stresses for characterization of the creep behavior.

Uniaxial compressive creep tests	Temperature (°C)	1300	1400	1500
	Applied stresses (MPa)	8.0	4.0	3.5
		9.0	4.5	4.0
10.0		5.0	4.5	
Uniaxial tensile creep tests	Temperature (°C)	1200	1300	1400
	Applied stresses (MPa)	0.25	0.15	0.12
		0.35	0.20	0.15
0.45		0.25	0.18	

In uniaxial compressive creep tests, a small preload of 0.05 MPa was applied on the specimen to stabilize it during the heating process. This preload was 0.01 MPa in the case of uniaxial tensile creep tests. In both tests, a cylindrical electrical furnace heats the specimens to the target temperature with a rate of 10 °C/min and 5 °C/min in uniaxial compressive and tensile creep tests, respectively. Afterwards, a dwell time of one hour was considered for thermal homogenization. After the dwell time, the defined mechanical load was applied on the specimen, and the displacements were measured directly on the surface of the specimen using two pairs of mechanical extensometers, which were placed at the front and rear sides of the furnace. The extensometers' initial arm distance was 50 mm.

After treatment of the experimentally measured displacements, the strain-time creep curves were obtained, and the ruler method was employed to determine the transition points of the three creep stages. In this method, the linear part of the curves, which is the secondary creep stage, is determined by a ruler. To illustrate the creep behavior, the strain hardening form of the Norton-Bailey creep rate equation [9] was employed (Eq. 1).

$$\dot{\epsilon}_{cr} = K(T)\sigma^n \epsilon_{cr}^a \quad (1)$$

where σ is the applied stress, $\dot{\epsilon}_{cr}$ is the creep strain rate, ϵ_{cr} is the equivalent/accumulated creep strain, $K(T)$ denotes a temperature dependent function, n is the stress exponent and a is the strain expo-

ment that is negative for the primary stage and zero for secondary stage. The inverse identification method developed in Ref. [7] was applied to identify the creep parameters. To this end, the Levenberg-Marquardt optimization algorithm [10] was applied to minimize the sum of the squared differences of measured and simulated creep strains.

STATISTICAL STUDY

The statistical study was presented in Ref. [4], and the results for the primary creep stage of the uniaxial compressive creep test results of the alumina spinel refractory were shown and discussed in that study. In the current paper, the same approach was considered to investigate the influence of material inhomogeneity on creep behavior for different loading regimes and different creep stages.

There are 9 available creep curves for each temperature and each loading regime, from which different arbitrary numbers of curves can be used as input dataset of the inverse evaluation method. The theoretical constraint to achieve a unique solution for a , n and K is that minimum two curves with different constant stresses must be in the input dataset. Therefore, to have a statistical overview of the data, all the possible combinations of 2 to 9 curves, including the primary and secondary creep stages of both compressive and tensile creep test results, were employed as the input datasets (8 in total). The dataset sizes are reported in table 2.

Tab. 2: dataset size from different number of curves in combination.

Number of curves in combination	2	3	4	5	6	7	8	9
Dataset size	27	81	126	126	84	36	9	1

For each dataset, the mean value, standard deviation and the confidence interval of creep parameters were calculated. Eq. (2) was used to calculate the common 99% confidence interval $(\frac{t_{0.99,n-1}S}{\sqrt{n}})$,

$$|\mu - \bar{y}| \leq \frac{t_{0.99,n-1}S}{\sqrt{n}} \tag{2}$$

where $|\mu - \bar{y}|$ represents the difference between the dataset mean value (\bar{y}) and the mean value of the whole population (μ), n denotes the dataset size, $n-1$ is the number of degrees of freedom, and S stands for the dataset standard deviation. The value is taken from the t-distribution table based on the degrees-of-freedom of the dataset and the percentage value (table II in Ref. [11]).

RESULTS AND DISCUSSIONS

The creep test results are shown in figures 1 and 2 for uniaxial compressive and tensile creep tests, respectively. An evident scatter was observed in the creep results of both loading regimes. Despite the scatter, another important observation was the asymmetric creep behavior of the material. The average of maximum compressive creep strains was one order of magnitude larger than the one of tensile creep, and it increased with temperature in the case of compressive creep curves, but decreased for tensile creep curves. Moreover, the tensile creep curves were more sensitive to the stress than the compressive creep curves.

To have a clear vision of the asymmetric creep behavior of the investigated alumina spinel refractory, creep stage duration and transition strain were compared between the two loading regimes. Figure 3 presents the creep stage duration ratios for primary and secondary creep, i. e., the ratios between each stage and the total test time.. It was observed that the duration ratio of primary creep stage was below 15% for tensile creep curves; but for secondary stage, this ratio was more than 50% for all temperatures. There-

fore, the secondary creep stage was the dominating stage in tensile creep of the current material. For tensile creep measurements, both primary and secondary stage durations increased with temperature; but for compressive creep measurements, primary stage duration increased, and secondary stage duration decreased with temperature.

Figure 4 shows the creep stage transition ratios of primary and secondary creep stages. The ratios were calculated by dividing the creep strain at the transition points by the total creep strain. It was observed that in compressive creep tests, the creep strain ratios of both primary and secondary stages to the maximum strain decreased with temperature. On the contrary, in tensile creep tests, the strain ratios of both primary and secondary stages to

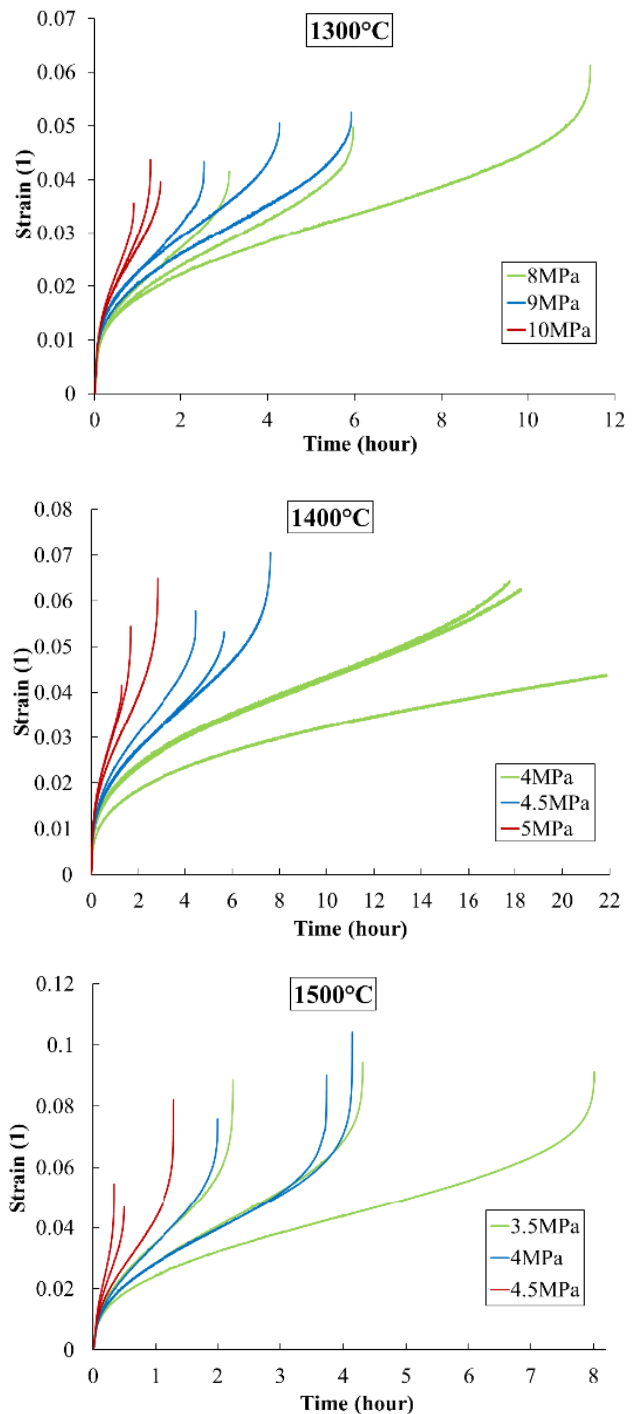


Fig. 1: Uniaxial compressive creep test results for 1300°C – 1400°C – 1500°C

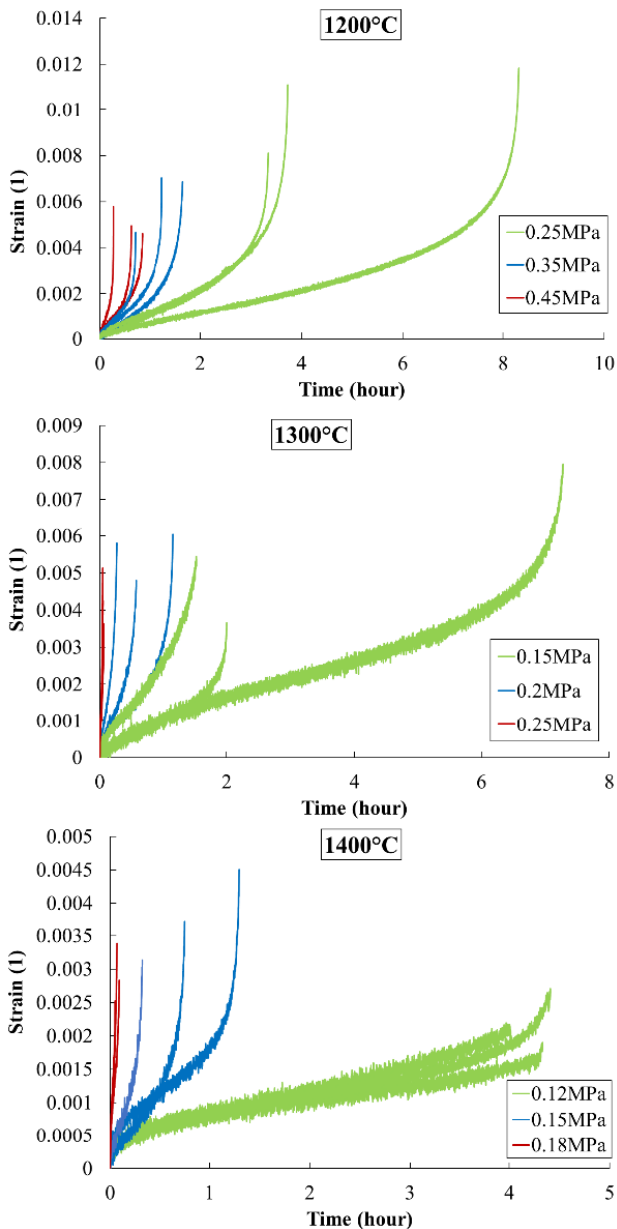


Fig. 2: Uniaxial tensile creep test results for 1200°C – 1300°C – 1400°C

the maximum strain increased with temperature. Additionally, for tensile creep curves, between 82-87 % of the creep strain occurred during the tertiary creep stage although the secondary creep stage was the longest one.

STATISTICAL STUDY RESULTS

The creep parameters (K , n and a) of primary and secondary stages were inversely evaluated for various combinations of curves. As it was shown in figure 3, the secondary stage was the most prominent one for tensile creep curves; therefore, in this section the results of the secondary stage are compared between compressive and tensile creep measurements. The mean values and standard deviations of n and the common logarithm of K ($\log K$) with respect to the number of curves in combination are plotted in figures 5 and 6, for tensile and compressive creep regimes, respectively. When using all the possible 9 curves for the inverse evaluation only one set of creep parameters is obtained and therefore, no standard deviation is reported for this dataset. For both parameters in both regimes, the standard deviations of the datasets decreased with increasing the number of combined curves, expectedly; but the mean values did not change signif-

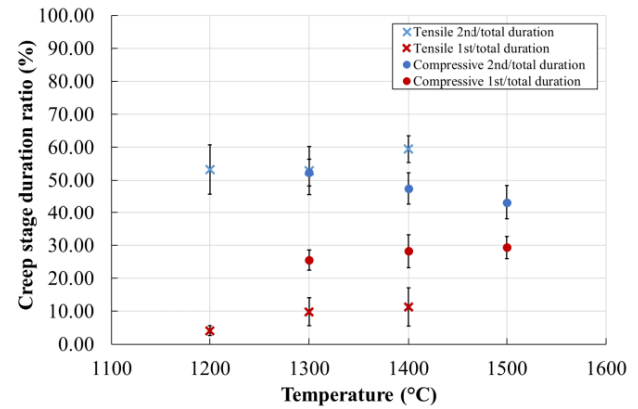


Fig. 3: Creep stage duration ratios of compressive and tensile creep curves for different temperatures (1st: primary creep stage, 2nd: secondary creep stage)

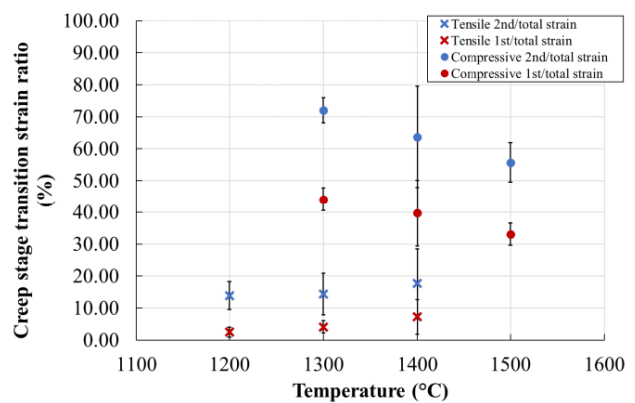


Fig. 4: Creep stage transition strain ratios of compressive and tensile creep curves for different temperatures (1st: primary creep stage, 2nd: secondary creep stage)

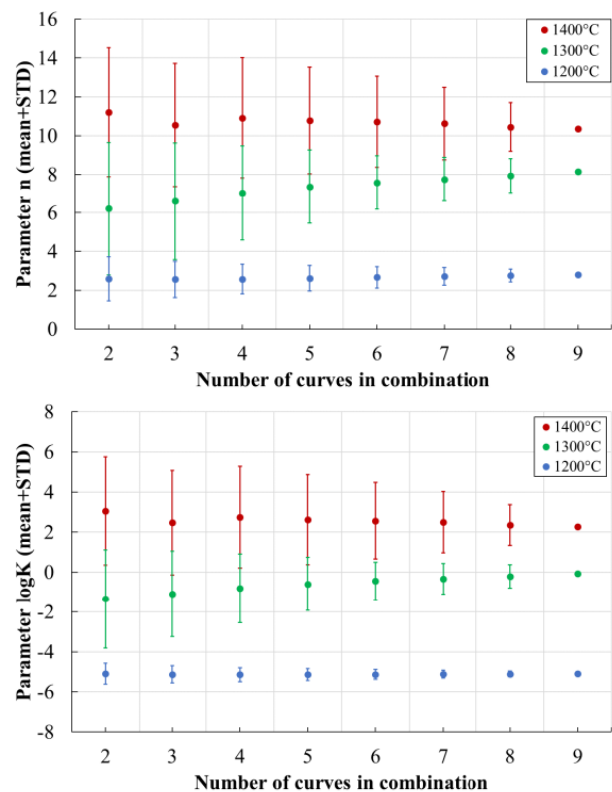


Fig. 5: Uniaxial tensile secondary creep parameters n and $\log K$ of different datasets for different temperature (with standard deviations)

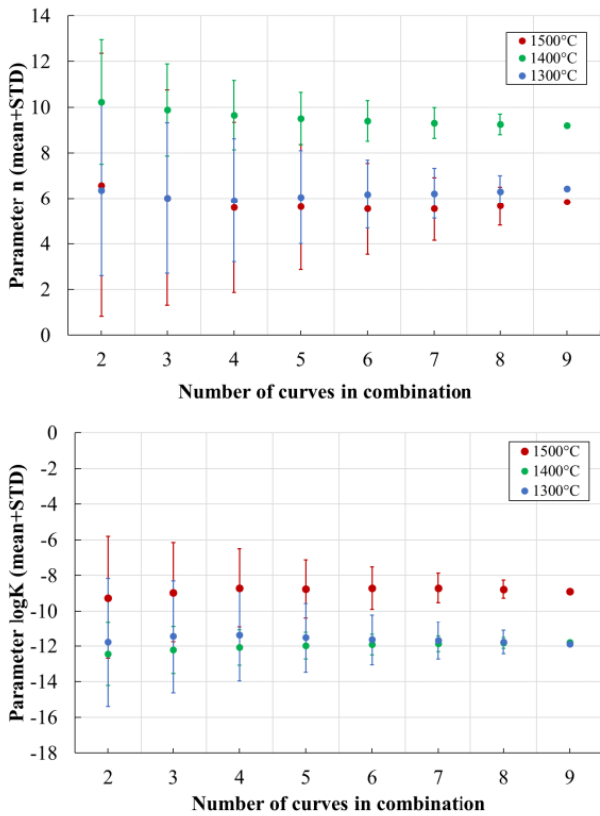


Fig. 6: Uniaxial compressive secondary creep parameters n and $\log K$ of different datasets for different temperature (with standard deviations)

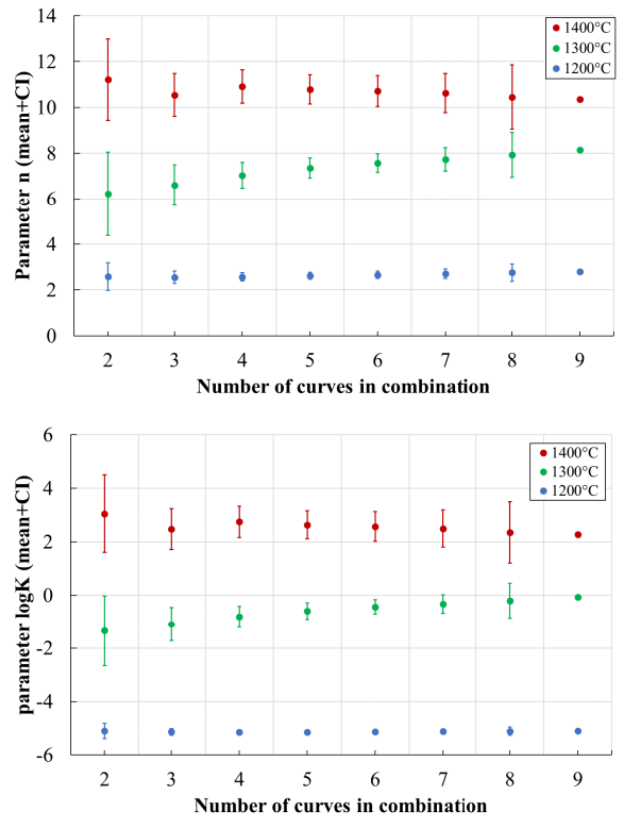


Fig. 7: Uniaxial tensile secondary creep parameters n and $\log K$ of different datasets for different temperature (with confidence intervals)

icantly. The mean value of tensile creep parameters n and $\log K$ increased with the temperature, whilst for compressive ones, the mean value of n was higher for 1400 °C and similar for 1300 °C and 1500 °C, and the mean value of $\log K$ was higher for 1500 °C and similar for 1300 °C and 1400 °C. It suggested that the compressive creep resistance of the alumina spinel refractory decreased more from 1300°C to 1400°C than from 1400°C to 1500°C.

For better comparison of the datasets, ninety-nine percent confidence intervals were calculated according to Eq. (2) for all datasets of two parameters, which were shown in figures 7 and 8 for all temperatures and tensile as well as compressive creep regimes, respectively. Datasets with shorter confidence interval suggest a closer proximity to the mean value of the whole population and a better sampling for the input data. Considering all cases, i.e., all parameters for all temperatures, all creep stages and both loading regimes; it was observed that combined curve numbers of 5, 6 or 7 had minimum confidence intervals. According to Eq. (2), three factors influenced the confidence interval: t , standard deviation and dataset size, which contributed to lower confidence intervals for datasets with combined 5, 6 and 7 curves.

Considering the dataset with combined 9 curves as a reference, for tensile creep parameters, figure 7 showed that parameters n and $\log K$ of this dataset lied in the confidence intervals of all other datasets at 1200°C and 1400°C; whilst they lied only in the confidence intervals of the datasets with combined 7 and 8 curves at 1300°C. For compressive creep, at 1300°C and 1500°C, parameters n and $\log K$ of the dataset with combined 9 curves lied in the confidence intervals of all other datasets; whilst they lied in the confidence intervals of the datasets with more than 5 combined curves at 1400°C.

Finally, to account for the heterogeneity of the material, the creep parameters obtained from the dataset with combined 7 curves were

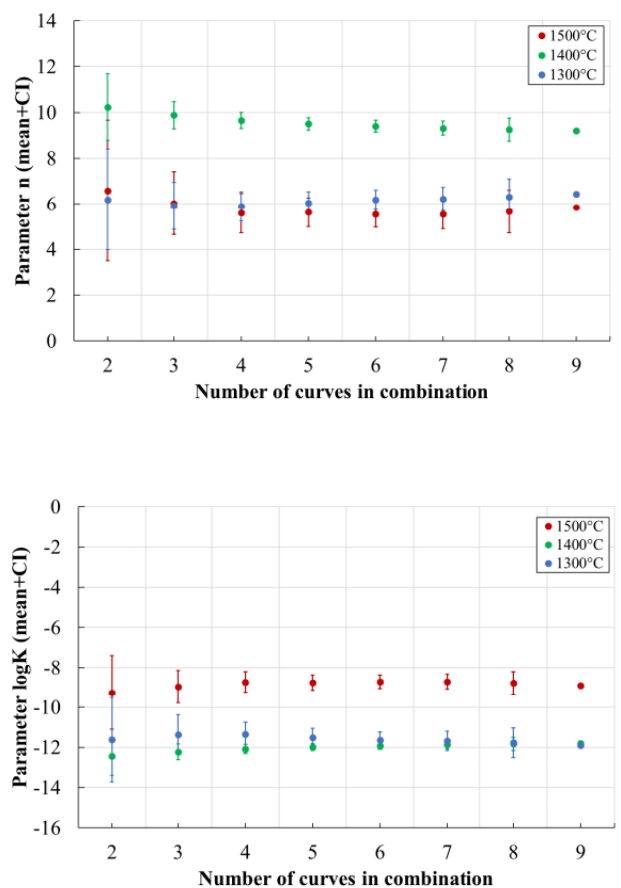


Fig. 8: Uniaxial compressive secondary creep parameters n and $\log K$ of different datasets for different temperature (with confidence intervals)

recommended for applications, as it showed a short confidence interval, and all parameters of the dataset with combined 9 curves lied in its confidence interval for all temperatures, in different creep stages and both loading regimes. The creep parameters for the primary and secondary stages from dataset with combined 7 curves were reported in table 3 and 4, respectively. Comparing the tensile and compressive creep parameters at 1300°C and 1400°C showed that all creep parameters were higher in the case of tensile creep, which confirmed the high asymmetry in the creep behavior of the alumina spinel refractory. Higher values of n in the case of tensile creep parameters explained why there was a high sensitivity to the load magnitude in tensile creep measurements, since n is the exponent of the stress in Eq. 1. Additionally, higher standard deviations for tensile creep parameters at the same temperatures leads to the conclusion that the tensile creep behavior is more influenced by the heterogeneity of the material microstructure.

Tab. 3: Compressive and tensile primary creep stage parameters at different temperatures with corresponding standard deviations.

	Temperature (°C)	n	a	Log (K[MPa ^{n} s ⁻¹])
Compressive creep parameters	1300	4.24 ± 0.22	- 2.72 ± 0.07	- 14.37 ± 0.25
	1400	5.88 ± 0.68	- 2.65 ± 0.24	- 13.75 ± 0.70
	1500	2.02 ± 0.55	- 1.93 ± 0.10	- 9.73 ± 0.44
Tensile creep parameters	1200	2.94 ± 0.82	- 1.01 ± 0.40	- 8.40 ± 1.31
	1300	5.72 ± 1.45	- 1.75 ± 0.34	- 7.56 ± 2.10
	1400	7.65 ± 1.42	- 1.90 ± 0.36	- 5.87 ± 1.97

Tab. 4: Compressive and tensile secondary creep stage parameters at different temperatures with corresponding standard deviations.

	Temperature (°C)	n	Log(K[MPa ^{n} s ⁻¹])
Compressive creep parameters	1300	6.22 ± 1.11	- 11.68 ± 1.05
	1400	9.32 ± 0.67	- 11.87 ± 0.44
	1500	5.54 ± 1.38	- 8.70 ± 0.82
Tensile creep parameters	1200	2.61 ± 0.65	- 5.14 ± 0.30
	1300	7.44 ± 1.70	- 0.53 ± 1.16
	1400	10.83 ± 2.77	2.67 ± 2.26

CONCLUSIONS

In the current paper, the influence of the heterogeneity in refractories on their common asymmetric creep behavior was investigated with the aid of a statistical analysis approach. Fifty-four uniaxial compressive and tensile creep tests at three different temperatures were performed on randomly chosen specimens drilled out of bricks

within the same batch. Low creep strains, short primary creep stage and significant secondary creep stage were the characteristics of the tensile creep behavior, while a noticeable primary creep stage and higher creep strains for the compressive creep curves.

Afterwards, the inverse evaluation of the Norton-Bailey creep parameters was done for various combinations of creep curves at three temperatures, two loading regimes, and primary and secondary creep stages. By comparing the 99% confidence intervals, the creep parameters evaluated from the dataset with combined 7 curves out of 9 curves was approved to be reasonable representative accounting for the material heterogeneity. The mean values and standard deviations of creep parameters at different temperatures were reported for both primary and secondary creep stages of uniaxial tensile and compressive creep behavior to be used in numerical simulation of the industrial linings.

ACKNOWLEDGEMENTS

This work was supported by the funding scheme of the European Commission, Marie Skłodowska-Curie Actions Innovative Training Networks in the frame of the project ATHOR – Advanced ThermoMechanical multiscale mOdelling of Refractory linings 764987 Grant.

REFERENCES

- [1] Schachner S, Jin S, Gruber D, Harmuth H. Three stage creep behavior of MgO containing ordinary refractories in tension and compression. *Ceram int.* 2019 May; 45(7-B):9483–90.
- [2] Dusserre G, Valentin O, Nazaret F, Cutard T. Experimental and numerical investigation of the asymmetric primary creep of a fibre reinforced refractory concrete at 1200 °C. *J Eur Ceram Soc.* 2016 Aug; 36(10):2627–39.
- [3] Blond E, Schmitt N, Hild F, Blumenfeld P, Poirier J. Modelling of high temperature asymmetric creep behavior of ceramics. *J Eur Ceram Soc.* 2005 Jul; 25(11):1819–27.
- [4] Samadi S, Jin S, Gruber D, Harmuth H, Schachner S. Statistical study of compressive creep parameters of an alumina spinel refractory. *Ceram Int.* 2020 Jul; 46(10-A):14662–8 (2020).
- [5] Hubalkova J, Stoyan D. On a qualitative relationship between degree of inhomogeneity and cold crushing strength of refractory castables. *Cem Concr Res.* 2003 May; 33(5):747–53.
- [6] Bakunov VS, Belyakov AV. Role of structural characteristics in high-temperature creep of ceramics. *Refract Ind Ceram.* 2000 Sep; 41:349–355.
- [7] Jin S, Harmuth H, Gruber D. Compressive creep testing of refractories at elevated loads—Device, material law and evaluation techniques. *J Eur Ceram Soc.* 2014 Dec; 34(15):4037–42.
- [8] Mammari AS, Gruber D, Harmuth H, Jin S. Tensile creep measurements of ordinary ceramic refractories at service related loads including setup, creep law, testing and evaluation procedures. *Ceram Int.* 2016 May 1; 42(6), 6791–9.
- [9] Boyle JT, Spence J. *Stress analysis for creep.* England: Butterworths; 1983.
- [10] Marquardt DW. An algorithm for least-squares estimation of nonlinear parameters. *J Soc Ind.* 1963; 11:431–441.
- [11] Montgomery CD. *Design and analysis of experiments.* Wiley; 2017.



A comparison of two damage models for inverse identification of mode I fracture parameters: Case study of a refractory ceramic

Soheil Samadi, Shengli Jin*, Dietmar Gruber, Harald Harmuth

Ceramics, Montanuniversitaet Leoben 8700, Austria

ARTICLE INFO

Keywords:

Damaged elasticity
Finite element analysis
Wedge splitting test
Ceramics

ABSTRACT

Fracture behavior of refractories influences their durability in high-temperature applications to a great extent. The fictitious crack model has been used for simulation of the fracture process of refractories and concrete materials. The present study investigates the effect of the lower post-failure stress limit of the softening law in the fictitious crack model by comparing an in-house developed subroutine for damaged elasticity model with the concrete damaged plasticity model implemented in Abaqus. The numerical wedge splitting tests show that in the case of brittle materials, the lower post-failure stress limit defined in the concrete damaged plasticity model resulted in energy consumption for crack propagation exceeding the defined fracture energy (114% higher in the case of a brittleness number of 4.4). Therefore, the developed damaged elasticity model allows for a more accurate simulation of fracture since the lower post-failure stress limit was decreased to 0.0001% of the tensile strength. Moreover, an inverse evaluation of the fracture parameters of an alumina spinel refractory material supported the developed model.

1. Introduction

Refractories are composite ceramic materials often used as lining materials in various high-temperature industrial vessels. In service, they experience thermal gradients and recurring thermal shocks, which could generate significant stresses resulting in tensile failure of materials. For instance, tensile stresses are generated in a distance from the hot face of the working lining of a steel ladle by the hot thermal shock and at the hot face by the cold thermal shock [1,2].

The wedge splitting test (WST) according to Tschegg [3] was well applied to determine the tensile behavior of refractories and concretes in laboratories because it offers stable crack propagation in relatively large specimens and allows for well development of a fracture process zone (FPZ) [4–8]. The fictitious crack model proposed by Hillerborg [9] implicitly accounts for the softening behavior of materials. It depicts that the maximum transferred stress between two crack faces decreases monotonically with increasing the distance of these crack faces after the stress reaches the tensile strength of a material, as shown in Fig. 1. The contribution of different fracture mechanisms in FPZ to the fracture behavior are represented by the softening law. With properly defined parameters for the fictitious crack model, the tensile failure of concretes and refractories can be well simulated with finite element methods. Researches indicate that the softening curve in the fictitious crack model plays a major role in material behavior [10–14]. For instance, after inverse evaluation of WST results on concrete, Skoček and Stang [11] and

Que and Tin-Loi [12] reported that with increasing the number of linear parts in the multi-linear softening law, the ultimate displacement in the softening law and the accuracy of the fit increased. Several research studies on concrete and refractory materials used and proposed bi-linear softening laws as an adequately accurate option; the ultimate displacement in concrete with steel fiber is often one order of magnitude larger than plain concretes, and two orders of magnitude larger than for refractory materials. In addition, concrete with steel fiber manifests less brittle behavior compared to plain concretes and refractories [10–20]. These observations indicate that the ultimate displacement of a softening law is an essential figure of merit in describing the brittleness of materials and defining their tensile failure behavior by finite element modeling.

Concrete damaged plasticity model (CDP) implemented in the commercial software Abaqus [21], which includes the fictitious crack model, was used to inversely determine the tensile strength, total fracture energy, and softening laws for concretes [22] and refractories [14–18]. However, it defines a lower limit of the post-failure stress, i.e. 1% of the tensile strength, to avoid computational instability [21]. That is to say, the stress experienced by two crack faces at the ultimate displacement does not drop to zero [22]. This definition could affect the inverse determination of tensile strength and total fracture energy, especially in the case of materials with high brittleness.

To investigate the influence of the critical residual force on the inverse estimation of tensile fracture properties, a damaged elasticity model (DE) was developed and implemented in a subroutine to model

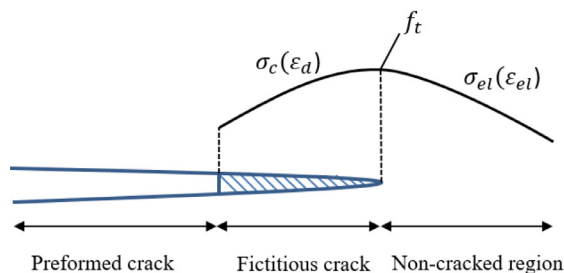
* Corresponding author.

E-mail address: shengli.jin@unileoben.ac.at (S. Jin).

Nomenclature

A	Fracture surface
b	Width of the ligament
B	Brittleness number evaluated using inversely estimated parameters
B'	Brittleness number evaluated using the experimental parameters
E_0	Initial Young's modulus
E_d	Damaged Young's modulus
E'	Measured Young's modulus
f_t	Tensile strength
F_V	Vertical force
F_H	Horizontal force
$F_{H,max}$	Maximum horizontal force
G_f	Total fracture energy
G_f'	Specific fracture energy calculated from experimental curves
G_f''	Specific fracture energy calculated from simulated curves
h	Height of the ligament
l	Characteristic dimension of the specimen
R_1	Ratio of the stress at transition point to the tensile strength in bilinear softening law
R_2	Ratio of the strain at transition point to the ultimate damage strain in bilinear softening law
y	Vertical distance from the loading position to the center of the ligament
α	Wedge angle
δV	Vertical displacement
$\delta V_{,ult}$	Ultimate vertical displacement
δ_H	Measured horizontal displacement
ϵ_{el}	Elastic strain
ϵ_d	Damage strain
$\epsilon_{d,ult}$	Ultimate damage strain
σ_c	Post-peak maximum transferred stress
σ_{el}	Elastic stress
σ_{ult}	Lower post-failure stress limit
σ_{NT}	Nominal notch tensile strength
$CELENT$	Characteristic length of element

the mode I fracture of refractories using the fictitious crack model principle [23]. In this model, the lower limit for the post-failure stress was decreased to 0.0001% of the tensile strength. The DE models, with linear and bilinear softening laws, were tested and verified, using a single unit element. Afterwards, the influences of DE and CDP models on the ratios of nominal notch tensile strength to pure tensile strength and specific fracture energy to total fracture energy were studied by modeling



the WST with different combinations of arbitrary material parameters. Additionally, a case study of a shaped alumina spinel refractory was carried out with both models for inverse identification of room temperature tensile fracture properties.

2. Methodology

2.1. Damaged elasticity model

The DE model defining the fictitious crack model, according to Hillerborg [9], consists of elastic behavior and softening one (Fig. 1). When the maximum tensile stress reaches the tensile strength (f_t) of a material, the damage initiates. The maximum sustainable stress by damaged elements decreases monotonically with increasing tensile damage strain, following a specified softening curve as the failure criterion in the Eq. (1).

$$\sigma \leq \sigma_c(\epsilon_d) \quad (1)$$

where σ is the tensile stress, σ_c the maximum transferred stress that is a function of the damage strain ϵ_d . Various softening laws can be defined for σ_c ; in the current study, linear and bilinear softening laws were defined as shown in Fig. 2 and compared together. The current model does not consider hardening and failure under compression, which are available in CDP of Abaqus.

In Fig. 2-a, DE model with linear softening law was illustrated, where E_d denotes the damaged Young's modulus and σ_{ult} is the lower post-failure stress limit after damage. The model parameters to be defined for a linear softening law were: tensile strength f_t , fracture energy G_f , and initial Young's modulus E_0 . Fig. 2-b illustrates DE model with bilinear softening law. Additional two parameters were necessary for the model definition: R_1 , the ratio of the stress at the transition point of a bilinear curve to the tensile strength, and R_2 , the ratio of the strain at the transition point of a bilinear curve to the ultimate damage strain ($\epsilon_{d,ult}$).

Two differences occur in the applications of DE and CDP models for the tensile failure modeling of the present study. Firstly, σ_{ult} was 1% of f_t in CDP model; in contrast, 0.0001% of f_t in DE model. Secondly, no damage variable was defined in CDP model, and thus the Young's modulus of material will stay constant; whilst in DE model the instantaneous Young's modulus of material changes with respect to the evolution of post-peak stress, assuming no irreversible displacement remains. Both models were tested using a single element to observe the differences.

An additional important factor in using DE and CDP models for mode I fracture simulation is the effect of element size and shape. To eliminate the element size effect on the consumed energy, in the formulation of the ultimate damage strain of a softening curve, fracture energy (G_f) is divided by a parameter termed as characteristic element length ($CELENT$) [21], whose definition depends on the element type and shape. In the case of a linear two-dimensional element used in the present study,

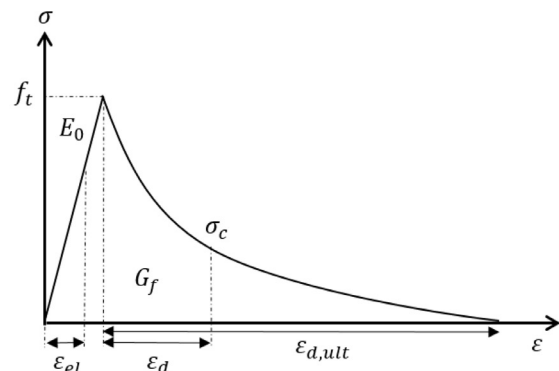


Fig. 1. Fictitious crack model [13].

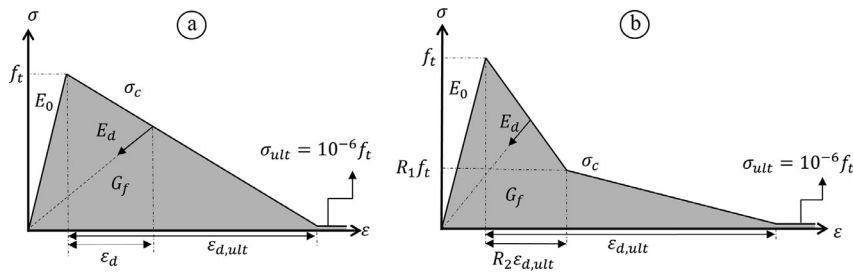


Fig. 2. DE model with (a) linear softening law and b) bilinear softening law.

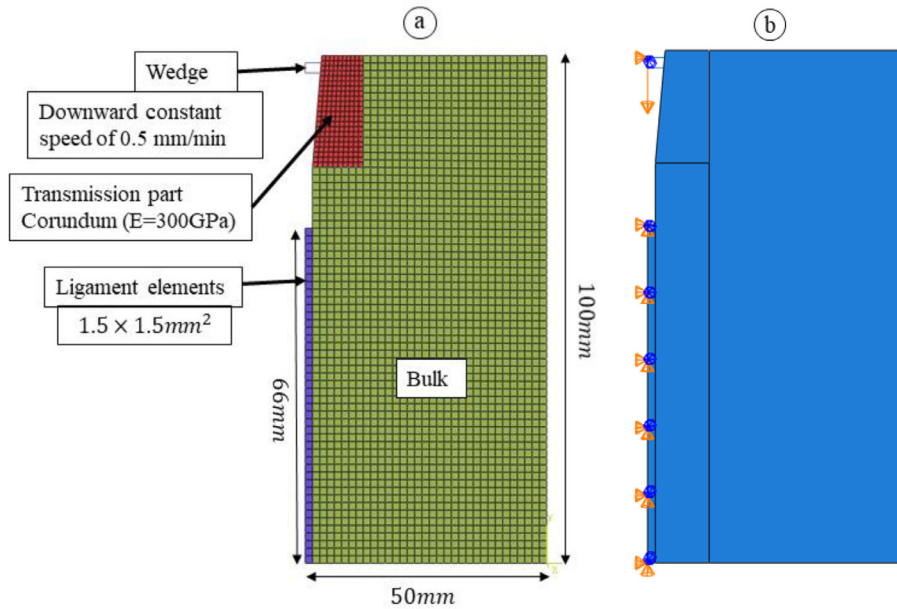


Fig. 3. (a) 2D and symmetrical model of the WST [14] (b) model boundary conditions.

it is equal to the root of the element area (Eq. (2)). This parameter is calculated by Abaqus and provided to the subroutine.

$$CELENT = \sqrt{Area_{element}} \quad (2)$$

When a linear softening law is applied, the ultimate damage strain is calculated using Eq. (3).

$$\epsilon_{d,ult} = \frac{2\left(G_f - \frac{f_t^2}{2E_0} \cdot CELENT\right)}{f_t \cdot CELENT} \quad (3)$$

In the case of the bilinear softening curve, the ultimate damage strain is calculated using the following formula:

$$\epsilon_{d,ult} = \frac{2\left(G_f - \frac{f_t^2}{2E_0} \cdot CELENT\right)}{f_t \cdot (R_1 + R_2) \cdot CELENT} \quad (4)$$

The fracture energy is the energy necessary for separation of the cracking edges, and in the case of elements with unit aspect ratio, the cracking edge size equals the element edge size. If other element shapes, such as triangular or rectangular elements, must be used in a model, different mechanical results might be received. The influences of different element shapes on the force-displacement curves were discussed in the Section 3.2.

2.2. Design of wedge splitting test modeling

According to the actual experiment design, 2D model of a half WST specimen was modeled with the size of $100 \times 50 \text{ mm}^2$, and with a ligament of $1.5 \times 66 \text{ mm}^2$ (Fig. 3-a). The model was meshed using linear plane strain square elements, called CPE4 in Abaqus, with the edge

Table 1

Material properties considered for the simulation.

Property	Level 1	Level 2	Level 3	Level 4
Young's modulus (GPa)	30	60	90	
Fracture Energy (N/m)	200	400	700	
Tensile strength (MPa)	1	5	10	20

size of 1.5 mm. A trapezoid was used to represent the transmission part made of corundum with 300 GPa Young's modulus. The transmission part was meshed with quadratic plane strain elements, called CPE8, with the overall size of 1 mm. This smaller and quadratic mesh was to avoid fluctuations in the load displacement curve since this part is in contact with the wedge. The wedge was modeled as an analytical rigid part. Frictionless contacts were defined between the wedge and the transmission part, as well as between the transmission part and the specimen. Loading and boundary conditions are shown in Fig. 3-b. The edge on the left side of ligament was completely fixed, and the wedge moved downwards with a constant speed of 0.5 mm/min similar to the experiment. Additionally, sensitivity analyses were performed on the wedge speed and element shape and size.

DE and CDP models were assigned to the ligament elements, and elastic behavior was assigned to the remaining bulk part, in order to guide the macroscopic crack to propagate in the ligament as it is observed in the WST experiment. A full combination of properties defined in Table 1 yields 36 arbitrarily defined materials. For the general comparison study of CDP and DE models, linear softening law was considered. The simulations were performed till the wedge arrives at the end

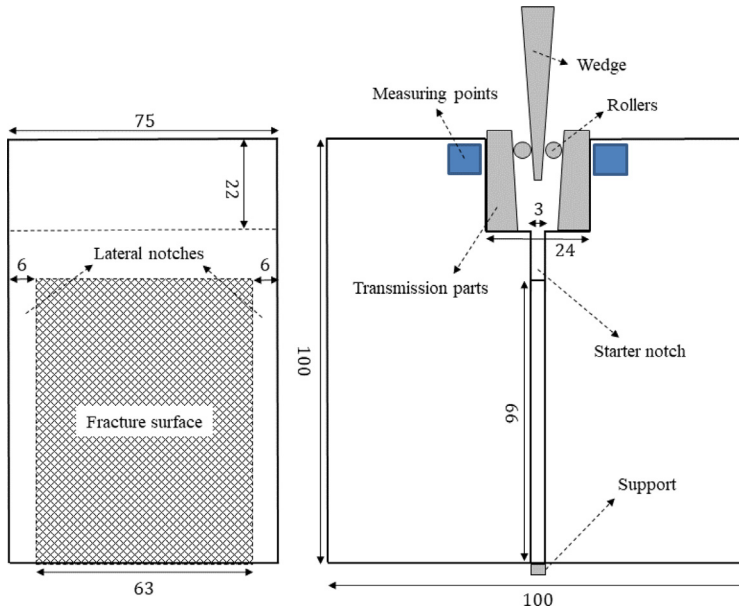


Fig. 4. Schematic representation of the WST specimen with dimensions (all numbers are in mm).

of the load transmission part, and the ultimate vertical displacement ($\delta_{v,ult}$) of the wedge was 16.7 mm.

After the simulations, the specific fracture energy (G_f'') was calculated using Eq. (4), which is the integration of the force-displacement curve with respect to the vertical displacement divided by the fracture area.

$$G_f'' = \frac{1}{A} \int_0^{\delta_{v,ult}} F_V d\delta_V \quad (4)$$

where F_V is the vertical force, δ_V denotes the vertical displacement of the wedge, and A denotes the fracture surface, which is $63 \times 66 \text{ mm}^2$. Additionally, based on the assumption of linear stress distribution in the ligament surface, the nominal notch tensile strength was calculated using Eq. (5) [24].

$$\sigma_{NT} = \frac{F_{H,max}}{bh} \left(1 + \frac{6y}{h} \right) \quad (5)$$

where b and h are the width and the height of the ligament, and y stands for the vertical distance from the loading position to the center of the ligament, and $F_{H,max}$ is the maximum horizontal force. Later, the ratios of the nominal notch tensile strengths received from DE and CDP models to the input tensile strength in the model were calculated and compared, as well as the ratios of the calculated specific fracture energy (G_f'') to the total fracture energy (G_f).

2.3. Case study

Alumina spinel refractory, which often works as the working lining material in the steel ladle of the steel industry, was chosen for the case study. Alumina spinel refractory bricks, which consist of 94 wt% alumina, 5 wt% of magnesia and 1 wt% of other oxides such as, silica and iron oxide, were cut into required dimensions for wedge splitting tests as shown in Fig. 4. The bulk density of bricks was 3.13 g/cm^3 , and open porosity was 19 vol%. The notches (one starter notch and two lateral notches) were cut on the specimen using an electrical circular saw with specific precautions to avoid cracking the specimen. They are designed to assure that crack propagates in the middle part of the specimen. Three specimens (cut out of three different bricks from the same batch) were tested at room temperature (termed RT in this paper), which follows the specimen number requirement of refractory testing standards.

A new testing apparatus for WST was designed and used in Ref. [18] for tests at various temperatures with laser speckle system for horizontal displacement measurement. Fig. 4 shows the specimen and loading components, i.e., one wedge, two rollers and two transmission parts. In the WST model (Fig. 3), the two rollers were not modeled to reduce the complexity of contact definition. After fixing the specimen with load transmission elements in the testing device, the wedge was pushed down with a speed of 0.5 mm/min. The former study showed that the fracture parameters of various refractory materials are not affected by the loading rate at room temperature and the fracture energy is representatively measured with the present specimen size [4].

The horizontal displacement measurement was done on both sides of the specimen at the measuring points shown in Fig. 4. The vertical force (F_V) was measured with a load cell, and the horizontal force (F_H) was calculated using Eq. (6).

$$F_H = \frac{F_V}{2 \tan \frac{\alpha}{2}} \quad (6)$$

where α is the wedge angle, which was 10° in this experiment. More details about the testing apparatus can be found in Ref. [18].

After the tests, the experimental fracture parameters, including specific fracture energy (G_f') and nominal notch tensile strength (σ_{NT}) were evaluated. To prevent the wedge from touching the specimen, the test was stopped at 15% of the maximum load; the specific fracture energy was calculated to this point, using Eq. (7).

$$G_f' = \frac{1}{A} \int F_H d\delta_H \quad (7)$$

where F_H is the horizontal force and δ_H is the average of horizontal displacements on the rear and front sides of the specimen measured using the laser extensometers.

Afterwards, the test results were applied for an inverse evaluation with the CDP and DE model to determine the fracture parameters of alumina spinel shaped refractory by the means of the minimization algorithm NL2SOL, which is an adaptive nonlinear least-square algorithm implemented in the open source code DAKOTA [25]. Using this algorithm, the difference between the experimental curve and the simulation curve was minimized, and the final parameters were received. Finally, the inversely evaluated and the experimental fracture parameters were compared.

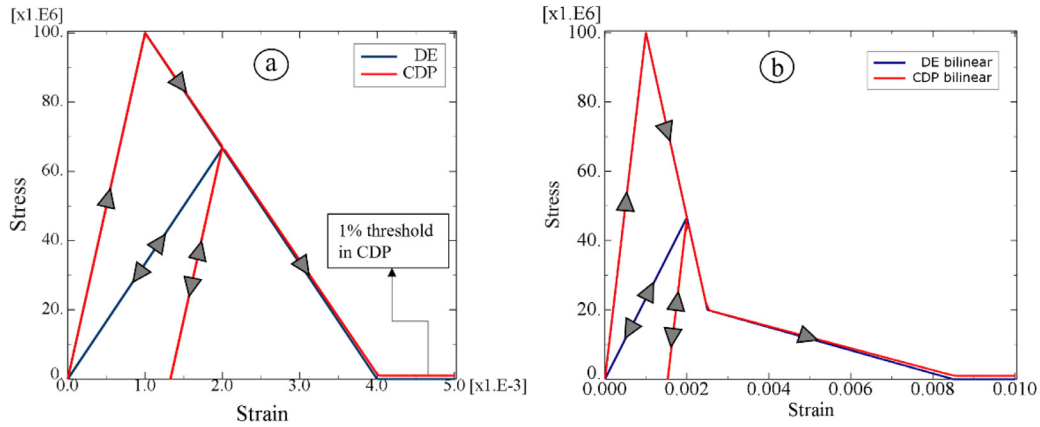


Fig. 5. DE and CDP models results on the single element model employing (a) linear softening law and (b) bilinear softening law.

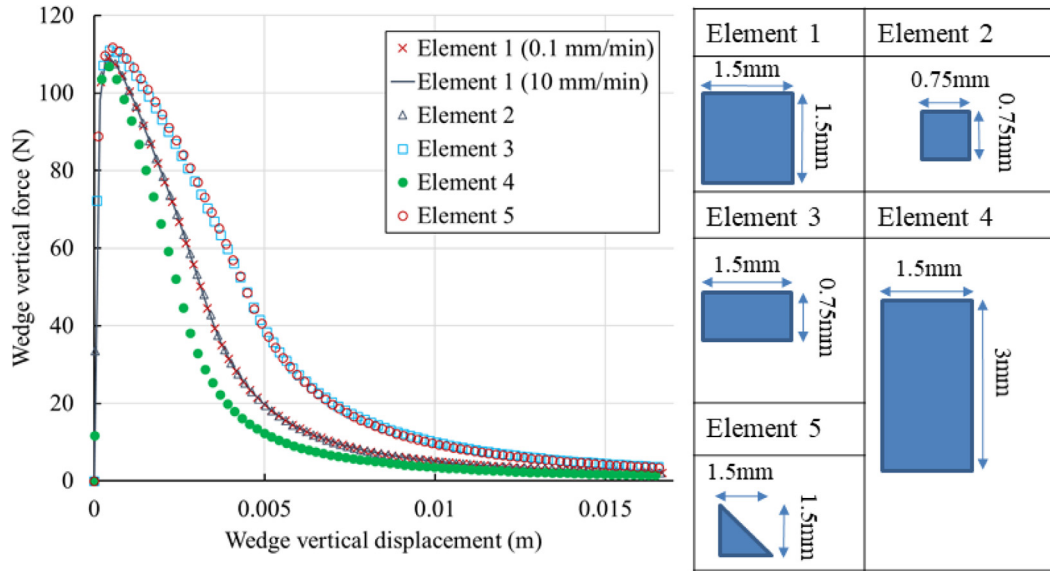


Fig. 6. Results of sensitivity analysis for different loading rates and various element shapes.

3. Results and discussion

3.1. DE tensile test modeling of single unit element

DE subroutines with linear and bilinear softening laws were tested with a single unit element model. As shown in Fig. 5, both DE and CDP models followed the same stress-strain path with the load increasing before damage started. Because in the DE model the stress/strain curve during unloading is governed by the decreasing Young's modulus, stresses and strains tended to null, whereas Young's modulus in the CDP model is constant, and the unloading stress path is parallel to the one before damage. Furthermore, the lower post-failure stress limit in the DE model was set to 0.0001% of the tensile strength. In contrast, CDP in Abaqus defines the lower post-failure stress limit with 1% of the tensile strength; in the investigated case, this gives a value of 1 MPa.

3.2. Parameter study using wedge splitting test modeling

Sensitivity of mechanical results on the loading rate and element size and shape were studied (Fig. 6). Firstly, the loading rate was changed from 0.1 mm/min to 10 mm/min for Element 1, and it had no influence on the mechanical result of the simulation, when time dependent material behavior was not considered in the model. Secondly, the square element size was changed from 1.5 mm (Element 1) to 0.75 mm (Ele-

ment 2), and the difference between the load-displacement curves from these two cases was not observed. Evident difference occurred when the element aspect ratio deviated from one, when the results of Elements 3 and 4 were compared to that of Element 1. Element 5 is a triangle mesh and has the same CELENT value (Eq. (2)) with Element 3. Therefore, its result was similar to the ones from Element 3.

In Fig. 7-a, the specific fracture energy (G_f') received from DE and CDP model results and the defined fracture energy (G_f) were compared with respect to different material brittleness numbers. The brittleness number was calculated using Eq. (8).

$$B = \frac{f_t^2 l}{G_f E_0} \quad (8)$$

where l is the characteristic dimension of the specimen, which in this case is 66 mm. It was observed that with increasing brittleness number, the ratio of received fracture energy to the defined one in the simulation increases with both models, but more significant with CDP model. For instance, for the material with the brittleness number of 1.47, the received fracture energy was about two times the defined fracture energy in the CDP model, but it was around the value of the defined fracture energy when DE model was applied.

Furthermore, the specific fracture energy was calculated until 15% of the maximum load since the experiments are normally stopped at this load. This procedure was applied for the numerical wedge splitting

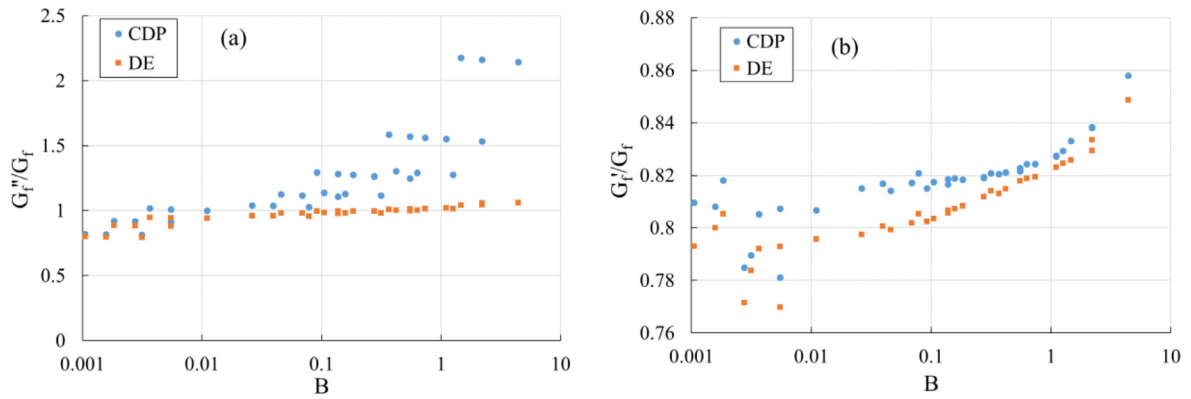


Fig. 7. The ratio of received fracture energy to defined fracture energy until (a) the end of the curve and (b) 15% of the maximum load from DE and CDP models for different brittleness numbers.

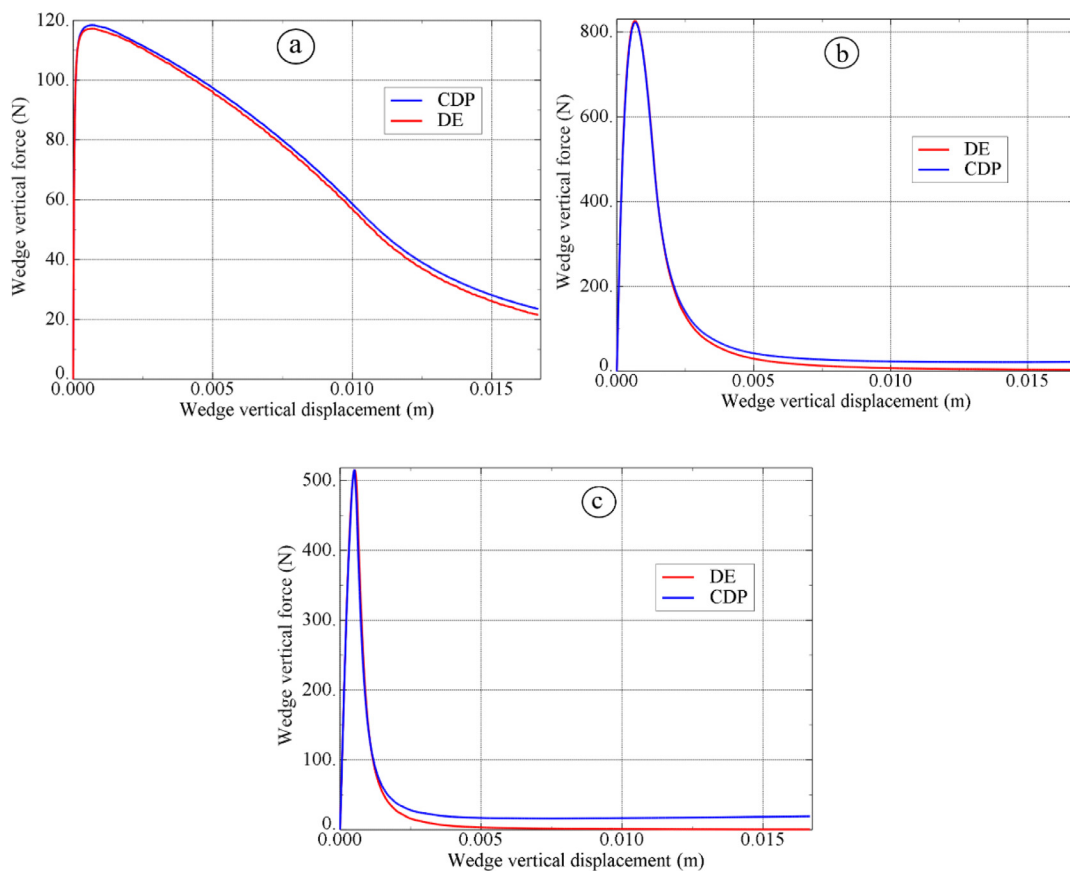


Fig. 8. Wedge horizontal force results of a material with (a) $B \approx 0.0015$, (b) $B \approx 0.15$ and (c) $B \approx 1.1$.

tests, which yields the specific fracture energy G_f' . As shown in Fig. 7-b, the difference of the ratio G_f''/G_f between DE and CDP models was less than 3%.

To understand the differences in energy ratios from the cases with DE and CDP models shown in Fig. 7-a, the simulation results for three materials with brittleness numbers of 0.0015, 0.15 and 1.1 were shown in Fig. 8-a, 8-b and 8-c, respectively. For materials with low brittleness ($B < 0.01$), the received fracture energy was lower than the defined fracture energy in both models ($G_f'' < G_f$) since more than half of the elements in the ligament were not fractured entirely and the residual force was evidently high when the wedge finished the sliding path. For instance, it was around 20% of the peak force in Fig. 8-a. For more brittle materials, like refractories, in the case of CDP model, the residual

force approached a constant value higher than null (Fig. 8-b and 8-c), and thus higher fracture energy was received from the simulated curve compared to the defined value ($G_f'' > G_f$). On the contrary, in the case of DE model, the consumed energy of the model was close to the defined fracture energy ($G_f'' \approx G_f$) (Fig. 7-a). Therefore, using CDP model in simulation of fracture behavior of materials could lead to higher consumption of energy in the model than defined and produce an error in inverse evaluation of material properties. Nevertheless, one should consider the influence of the brittleness number, the testing conditions and the softening law, which in this case was linear softening.

The ratio of nominal notch tensile strength to the tensile strength (σ_{NT}/f_t) was nearly the same in the cases with DE and CDP models for all the brittleness numbers (Fig. 9). As it was reported in the work of

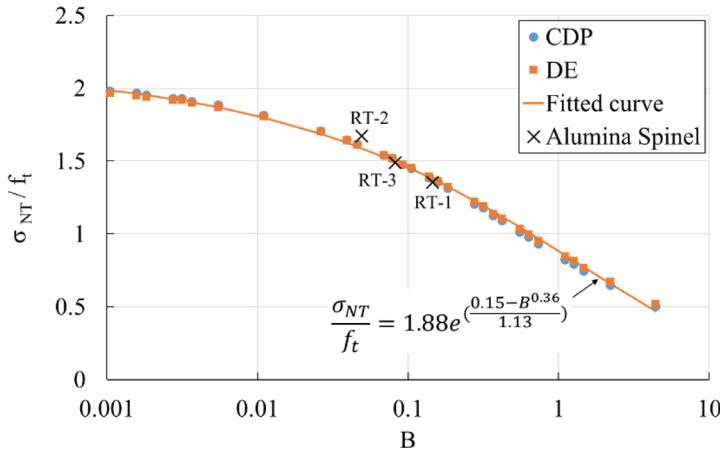


Fig. 9. The ratio of nominal notch tensile strength to the tensile strength in DE and CDP models for different brittleness numbers. The curve is fitted to the simulation results of DE model, and the results of alumina spinel were received by inverse estimation and inserted for comparison.

Table 2
Inverse evaluated fracture parameters using DE and CDP model.

	DE						CDP					
	G_f (N/m)	f_t (MPa)	E_0 (GPa)	R_1	R_2	$\epsilon_{d,ult}$	G_f (N/m)	f_t (MPa)	E_0 (GPa)	R_1	R_2	$\epsilon_{d,ult}$
RT-1	114.1	3.24	41.63	0.206	0.225	0.114	112.4	3.27	42.43	0.196	0.214	0.106
RT-2	159.6	2.64	58.20	0.186	0.376	0.134	155.6	2.63	59.00	0.214	0.389	0.140
RT-3	147.3	2.79	42.41	0.247	0.283	0.139	140.0	2.81	43.16	0.234	0.274	0.125
RT-Mean	140.3	2.89	47.41	0.215	0.292	0.129	136.0	2.90	48.19	0.213	0.295	0.124

Auer and Harmuth [24], the σ_{NT}/f_t ratio is influenced by the specimen geometry and material brittleness. For WST specimens, an equation was proposed for the relation between the σ_{NT}/f_t ratio and the brittleness number as shown in Eq. (9) [23].

$$\frac{\sigma_{NT}}{f_t} = ae^{\left(\frac{b-B^c}{d}\right)} \quad (9)$$

The constants a , b , c and d were evaluated by fitting the equation to the simulation results of DE model shown in Fig. 9, and their values were 1.88, 0.15, 0.36 and 1.13, respectively. There was a minor difference between these evaluated parameters and the ones from the study of Auer and Harmuth [24], which was caused by the differences in the dimensions of the model.

3.3. Case study results

The WST results of three different specimens and their inverse identified curves were shown in Fig. 10. The specimens were checked after the experiment, and the crack propagated in the ligament for all of them. The inverse identification of the model parameters was done considering linear and bilinear post-peak behavior, respectively. As it was observed, the models with linear post-peak behavior could not fit well to the experimental results; in this regard, studies also showed that bilinear and trilinear post-peak behavior generates better fittings to the experimental curves and further increase of number of linear parts introduces more parameters for identification, which brings about the risk of a local minimum [10–14]. The aim of this study is to compare DE and CDP models, and thus the inverse evaluated parameters of the models with bilinear softening law were compared in the Table 2.

In Table 2, it was shown that similar results were inversely evaluated from DE and CDP models and reducing the lower stress limit of the post-peak curve did not influence the result for the fracture energy, tensile strength and Young's modulus significantly. The inverse evaluated fracture energy of three specimens with CDP model was 1%–5% lower than that with DE model, and the tensile strength and Young's modulus of three specimens with CDP model were 1%–2% higher than those with DE model. The results were expected; as it was observed from the parameter study, the simulated load-displacement curves with

two models started to deviate from each other after 20% of the maximum force (Fig. 8). In addition, there was less than 3% difference in the specific fracture energy of the two models until 15% of the maximum load (Fig. 7-b), which was used as one threshold to terminate the wedge splitting tests in the laboratory. On the other hand, if the tests are allowed to be performed until the load approaches null, the CDP model would not be able to predict the exact fracture energy of the material. A relatively large difference can be observed on the determination of ultimate damage strain and transition points of stress and strain, which is 4%–13%. These differences were caused by the lower post-failure stress limit decrease in the DE model since they were not received when the same value (1% of f_t) was considered in the DE model.

Finally, the results of the model DE were compared with the experimental results in Table 3. The brittleness number B' was calculated using the experimental data according to Eq. (10).

$$B' = \frac{\sigma_{NT}^2 l}{G_f' E'} \quad (10)$$

Here, E' denotes the measured Young's modulus of the investigated material. The Young's modulus of three different specimens cut out of another brick from the same batch was measured using the ultrasonic method according to ASTM standard C597–09 [26]. The mean value and standard deviation were 38.72 GPa and 3.70 GPa, respectively. The inverse evaluated Young's modulus of the two WST specimens in RT1 and RT3 were in the range of the measurements, in contrary to the one from RT2. Giving that a high heterogeneity was reported for the investigated shaped alumina spinel refractory in the statistical study of Samadi, et al. [27], the difference between the inverse evaluated parameters and the ultrasonic measurement was expected.

The differences between inversely estimated and experimental received fracture parameters were shown in Table 3. The ratio of G_f' to G_f was in 77.1%–81.6%; significant differences were observed on the ratio of σ_{NT} to f_t and the ratio of B' to B , which were in 1.35–1.67 and in 2.46–5.18, respectively. The σ_{NT}/f_t ratios with respect to the brittleness number B were also added in Fig. 9. It was observed that the inversely estimated data fit well to the simulation results and the proposed equation.

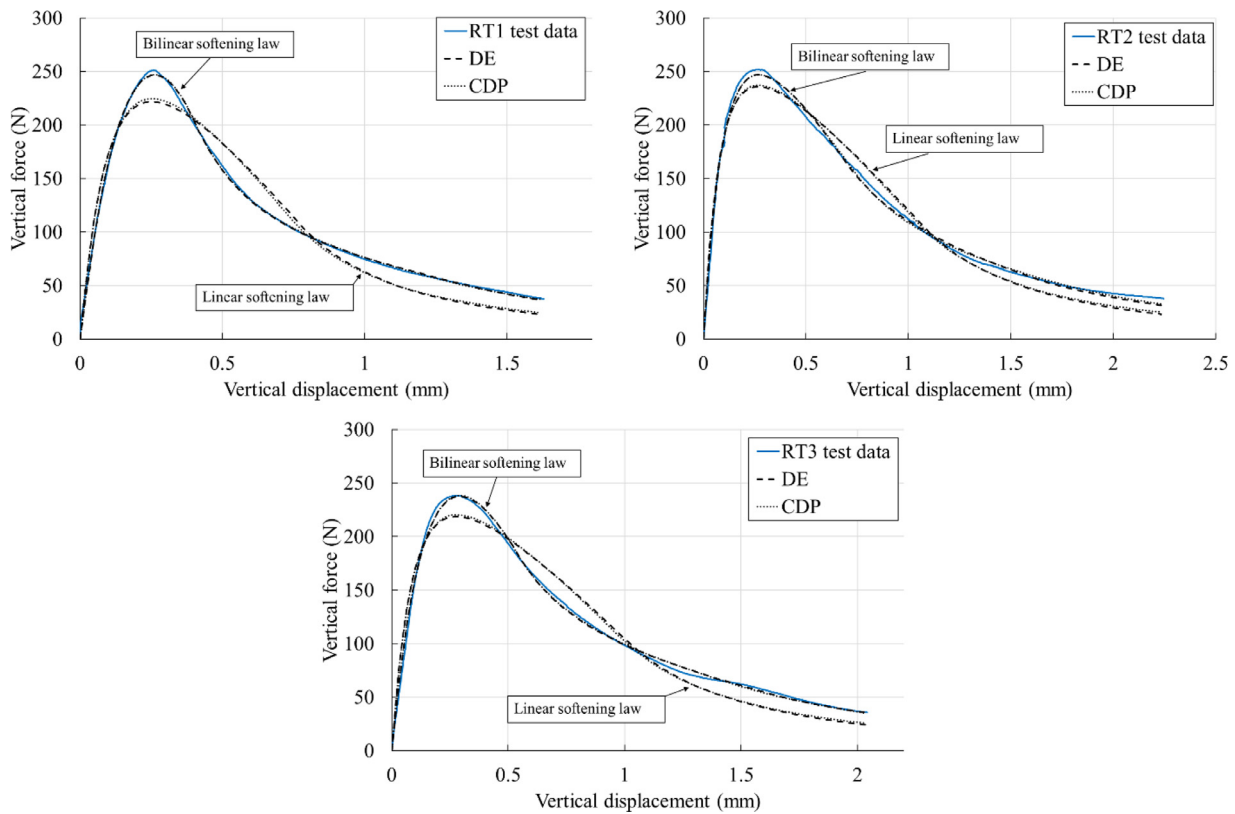


Fig. 10. Wedge splitting test results at room temperature with their inverse identified curves using DE and CDP models with linear and bilinear post-peak behavior respectively.

Table 3
Comparison of DE inverse evaluated and experimental fracture parameters.

	G_f' (N/m)	G_f (N/m)	$\frac{G_f'}{G_f}$ (%)	σ_{NT} (MPa)	f_t (MPa)	$\frac{\sigma_{NT}}{f_t}$	E_0 (GPa)	B'	B	$\frac{B'}{B}$
RT-1	91.2	114.1	79.9	4.39	3.24	1.35	41.63	0.359	0.146	2.46
RT-2	130.3	159.6	81.6	4.41	2.64	1.67	58.20	0.254	0.049	5.18
RT-3	113.6	147.3	77.1	4.15	2.79	1.49	42.41	0.259	0.082	3.16
RT-Mean	111.7	140.3	79.6	4.32	2.89	1.49	47.41	0.291	0.092	3.16
RT-STD	19.7	23.5	2.3	0.14	0.31	0.16	9.34	0.059	0.049	1.39

4. Conclusion

In the current study an improved damaged elasticity model, termed DE, was developed to investigate the effect of the lower post-failure stress limit in the softening law of a fictitious crack model on the simulated mode I fracture behavior of a wedge splitting test. It was confirmed that the in-house developed DE subroutine and the CDP model in Abaqus showed the same behavior during the tensile loading until the ultimate damage strain, after which, the lower post-failure stress limit in CDP model was limited to 1% of the tensile strength, but it was decreased to 0.0001% in DE model.

With the aid of the WST simulation and an arbitrary material database, it was observed that the results with CDP and DE models deviate after a drop from the maximum load dependent on the brittleness number, and CDP model arrived at a constant load higher than zero in contrary to the DE model. It was shown that the amount of energy consumed because of the larger lower post-failure stress limit leads to a large difference in the fracture energy calculation for brittle materials (up to 114% higher energy consumption in CDP model for a material with the brittleness number of 4.4). Additionally, the inversely evaluated fracture energies from the WST experiments on a shaped alumina spinel refractory were up to 5% higher, applying DE model. It was con-

cluded that stopping the tests at 15% of the maximum load does not provide enough experimental results to augment the difference in DE and CDP models.

In the case of tensile strength determination, both models yielded rather close results, and the ratio of nominal notch tensile strength to the pure tensile strength decreased monotonically with increasing brittleness number. Moreover, an equation for the ratio of the nominal notch tensile strength to the tensile strength was proposed to which the experimental results matched well.

Finally, it was concluded that the DE model is a more accurate mean for fracture simulation compared to the CDP model. Nevertheless, the extent of decreasing the lower post-failure stress limit impact on the fracture parameters identification depends on the brittleness of the defined material, the simulated experiment, and the employed softening law.

Declaration of Competing Interest

The authors declare that they have no known competing financial interests or personal relationships that could have appeared to influence the work reported in this paper.

CRediT authorship contribution statement

Soheil Samadi: Conceptualization, Methodology, Software, Validation, Formal analysis, Investigation, Writing - original draft, Visualization. **Shengli Jin:** Conceptualization, Validation, Writing - original draft, Writing - review & editing, Supervision. **Dietmar Gruber:** Validation, Writing - review & editing, Project administration. **Harald Harmuth:** Resources, Writing - review & editing, Funding acquisition.

Acknowledgements

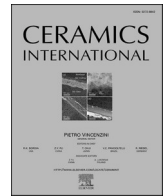
This work was supported by the funding scheme of the [European Commission](#), Marie Skłodowska-Curie Actions Innovative Training Networks in the frame of the project ATHOR - Advanced THERmomechanical multiscale modeling of Refractory linings [764987](#) Grant.

Supplementary materials

Supplementary material associated with this article can be found, in the online version, at doi:[10.1016/j.ijmecsci.2021.106345](https://doi.org/10.1016/j.ijmecsci.2021.106345).

References

- [1] Jin S, Gruber D, Harmuth H, Rössler R. Thermomechanical failure modeling and investigation into lining optimization for a Ruhrstahl Heraeus snorkel. *Eng Fail Anal* 2016;62:254–62. doi:[10.1016/j.engfailanal.2016.01.014](https://doi.org/10.1016/j.engfailanal.2016.01.014).
- [2] Gruber D, Harmuth H. Thermomechanical behavior of steel ladle linings and the influence of insulations. *Steel Res Int* 2014;85(4):512–18. doi:[10.1002/srin.201300129](https://doi.org/10.1002/srin.201300129).
- [3] Tschegg EK. Equipment and appropriate specimen shapes for tests to measure fracture values. *Austria Patent* 31 January 1986;390328.
- [4] Harmuth H, Rieder K, Krobath M, Tschegg EK. Investigation of the nonlinear fracture behaviour of ordinary ceramic refractory materials. *Mater Sci Eng* 1996;214:53–61. doi:[10.1016/0921-5093\(96\)10221-5](https://doi.org/10.1016/0921-5093(96)10221-5).
- [5] Harmuth H, Tschegg EK. A fracture mechanics approach for the development of refractory materials with reduced brittleness. *Fatigue Fract Eng Mater Struct* 1997;20(11):1585–603. doi:[10.1111/j.1460-2695.1997.tb01513.x](https://doi.org/10.1111/j.1460-2695.1997.tb01513.x).
- [6] Harmuth H. Stability of crack propagation associated with fracture energy determined by wedge splitting specimen. *Theor Appl Fract Mech* 1995;23:103–8. doi:[10.1016/0167-8442\(95\)00008-3](https://doi.org/10.1016/0167-8442(95)00008-3).
- [7] Tschegg EK, Fendt KT, Manhart Ch, Harmuth H. Uniaxial and biaxial fracture behaviour of refractory materials. *Eng Fract Mech* 2009;76:2249–59. doi:[10.1016/j.engfracmech.2009.07.011](https://doi.org/10.1016/j.engfracmech.2009.07.011).
- [8] Dai Y, Gruber D, Harmuth H. Observation and quantification of the fracture process zone for two magnesia refractories with different brittleness. *J Eur Ceram Soc* 2017;37(6):2521–9. doi:[10.1016/j.jeurceramsoc.2017.02.005](https://doi.org/10.1016/j.jeurceramsoc.2017.02.005).
- [9] Hillerborg A, Modeer M, Petersson PE. Analysis of crack formation and crack growth in concrete by means of fracture mechanics and finite elements. *Cem Concr Res* 1976;6:773–82. doi:[10.1016/0008-8846\(76\)90007-7](https://doi.org/10.1016/0008-8846(76)90007-7).
- [10] Slowik V, Villmann B, Bretschneider N, Villmann T. Computational aspects of inverse analyses for determining softening curves of concrete. *Comput Methods Appl Mech Eng* 2006;195(52):7223–36. doi:[10.1016/j.cma.2005.04.021](https://doi.org/10.1016/j.cma.2005.04.021).
- [11] Skoček J, Stang H. Inverse analysis of the wedge-splitting test. *Eng Fract Mech* 2008;75:3173–88. doi:[10.1016/j.engfracmech.2007.12.003](https://doi.org/10.1016/j.engfracmech.2007.12.003).
- [12] Que NS, Tin-Loi F. Numerical evaluation of cohesive fracture parameters from a wedge splitting test. *Eng Fract Mech* 2002;69:1269–86. doi:[10.1016/S0013-7944\(01\)00131-X](https://doi.org/10.1016/S0013-7944(01)00131-X).
- [13] Roelfstra, P.E., Wittmann, F.H. Numerical method to link strain softening with failure of concrete. In: Wittmann FH, editor. *Fracture toughness and fracture energy of concrete*. Amsterdam: Elsevier; p. 163–75 (1986).
- [14] Jin S, Gruber D, Harmuth H. Determination of Young's modulus, fracture energy and tensile strength of refractories by inverse estimation of a wedge splitting procedure. *Eng Fract Mech* 2014;116:228–36. doi:[10.1016/j.engfracmech.2013.11.010](https://doi.org/10.1016/j.engfracmech.2013.11.010).
- [15] Dai Y, Gruber D, Jin S, Harmuth H. Modelling and inverse investigation of the fracture process for a magnesia spinel refractory using a heterogeneous continuum model. *Eng Fract Mech* 2017;182:438–48. doi:[10.1016/j.engfracmech.2017.05.005](https://doi.org/10.1016/j.engfracmech.2017.05.005).
- [16] Fasching C, Gruber D, Harmuth H. Simulation of micro-crack formation in a magnesia spinel refractory during the production process. *J Eur Ceram Soc* 2015;35:4593–601. doi:[10.1016/j.jeurceramsoc.2015.08.012](https://doi.org/10.1016/j.jeurceramsoc.2015.08.012).
- [17] Gruber D, Sistaninia M, Fasching C, Kolednik O. Thermal shock resistance of magnesia spinel refractories - investigation with the concept of configurational forces. *J Eur Ceram Soc* 2016;36:4301–8. doi:[10.1016/j.jeurceramsoc.2016.07.001](https://doi.org/10.1016/j.jeurceramsoc.2016.07.001).
- [18] Stückelschweiger M, Gruber D, Jin S, Harmuth H. Wedge splitting test on carbon-containing refractories at high temperatures. *Appl Sci* 2019;9(16):3249. doi:[10.3390/app9163249](https://doi.org/10.3390/app9163249).
- [19] Pan L, He Z, Li Y, Li B, Jin S. Inverse simulation of fracture parameters for cement-bonded corundum refractories. *J Miner Met Mater Soc* 2019;71:3996–4004. doi:[10.1007/s11837-019-03750-y](https://doi.org/10.1007/s11837-019-03750-y).
- [20] Murthy AR, Karihaloo BL, Iyer NR, Raghu Prasad BK. Bilinear tension softening diagrams of concrete mixes corresponding to their size-independent specific fracture energy. *Constr Build Mater* 2013;47:1160–6. doi:[10.1016/j.conbuildmat.2013.06.004](https://doi.org/10.1016/j.conbuildmat.2013.06.004).
- [21] ABAQUS (2018) 'ABAQUS documentation', Dassault systems, Providence, RI, USA.
- [22] Sitek M, Adamczewski G, Szyszko M, Migacz B, Tutka P, Natorff M. Numerical simulations of a wedge splitting test for high-strength concrete. *Proc Eng* 2014;91:99–104. doi:[10.1016/j.proeng.2014.12.021](https://doi.org/10.1016/j.proeng.2014.12.021).
- [23] Samadi, S. UMAT subroutine code for damaged elasticity, Mendeley data, v1 (2020). [10.17632/nph64c5pvy.1](https://doi.org/10.17632/nph64c5pvy.1) </Dataset>
- [24] Auer T, Harmuth H. Numerical simulation of a fracture test for brittle disordered materials. In: *Proceedings of the 16th European Conference of Fracture*, Alexandroupolis, Greece; July 2006. p. 3–7. doi:[10.1007/1-4020-4972-2_293](https://doi.org/10.1007/1-4020-4972-2_293).
- [25] DAKOTA, User's Manual, Version 5.2, unlimited release, November 30; 2011.
- [26] *ASTM C 597-09 Standard test method for pulse velocity through concrete*. West Conshohocken, PA, USA: ASTM International; 2009.
- [27] Samadi S, Jin S, Gruber D, Harmuth H, Schachner S. Statistical study of compressive creep parameters of an alumina spinel refractory. *Ceram Int* 2020;46(10–A):14662–8. doi:[10.1016/j.ceramint.2020.02.267](https://doi.org/10.1016/j.ceramint.2020.02.267).



Combined damaged elasticity and creep modeling of ceramics with wedge splitting tests

S. Samadi, S. Jin^{*}, H. Harmuth

Chair of Ceramics, Montanuniversitaet, Leoben, 8700, Austria

ARTICLE INFO

Keywords:

Mode I fracture
Creep
Material constitutive model
Wedge splitting test

ABSTRACT

During the crack propagation in common refractory ceramics at high temperatures, creep may occur in the wake of a process zone and in front of a crack tip. To account for this phenomenon, an integrated material constitutive model was developed by combining the mechanical behavior following isotropic damaged elasticity concept and Norton-Bailey creep. The post peak fracture behavior followed the bilinear softening law and a simple criterion was defined to consider the creep asymmetricity in uniaxial tension and compression. The material constitutive model was applied to inversely identify mode I fracture parameters with wedge splitting tests of an alumina spinel material at 1200 °C. It showed that the mean ratio of the nominal notch tensile strength to the actual tensile strength was 1.93 and the mean pure fracture energy was 297.6 N/m. In addition, the creep contributed 12.9% on average into the total fracture energy.

1. Introduction

Modeling of cracking in quasi-brittle materials like concrete and refractories progressed greatly in recent years. Fictitious crack model proposed by Hillerborg [1] was successfully applied to reproduce the fracture phenomenon in refractory materials [2]. This model assumes that interfaces of one crack follow softening behavior caused by the micromechanical mechanisms in the fracture process zone (FPZ), for instance, microcrack initiation, crack branching, etc. Using this model, satisfactory results for fracture simulation of refractories at room temperature [2–4] were obtained.

From the micromechanical point of view, at elevated temperatures, creep could also occur in the wake and front of the FPZ [5]. In the case of fracture energy and tensile strength determination utilizing wedge splitting test (WST), creep contributes to the determined fracture energy and influences the inverse estimation of tensile strength. This was confirmed in the findings of Stückelschweiger et al. [4], in which it was assumed that crack propagates in the ligament area and creep occurs in the residual area of the specimen. The results showed the creep influence on the inversely evaluated fracture parameters; for instance, the inversely evaluated fracture energy was decreased between 15% and 47% when considering creep. Nevertheless, the creep in the FPZ was not considered. In addition, studies showed that the tensile failure and creep in the refractory linings of industrial metallurgical vessels could occur in

a complex manner, for instance, they can exist in the same areas of bricks, or alternatively in different areas [6–9]. Therefore, a material constitutive model considering tensile failure and creep that matches well to refractory materials behavior is necessary.

There have been several studies working on numerical approaches to model the interaction between creep and damage in concrete, mainly to predict concrete behavior in fire situations [10–14]. In these models, different active material constitutive phenomena are coupled in a series manner, i.e., the total strain tensor is decomposed into several terms at the same stress state, as shown in Eq. (1).

$$\bar{\epsilon}_{tot} = \bar{\epsilon}_{el} + \bar{\epsilon}_p + \bar{\epsilon}_{th} + \bar{\epsilon}_{tr} + \bar{\epsilon}_{cr} \quad (1)$$

Here, $\bar{\epsilon}_{tot}$ denotes the total 2nd order strain tensor. $\bar{\epsilon}_{el}$, $\bar{\epsilon}_p$ and $\bar{\epsilon}_{th}$ are the 2nd order elastic, plastic and thermal strain tensors, respectively, which are time-independent. The other two strain tensors are time-dependent, namely, the classical creep strain tensor ($\bar{\epsilon}_{cr}$) and the transient thermal creep strain tensor ($\bar{\epsilon}_{tr}$).

The classical creep strain is a term used for the time-dependent strain under constant stress and temperature, which occurs due to mechanical motion of particles and grains; the transient thermal creep strain [11], also called load-induced thermal strain in Ref. [12], is used for the strain measured on a loaded concrete in transient thermal conditions due to the changes in chemical composition and moisture concentration of concrete and is accounted only during the first heating cycle. Separation

^{*} Corresponding author.

E-mail address: shengli.jin@unileoben.ac.at (S. Jin).

Nomenclature			
A_c, m_c, n_c and A_t, m_t, n_t	Compressive and tensile creep parameters	y	Vertical distance from the loading position to the center of the ligament
b and h	Width and height of the ligament	α	Wedge angle
$\overset{\equiv}{\equiv}$		δ_v	Vertical displacement
$\overset{\equiv}{\equiv}$	Forth-order initial stiffness tensor	$\delta_{v,ult}$	Ultimate vertical displacement
$\overset{\equiv}{\equiv}$		δ_H	Measured horizontal displacement
$\overset{\equiv}{\equiv}$	Forth-order damage tensor	Δt	Time increment
D	Damage variable	$\Delta \varepsilon_{cr,t+\Delta t}$	Creep strain increment using the stress from last increment
E_0	Initial Young's modulus	$\Delta \varepsilon_{cr,t+\Delta t}'$	Creep strain increment using the updated stress
E_d	Damaged Young's modulus	$\overset{\equiv}{\equiv}_{tot}$	Second-order total strain tensor
f_t	Tensile strength	$\overset{\equiv}{\equiv}_{el}$	Second-order elastic strain tensor
F_V and F_H	Vertical and horizontal force	$\overset{\equiv}{\equiv}_p$	Second-order plastic strain tensor
$F_{H,max}$	Maximum horizontal force	$\overset{\equiv}{\equiv}_{th}$	Second-order thermal strain tensor
$F_{simulated}$	Simulated load	$\overset{\equiv}{\equiv}_{tr}$	Second-order transient thermal creep strain tensor
F_{exp}	$(\overline{F_{exp}})$ Experimental load (mean value)	$\overset{\equiv}{\equiv}_{cr}$	Second-order classical creep strain tensor
G_f	Total fracture energy inversely evaluated considering creep	$\overset{\equiv}{\equiv}_r$	Second-order reversible strain tensor
$G_{fno-creep}$	Total fracture energy inversely evaluated without considering creep	$\overset{\equiv}{\equiv}_{ir}$	Second-order irreversible strain tensor
G_f'	Specific fracture energy calculated from experimental curves	$\overset{\equiv}{\equiv}_d$	Second-order damage strain tensor
$\overset{\equiv}{\equiv}$		ε_d	Equivalent damage strain
$\overset{\equiv}{\equiv}$	Forth-order identity tensor	$\varepsilon_{d,ult}$	Ultimate equivalent damage strain
l	Characteristic dimension of the specimen	ε_{maxP}	Maximum principal strain
q	Equivalent von Mises stress	ε_{cr}	Equivalent creep strain
R_1	Ratio of the stress at the transition point to the tensile strength in bilinear softening law	$\dot{\varepsilon}_{cr}$	Equivalent creep strain rate
R_2	Ratio of the strain at the transition point to the ultimate damage strain in bilinear softening law	$\overset{\equiv}{\equiv}$	Second-order stress tensor
R^2	Degree of determination	$\sigma_{maxP}, \sigma_{midP}, \sigma_{minP}$	Maximum, middle, minimum principal stress
$RSME$	Root-mean-square error	σ_c	Post-peak maximum transferred stress
		σ_{ult}	Lower post-failure stress limit
		σ_{NT}	Nominal notch tensile strength
		$\overset{\equiv}{\equiv}_t$	Second-order deviatoric stress tensor at time t

of these two strains in concrete experiments is not feasible, because the classical creep strain can also occur during the first heating cycle [11–14]. The transient thermal creep strain rate is also a function of stress and temperature, and was represented with different formulations in different studies [15,16].

The microstructure damage is usually represented in the material constitutive models by degradation of stiffness matrix. For instance, in the Gernay et al. study [13], mechanical damage is defined with a 4th order damage tensor ($\overset{\equiv}{\equiv}$) in the stress-strain relation as follows:

$$\overset{\equiv}{\sigma} = \left(\overset{\equiv}{\overset{\equiv}{I}} - \overset{\equiv}{\overset{\equiv}{D}} \right) \overset{\equiv}{\overset{\equiv}{C}}_0 : \left(\overset{\equiv}{\overset{\equiv}{\varepsilon}}_{tot} - \overset{\equiv}{\overset{\equiv}{\varepsilon}}_p - \overset{\equiv}{\overset{\equiv}{\varepsilon}}_{th} - \overset{\equiv}{\overset{\equiv}{\varepsilon}}_{ir} \right) \quad (2)$$

where $\overset{\equiv}{\sigma}$ is the 2nd order stress tensor, $\overset{\equiv}{\overset{\equiv}{I}}$ is the 4th order identity tensor and $\overset{\equiv}{\overset{\equiv}{C}}_0$ denotes the initial 4th order isotropic linear elastic stiffness tensor. The mechanical damage was defined either isotropic [12] or orthotropic [14].

Different to concrete, shaped refractories are often burned at high temperatures to achieve sintering. Rather than the transient creep strain, the classical creep prevails in service, which is well reproduced by means of Norton-Bailey creep formulations [17–19]. Additionally, there is an evident asymmetry in creep of refractories, which is induced by their microstructure. Studies showed that refractories present higher creep resistance under compressive stresses compared to tensile ones [18–22]. In the case of refractory ceramics, the model of Blond et al. [22], has been successfully applied to represent the creep asymmetry. In this model, the stress tensor is decomposed to positive and negative parts based on principal stress vectors, and the associated deviatoric tensors are used to calculate the creep strain rate by using the one-dimensional

compressive and tensile creep parameters.

The current study aims to develop a material constitutive model that can be used for simulation of mode I fracture and creep in refractory materials. To this end, a model called DECR considering asymmetric creep behavior based on Norton-Bailey creep law and isotropic damaged elasticity was developed. The creep parameters of the material were obtained from previous studies employing uniaxial compressive and uniaxial tensile creep tests [20,21]. To account for the creep asymmetry, the absolute values of the principal stresses of each element were compared to allow the code automatically selecting the corresponding creep parameters under tension and compression. The application of this model in the simulation of WST at high temperature is to receive an insight into the influence of creep on the fracture property characterization. The manuscript was organized as follows: Firstly, DECR model was introduced and was tested using a single unit element; then, WST at 1200 °C was employed to compare the DECR model with the concrete damaged plasticity model (CDP) in Abaqus [23], and to inversely evaluate the tensile failure properties of an alumina spinel refractory, which is used as the working lining material in steel ladles. Finally, the validity of the asymmetric creep model criteria in the WST model was discussed in detail and the inversely evaluated fracture parameters were compared to the experimental ones.

2. Methodology

2.1. Damaged elasticity-creep model

A schematic of the damaged elasticity model, termed DE, developed in a previous study [24], is shown in Fig. 1. In this model, material behaves elastically until the maximum principal stress reaches the tensile strength; afterwards, it follows a softening curve, which is a function

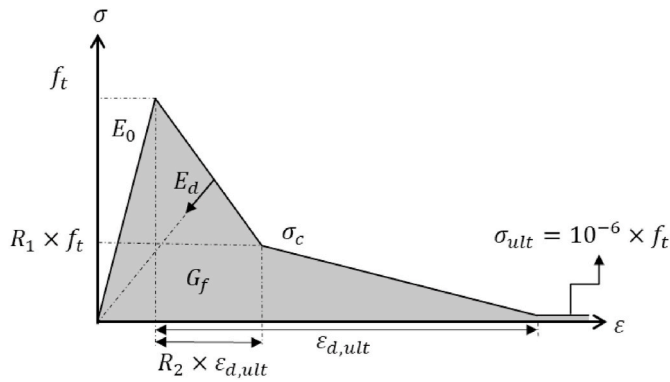


Fig. 1. DE model with bilinear softening law [23].

of equivalent damage strain (ϵ_d) (Eq. (3)).

$$\sigma_{\max P} \leq \sigma_c(\epsilon_d) \quad (3)$$

where $\sigma_{\max P}$ is the maximum principal stress, σ_c denotes the critical stress, which was chosen to be in a bilinear form in this case since its better fitting to experimental results was confirmed in previous studies [2,24]. The equivalent damage strain is a scalar calculated as follows:

$$\epsilon_d = \epsilon_{\max P} - \frac{f_t}{E_0} \quad (4)$$

where $\epsilon_{\max P}$ denotes the maximum principal strain, and E_0 and f_t are the initial Young's modulus and tensile strength, respectively. According to Fig. 1, the model parameters are the initial Young's modulus, tensile strength, fracture energy (G_f), and ratio constants R_1 and R_2 . The previous study showed that by decreasing the lower post-failure stress limit (σ_{ult}) to 0.0001% of the tensile strength, the accuracy of the model increased for WST simulation of brittle materials compared to the CDP model in which this value is 1% of the tensile strength [24]. The influence of the σ_{ult} on high temperature WST simulation was further investigated in the current study.

Due to the fact that the compressive strength of refractory materials is much higher than the tensile one [25], no failure is considered under compression in the model. Another underlying assumption is that the damage strain is reversible and only used for calculation of the damaged stiffness and the reduced tensile strength. Similar simplification was observed in the work of Pearce et al. [12]. Finally, the damage is considered isotropic, i.e. the same stiffness is assumed for all directions according to Eq. (5).

$$E_d = E_0(1 - D) \quad (5)$$

where E_d is the stiffness after damage, and D is the damage variable.

The creep model follows the Norton-Bailey type equation [26] and representation defined in the Abaqus software [23] in which the equivalent creep strain rate ($\dot{\epsilon}_{cr}$), which is a scalar, is a function of the equivalent von Mises stress (q) and the total scalar equivalent creep strain (ϵ_{cr}) as Eq. (6).

$$\dot{\epsilon}_{cr} = (Aq^n[(m + 1)\epsilon_{cr}]^m)^{\frac{1}{m+1}} \quad (6)$$

where A , n , and m are the creep parameters, which can be obtained using an inverse evaluation algorithm and creep experiments [27]. The equivalent von Mises stress is calculated using the following equation.

$$q = \sqrt{\frac{3}{2} \bar{\sigma} : \bar{\sigma}} \quad (7)$$

In the current study, only the primary creep stage was considered for the creep behavior of the material, which is plausible due to the comparably short duration of WST and intermediate temperature.

Asymmetric creep behavior was defined using the principal stresses according to the following specific criterion for WST simulation:

$$\sigma_{\max P} \geq \sigma_{\min P} \geq \sigma_{\min P} \rightarrow \begin{cases} \dot{\epsilon}_{cr} = (A_c q^{n_c} [(m_c + 1)\epsilon_{cr}]^{m_c})^{\frac{1}{m_c+1}} \text{ if } |\sigma_{\max P}| < |\sigma_{\min P}| \\ \dot{\epsilon}_{cr} = (A_t q^{n_t} [(m_t + 1)\epsilon_{cr}]^{m_t})^{\frac{1}{m_t+1}} \text{ if } |\sigma_{\max P}| \geq |\sigma_{\min P}| \end{cases} \quad (8)$$

where subscripts c and t are for compressive and tensile creep parameters, respectively. In the case that $\sigma_{\max P} = \sigma_{\min P} = \sigma_{\min P}$, the compressive or tensile case depends on the sign of principal stresses. The Yield surface of the model in two-dimensional principal stress space is shown in Fig. 2. This criterion is suitable for consideration of asymmetric creep in the simulation of wedge splitting test because the minimum and maximum principle stresses are in line with the loading direction in the FPZ, as it will be confirmed by showing the stress distribution in the results section. However, refractory materials could present more complicated stress state in service and further improvement of the model should be done for application in thermomechanical simulation of refractory lining.

Combination of damaged elasticity and creep is defined based on strain splitting assumption. The total strain tensor is decomposed into two parts (Eq. (9)), reversible ($\bar{\epsilon}_r$) and irreversible ($\bar{\epsilon}_{ir}$) strain tensors; the former one includes both elastic and damage strain ($\bar{\epsilon}_d$) tensors, and the latter one refers to the creep strain tensor.

$$\bar{\epsilon}_{tot} = \bar{\epsilon}_r + \bar{\epsilon}_{ir} = (\bar{\epsilon}_d + \bar{\epsilon}_{cr}) + \bar{\epsilon}_{cr} \quad (9)$$

After integrating Eq. (6), a forward explicit method is employed for calculation of the equivalent creep strain increment ($\Delta\epsilon_{cr,t+\Delta t}$) according to the following equation:

$$\Delta\epsilon_{cr,t+\Delta t} = \left[\left(\frac{Aq_t^n}{m+1} \right)^{\frac{1}{m+1}} \Delta t + \epsilon_{cr,t}^{\frac{1}{m+1}} \right]^{m+1} - \epsilon_{cr,t} \quad (10)$$

where the stress from the last increment (q_t) is used. Using a flow rule, the creep strain tensor is calculated as follows:

$$\bar{\epsilon}_{cr,t+\Delta t} = \bar{\epsilon}_{cr,t} + \bar{\epsilon}_{cr,t+\Delta t} \frac{\bar{\tau}_t}{q_t} \quad (11)$$

where $\bar{\tau}_t$ is the 2nd order deviatoric stress tensor at the beginning of the increment. Afterwards, the rest of the strain increment tensor is allocated to reversible strain tensor, which is used to calculate the damage

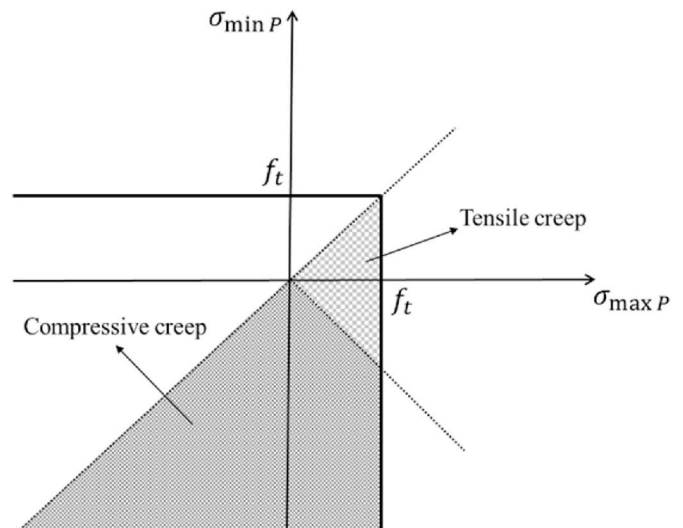


Fig. 2. Yield surface in the two-dimensional principal stress space.

variable and the stress tensor at the end of the increment ($\bar{\sigma}_{t+\Delta t}$). Using the updated von Mises stress after creep, a new equivalent creep strain increment ($\Delta \epsilon_{cr,t+\Delta t}$) is calculated (Eq. (10)), and an accuracy criterion is checked at the end of the increment according to Eq. (12). If the accuracy criterion is not met, the time increment is decreased to a shorter one; for instance, in the present study the time increment was reduced by a factor of 0.2.

$$\Delta \epsilon_{cr,t+\Delta t} - \Delta \epsilon_{cr,t+\Delta t} < 0.001 \quad (12)$$

The DECR model was developed in a Fortran subroutine format, which is used as a supplementary material for simulation in Abaqus software. For better understanding of the model, a flowchart of DECR model is shown in Fig. 3. Furthermore, the subroutine was tested using a single element model whose results will be shown in section 3.

2.2. Wedge splitting test and inverse evaluation of material parameters

The WST introduced by Tschegg [28] has been applied widely to characterize the tensile behavior of refractories because it enables stable crack propagation in relatively large specimens and allows for well development of a FPZ [29–33]. Alumina spinel refractory is a well-known refractory ceramic used mostly as the working lining material in iron and steel production. In the current study, alumina spinel refractory bricks, which consist of 94 wt% alumina, 5 wt% of magnesia and 1 wt% of other oxides such as, silica and iron oxide, were used to produce WST samples. For more information on the material microstructure, one could refer to Ref. [21]. The WST was performed on three specimens at 1200 °C employing the apparatus developed in Ref. [4]. In this experiment, after placing the specimen into the device, the heating started with the rate of 10 °C/min up to the desired temperature. After 1 h holding time for temperature homogenization in the specimen, the wedge started moving down with constant speed of 0.5 mm/min. The vertical load was measured using a load cell and horizontal displacement was measured on both sides of the specimen (on the area shown in Fig. 4) with a laser speckle measurement system.

Afterwards, the test results were used together with a 2-dimensional model of WST to inversely evaluate the fracture parameters of the shaped alumina spinel refractory. The model shown in Fig. 4 is half of a WST specimen according to the symmetry conditions of the test. Plain strain square elements, termed CPE4 in Abaqus, were assigned to the model. The wedge was modeled as an analytical rigid part and the contacts defined between the parts were frictionless. The load transmission part

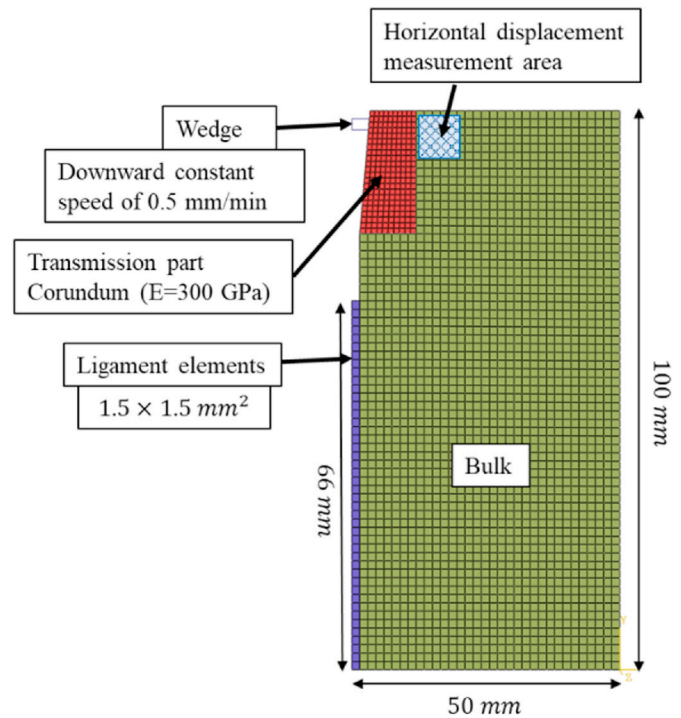


Fig. 4. 2D and symmetrical model of the WST.

is made of corundum with a high stiffness compared to the refractory material under the test; its Young’s modulus is assumed to be 300 GPa in this study. More details on the model specifications and testing preparations can be seen in Ref. [24].

The material constitutive models used in the simulation are shown in Table 1. Two cases were considered, Case 1 with DECR model in the

Table 1
Material models used in the WST simulation and inverse evaluation.

	Case 1	Case 2
Ligament	DECR subroutine	CDP model
Bulk	Asymmetric creep subroutine	Asymmetric creep subroutine

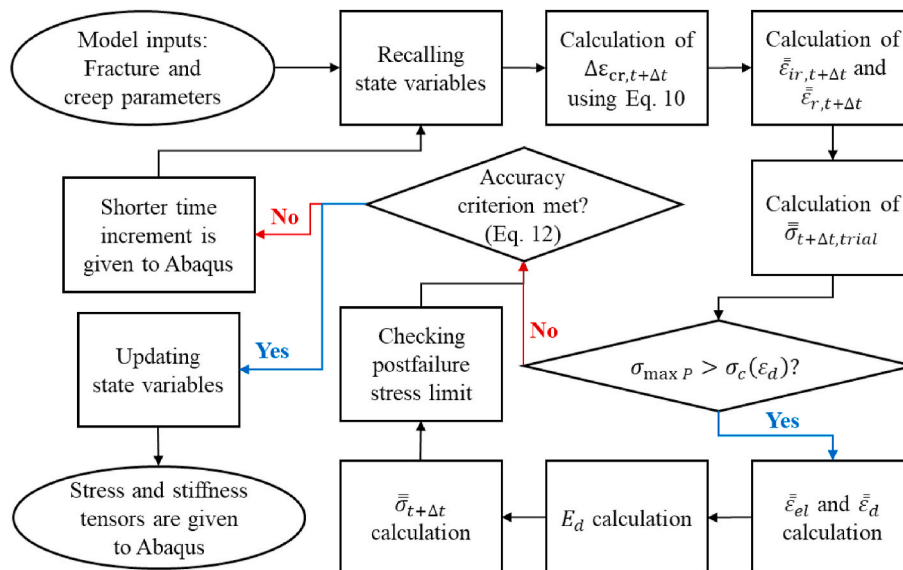


Fig. 3. DECR subroutine flowchart.

ligament and Case 2 with CDP model in the ligament. In both cases, the asymmetric creep model, which applies the same asymmetric criteria (Eq. (8)) defined in DECR model, was assigned to the bulk. The fracture was only assigned to the ligament and the macroscopic crack propagated in this region as observed in the experiments, where precut notches on the specimens guided the crack to propagate in the middle part of the specimen.

Primary creep stage parameters, listed in Table 2, were obtained from previous studies on the same material at 1200 °C [20,21]. Tensile creep tests were done at 1200 °C, but compressive creep tests were at higher temperature due to the load capacity of the testing apparatus. Compressive creep parameters were linearly extrapolated from parameters of three higher temperatures (1300 °C, 1400 °C and 1500 °C). With the aid of these parameters and the models in Table 1, inverse evaluation of fracture parameters was done for three experiments. An adaptive nonlinear least-square minimization algorithm, termed NL2SOL, implemented in the open source code DAKOTA [34], was used for this regard.

3. Results and discussion

3.1. DECR subroutine test with a single unit element

The DECR model was tested using a 3D single unit element simulation. The material parameters were assumed as following: $E = 100 \text{ GPa}$, $G_f = 2e^5 \text{ N/m}$, $f_t = 100 \text{ MPa}$, $R_1 = R_2 = 0.5$, $A_c = A_t = 1e^{-16}$, $n_c = n_t = 1.5$, and $m_c = m_t = -0.8$. The loading was defined in four steps:

1. Constant tensile load of 50 MPa for 100 s;
2. Load was released immediately to zero and kept for 100 s;
3. Linear increase of tensile strain up to 0.003 in 100 s;
4. Constant tensile strain of 0.003 for 100 s.

In Fig. 5, the stress and strain results of DECR model were compared with CDP and Norton-Bailey creep model implemented in Abaqus [23]. Stress responses for steps 1 and 2, and total strain responses for steps 3 and 4 were the same for all models. It was observed that DECR subroutine and Norton-Bailey creep model generate equal results before tensile failure, as intended. In third step, after the tensile failure, in the model with DECR subroutine, stress decreases according to the softening law; therefore, the irreversible strain (creep strain) does not increase as much as Norton-Bailey creep model, since the creep strain has a direct correlation to stress magnitude. During the last step, higher relaxation occurs in the case of Norton-Bailey creep law, since the higher stress magnitude causes higher increase in creep strain. In CDP model, fracture starts earlier in the third step since there is no creep in the model, and the stress drops to a lower value than DECR. The damage strain is irreversible in CDP, and no relaxation occurs.

3.2. Wedge splitting test results and inverse evaluated material parameters

Three WST experimental and inverse evaluated curves for alumina spinel refractory at 1200 °C are shown together in Fig. 6. The vertical displacement of the wedge (δ_v) is calculated based on Eq. (13).

$$\delta_v = \frac{\delta_H}{2 \tan \frac{\alpha}{2}} \tag{13}$$

where δ_H is the measured horizontal displacement, and α denotes the

Table 2

Creep parameters in compression and tension at 1200 °C.

	n	m	$A \text{ [Pa}^{-n}\text{s}^{-1}\text{]}$
Compressive creep	1.60	-0.78	$5.07e^{15}$
Tensile creep	1.44	-0.47	$8.82e^{14}$

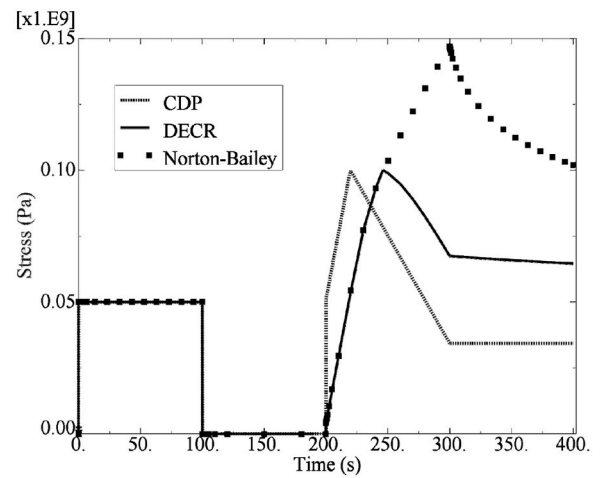
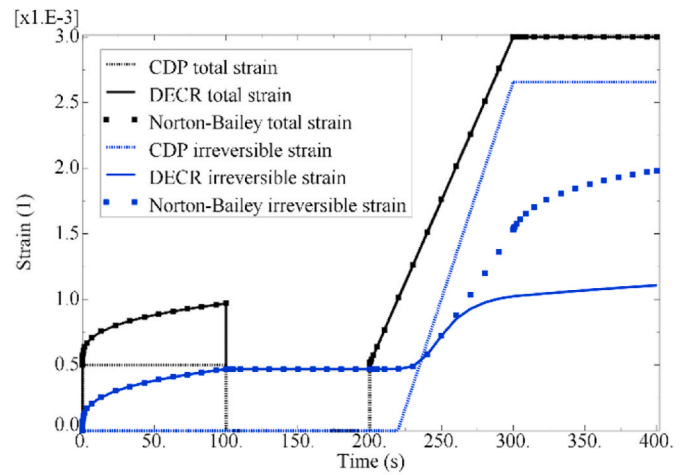


Fig. 5. Comparison of DECR subroutine with CDP and Norton-Bailey creep models using a single element.

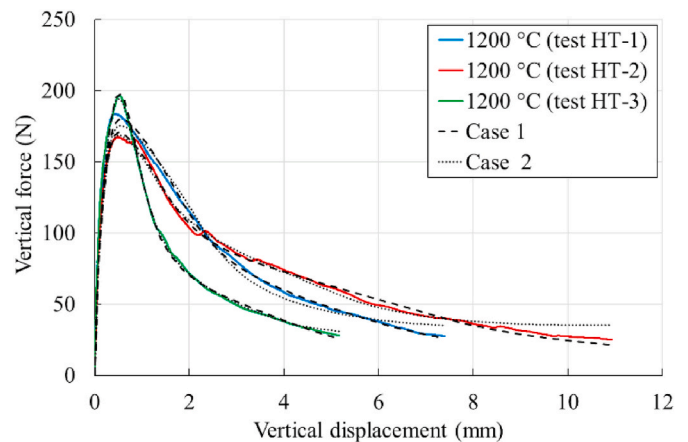


Fig. 6. WST experimental results and their inversely identified curves using Case 1 and Case 2.

wedge angle, which was 10° for these experiments. For inverse evaluation of fracture parameters, the initial Young’s modulus (E_0) was considered 45 GPa as it was the average of measured Young’s modulus on three specimens using impulse excitation technique at 1200 °C [35]. It was observed that inversely evaluated curves of Case 1 fit better to the experimental curves compared to the Case 2, especially at the tails of the

curves. This can also be inferred from Table 3 according to the degree of determination (R^2) and root-mean-square error (RSME), which were 0.993 and 3.824 for Case 1, whilst 0.989 and 4.598 for Case 2, respectively. R^2 is calculated as follows:

$$R^2 = 1 - \frac{\sum (F_{simulated} - F_{exp})^2}{\sum (F_{exp} - \overline{F_{exp}})^2} \quad (14)$$

where $F_{simulated}$ and F_{exp} are the simulated and experimental loads, respectively. $\overline{F_{exp}}$ is the mean value of the experimental load.

The inverse evaluated parameters are listed in Table 3, where G_f is the pure total fracture energy. It was observed that the difference between the inverse evaluated tensile strengths was less than 3%. However, with DECR model, the fracture energy was 13–22% higher than with CDP model. The reason is that when CDP model is used, the post-peak failure limit does not allow the stress to fall to zero and it adds to the consumed energy numerically [24].

In order to check the validity of asymmetric creep criteria, the state of the creep was checked during the simulation. In Fig. 7, the compressive and tensile creep states for each element were marked with the colors blue and red, respectively. Four different time points were chosen from the simulation of the test HT-2. It was observed that the area close to the ligament was affected by tensile creep, and this area enlarged with the crack propagation. The damaged elements in the ligament were checked for different times. At $t = 30$ s, 27% of the ligament, and at $t = 70$ s, 82% of it were damaged. At $t = 210$ s, all the ligament elements were damaged, but the traction in the first ligament element dropped to zero at $t = 880$ s when the post peak reached 23% of maximum load. It indicates that the creep interacts with the fracture for a long time even in the first ligament element, and proves the importance of integrated creep and mode I failure constitutive model.

In Fig. 8, the stress state of two columns of elements is shown for the peak load at $t = 70$ s. It was observed that around 86% of ligament elements were under tensile stresses at this time point. Additionally, it was shown that the horizontal stress cohered with the principal stress with the higher absolute value for the ligament; in contrast, the last column of elements on the right side of the model showed that the vertical stress cohered with the principal stress with the higher absolute value. This fact that the area experiencing shear stresses is relatively small justifies the application of the proposed asymmetric creep model in WST simulation. Although the tensile creep is acting in the most area of the ligament and that close to the ligament, the compressive creep is also consuming energy in outer region of the specimen.

The results of the Case 1 were compared with the experimental ones in Table 4. The specific fracture energy is the area under the experimental load displacement curve divided by the fracture surface (S), according to Eq. (15).

$$G_f' = \frac{1}{S} \int F_H d\delta_H \quad (15)$$

where F_H is the horizontal force, calculated using Eq. (16).

Table 3
Inversely evaluated fracture parameters using DECR and CDP model.

	Case 1 (DECR + Creep)					Case 2 (CDP + Creep)				
	G_f (N/m)	f_t (MPa)	R_1	R_2	R^2 RMSE (MPa ²)	G_f (N/m)	f_t (MPa)	R_1	R_2	R^2 RMSE (MPa ²)
HT-1	309.0	1.62	0.239	0.264	0.979 4.137	273.0	1.57	0.104	0.315	0.961 5.609
HT-2	384.0	1.53	0.380	0.167	0.995 2.729	314.3	1.53	0.438	0.214	0.988 4.049
HT-3	195.2	1.90	0.239	0.134	0.992 4.606	172.4	1.87	0.238	0.192	0.993 4.137
HT-Mean	296.0	1.68	0.286	0.188	0.993 3.824	253.2	1.65	0.260	0.240	0.989 4.598

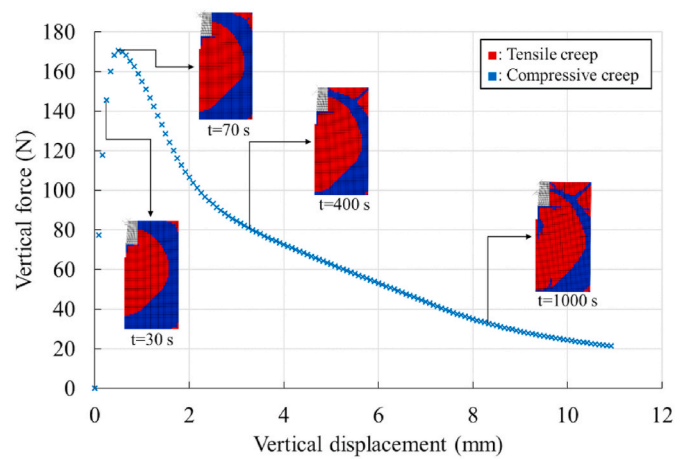


Fig. 7. Compressive and tensile creep regions during WST at 1200 °C (HT- 2).

$$F_H = \frac{F_V}{2 \tan \frac{\alpha}{2}} \quad (16)$$

where F_V denotes the vertical force. The nominal notch tensile strength (σ_{NT}) was calculated using Eq. (17).

$$\sigma_{NT} = \frac{F_{H,max}}{bh} \left(1 + \frac{6y}{h} \right) \quad (17)$$

where $F_{H,max}$ denotes the maximum horizontal force; b , h , and y stand for the width and the height of the ligament, and the vertical distance from the loading position to the center of the ligament, respectively. The ratio of G_f' to G_f was in the range of 96.9%–102.8%, in contrary to the cases at room temperature for which this ratio was around 80% due to stopping the test at 15% of the maximum load [24]. The increased ratio is caused by creep energy consumption. The total fracture energy without considering creep in the ligament and bulk, $G_{f no-creep}$, was also inversely identified with DE model. The creep contribution was calculated by the relative difference between G_f and $G_{f no-creep}$ to $G_{f no-creep}$. It shows that 12.9% of the energy was consumed by creep at 1200 °C. The mean ratio of the nominal notch tensile strength to the pure tensile strength is 1.93. It is worth to mention that the determined creep contribution and mean ratio are valid for the investigated material under the specific loading conditions. In other words, they might be dependent on the loading conditions and material properties.

Finally, the mean values and the standard deviations of DECR inversely evaluated parameters were used to predict the mean WST curve and its range (Fig. 9). It was observed that the three experimental curves lie within one standard deviation of the mean.

4. Conclusion

In this research work, a new material constitutive model (DECR) was

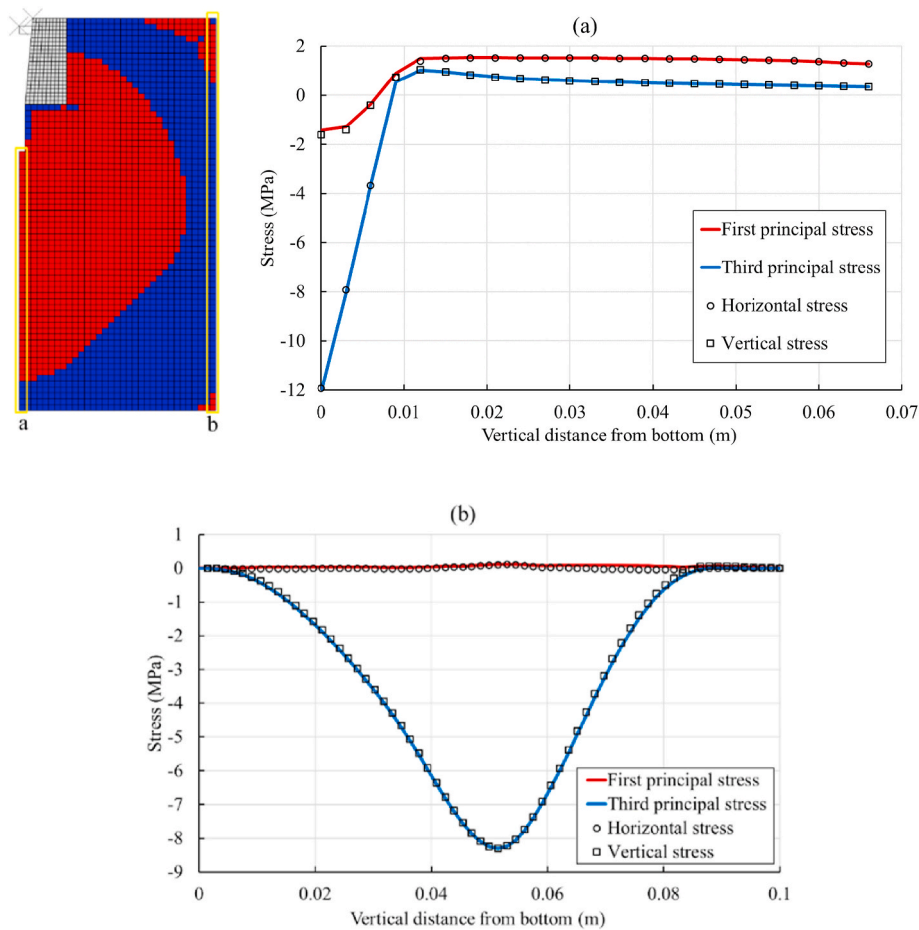


Fig. 8. Stress state in two columns of elements at the peak load (t = 70 s).

Table 4

Comparison of DECR inversely evaluated fracture parameters and experimental fracture parameters (mean values and standard deviations).

	G_f' (N/m)	G_f (N/m)	$\frac{G_f'}{G_f}$ (%)	$G_{f \text{ no-creep}}$ (N/m)	Creep contribution (%)	σ_{NT} (MPa)	f_t (MPa)	$\frac{\sigma_{NT}}{f_t}$
HT-1	299.3	309.0	96.9	350.8	11.9	3.21	1.62	1.98
HT-2	376.4	384.0	98.0	421.4	8.9	2.97	1.53	1.94
HT-3	200.7	195.2	102.8	237.8	17.9	3.53	1.90	1.86
HT-Mean	292.1	296.0	99.2	336.7	12.9	3.24	1.68	1.93
HT-STD	88.1	95.1	3.1	92.6	4.6	0.28	0.19	0.06

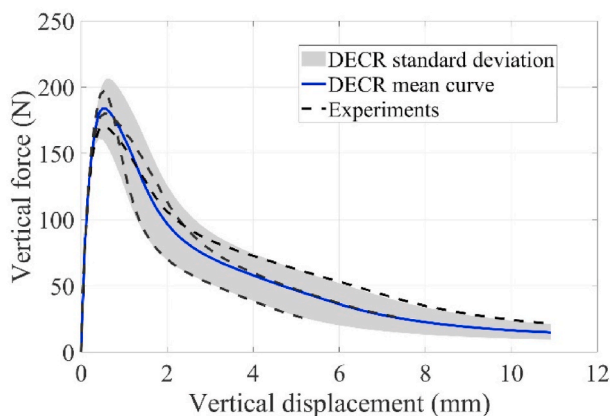


Fig. 9. DECR prediction of WST test result (mean and range).

successfully developed to combine an isotropic damaged elasticity model with an asymmetric Norton-Bailey creep law. The numerical tests with a single element proved that this model is capable to account creep and mode I fracture in the same element. Further comparison study between DECR and CDP models was carried out by modeling the wedge splitting tests of shaped alumina spinel refractory at 1200 °C. With the two material models, the fracture parameters were inversely identified. Better fittings were received, especially to the tail of the post peak curve below 25% post peak, when DECR model was applied. The creep occurs in ligament and bulk of the specimens and the mean creep energy contribution was 12.9% of the experimental total fracture energy. The developed material constitutive model contributes to the accurate determination of mode I fracture parameters at high temperatures.

Declaration of competing interest

The authors declare that they have no known competing financial interests or personal relationships that could have appeared to influence the work reported in this paper.

Acknowledgements

This work was supported by the funding scheme of the European Commission, Marie Skłodowska-Curie Actions Innovative Training Networks in the frame of the project ATHOR - Advanced THERmo-mechanical multiscale modeling of Refractory linings 764987 Grant.

References

- [1] A. Hillerborg, M. Modéer, P.-E. Petersson, Analysis of crack formation and crack growth in concrete by means of fracture mechanics and finite elements, *Cement Concr. Res.* 6 (6) (Nov. 1976) 773–781, [https://doi.org/10.1016/0008-8846\(76\)90007-7](https://doi.org/10.1016/0008-8846(76)90007-7).
- [2] S. Jin, D. Gruber, H. Harmuth, Determination of Young's modulus, fracture energy and tensile strength of refractories by inverse estimation of a wedge splitting procedure, *Eng. Fract. Mech.* 116 (Jan. 2014) 228–236, <https://doi.org/10.1016/j.engfracmech.2013.11.010>.
- [3] L. Pan, Z. He, Y. Li, B. Li, S. Jin, Inverse simulation of fracture parameters for cement-bonded corundum refractories, *J. Occup. Med.* 71 (11) (Nov. 2019) 3996–4004, <https://doi.org/10.1007/s11837-019-03750-y>.
- [4] Stückelschweiger, Jin Gruber, Harmuth, Wedge-splitting test on carbon-containing refractories at high temperatures, *Appl. Sci.* 9 (16) (Aug. 2019) 3249, <https://doi.org/10.3390/app9163249>.
- [5] Z.P. Bazant, Current status and advances in the theory of creep and interaction with fracture, in: *Proceedings of the Fifth International RILEM Symposium on Creep and Shrinkage of Concrete (ConCreep 5)*, 1993, pp. 291–307.
- [6] K. Andreev, H. Harmuth, “FEM simulation of the thermo-mechanical behaviour and failure of refractories—a case study, *J. Mater. Process. Technol.* 143–144 (1) (Dec. 2003) 72–77, [https://doi.org/10.1016/S0924-0136\(03\)00322-4](https://doi.org/10.1016/S0924-0136(03)00322-4).
- [7] S. Jin, D. Gruber, H. Harmuth, R. Rössler, Thermomechanical failure modeling and investigation into lining optimization for a Ruhrstahl Heraeus snorkel, *Eng. Fail. Anal.* 62 (Apr. 2016) 254–262, <https://doi.org/10.1016/j.engfailanal.2016.01.014>.
- [8] X. Liang, W.L. Headrick, L.R. Dharani, S. Zhao, Modeling of failure in a high temperature black liquor gasifier refractory lining, *Eng. Fail. Anal.* 14 (7) (Oct. 2007) 1233–1244, <https://doi.org/10.1016/j.engfailanal.2006.11.043>.
- [9] M. Ali, T. Sayet, A. Gasser, E. Blond, Transient thermo-mechanical analysis of steel ladle refractory linings using mechanical homogenization approach, *Ceramics 3* (2) (Apr. 2020) 171–189, <https://doi.org/10.3390/ceramics3020016>.
- [10] R.G. Oliveira, J.P.C. Rodrigues, J. Miguel Pereira, P.B. Lourenço, R.F.R. Lopes, Experimental and numerical analysis on the structural fire behaviour of three-cell hollowed concrete masonry walls, *Eng. Struct.* 228 (November 2019) 2021, <https://doi.org/10.1016/j.engstruct.2020.111439>.
- [11] L. Li, J. Purkiss, “Stress–strain constitutive equations of concrete material at elevated temperatures, *Fire Saf. J.* 40 (7) (Oct. 2005) 669–686, <https://doi.org/10.1016/j.firesaf.2005.06.003>.
- [12] C.J. Pearce, C.V. Nielsen, N. Bićanić, Gradient enhanced thermo-mechanical damage model for concrete at high temperatures including transient thermal creep, *Int. J. Numer. Anal. Methods GeoMech.* 28 (78) (Jun. 2004) 715–735, <https://doi.org/10.1002/nag.376>.
- [13] T. Gernay, A. Millard, J.-M. Franssen, A multiaxial constitutive model for concrete in the fire situation: theoretical formulation, *Int. J. Solid Struct.* 50 (22–23) (Oct. 2013) 3659–3673, <https://doi.org/10.1016/j.ijsolstr.2013.07.013>.
- [14] C. de Sa, F. Benboudjema, Modeling of concrete nonlinear mechanical behavior at high temperatures with different damage-based approaches, *Mater. Struct.* 44 (8) (Oct. 2011) 1411–1429, <https://doi.org/10.1617/s11527-011-9707-z>.
- [15] M.J. Terro, Numerical modeling of the behavior of concrete structures in fire, *ACI Struct. J.* 95 (1998) 183–193.
- [16] U. Schneider, Modelling of concrete behaviour at high temperatures, *Des. Struct. Against Fire* (1986) 53–69.
- [17] S. Schachner, S. Jin, D. Gruber, H. Harmuth, Three stage creep behavior of MgO containing ordinary refractories in tension and compression, *Ceram. Int.* 45 (7) (May 2019) 9483–9490, <https://doi.org/10.1016/j.ceramint.2018.09.124>.
- [18] A. Sidi Mammari, D. Gruber, H. Harmuth, S. Jin, Tensile creep measurements of ordinary ceramic refractories at service related loads including setup, creep law, testing and evaluation procedures, *Ceram. Int.* 42 (6) (May 2016) 6791–6799, <https://doi.org/10.1016/j.ceramint.2016.01.056>.
- [19] L. Teixeira, et al., Experimental investigation of the tension and compression creep behavior of alumina-spinel refractories at high temperatures, *Ceramics 3* (3) (Sep. 2020) 372–383, <https://doi.org/10.3390/ceramics3030033>.
- [20] S. Samadi, S. Jin, D. Gruber, H. Harmuth, Creep parameter determination of a shaped alumina spinel refractory using statistical analysis, in: *Proceedings of 63rd International Colloquium on Refractories, Raw Materials and Reuse*, 2020, pp. 1–5.
- [21] S. Samadi, S. Jin, D. Gruber, H. Harmuth, S. Schachner, Statistical study of compressive creep parameters of an alumina spinel refractory, *Ceram. Int.* 46 (10) (Jul. 2020) 14662–14668, <https://doi.org/10.1016/j.ceramint.2020.02.267>.
- [22] E. Blond, N. Schmitt, F. Hild, Ph Blumenfeld, J. Poirier, Modelling of high temperature asymmetric creep behavior of ceramics, *J. Eur. Ceram. Soc.* 25 (11) (2019) 1819–1827, <https://doi.org/10.1016/j.jeurceramsoc.2004.06.004>.
- [23] “Abaqus, ABAQUS Documentation, Dassault systems, Providence, RI, USA, 2018.
- [24] S. Samadi, S. Jin, D. Gruber, H. Harmuth, A comparison of two damage models for inverse identification of mode I fracture parameters: case study of a refractory ceramic, *Int. J. Mech. Sci.* (Feb. 2021) 106345, <https://doi.org/10.1016/j.ijmeccsci.2021.106345>.
- [25] P. Boisse, A. Gasser, J. Rousseau, Computations of refractory lining structures under thermal loadings, *Adv. Eng. Software* 33 (7–10) (Jul. 2002) 487–496, [https://doi.org/10.1016/S0965-9978\(02\)00064-9](https://doi.org/10.1016/S0965-9978(02)00064-9).
- [26] J.T. Boyle, J. Spence, *Stress Analysis for Creep*, Butterworths, England, 1983.
- [27] S. Jin, H. Harmuth, D. Gruber, “Compressive creep testing of refractories at elevated loads—device, material law and evaluation techniques, *J. Eur. Ceram. Soc.* 34 (15) (Dec. 2014) 4037–4042, <https://doi.org/10.1016/j.jeurceramsoc.2014.05.034>.
- [28] E. K. Tschegg, “Equipment and Appropriate Specimen Shapes for Tests to Measure Fracture Values,” Pat. AT-390328, 1986.
- [29] H. Harmuth, K. Rieder, M. Krobath, E. Tschegg, Investigation of the nonlinear fracture behaviour of ordinary ceramic refractory materials, *Mater. Sci. Eng.* 214 (1–2) (1996) 53–61, [https://doi.org/10.1016/0921-5093\(96\)10221-5](https://doi.org/10.1016/0921-5093(96)10221-5).
- [30] H. Harmuth, E.K. Tschegg, A fracture mechanics approach for the development of refractory materials with reduced brittleness, *Fatig. Fract. Eng. Mater. Struct.* 20 (11) (1997) 1585–1603, <https://doi.org/10.1111/j.1460-2695.1997.tb01513.x>.
- [31] H. Harmuth, Stability of crack propagation associated with fracture energy determined by wedge splitting specimen, *Theor. Appl. Fract. Mech.* 23 (1) (1995) 103–108, [https://doi.org/10.1016/0167-8442\(95\)00008-3](https://doi.org/10.1016/0167-8442(95)00008-3).
- [32] K. Andreev, V. Tadaion, Q. Zhu, W. Wang, Y. Yin, T. Tonnesen, “Thermal and mechanical cyclic tests and fracture mechanics parameters as indicators of thermal shock resistance – case study on silica refractories, *J. Eur. Ceram. Soc.* 39 (4) (2019) 1650–1659, <https://doi.org/10.1016/j.jeurceramsoc.2018.12.062>.
- [33] Y. Dai, D. Gruber, H. Harmuth, Observation and quantification of the fracture process zone for two magnesia refractories with different brittleness, *J. Eur. Ceram. Soc.* 37 (6) (2017) 2521–2529, <https://doi.org/10.1016/j.jeurceramsoc.2017.02.005>.
- [34] “Dakota, User's Manual.” Unlimited Release, Version 5.2, 2011.
- [35] G. Roebben, B. Bollen, A. Brebels, J. Van Humbeeck, O. Van der Biest, Impulse excitation apparatus to measure resonant frequencies, elastic moduli, and internal friction at room and high temperature, *Rev. Sci. Instrum.* 68 (12) (Dec. 1997) 4511–4515, <https://doi.org/10.1063/1.1148422>.

Title: Thermomechanical finite element modeling of steel ladle containing alumina spinel refractory lining

Authors: S. Samadi, S. Jin, D. Gruber, H. Harmuth

Prepared to be submitted

Abstract

Refractory linings are used in steel ladles in iron and steel industry, to protect the vessel structure from the molten steel (with temperature above 1600°C). To increase the durability of the refractory lining, researching the possible failure causes is of importance. In recent decades, alumina spinel refractories have become a common material in the barrel zone of steel ladles in direct contact with steel. In this regard, the current study employed thermomechanical FEM simulations to investigate the irreversible material behavior of alumina spinel bricks. At first, a study on the joint size and friction effect was conducted. Then, three distinct constitutive material models were assigned to the working lining, each corresponding to an irreversible deformation mechanism. The Norton-Bailey creep model was used to simulate creep behavior, the Drucker-Prager yield criterion was used to simulate shear failure, and concrete damaged plasticity was used to mimic tensile failure. The findings of the three models were compared to see how each phenomenon affected the lining's and steel shell's stress-strain response. The simulations showed the occurrence location and time of each irreversible behavior. The effect of considering plasticity for the steel shell on the mechanical behavior of the refractory lining was also investigated, which showed a decrease of irreversible strains in the working lining.

1. Introduction

Refractory materials are largely used as the lining material of several high-temperature vessels in iron and steel production industry due to their high resistance and stability under severe thermal, mechanical, and chemical conditions [1–4]. Steel ladles, consisting of refractory layers and a steel container, are used for transporting and refining the molten steel. Refractory linings in this vessel are subjected to harsh chemical environment in direct contact with the molten steel and slag, cyclic thermal shocks, and operating temperature above 1600 °C, which cause high thermo-mechanical stresses [5–7]. The refractory properties and the lining design have direct influence on the steel quality and energy consumption, and failure of the lining can lead to huge costs [8–12]. Therefore, prediction of the lining performance using numerical approaches is of great help, since the direct measurements and observations of the refractories performance in service is very challenging.

Introduction of magnesium aluminate spinel in alumina refractories has been an important invention for high quality steel production since it brought two important benefits, enhancement of the slag resistance and improvement of the thermo-mechanical properties such as thermal shock resistance [13]. Therefore, application of alumina spinel refractories in steel production started to develop in late 1980s [14–16] and since then, there has been many advancements to the microstructure of these refractories [17–21]. Alumina spinel refractories have been applied in steel

ladles in both forms of shaped and unshaped products [22]. But in the case of shaped products (bricks), the joints between the bricks provide the lining with an expansion allowance, which reduces the stress magnitude in the lining [23]. Although many researchers investigated the behavior of this refractory product experimentally [24–26], very few studies worked on the thermo-mechanical modeling of their application [4]. Therefore, the current study aimed to investigate the thermo-mechanical response and irreversible behavior of a shaped alumina spinel refractory in the barrel zone of a steel ladle with the aid of finite elements method (FEM).

Thermomechanical FE-simulations have been employed to predict the stress-strain response of refractory linings and their possible failure [27–32]. Steel ladle refractory lining consists of many refractory bricks, joints, and other structural details. Therefore, mechanical modeling of this complex structure with all the details results in huge computational time and cost, and simplification of the numerical models together with maintaining the accuracy of the results has always been a challenge for researchers. In this regard, some researchers only used a 2D cut of the lining to reduce the computation cost [33]; for instance, Hou et al. [10] investigated the effect of linings thickness and material properties using a 2D model of only two bricks in the working lining and considering only the elastic behavior. Nevertheless, the problem of 2D models is the necessity of a stress-strain condition for the third direction, which is an imprecise simplification of the real condition.

Regarding 3D modeling of refractory linings, researchers have proposed two approaches: homogenization technique [34] and unit-cell modeling technique [35]. In the former technique, an equivalent anisotropic material model is developed to represent the overall behavior of bricks and joints in the lining. Using this technique, a large portion of the structure can be modeled with low computational cost [23,36]. On the other hand, the unit-cell modeling technique explicitly considers the expansion allowances and interfaces of bricks and linings. To do so and not ending with a high computational cost, this technique reduces the model size and considers a small section of the lining, which is periodically repeated in the structure [35]. This allows for investigating the local joint openings, relative sliding of bricks, and including more complex material models for the refractory linings [28,30,31,35].

The present study focuses on the application evaluation of alumina spinel bricks in the steel ladle and their thermomechanical behavior and contributions to the joint opening and mechanical loads on the steel shell. To this end, the 3D unit-cell model was necessary and applied. In the current paper, irreversible behavior of refractories, i.e., creep, shear failure, and tensile failure, was considered with Norton-Bailey type creep model [37], Drucker-Prager model [38], Concrete damaged plasticity model [39], respectively. Additionally, the plastic behavior of the steel shell was taken into account.

2. Model and boundary conditions

The studied steel ladle was assumed to be asymmetric in the axial direction. Thus, a wedge-shaped cut was performed on the entire ladle structure, which included one half of an alumina spinel brick in the barrel zone, as shown in Figure 1. The element type used in the model was C3D8T with

cubic shape and 8 integration points. The total number of elements in the model was 82783 and the element size for the working lining was 1 cm.

The steel ladle is divided into three sections: slag zone, barrel zone, and bottom. The refractory lining concept is a multi-layer arrangement, chosen according to the operation conditions of each section. The working layer is responsible for the steel quality since it is in direct contact with the molten steel and must sustain the most severe loading conditions. The next layer, safety lining, works as a support in case the working lining fails, and it is responsible for the integrity and stability of the lining. The layer behind the safety lining is the insulation lining, and after that an insulation board, which have the responsibility of reducing the heat loss and protecting the steel shell from the high temperatures [40,41]. The insulation board has a thickness of 5 mm and very low Young's modulus. Therefore, it was not modeled in the simulations to reduce the model complexity. Instead, its conductivity (around 0.06 J/smK) was defined in the contact definition between the steel shell and the insulation lining. Gravity was applied in the simulation, and the steel shell bottom was constrained from moving in axial direction.

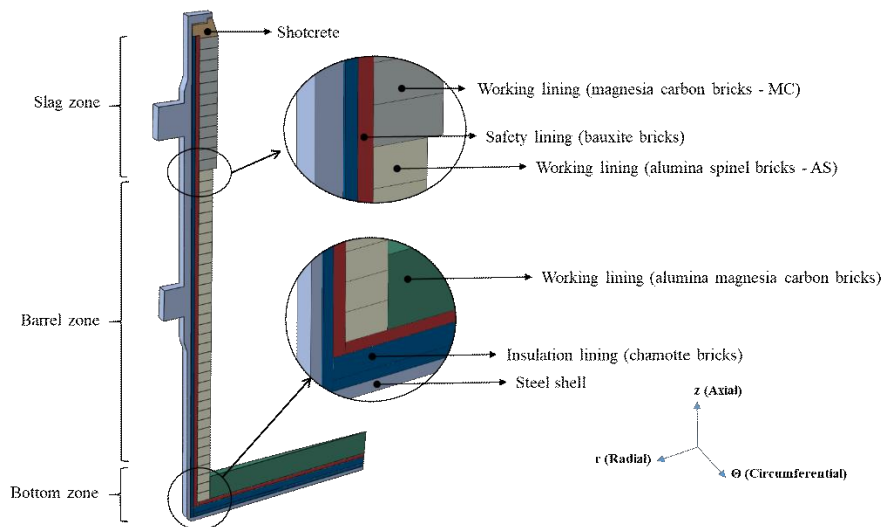


Figure 1: 3D unit-cell model of the steel ladle

2.1 Joint and contact modeling

Vertical and horizontal joints between the bricks provide the whole refractory lining with an expansion allowance. In service, joints are results of brick surface roughness and dimension errors, or sometimes additionally created with cupboards during the installation of the linings. In the model of this study, vertical joints were modeled using a rigid plate, which was placed in the middle of the gap between two bricks. This vertical joint was considered for all the refractory layers. The horizontal joints were not modeled between individual bricks; instead, a total gap of 1cm was considered on top of the layers.

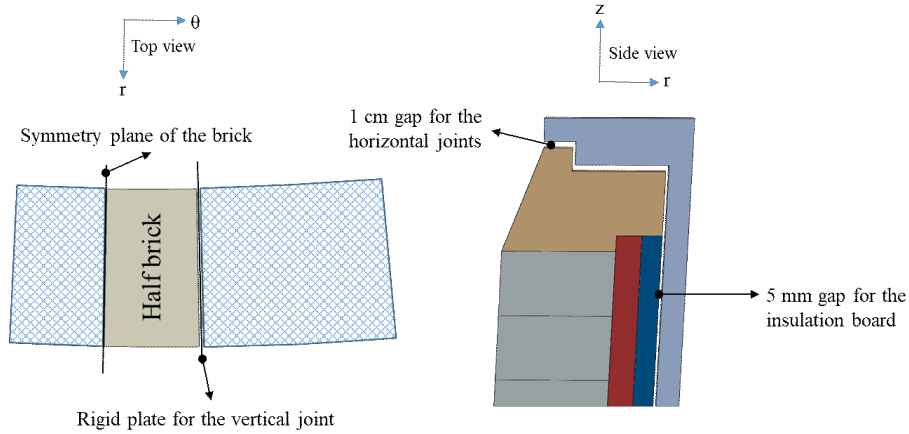


Figure 2: Schematic representation of joint consideration

For contact modeling between parts, contact pairs were defined between each two parts in contact. Discretization method used was “Surface to surface”, and the sliding formulation defined was “Finite sliding”. For the contact property, the so-called “Penalty” friction formulation, based on the Coulomb friction model, was defined [42].

2.2 Working cycles and boundary conditions

Steel ladle working cycle consists of three steps as shown in Figure 3. After the lining installation, the ladle goes through a preheating phase, which is necessary to reduce the thermal shock for refractories and to maintain refining efficiency. In the studied ladle, the preheating was around 16 hours, and the temperature of the simulation was defined according to the measurements. Afterwards, the ladle is ready for pouring, processing, and casting of the molten steel, all of which are named as a processing step in the simulations. During this step, the molten steel temperature of 1650 °C was applied at the hot face of the lining. After the casting, the ladle went through an idle time, during which inspection of the refractory linings and necessary repairs can be done. Idle time of the studied ladle was around 2 hours. During the idle time, when no reinstallation is required, a lid is put on top of the ladle to prevent the heat loss. To consider this in the simulation, an adiabatic condition was defined for the inner surface of the model during the idle time. For all the steps the ambient temperature was set to be 25 °C.

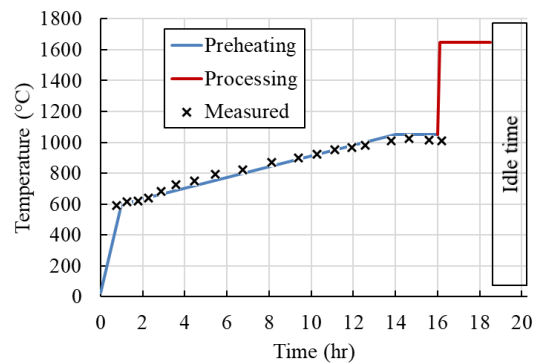


Figure 3: Temperature definition at the hot face during preheating and first steel ladle working cycle (together with the measured data during the preheating step)

3. Material mechanical constitutive models and their characterization methods

3.1 Creep

Creep is time-dependent deformation of materials under constant stress and temperature [43]. Several numerical models have been proposed for modeling the creep of materials. Regarding refractories, the Norton-Bailey creep law has been capable of reproducing the creep experimental results [44,45] and has been applied in thermomechanical simulations of refractory linings [46]. The representation of the creep law in Abaqus software [42] is as following:

$$\dot{\varepsilon}_{cr} = (A\sigma_{Mises}^n[(m+1)\varepsilon_{cr}]^m)^{\frac{1}{m+1}} \quad \text{Eq. 1}$$

where, ε_{cr} and $\dot{\varepsilon}_{cr}$ are the equivalent creep strain and its rate, respectively. σ_{Mises} is the von Mises stress calculated using Eq. 2. A , n , and m are the material creep parameters, which are evaluated using an inverse evaluation algorithm and creep testing techniques [47,48]. The compressive creep parameters of the alumina spinel bricks were evaluated in another study of Samadi et al. using uniaxial compressive creep experiments [49,50].

$$\sigma_{Mises} = \sqrt{\frac{3}{2}(\bar{S}:\bar{S})} \quad \text{Eq. 2}$$

In this equation \bar{S} is the deviatoric part of the stress tensor. The creep parameters of working lining materials are reported in Table 1.

Material	Temperature	900 °C	1300 °C	1400 °C	1500 °C		
		A (Pa ⁻ⁿ /s)	n	m			
Alumina spinel bricks [50]	A (Pa ⁻ⁿ /s)	1e ⁻²⁶	7.75e ⁻¹²	1.72e ⁻¹⁴	2.18e ⁻⁰⁸		
	n	0.0001	1.1387	1.5905	0.6749		
	m	-0.5	-0.7322	-0.7257	-0.6631		
Magnesia carbon bricks [51]	Temperature	900 °C	1270 °C	1370 °C	1470 °C		
	A (Pa ⁻ⁿ /s)	1e ⁻²⁶	4.01e ⁻¹⁰	4.19e ⁻¹⁰	4.58e ⁻¹⁰		
	n	0.0001	0.8013	0.8013	0.8013		
	m	-0.5	-0.8025	-0.8025	-0.8025		
Alumina magnesia carbon bricks*	Temperature	900 °C	1300 °C	1350 °C	1400 °C	1450 °C	1500 °C
	A (Pa ⁻ⁿ /s)	1e ⁻²⁶	2.73e ⁻²⁵	6.63e ⁻²³	2.00e ⁻¹⁵	1.71e ⁻¹⁵	1.13e ⁻¹⁵
	n	0.0001	2.391	2.162	1.150	1.210	1.292
	m	0	0	0	0	0	0

*These material parameters were received from an industrial partner.

3.2 Shear failure

Shear failure could occur in refractory linings and has been modeled using Mohr-Coulomb criterion and Drucker-Prager model [52] in different studies. The Drucker-Prager [38] model in Abaqus software is applied to simulate granular materials like refractories with high compressive yield strengths compared to their tensile yield strengths [42]. The yield criterion is shown in Figure 4 and characterized with two parameters: cohesion (c), and friction angle (β). In this criterion, the

stress space is split using two axes: von Mises stress and hydrostatic pressure (σ_p). The latter is obtained using Eq. 3.

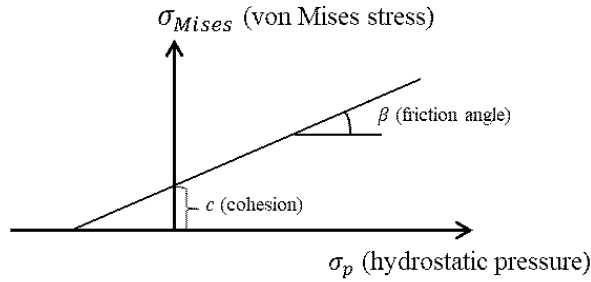


Figure 4: Linear Drucker-Prager yield surface [42]

$$\sigma_p = -\frac{1}{3} \text{trace}(\bar{\sigma})$$

Eq. 3

The modified shear test developed by Dahlem et al [53] was applied to evaluate the cohesion and friction angle of the alumina spinel bricks at high temperatures. The shear failure parameters of the working lining materials are reported in Table 2. The shear failure parameters were not available for the alumina magnesia carbon bricks.

Table 2: Working lining shear failure parameters

Material	Temperature	25 °C	1000 °C	1200 °C
	Alumina spinel bricks	Cohesion (MPa)	21.7	13.5
Friction angle (°)		48.6	49.0	69.9
Magnesia carbon bricks*	Temperature	25 °C	1000 °C	1200 °C
	Cohesion (MPa)	40	40	10
	Friction angle (°)	49.2	49.2	60

*These material parameters were received from a research at the chair of Ceramics, Montanuniversität Leoben.

3.3 Tensile failure

High tensile stresses are common in refractory linings due to hot shocks at the beginning of pouring and cold shocks at the end of casting phase. Tensile failure was reported in some previous numerical studies on refractory linings. The fictitious crack model proposed by Hillerborg [54] has successfully reproduced the refractory mode I fracture behavior [55,56]. It is implemented in concrete damaged plasticity model in Abaqus software [42], which has been used in this paper. In this model, material behaves elastically till the maximum tensile stress reaches material's tensile strength. Afterwards, the stress decreases according to a defined softening law (σ_c). Studies showed that in addition to the initial Young's modulus (E_0), tensile strength (f_t), and fracture energy (G_f), the post-peak softening law influences the depiction of fracture behavior [57]. For refractories, it has been shown that a bilinear post-peak behavior (Figure 5) fit well to the wedge splitting test results [57–59].

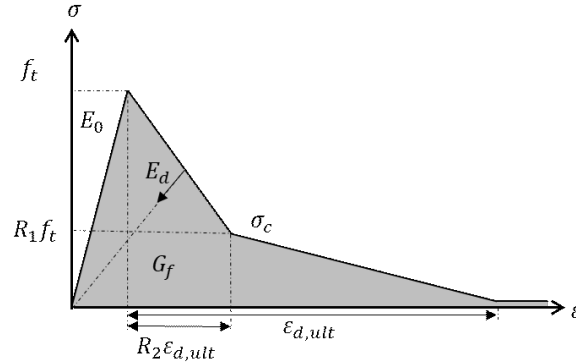


Figure 5: Fictitious crack model with bilinear post-peak behavior [59]

The wedge splitting test is a commonly applied method to investigate the fracture behavior of refractories [60–62]. A newly developed wedge splitting test apparatus [56] was employed in this study to evaluate the fracture parameters shown in Figure 5 for the alumina spinel bricks. The tensile failure parameters of the working lining materials are reported in Table 3. The tensile failure parameters were not available for the alumina magnesia carbon bricks.

Table 3: Working lining tensile failure parameters

Material	Temperature	25 °C	1200 °C	1400 °C	
		Alumina spinel bricks			
	Fracture energy (N.m/m ²)	136.0	337.5	258.7	
	Tensile strength (MPa)	2.91	1.66	0.68	
	R_1	0.213	0.239	0.272	
	R_2	0.295	0.263	0.305	
Magnesia carbon bricks [56]	Temperature	25 °C	1100 °C	1370 °C	1470 °C
		Fracture energy (N.m/m ²)			
	Fracture energy (N.m/m ²)	270	162	453	563
	Tensile strength (MPa)	1.51	1.42	2.26	2.4

3.4 Simulation plan

The simulation plan is shown in Table 4. At first two studies were conducted on the effect of joint size and friction coefficient, with simulation of one ladle working cycle. In the “joint size study” simulation, the vertical joint size was assigned 0.2, 0.3, 0.4, and 0.5 mm. In the “friction coefficient study”, the friction coefficient was applied between the bricks, with the values 0.1, 0.2, and 0.4. The material model for all the parts in these two studies was linear elasticity. In the next step, the simulation cases using different material constitutive models for the working lining were performed considering five ladle working cycles. Elasticity, creep, tensile failure, and shear failure were considered for the working lining, and the respective simulations were titled “E_WL”, “C_WL”, “CDP_WL”, and “DP_WL”, respectively. These four simulation cases were performed once with elasticity and once with plasticity in the steel shell; in the latter case, a “shell plasticity” is added to the case title. In addition, it should be mentioned that all thermomechanical simulation were performed in coupled manner, i.e., the thermal and mechanical modeling equations are solved simultaneously in each simulation increment. Finally, the mechanical properties of the alumina spinel bricks were evaluated in this research work. The thermal properties of the alumina spinel bricks were investigated in another research work in ATHOR project [41]. Other materials’ properties were received either from industrial partners or other studies at the Chair of Ceramics, Montanuniversitaet Leoben.

Table 4: Material constitutive models applied for different lining components and simulation cases

Simulation case title:		Joint size study	Friction coefficient study	E_WL	C_WL	CDP_WL	DP_WL
Part		Assigned material constitutive model					
Working lining (wall)	Alumina spinel bricks	Linear elasticity	Linear elasticity	Linear elasticity	Creep	Concrete damaged plasticity	Drucker Prager
	Magnesia Carbon bricks						
Working lining (bottom)	Alumina magnesia carbon bricks	Linear elasticity	Linear elasticity	Linear elasticity	Creep	Creep	Creep
Residual refractory lining	Chamotte bricks				Linear elasticity	Linear elasticity	
	Bauxite bricks				Linear elasticity	Linear elasticity	
Steel shell				Linear elasticity and von Mises plasticity (separately)	Linear elasticity and von Mises plasticity (separately)	Linear elasticity and von Mises plasticity (separately)	Linear elasticity and von Mises plasticity (separately)
Other parameters		Value					
Number of working cycles		1	1	5	5	5	5
Vertical joint size (mm)		0.2, 0.3, 0.4, 0.5	0.4	0.4	0.4	0.4	0.4
Friction coefficient (1)		0	0.1, 0.2, 0.4	0	0	0	0

4. Results and discussion

4.1 Temperature distribution

Temperature distribution results at different points in barrel zone are shown in Figure 6. Five steel ladle working cycles were simulated in total. Thermal results were the same for all simulations. It was observed that the temperature at the steel shell reached a value around 290 °C at the end of 5th cycle. The cold face temperature of the insulation layer was approximately 900°C, demonstrating the significance of the insulation board placed between the insulation bricks and the steel shell. The temperatures at safety and insulation linings increased continuously because an adiabatic condition was considered at the hot face of the bricks.

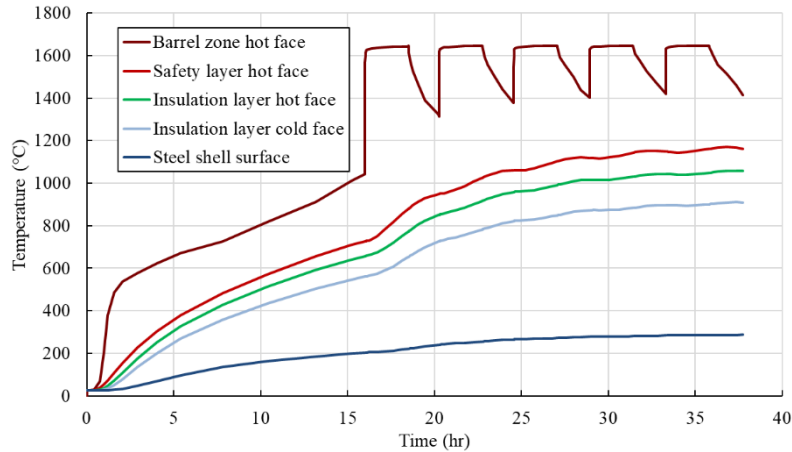


Figure 6: Simulated temperatures at different layers in barrel zone (preheating and five working cycles)

4.2 Stress and strain analysis

4.2.1 Joint size and friction coefficient impact

The impact of vertical joint size and friction coefficient between the bricks are depicted in Figure 7. The radial displacement at the steel shell was reduced by increasing the initial joint size, as was the maximum von Mises stress at both the shell and working lining. The upper part of the steel shell, which confines the axial movement of the refractories, showed the highest von Mises stress. Furthermore, increasing the friction coefficient resulted in an increase of the maximum von Mises stress at the working lining while a decrease of the maximum von Mises stress at the steel shell. This was observed because with increasing the friction, the bricks slid less and the bending effect on the upper part of the ladle was reduced. Also, the radial displacement at the steel shell was reduced around 5% when a friction coefficient of 0.1 was applied to the brick contacts but did not change considerably with increasing the friction coefficient.

Both vertical and horizontal joints of the working lining were fully closed at the end of the idle time for all initial joint opening sizes and all the friction coefficients. At the end of the preheating, all vertical joints were closed at the hot face, while some joints at the cold face of AS bricks remained open, and the opening size increased with the initial joint opening size. Regarding the relative movement of bricks against each other, for the simulations without friction, the average slipping distance between the AS bricks (measured from node at the hot face) increased with increasing the initial joint opening size (0.3 mm for initial joint size of 0.2 mm and 2.2 mm for initial joint size of 0.5 mm). The sliding was not observed for the simulations with friction (less than 5 micro-meter).

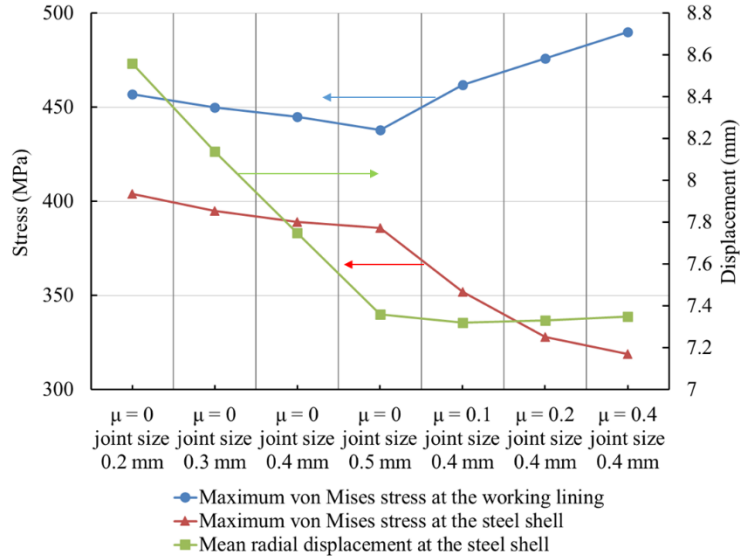


Figure 7: Influence of vertical joint size and friction coefficient on the maximum von Mises stresses at the working lining and steel shell, and the mean circumferential strain of the steel shell at the end of idle time

4.2.2 Irreversible behavior of the ladle barrel zone lining

To compare the thermomechanical response of the alumina spinel bricks caused by different irreversible mechanisms, an alumina spinel brick from the middle of the barrel zone was chosen. Figure 8 shows the brick and the terminology used in the current paper.

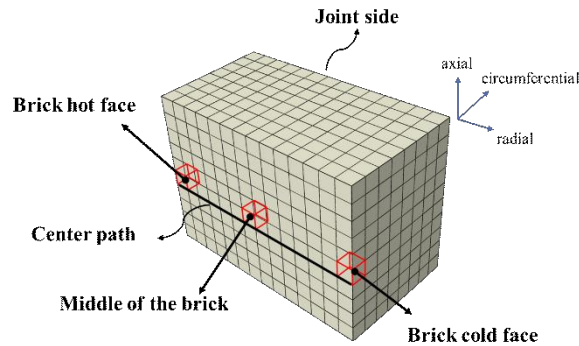


Figure 8: Schematic of a half alumina spinel brick

Radial, circumferential, and axial stresses at the hot face and the middle of the chosen alumina spinel brick are shown in Figure 9. The stress is the average value of one element's eight integration points. The stress magnitudes at the middle of the brick during preheating are similar for all simulations, whereas at the hot face lower for the shear failure simulation (Figure 9-c), indicating that shear failure occurred at the hot face already during the preheating. Furthermore, creep reduced stresses at the hot face at the start of the first processing, and it occurred later during the second processing at the middle of the brick (Figure 9-b). This shows that the temperature was not yet high enough to result in creep at the middle of the brick during the first working cycle. The stresses in the other three simulations exhibited a similar fluctuation. The results also showed that shear failure has greater impact on reducing axial stress than circumferential stress; it decreased axial stress around 58% and circumferential stress around 16% compared to the elastic simulation at the end

of the 5th cycle at the hot face (Figure 9-c). In contrast, tensile failure decreased the both axial and circumferential stresses only at the middle of the brick by approximately 29% compared to the elastic simulation at the end of the 5th cycle (Figure 9-d).

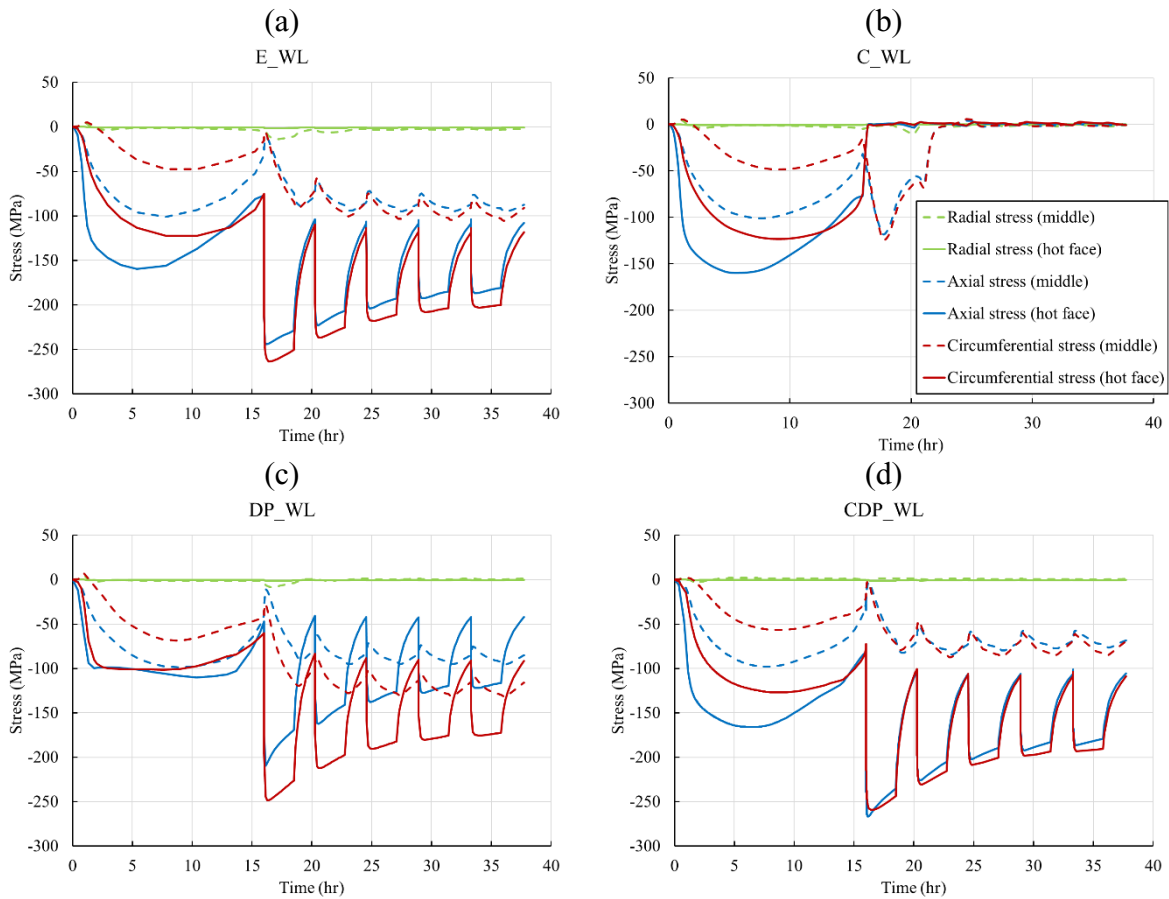


Figure 9: Stress history at the middle and hot face of the selected alumina spinel brick considering (a) elastic behavior, (b) creep behavior, (c) shear failure, and (d) tensile failure

In addition to the lining, stresses in the steel shell are of interest. When no plasticity was considered for the steel material, the stress values were significantly higher than steel yield stress. The highest and lowest maximum von Mises stresses received from elasticity and creep simulations, were 3.78 GPa and 1.02 GPa, respectively. This could also be the reason for high stresses in the lining. Therefore, isotropic von Mises plasticity was assigned to the steel shell according to steel standards [63] and the simulations were performed. The results showed that the maximum von Mises stress in the steel shell dropped to 380 MPa in all simulations. The maximum plastic strain in the steel shell occurred at its top part (the highest was 0.21 for the simulation case “E_WL with shell plasticity” and the lowest was 0.11 for the simulation case “C_WL with shell plasticity”) and in the other areas of the steel shell it was below 0.005.

Including shell plasticity decreased the stress magnitudes in the linings for all directions. Nevertheless, the axial stress decreased more than circumferential and radial stresses. For instance, after including shell plasticity in the simulation case “E_WL”, the compressive stress in axial direction at the end of 5th cycle decreased from 107 MPa to 9 MPa, and in circumferential direction, from 119 MPa to 92 MPa. The reason is that the plasticity occurred mostly in the top part of the

shell, which confines the axial movement of the bricks. It was also observed that the shell plasticity effect on the axial stress started during the last 2 hours of preheating, and it caused a sharp decrease of the axial stress during the first processing compared to the cases without shell plasticity.

Another important parameter to compare the simulation results, was the strain. In this regard, the equivalent strain (ε_{eq}) was defined according to Eq. 4.

$$\varepsilon_{eq} = \sqrt{\varepsilon_{ii}^2} \quad \text{Eq. 4}$$

where, ε_{ii} are the components on the main diagonal of the strain tensor. The equivalent strain on the center path of the selected alumina spinel brick for simulation cases with and without shell plasticity at the end of the 5th cycle is shown in Figure 10. For the simulation cases with irreversible material behavior in the lining, only the irreversible part of the strain tensor was used for the calculation in Eq. 4. In addition, the reversible strains from the simulation case “E_WL” are shown for comparison. Several important observations can be derived from these results. The first one is about the location of action for each irreversible phenomenon. The Figure 10-a shows that creep equivalent strain magnitude is higher at the hot face and almost zero at the cold face. Figure 6 showed that the temperature at the cold face of the alumina spinel bricks reached maximum 1190°C during the 5th working cycle. This lower temperature at the cold face could be the reason for lower creep occurrence. In the simulation case “DP_WL”, the equivalent irreversible strain was higher at hot face and lower at the cold face since the von Mises stress was higher closer to the hot face. In contrary, the equivalent tensile failure strain was almost zero at the hot face, since almost no tensile stress occurred at the hot face. It increased in a distance from the hot face, where tensile stresses occur due to hot shocks. Another important observation for the simulation case “CDP_WL” is the effect of shell plasticity. It was observed that there is an increase in the equivalent tensile failure strain in a distance around 4 cm from the hot face when shell plasticity is considered. This was received because the shell plasticity decreases the compressive stresses, and the hot shock could cause higher tensile stresses in this region.

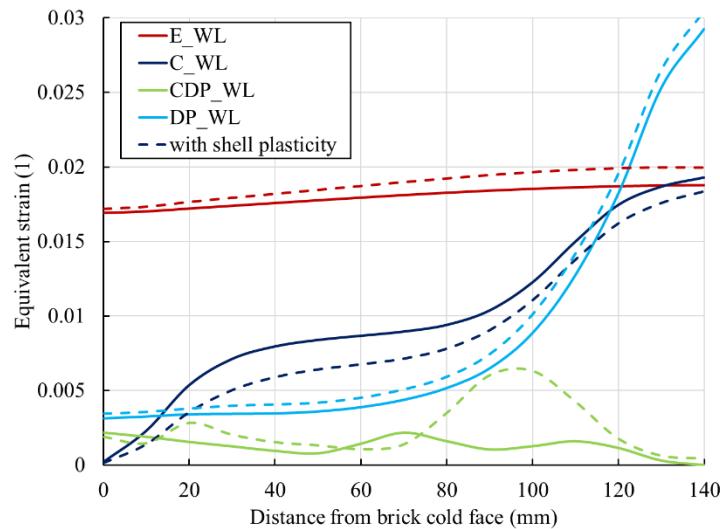


Figure 10: Equivalent strain on the center path of the selected alumina spinel brick at the end of the 5th cycle

To observe the irreversible phenomena over time, the equivalent irreversible strains at the brick hot face, middle point, and cold face are shown in Figure 11. The results showed that shear failure and tensile failure occurred during the preheating, but creep occurred after the temperature increased sufficiently.

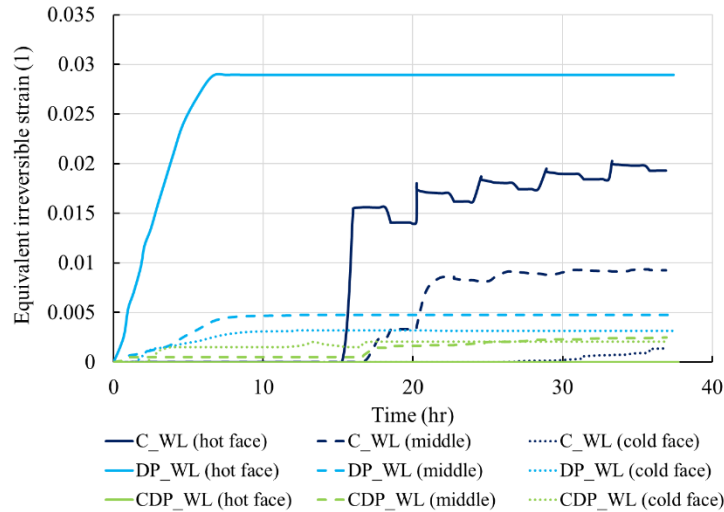


Figure 11: Equivalent irreversible strain under different failure mechanisms with time

In addition, the strain energies were also compared between simulations. The recoverable strain energy, the plastic dissipated energy, and the creep dissipated energy were received for the whole steel ladle at the end of 5th working cycle. The influence of the shell plasticity on the strain energies are shown in Figure 12. The recoverable strain energy and the dissipated creep energy decreased after including plasticity in the shell for all simulation cases. Dissipated energy due to plasticity increased because of additional plasticity of the steel shell.

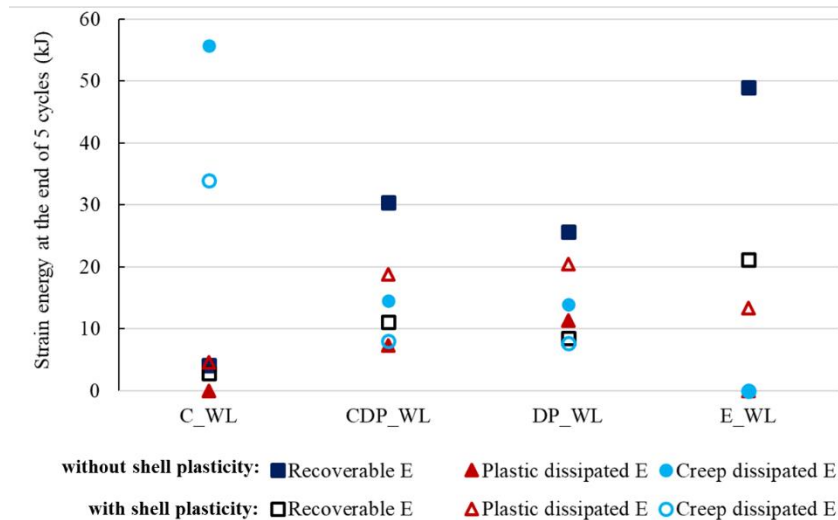


Figure 12: Influence of the shell plasticity on strain energies (E) at the end of 5th working cycle in different simulations

Another important point for the studied refractory linings is the joint openings between the bricks at the hot face since this might cause infiltration of the molten steel. The vertical joint opening was

measured at the hot face of the AS bricks at the end of each step. For all simulations, the joints became closed during the preheating and were closed at the end of the preheating. For the creep simulations the joints at the hot face started to open when creep started during the first processing and stayed open till the end of 5th cycle (Figure 13-a). For other simulations, the joints at the hot face stayed closed for the AS bricks till the end of the 5th cycle. Additionally, it should be mentioned that the horizontal joint openings were negligible compared to the vertical ones. The joint opening size at the hot face of the selected alumina spinel brick is shown in Figure 13-b. It was observed that the consideration of the steel shell plasticity in the simulation increased the vertical joint opening size slightly at the hot face in case of creep simulation but did not cause additional opening at the hot face in the other simulations.

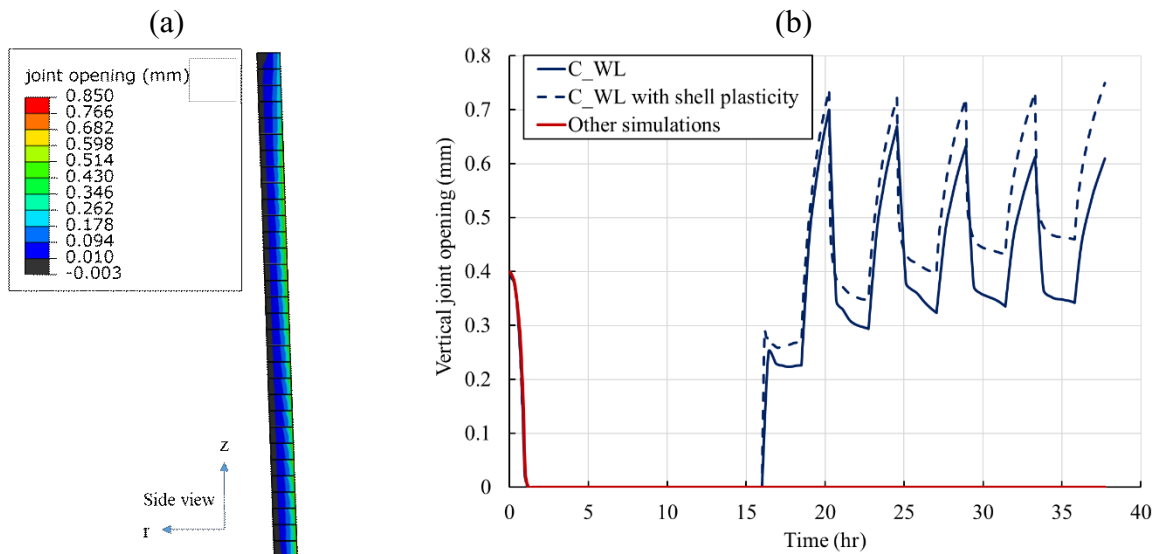


Figure 13: (a) The joint opening contour of AS bricks for creep simulation (b) Vertical joint opening size at the hot face of selected AS brick for different simulations

5. Conclusion

In this paper, thermomechanical simulation of a steel ladle refractory lining was performed using 3D unit-cell modeling approach. The irreversible behavior of a shaped alumina spinel refractory in service was investigated. In this regard, high-temperature mechanical experiments were employed to obtain the necessary material properties.

Firstly, elastic thermomechanical simulation (of one process cycle) was used to investigate the impact of vertical joint size and friction between bricks. It was seen that reducing the joint size from 0.5 mm to 0.2 mm raised the maximum von Mises stress both in the working lining and in the steel shell. Moreover, the maximum von Mises stress in the bricks was increased by considering friction between the bricks, while it was lowered in the steel shell.

Secondly, three major irreversible phenomena, creep, shear failure and tensile failure, were modeled using Norton-Bailey creep model, Drucker-Prager yield criterion, and concrete damaged plasticity model, respectively. Five process cycles of the ladle were simulated. It was seen that shear and tensile failure did not contribute to joint opening and stress reduction in the working

lining as much as creep did. Additionally, it was observed that a biaxial stress state exists in the brick, where radial stress was negligible in comparison to axial and circumferential stress. Nevertheless, creep parameters were evaluated using uniaxial creep tests, which might be the reason for overestimation of creep strains and joint openings.

Moreover, the impact of incorporating plasticity into the steel shell modeling was studied. It was observed that it reduced the working linings' irreversible strains caused by creep, shear failure, and tensile failure, and it reduced the axial stress evidently.

Finally, it should be noted that further research on the combined effect of different irreversible phenomena is necessary to understand the refractory material behavior at high-temperature applications.

6. Acknowledgements

This work was supported by the funding scheme of the European Commission, Marie Skłodowska-Curie Actions Innovative Training Networks in the frame of the project ATHOR - Advanced Thermo-mechanical multiscale modeling of Refractory linings 764987 Grant.

7. References

- [1] G. Wu, W. Yan, S. Schafföner, Y. Dai, B. Han, T. Li, S. Ma, N. Li, G. Li, A comparative study on the microstructures and mechanical properties of a dense and a lightweight magnesia refractories, *Journal of Alloys and Compounds*. 796 (2019) 131–137. <https://doi.org/10.1016/j.jallcom.2019.05.064>.
- [2] S. Smets, S. Parada, J. Weytjens, G. Heylen, P.T. Jones, M. Guo, B. Blanpain, P. Wollants, Behaviour of magnesia-carbon refractories in vacuum-oxygen decarburisation ladle linings, *Ironmaking and Steelmaking*. 30 (2003) 293–300. <https://doi.org/10.1179/030192303225003971>.
- [3] J. Qi, W. Yan, Z. Chen, S. Schafföner, W. Zhou, G. Li, Q. Wang, Preparation and characterization of microporous mullite-corundum refractory aggregates with high strength and closed porosity, *Ceramics International*. 46 (2020) 8274–8280. <https://doi.org/10.1016/j.ceramint.2019.12.056>.
- [4] R.L.G. Oliveira, J.P.C. Rodrigues, J.M. Pereira, P.B. Lourenço, H.U. Marschall, Thermo-mechanical behaviour of refractory dry-stacked masonry walls under uniaxial compression, *Engineering Structures*. 240 (2021). <https://doi.org/10.1016/j.engstruct.2021.112361>.
- [5] Y. Dai, J. Li, W. Yan, C. Shi, Corrosion mechanism and protection of BOF refractory for high silicon hot metal steelmaking process, *Journal of Materials Research and Technology*. 9 (2020) 4292–4308. <https://doi.org/10.1016/j.jmrt.2020.02.055>.

- [6] J. Chen, L. Chen, Y. Wei, N. Li, S. Zhang, Corrosion and penetration behaviors of slag/steel on the corroded interfaces of Al₂O₃-C refractories: Role of Ti₃AlC₂, *Corrosion Science*. 143 (2018) 166–176. <https://doi.org/10.1016/j.corsci.2018.08.022>.
- [7] J. Fruhstorfer, L. Schöttler, S. Dudczig, G. Schmidt, P. Gehre, C.G. Aneziris, Erosion and corrosion of alumina refractory by ingot casting steels, *Journal of the European Ceramic Society*. 36 (2016) 1299–1306. <https://doi.org/10.1016/j.jeurceramsoc.2015.11.038>.
- [8] O. Volkova, D. Janke, Modelling of Temperature Distribution in Refractory Ladle Lining for Steelmaking, *ISIJ International*. 43 (2003) 1185–1190. <https://doi.org/10.2355/isijinternational.43.1185>.
- [9] A. Zimmer, Á.N.C. Lima, R.M. Trommer, S.R. Bragança, C.P. Bergmann, Heat Transfer in Steelmaking Ladle, *Journal of Iron and Steel Research International*. 15 (2008) 11–14. [https://doi.org/10.1016/S1006-706X\(08\)60117-X](https://doi.org/10.1016/S1006-706X(08)60117-X).
- [10] A. Hou, S. Jin, H. Harmuth, D. Gruber, A Method for Steel Ladle Lining Optimization Applying Thermomechanical Modeling and Taguchi Approaches, *JOM*. 70 (2018) 2449–2456. <https://doi.org/10.1007/s11837-018-3063-1>.
- [11] A. Hou, S. Jin, D. Gruber, H. Harmuth, Influence of variation/response space complexity and variable completeness on BP-ANN model establishment: Case study of steel ladle lining, *Applied Sciences (Switzerland)*. 9 (2019). <https://doi.org/10.3390/app9142835>.
- [12] A. Hou, S. Jin, H. Harmuth, D. Gruber, Thermal and Thermomechanical Responses Prediction of a Steel Ladle Using a Back-Propagation Artificial Neural Network Combining Multiple Orthogonal Arrays, *Steel Research International*. 90 (2019). <https://doi.org/10.1002/srin.201900116>.
- [13] R.P. Racher, R.W. McConnell, A. Buhr, Magnesium Aluminate Spinel Raw Materials for High Performance Refractories for Steel Ladles, in: *Proceedings of 43rd Conference of Metallurgy*, 2004.
- [14] M.A.L. Braulio, M. Rigaud, A. Buhr, C. Parr, V.C. Pandolfelli, Spinel-containing alumina-based refractory castables, *Ceramics International*. 37 (2011) 1705–1724. <https://doi.org/10.1016/j.ceramint.2011.03.049>.
- [15] R. Dal Maschio, B. Fabbri, C. Fiori, Industrial applications of refractories containing magnesium aluminate spinel, *Industrial Ceramics*. 8 (1988) 121–126. <https://www.researchgate.net/publication/284418284>.
- [16] R. Sarkar, Refractory applications of magnesium aluminate spinel, *InterCeram: International Ceramic Review*. (2010). <https://www.researchgate.net/publication/279691599>.

- [17] W. Yan, G. Wu, S. Ma, S. Schafföner, Y. Dai, Z. Chen, J. Qi, N. Li, Energy efficient lightweight periclase-magnesium alumina spinel castables containing porous aggregates for the working lining of steel ladles, *Journal of the European Ceramic Society*. 38 (2018) 4276–4282. <https://doi.org/10.1016/j.jeurceramsoc.2018.05.002>.
- [18] C. Ghosh, A. Ghosh, M.K. Haldar, Studies on densification, mechanical, micro-structural and structure-properties relationship of magnesium aluminate spinel refractory aggregates prepared from Indian magnesite, *Materials Characterization*. 99 (2015) 84–91. <https://doi.org/10.1016/j.matchar.2014.11.020>.
- [19] K. Moritz, C.G. Aneziris, Enhancing the thermal shock resistance of alumina-rich magnesium aluminate spinel refractories by an aluminum titanate phase, *Ceramics International*. 42 (2016) 14155–14160. <https://doi.org/10.1016/j.ceramint.2016.06.037>.
- [20] E.Y. Sako, M.A.L. Braulio, D.H. Milanez, P.O. Brant, V.C. Pandolfelli, Microsilica role in the CA6 formation in cement-bonded spinel refractory castables, *Journal of Materials Processing Technology*. 209 (2009) 5552–5557. <https://doi.org/10.1016/j.jmatprotec.2009.05.013>.
- [21] B. Akbari, D. Gruber, S. Jin, H. Harmuth, Investigation of three-stage compressive creep of a spinel forming refractory castable containing 8% MgO, *Ceramics International*. (2021). <https://doi.org/10.1016/j.ceramint.2021.10.103>.
- [22] S. Chatterjee, A. Buhr, R. Kockegey-Lorenz, A. Ranjan Pal, B. Singh, Effectiveness of fired alumina-spinel brick in secondary metallurgy, in: *Unitecr2017*, 2017.
- [23] M. Ali, T. Sayet, A. Gasser, E. Blond, Transient Thermo-Mechanical Analysis of Steel Ladle Refractory Linings Using Mechanical Homogenization Approach, *Ceramics*. 3 (2020) 171–189. <https://doi.org/10.3390/ceramics3020016>.
- [24] Y. Cheng, Y. Zhang, Y. Li, J. Chen, J. Xiao, Y. Wei, G. Liu, G. Li, S. Zhang, N. Li, Degradation behaviors of cement-free corundum-spinel castables in Ruhrstahl Heraeus refining ladle: Role of infiltrated steel, *Ceramics International*. 47 (2021) 32008–32014. <https://doi.org/10.1016/j.ceramint.2021.08.087>.
- [25] J. Chen, Y. Cheng, Y. Li, J. Xiao, Y. Zhang, G. Liu, Y. Wei, G. Li, S. Zhang, N. Li, Formation of ferrosphal layer at the corroded interface between Al₂O₃-spinel refractory and molten steel in RH refining ladle, *Journal of the American Ceramic Society*. 104 (2021) 6044–6053. <https://doi.org/10.1111/jace.17980>.
- [26] M.A.L. Braulio, E.W. Zinngrebe, S.R. van der Laan, V.C. Pandolfelli, Steel ladle well block post mortem analysis, *Ceramics International*. 38 (2012) 1447–1462. <https://doi.org/10.1016/j.ceramint.2011.09.027>.

- [27] G. Li, J. Liu, G. Jiang, H. Liu, Numerical simulation of temperature field and thermal stress field in the new type of ladle with the nanometer adiabatic material, *Advances in Mechanical Engineering*. 7 (2015) 1–13. <https://doi.org/10.1177/1687814015575988>.
- [28] D. Gruber, H. Harmuth, Thermomechanical Behavior of Steel Ladle Linings and the Influence of Insulations, *Steel Research International*. 85 (2014) 512–518. <https://doi.org/10.1002/srin.201300129>.
- [29] A. Gasser, E. Blond, J.-L. Daniel, K. Andreev, Influence of different masonry designs of refractory bottom linings, in: 9th International Masonry Conference, 2014: p. Electronic--file.
- [30] S. Jin, D. Gruber, H. Harmuth, M.H. Frechette, Thermomechanical steel ladle simulation including a Mohr–Coulomb plasticity failure model, *RHI Bull.* 1 (2012) 39–43.
- [31] D. Gruber, H. Harmuth, Durability of Brick Lined Steel Ladles from a Mechanical Point of View, *Steel Research International*. 79 (2008) 913–917. <https://doi.org/10.1002/srin.200806220>.
- [32] F. Damhof, W.A.M. Brekelmans, M.G.D. Geers, Predictive FEM simulation of thermal shock damage in the refractory lining of steelmaking installations, *Journal of Materials Processing Technology*. 211 (2011) 2091–2105. <https://doi.org/10.1016/j.jmatprotec.2011.07.005>.
- [33] S. Yilmaz, Thermomechanical Modelling for Refractory Lining of a Steel Ladle Lifted by Crane, *Steel Research International*. 74 (2003) 485–490. <https://doi.org/10.1002/srin.200300221>.
- [34] T.M.H. Nguyen, E. Blond, A. Gasser, T. Prietl, Mechanical homogenisation of masonry wall without mortar, *European Journal of Mechanics, A/Solids*. 28 (2009) 535–544. <https://doi.org/10.1016/j.euromechsol.2008.12.003>.
- [35] K. Andreev, H. Harmuth, FEM simulation of the thermo-mechanical behaviour and failure of refractories—a case study, *Journal of Materials Processing Technology*. 143–144 (2003) 72–77. [https://doi.org/10.1016/S0924-0136\(03\)00322-4](https://doi.org/10.1016/S0924-0136(03)00322-4).
- [36] M. Ali, T. Sayet, A. Gasser, E. Blond, Computational homogenization of elastic-viscoplastic refractory masonry with dry joints, *International Journal of Mechanical Sciences*. 196 (2021) 106275. <https://doi.org/10.1016/j.ijmecsci.2021.106275>.
- [37] J. Lemaitre, J.L. Chaboche, *Mechanics of solid materials*, Cambridge university press, 1994.
- [38] D.C. Drucker, W. Prager, Soil mechanics and plastic analysis or limit design, *Quarterly of Applied Mathematics*. 10 (1952) 157–165.

- [39] J. Lubliner, J. Oliver, S. Oller, E. Onate, A plastic-damage model for concrete, *International Journal of Solids and Structures*. 25 (1989) 299–326. [https://doi.org/10.1016/0020-7683\(89\)90050-4](https://doi.org/10.1016/0020-7683(89)90050-4).
- [40] D. Vitiello, B. Nait-Ali, N. Tessier-Doyen, T. Tonnesen, L. Laím, L. Rebouillat, D.S. Smith, Thermal conductivity of insulating refractory materials: Comparison of steady-state and transient measurement methods, *Open Ceramics*. 6 (2021). <https://doi.org/10.1016/j.oceram.2021.100118>.
- [41] Diana VITIELLO, L. REBOUILLARSCHASINNEMA, Thermo-physical properties of insulating refractory materials, 2021.
- [42] Dassault systems, ABAQUS (2018) ‘ABAQUS Documentation,’ (2018).
- [43] L. Teixeira, J. Gillibert, T. Sayet, E. Blond, A creep model with different properties under tension and compression — Applications to refractory materials, *International Journal of Mechanical Sciences*. 212 (2021) 106810. <https://doi.org/10.1016/j.ijmecsci.2021.106810>.
- [44] L. Teixeira, S. Samadi, J. Gillibert, S. Jin, T. Sayet, D. Gruber, E. Blond, Experimental Investigation of the Tension and Compression Creep Behavior of Alumina-Spinel Refractories at High Temperatures, *Ceramics*. 3 (2020) 372–383. <https://doi.org/10.3390/ceramics3030033>.
- [45] A. Sidi Mammar, D. Gruber, H. Harmuth, S. Jin, Tensile creep measurements of ordinary ceramic refractories at service related loads including setup, creep law, testing and evaluation procedures, *Ceramics International*. 42 (2016) 6791–6799. <https://doi.org/10.1016/j.ceramint.2016.01.056>.
- [46] S. Jin, D. Gruber, H. Harmuth, R. Rössler, Thermomechanical failure modeling and investigation into lining optimization for a Ruhrstahl Heraeus snorkel, *Engineering Failure Analysis*. 62 (2016) 254–262. <https://doi.org/10.1016/j.engfailanal.2016.01.014>.
- [47] S. Jin, H. Harmuth, D. Gruber, Compressive creep testing of refractories at elevated loads - Device, material law and evaluation techniques, *Journal of the European Ceramic Society*. 34 (2014) 4037–4042. <https://doi.org/10.1016/j.jeurceramsoc.2014.05.034>.
- [48] S. Schachner, S. Jin, D. Gruber, H. Harmuth, Three stage creep behavior of MgO containing ordinary refractories in tension and compression, *Ceramics International*. 45 (2019) 9483–9490. <https://doi.org/10.1016/j.ceramint.2018.09.124>.
- [49] S. Samadi, S. Jin, D. Gruber, H. Harmuth, S. Schachner, Statistical study of compressive creep parameters of an alumina spinel refractory, *Ceramics International*. 46 (2020) 14662–14668. <https://doi.org/10.1016/j.ceramint.2020.02.267>.

- [50] S. Samadi, S. Jin, D. Gruber, H. Harmuth, Creep parameter determination of a shaped alumina spinel refractory using statistical analysis, in: Proceedings of 63rd International Colloquium on Refractories, Raw Materials and Reuse, 2020: pp. 1–5.
- [51] M. Stueckelschweiger, D. Gruber, S. Jin, H. Harmuth, Creep testing of carbon containing refractories under reducing conditions, *Ceramics International*. 45 (2019) 9776–9781. <https://doi.org/https://doi.org/10.1016/j.ceramint.2019.02.013>.
- [52] S. Jin, H. Harmuth, D. Gruber, R. Rössler, Influence of creep on the thermomechanical behavior of a rh-snorkel, in: 14th Biennial Worldwide Congress on Unified International Technical Conference on Refractories, UNITECR 2015, in Conjunction with the 58th International Colloquium on Refractories, 2015.
- [53] E. Dahlem, D. Gruber, T. Auer, H. Harmuth, M. Huger, T. Chotard, Evaluation of the Drucker-Prager parameters (Cohesion and Friction angle) at elevated temperature for two refractories, in: *Refractories-Technology to Sustain the Global Environment*, 2011: p. 93.
- [54] A. Hillerborg, M. Modéer, P.-E. Petersson, Analysis of crack formation and crack growth in concrete by means of fracture mechanics and finite elements, *Cement and Concrete Research*. 6 (1976) 773–781. [https://doi.org/10.1016/0008-8846\(76\)90007-7](https://doi.org/10.1016/0008-8846(76)90007-7).
- [55] S. Samadi, S. Jin, H. Harmuth, Combined damaged elasticity and creep modeling of ceramics with wedge splitting tests, *Ceramics International*. 47 (2021) 25846–25853. <https://doi.org/10.1016/j.ceramint.2021.05.315>.
- [56] Stüeckelschweiger, Gruber, Jin, Harmuth, Wedge-Splitting Test on Carbon-Containing Refractories at High Temperatures, *Applied Sciences*. 9 (2019) 3249. <https://doi.org/10.3390/app9163249>.
- [57] S. Jin, D. Gruber, H. Harmuth, Determination of Young's modulus, fracture energy and tensile strength of refractories by inverse estimation of a wedge splitting procedure, *Engineering Fracture Mechanics*. 116 (2014) 228–236. <https://doi.org/10.1016/j.engfracmech.2013.11.010>.
- [58] M. Sitek, G. Adamczewski, M. Szyszko, B. Migacz, P. Tutka, M. Natorff, Numerical simulations of a wedge splitting test for high-strength concrete, *Procedia Engineering*. 91 (2014) 99–104. <https://doi.org/10.1016/j.proeng.2014.12.021>.
- [59] S. Samadi, S. Jin, D. Gruber, H. Harmuth, A comparison of two damage models for inverse identification of mode I fracture parameters: case study of a refractory ceramic, *International Journal of Mechanical Sciences*. (2021) 106345. <https://doi.org/10.1016/j.ijmecsci.2021.106345>.
- [60] H. Harmuth, E.K. Tschegg, Fracture mechanical characterisation of ordinary ceramic refractory materials, *Veitsch-Radex Rundsch.* (1994) 465–480.

- [61] Y. Dai, D. Gruber, S. Jin, H. Harmuth, Modelling and inverse investigation of the fracture process for a magnesia spinel refractory using a heterogeneous continuum model, *Engineering Fracture Mechanics*. 182 (2017) 438–448. <https://doi.org/10.1016/j.engfracmech.2017.05.005>.
- [62] S. Jin, H. Harmuth, Asymmetric creep modeling of common refractory ceramics with high temperature wedge splitting test, *Engineering Fracture Mechanics*. 252 (2021). <https://doi.org/10.1016/j.engfracmech.2021.107819>.
- [63] German version EN 10028-2:2017., DIN EN 10028-2 (2017) Flat products made of steels for pressure purposes - Part 2: Non-alloy and alloy steels with specified elevated temperature properties, 2017.
- [64] J. Poirier, E. Blond, E. de Bilbao, R. Michel, A. Coulon, J. Gillibert, M. Boussuge, Y. Zhang, D. Ryckelynck, G. Dusserre, T. Cutard, P. Leplay, New advances in the laboratory characterization of refractories: Testing and modelling, *Metallurgical Research and Technology*. 114 (2017). <https://doi.org/10.1051/metal/2017068>.